Hydrogen Abstraction by the Nighttime Atmospheric Detergent NO_3·: Fundamental Principles

Mark Daniel Paradzinsky

Dissertation submitted to the faculty of the Virginia Polytechnic Institute and State University in partial fulfillment of the requirements for the degree of

Doctor of Philosophy
In
Chemistry

James M. Tanko
Richard Gandour
John Matson
Amanda Morris

May 5th, 2021
Blacksburg VA, 24061

Keywords: polar effects, hydrogen atom transfer, laser flash photolysis, nitrate radical, solvent effects, hydrogen bonding,

Hydrogen Abstraction by the Nighttime Atmospheric Detergent NO_3·: Fundamental Principles

Mark D. Paradzinsky

Abstract

The nitrate radical (NO_3·) was first identified as early as the 1881, but its role in atmospheric oxidation has only been identified within recent decades. Due to its high one-electron reduction potential and its reactivity toward a diverse set of substrates, it dominates nighttime atmospheric oxidation and has since been the subject of much work. Despite this, studies on NO_3· hydrogen atom transfer reactions have been somewhat neglected in favor of its more reactive oxidative pathways.

The first section of the dissertation will highlight the role of substrate structure, solvent effects, and the presence of a polar transition state on NO_3· hydrogen abstractions from alcohols, alkanes, and ethers. In this work the acquisition of absolute rate constants from previously unexamined substrates was analyzed alongside a curated list of common organic pollutants degraded through hydrogen atom abstraction. It was found that NO_3· reacts with low selectivity through an early polarized transition state with a modest degree of charge transfer. Compared to the gas-phase, condensed-phase reactions experience rate enhancement—consistent with Kirkwood theory—as a result of the polarized transition state.

These insights are then applied to abstractions by NO_3· from carboxylic acids in the next section. It was found that the rate constants for abstraction of α-carbons were diminished through induction by the adjacent carbonyl compared to the activation seen for the aforementioned substrates. The deactivation of abstraction by the carbonyl was

found to be dramatically reduced as the substrate's alkyl chain was lengthened and/or branched. This apparent change in mechanism coincides with hydrogen abstraction of the alkyl chain for sufficiently large carboxylic acids and rules out the possibility of concerted bond breaking elsewhere in the molecule.

Finally, the dissertation will cover some additional projects related to the overall nature of the work including examination of the kinetics of radical clock systems when complexed with metal ions and the examination of a highly oxidative biosourced monomer.

Hydrogen Abstraction by the Nighttime Atmospheric Detergent NO_3·: Fundamental Principles

Mark D. Paradzinsky

General Audience Abstract

The nitrate radical (NO_3·) was first identified as early as the 1881, but its role in the breakdown of atmospheric pollutants has only been identified within recent decades. Operating primarily at night, NO_3· serves as a major atmospheric oxidant—it breaks down pollutants by reactions that involve the removal of electrons from those substrates. This chemistry is particularly important in understanding the consequences of an increasingly industrialized world and the subsequent short-term health and environmental implications. Geographically, these reactions will occur in large concentrations near locations that contribute greatly to atmospheric pollution, such as above coal-powered plants, heavily industrialized areas, above the canopy of large forests, and immediately behind the engines of airplanes as they move through the sky. The proximity of these locations to large population centers has caused the pollutants to greatly impact human health. These contaminants have been linked to several of the leading global causes of death, such as ischemic heart disease, stroke, and respiratory illnesses.

This dissertation will focus on furthering the understanding of reactions of NO_3· with various classes of substrates. Traditionally, these reactions were examined in the gas-phase, but atmospheric chemistry can also occur within a liquid water environment such as in cloud formation, aerosol particles, and rain droplets. The presence of this liquid water alters the way in which NO_3· reacts with substrates because it can stabilize different orientations of the colliding molecules. Additionally, prior work has not addressed substrates formed from emerging pollution sources such as biodiesel fuels. Since these fuels decompose through alternate

pathways, they generate substrates that have not been previously examined. This work will help to provide a better grasp on the fundamental routes in which the atmosphere is able to undergo self-cleansing process in response to pollution.

Dedication

This dissertation is dedicated to my parents, Michael and Mary Paradzinsky, to my brother, Michael Paradzinsky, and to my wife, Megan Paradzinsky.

Acknowledgments

First I would like to thank my Ph.D. advisor, Dr. Tanko. When we were deciding what groups we would join at the beginning of graduate school, I remember telling Dr. Tanko that it was important I have an advisor that I could learn from both inside and outside the world of chemistry. He has constantly helped me through struggles both in the lab, and in my personal life. He represents the very best an educator can offer. He is kind, compassionate, and patient. He would often make me laugh while spinning off on some tangent. Thank you, Dr. Tanko, for nurturing me throughout graduate school and kicking me into action when I needed it. When I think back on my time as a graduate student, I shall only ever have fond thoughts of you.

I would also like to thank my committee members, Dr. Gandour, Dr. Matson, and Dr. Morris. I have had the privilege of getting away with far too many antics in their classes and appreciate that they allowed me to learn in my own way. Dr. Gandour's punctiliousness has taught me that there is value in doing things the right way; that words have meaning, and that those meanings help to share clear and concise thoughts—*something I pray I managed to accomplish here*. Dr. Matson has challenged me to enhance my lecturing; to find ways to make others engage with my science in a way that is relevant to them. He has encouraged me to think about how others perceive my talk in real time and to adjust accordingly. And finally, Dr. Morris, whose brutal questioning—*at least it always felt that way in the moment but was most likely perfectly fair and reasonable*—challenged me to engage with the chemistry and to grow as a researcher. I appreciate all of your support and patience. I will continue to develop the skills you have all taught me and hope to be able to share similar lessons with others as I progress through my career.

To my friends, who helped to keep me grounded and sane throughout the rollercoaster ride that is graduate school. Josh Wolfgang, thank you for the candid discussions pertaining to anything and everything that we would semi-regularly get involved with. Kearsley Dillon and Ryan Carrazzone, who were always down for anything and always ready to talk chemistry. Thanks to Samantha Scannelli who would often go with me to Panera where I could get stuffed on mac n' cheese and we could talk about our lives. Corrin Lundquist who would often entertain me in her office while I passively worked through issues plaguing me in the lab. She also introduced me to bouldering which has allowed me to exercise while solving puzzles at the same time. I'm sorry that I didn't get to spend more time with all of you, but pandemics, right?

To my family who has shown unconditional support even though I often did not feel like explaining what I was up to. To my parents, who have raised me and been with me through every major accomplishment in my life. I appreciate all of the lessons you've taught me, even when it didn't seem like I was willing to learn/listen, thank you. To my brother, who despite moving so far away, has always made me laugh when I needed it most, thank you. To my wife—well almost wife as of my writing this—thank you. I'm finding it very hard to say what I want here as it all makes for excellent material to include in my vows. So, suffice it to say, I appreciate the support in every aspect of my life. I know you do everything you can to help me and often you do even more. I look forward to spending the rest of my life with you, even if it is in the blistering cold for the foreseeable future. I love all of you to an immeasurable extent.

To anyone that has helped me through this stage of my life and went without mention, I appreciate your support and leave you with a heartfelt thank you.

Table of Contents

List of Figures

Figure A.14. Transient signal for the decay of $NO_3\cdot$ at 635 nm in the presence of *tert*-butyl methyl ether in H_2O generated by laser flash photolysis of 3×10^{-3} mol L^{-1} CKN. The inset depicts a magnified view of the decay profiles for higher concentrations of substrate.
Figure A.15. Plot of the observed rate constant for $NO_3\cdot$ vs. *tert*-butyl methyl ether concentration in CH_3CN (●) and H_2O (●) at 25 °C; the slope is equal to the hydrogen abstraction rate constant ($k_{AN} = 3.0 \times 10^6$ $M^{-1}s^{-1}$, $k_W = 0.8 \times 10^6$ $M^{-1}s^{-1}$).
Figure A.16. Transient signal for the decay of $NO_3\cdot$ at 635 nm in the presence of 1,2-dimethoxyethane in neat CH_3CN generated by laser flash photolysis of 3×10^{-3} mol L^{-1} CKN. The inset depicts a magnified view of the decay profiles for higher concentrations of substrate.
Figure A.17. Transient signal for the decay of $NO_3\cdot$ at 635 nm in the presence of 1,2-dimethoxyethane in H_2O generated by laser flash photolysis of 3×10^{-3} mol L^{-1} CKN. The inset depicts a magnified view of the decay profiles for higher concentrations of substrate.
Figure A.18. Plot of the observed rate constant for $NO_3\cdot$ vs. 1,2-dimethoxyethane concentration in CH_3CN (●) and H_2O (●) at 25 °C; the slope is equal to the hydrogen abstraction rate constant ($k_{AN} = 5.3 \times 10^6$ $M^{-1}s^{-1}$, $k_W = 1.9 \times 10^6$ $M^{-1}s^{-1}$).
Figure A.19. Transient signal for the decay of $NO_3\cdot$ at 635 nm in the presence of bis(2-methoxyethyl) ether in neat CH_3CN generated by laser flash photolysis of 3×10^{-3} mol L^{-1} CKN. The inset depicts a magnified view of the decay profiles for higher concentrations of substrate.
Figure A.20. Transient signal for the decay of $NO_3\cdot$ at 635 nm in the presence of bis(2-methoxyethyl) ether in H_2O generated by laser flash photolysis of 3×10^{-3} mol L^{-1} CKN. The inset depicts a magnified view of the decay profiles for higher concentrations of substrate.
Figure A.21. Plot of the observed rate constant for $NO_3\cdot$ vs. bis(2-methoxyethyl) ether concentration in CH_3CN (●) and H_2O (●) at 25 °C; the slope is equal to the hydrogen abstraction rate constant ($k_{AN} = 8.8 \times 10^6$ $M^{-1}s^{-1}$, $k_W = 3.6 \times 10^6$ $M^{-1}s^{-1}$).
Figure A.22. Transient signal for the decay of $NO_3\cdot$ at 635 nm in the presence of 1,2-bis(2-methoxyethoxy)ethane in neat CH_3CN generated by laser flash photolysis of 3×10^{-3} mol L^{-1} CKN. The inset depicts a magnified view of the decay profiles for higher concentrations of substrate.
Figure A.23. Transient signal for the decay of $NO_3\cdot$ at 635 nm in the presence of 1,2-bis(2-methoxyethoxy)ethane in H_2O generated by laser flash photolysis of 3×10^{-3} mol L^{-1} CKN. The inset depicts a magnified view of the decay profiles for higher concentrations of substrate.
Figure A.24. Plot of the observed rate constant for $NO_3\cdot$ vs. 1,2-bis(2-methoxyethoxy)ethane concentration in CH_3CN (●) and H_2O (●) at 25 °C; the slope is equal to the hydrogen abstraction rate constant ($k_{AN} = 14.0 \times 10^6$ $M^{-1}s^{-1}$, $k_W = 5.4 \times 10^6$ $M^{-1}s^{-1}$).
Figure A.25. Transient signal for the decay of $NO_3\cdot$ at 635 nm in the presence of tetrahydrofuran in neat CH_3CN generated by laser flash photolysis of 3×10^{-3} mol L^{-1} CKN. The inset depicts a magnified view of the decay profiles for higher concentrations of substrate.
Figure A.26. Transient signal for the decay of $NO_3\cdot$ at 635 nm in the presence of tetrahydrofuran in H_2O generated by laser flash photolysis of 3×10^{-3} mol L^{-1} CKN. The inset depicts a magnified view of the decay profiles for higher concentrations of substrate.
Figure A.27. Plot of the observed rate constant for $NO_3\cdot$ vs. tetrahydrofuran concentration in CH_3CN (●) and H_2O (●) at 25 °C; the slope is equal to the hydrogen abstraction rate constant ($k_{AN} = 29.5 \times 10^6$ $M^{-1}s^{-1}$, $k_W = 12.8 \times 10^6$ $M^{-1}s^{-1}$).
Figure A.28. Transient signal for the decay of $NO_3\cdot$ at 635 nm in the presence of 1,3-dioxane in neat CH_3CN generated by laser flash photolysis of 3×10^{-3} mol L^{-1} CKN. The inset depicts a magnified view of the decay profiles for higher concentrations of substrate.

Figure A.29. Transient signal for the decay of $NO_3\cdot$ at 635 nm in the presence of 1,3-dioxane in H_2O generated by laser flash photolysis of 3×10^{-3} mol L^{-1} CKN. The inset depicts a magnified view of the decay profiles for higher concentrations of substrate.
Figure A.30. Plot of the observed rate constant for $NO_3\cdot$ vs. 1,3-dioxane concentration in CH_3CN (●) and H_2O (●) at 25 °C; the slope is equal to the hydrogen abstraction rate constant ($k_{AN} = 4.6 \times 10^6$ $M^{-1}s^{-1}$, $k_W = 1.1 \times 10^6$ $M^{-1}s^{-1}$).
Figure A.31. Transient signal for the decay of $NO_3\cdot$ at 635 nm in the presence of 1,4-dioxane in neat CH_3CN generated by laser flash photolysis of 3×10^{-3} mol L^{-1} CKN. The inset depicts a magnified view of the decay profiles for higher concentrations of substrate.
Figure A.32. Transient signal for the decay of $NO_3\cdot$ at 635 nm in the presence of 1,4-dioxane in H_2O generated by laser flash photolysis of 3×10^{-3} mol L^{-1} CKN. The inset depicts a magnified view of the decay profiles for higher concentrations of substrate.
Figure A.33. Plot of the observed rate constant for $NO_3\cdot$ vs. 1,4-dioxane concentration in CH_3CN (●) and H_2O (●) at 25 °C; the slope is equal to the hydrogen abstraction rate constant ($k_{AN} = 5.0 \times 10^6$ $M^{-1}s^{-1}$, $k_W = 2.1 \times 10^6$ $M^{-1}s^{-1}$).
Figure A.34. Transient signal for the decay of $NO_3\cdot$ at 635 nm in the presence of 1,3,5-trioxane in neat CH_3CN generated by laser flash photolysis of 3×10^{-3} mol L^{-1} CKN. The inset depicts a magnified view of the decay profiles for higher concentrations of substrate.
Figure A.35. Transient signal for the decay of $NO_3\cdot$ at 635 nm in the presence of 1,3,5-trioxane in H_2O generated by laser flash photolysis of 3×10^{-3} mol L^{-1} CKN. The inset depicts a magnified view of the decay profiles for higher concentrations of substrate.
Figure A.36. Plot of the observed rate constant for $NO_3\cdot$ vs. 1,3,5-trioxane concentration in CH_3CN (●) and H_2O (●) at 25 °C; the slope is equal to the hydrogen abstraction rate constant ($k_{AN} = 0.6 \times 10^6$ $M^{-1}s^{-1}$, $k_W = 0.2 \times 10^6$ $M^{-1}s^{-1}$).
Figure A.37. Transient signal for the decay of $NO_3\cdot$ at 635 nm in the presence of diisopropyl ether in neat CH_3CN generated by laser flash photolysis of 3×10^{-3} mol L^{-1} CKN. The inset depicts a magnified view of the decay profiles for higher concentrations of substrate.
Figure A.38. Transient signal for the decay of $NO_3\cdot$ at 635 nm in the presence of diisopropyl ether in 4:6 CH_3CN/H_2O generated by laser flash photolysis of 3×10^{-3} mol L^{-1} CKN. The inset depicts a magnified view of the decay profiles for higher concentrations of substrate.
Figure A.39. Plot of the observed rate constant for $NO_3\cdot$ vs. diisopropyl ether concentration in CH_3CN (●) and 4:6 CH_3CN/H_2O (●) at 25 °C; the slope is equal to the hydrogen abstraction rate constant ($k_{AN} = 14.5 \times 10^6$ $M^{-1}s^{-1}$, $k_W = 7.2 \times 10^6$ $M^{-1}s^{-1}$).
Figure A.40. Transient signal for the decay of $NO_3\cdot$ at 635 nm in the presence of *sec*-butyl methyl ether in neat CH_3CN generated by laser flash photolysis of 3×10^{-3} mol L^{-1} CKN. The inset depicts a magnified view of the decay profiles for higher concentrations of substrate.
Figure A.41. Transient signal for the decay of $NO_3\cdot$ at 635 nm in the presence of *sec*-butyl methyl ether in 4:6 CH_3CN/H_2O generated by laser flash photolysis of 3×10^{-3} mol L^{-1} CKN. The inset depicts a magnified view of the decay profiles for higher concentrations of substrate.
Figure A.42. Plot of the observed rate constant for $NO_3\cdot$ vs. *sec*-butyl methyl ether concentration in CH_3CN (●) and 4:6 CH_3CN/H_2O (●) at 25 °C; the slope is equal to the hydrogen abstraction rate constant ($k_{AN} = 11.2 \times 10^6$ $M^{-1}s^{-1}$, $k_W = 6.3 \times 10^6$ $M^{-1}s^{-1}$).
Figure A.43. Transient signal for the decay of $NO_3\cdot$ at 635 nm in the presence of cyclopentyl methyl ether in neat CH_3CN generated by laser flash photolysis of 3×10^{-3} mol L^{-1} CKN. The inset depicts a magnified view of the decay profiles for higher concentrations of substrate.

Figure A.60. Transient signal for the decay of $NO_3\cdot$ at 635 nm in the presence of 2-methylpentane in neat CH_3CN generated by laser flash photolysis of 3×10^{-3} mol L^{-1} CKN. The inset depicts a magnified view of the decay profiles for higher concentrations of substrate.
Figure A.61. Transient signal for the decay of $NO_3\cdot$ at 635 nm in the presence of 2-methylpentane in 8:2 CH_3CN/H_2O generated by laser flash photolysis of 3×10^{-3} mol L^{-1} CKN. The inset depicts a magnified view of the decay profiles for higher concentrations of substrate.
Figure A.62. Plot of the observed rate constant for $NO_3\cdot$ vs. 2-methylpentane concentration in CH_3CN at 25 °C; the slope is equal to the hydrogen abstraction rate constant ($k_{AN} = 1.1 \times 10^6$ $M^{-1}s^{-1}$).
Figure A.63. Plot of the observed rate constant for $NO_3\cdot$ vs. 2-methylpentane concentration in 8:2 CH_3CN/H_2O at 25 °C; the slope is equal to the hydrogen abstraction rate constant ($k_W = 1.3 \times 10^6$ $M^{-1}s^{-1}$).
Figure A.64. Transient signal for the decay of $NO_3\cdot$ at 635 nm in the presence of 3-methylpentane in neat CH_3CN generated by laser flash photolysis of 3×10^{-3} mol L^{-1} CKN. The inset depicts a magnified view of the decay profiles for higher concentrations of substrate.
Figure A.65. Transient signal for the decay of $NO_3\cdot$ at 635 nm in the presence of 3-methylpentane in 8:2 CH_3CN/H_2O generated by laser flash photolysis of 3×10^{-3} mol L^{-1} CKN. The inset depicts a magnified view of the decay profiles for higher concentrations of substrate.
Figure A.66. Plot of the observed rate constant for $NO_3\cdot$ vs. 3-methylpentane concentration in CH_3CN at 25 °C; the slope is equal to the hydrogen abstraction rate constant ($k_{AN} = 1.2 \times 10^6$ $M^{-1}s^{-1}$).
Figure A.67. Plot of the observed rate constant for $NO_3\cdot$ vs. 3-methylpentane concentration in 8:2 CH_3CN/H_2O at 25 °C; the slope is equal to the hydrogen abstraction rate constant ($k_W = 1.3 \times 10^6$ $M^{-1}s^{-1}$).
Figure A.68. Transient signal for the decay of $NO_3\cdot$ at 635 nm in the presence of 2,3-dimethylbutane in neat CH_3CN generated by laser flash photolysis of 3×10^{-3} mol L^{-1} CKN. The inset depicts a magnified view of the decay profiles for higher concentrations of substrate.
Figure A.69. Transient signal for the decay of $NO_3\cdot$ at 635 nm in the presence of 2,3-dimethylbutane in 8:2 CH_3CN/H_2O generated by laser flash photolysis of 3×10^{-3} mol L^{-1} CKN. The inset depicts a magnified view of the decay profiles for higher concentrations of substrate.
Figure A.70. Plot of the observed rate constant for $NO_3\cdot$ vs. 2,3-dimethylbutane concentration in CH_3CN at 25 °C; the slope is equal to the hydrogen abstraction rate constant ($k_{AN} = 2.3 \times 10^6$ $M^{-1}s^{-1}$).
Figure A.71. Plot of the observed rate constant for $NO_3\cdot$ vs. 2,3-dimethylbutane concentration in 8:2 CH_3CN/H_2O at 25 °C; the slope is equal to the hydrogen abstraction rate constant ($k_W = 1.2 \times 10^6$ $M^{-1}s^{-1}$).
Figure A.72. Reaction of $NO_3\cdot$ with ethers and alcohols in H_2O: Plot of 2.303RT *log*(k_H) vs. the ionization potential of the substrate; ethers (●), alkanes (■), and alcohols (▲) by $NO_3\cdot$.
Figure A.73. Reaction of $NO_3\cdot$ with ethers and alcohols in H_2O: Plot of the experimental vs. predicted value of 2.303RT *log*(k_H/H) on the basis of Eq. 5 (a = 0.26, b = 0.04; R = 0.920); ethers (●), alkanes (■), and alcohols (▲).
Figure A.74. Reaction of $NO_3\cdot$ with ethers, alkanes, and alcohols in the gas-phase: Plot of 2.303RT *log*(k_H) vs. the ionization potential of the substrate; ethers (●), alkanes (■), and alcohols (▲) by $NO_3\cdot$.

List of Tables

List of Schemes

List of Abbreviations

A = pre-exponential factor
α = measure of transition state location, as measured by Evans–Polanyi relationship
BDE = bond dissociation energy
BFDMA = 2, 2'-bifuran-5,5'-dimethanol diacetate
BFE = dimethyl-2,2'-bifuran-5,5'-dicarboxylate
CAN = ceric ammonium nitrate
CH_3CN = acetonitrile
CH_3CO_2H = acetic acid
CKN = ceric potassium nitrate
DMSO = dimethyl sulfoxide
DSC = differential scanning calorimetry
$\mathcal{E}$ = dielectric constant
E_a = activation energy
ΔH° = change in standard enthalpy of reaction
H-bonding = hydrogen bonding
HAT = hydrogen atom transfer
HBEBF = bis (2-hydroxyethoxy) 2,2'-bifuran-5,5'-dicarboxylate
HCO_2H = formic acid
H_2O = water
HNO_3 = nitric acid
$HO\cdot$ = hydroxyl radical
IP = ionization potential
J_o = steady state flux
k = rate constant
kcal = kilocalorie
l = average thickness
LFP = laser flash photolysis
KOH = potassium hydroxide
LFP = laser flash photolysis
μ = dipole moment
M = molarity
mol = mole
N = Avogadro's number
Nd:YAG = neodymium-doped yttrium aluminum garnet
η_{inh} = inherent viscosity
nm = nanometer
NMR = nuclear magnetic resonance
$NO_3\cdot$ = nitrate radical
N_2O_5 = dinitrogen pentoxide
ns = nanosecond
O_3 = ozone
P = permeability
Δp = permeant gas pressure drop
PCET = proton-coupled electron-transfer
PEBF = poly(ethylene 2,2'-bifuran-5,5'dicarboxylate)

PEF = poly(ethylene furanoate)
PET = poly(ethylene terephthalate)
ppt = parts per trillion
r = radius
R = correlation
R = gas constant
s = second
SEC = size exclusion chromatography
T = temperature
T_g = glass transition temperature
UV = ultraviolet
V = volts

Attributions

The work described herein was aided by several colleagues. A brief description of their contributions is included in this section.

Chapter 1: Mark Paradzinsky (graduate student, Department of Chemistry, Virginia Tech) performed the writing and editing of this chapter. James M. Tanko (Ph.D., Department of Chemistry, Virginia Tech) is the advisor and committee chair who provided guidance, writing, and editing of this chapter.

Chapter 2: Mark Paradzinsky (graduate student, Department of Chemistry, Virginia Tech) performed most of the experimentation, writing, and editing of this chapter. Diego Troya (Ph.D., Department of Chemistry, Virginia Tech) provided computational support, writing, and editing of this chapter. James M. Tanko (Ph.D., Department of Chemistry, Virginia Tech) is the advisor and committee chair who provided guidance, writing, and editing of this chapter.

Chapter 3: Mark Paradzinsky (graduate student, Department of Chemistry, Virginia Tech) performed most of the data curation, writing, and editing of this chapter. Aditya Ponukumati (undergraduate student, Department of Chemistry, Virginia Tech) provided experimental assistance for this chapter. James M. Tanko (Ph.D., Department of Chemistry, Virginia Tech) is the advisor and committee chair who provided guidance, writing, and editing of this chapter.

Chapter 4: Marwa K. Abdel Latif (Ph.D., Department of Chemistry, Virginia Tech) performed most of the experimentation, writing, and editing of this chapter. Jared N. Spencer (Ph.D., Department of Chemistry, Virginia Tech) provided computational support, writing, and editing of this chapter. Mark Paradzinsky (graduate student, Department of Chemistry, Virginia Tech) provided experimental assistance and editing of this chapter. James M. Tanko (Ph.D.,

Department of Chemistry, Virginia Tech) is the advisor and committee chair who provided guidance, writing, and editing of this chapter.

Chapter 5: H. Eliot Edling (Ph.D., Department of Chemistry, Virginia Tech) performed most of the methodology, writing, and editing of this chapter. Hua Sun (Ph.D., Department of Electrical Engineering, University of North Texas) provided data curation and formal analysis for this chapter. Edward Paschke (Ph.D., BP Petrochemicals) provided guidance for this chapter. David A. Schiraldi (Ph.D., Department of Macromolecular Science & Engineering, Case Western Reserve University) provided guidance, writing, and editing of this chapter. James M. Tanko (Ph.D., Department of Chemistry, Virginia Tech) provided guidance, writing, and editing of this chapter. Mark Paradzinsky (graduate student, Department of Chemistry, Virginia Tech) provided experimental assistance and writing of this chapter. S. Richard Turner (Ph.D., Department of Chemistry, Virginia Tech) is the advisor and committee chair who provided guidance, writing, and editing of this chapter.

Chapter 1. Nitrate Radical as an Atmospheric Cleansing Agent

1.1 Introduction and Motivation

Along with increasing globalization and industrialization, the consumption of fossil fuels has exploded in recent decades, nearly doubling since the 1980s.[1] This has led to an increase in the use of diesel vehicles, waste and crop burning, and coal-fired power plants. When combined with biogenic sources such as isoprene emission from broadleaf trees,[2] levels of organic pollutants in the atmosphere have only increased. In addition to the long-term consequences of global warming, there are also many short-term implications from excess levels of organic pollutants.

Micro-scale particles generated when fossil fuels are burned contribute to ambient air pollution. The World Health Organization determined that 6.4 million premature deaths were caused by contaminated air in 2015, of which 4.2 million were from ambient air pollution.[3] By 2060, this figure is predicted to rise by more than 50%. Polluted air directly impacts ischemic heart disease, stroke, and respiratory illnesses, three of the leading global causes of death.[3]

Polluted air can also impact humans indirectly. Atmospheric organic acids, byproducts of combustion and isoprene oxidation, can also impact the climate on a more immediate timescale. Formic acid is believed to contribute 30–50% of summertime rainwater acidity in the southeastern United States.[2] Acid rain has many downstream implications including acid deposition, soil and water acidification, and weathering.[4] While the atmosphere has methods of self-cleansing through free radical reactions, these reactions are not yet fully understood.

1.2 $NO_3\cdot$ as an Atmospheric "Detergent"

1.2.1 Atmospheric Generation of Nitrate Radical

There exist several reactive pathways to generate nitrate radical ($NO_3\cdot$) in the atmosphere including reactions of other radical species and photolytic processes. However, the primary source of these radicals are reactions of ozone (O_3) with $NO_2\cdot$ to form $NO_3\cdot$.[5]

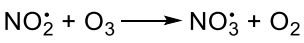

$$NO_2^{\bullet} + O_3 \longrightarrow NO_3^{\bullet} + O_2 \quad (1)$$

Since $NO_3\cdot$ also exists in equilibria with dinitrogen pentoxide (N_2O_5) and is often generated from the homolytic cleavage of N_2O_5 for gas-phase studies, the origin of N_2O_5 in the atmosphere is ultimately dependent upon the reactions of O_3.[5]

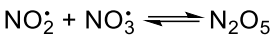

$$NO_2^{\bullet} + NO_3^{\bullet} \rightleftharpoons N_2O_5 \quad (2)$$

While $NO_3\cdot$ is continuously generated during the day, it rapidly photo-dissociates into NO_x gases and consequently its concentration peaks at night.[5]

$$NO_3^{\bullet} + h\nu \longrightarrow NO^{\bullet} + O_2 \quad (3a)$$

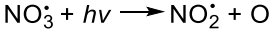

$$NO_3^{\bullet} + h\nu \longrightarrow NO_2^{\bullet} + O \quad (3b)$$

Although the abundance of $NO_3\cdot$ (peaking between 10–100 ppt)[6] must always be lower than O_3, which itself is an atmospheric oxidizing agent, its reaction with organic pollutants constitutes a major oxidative pathway within the atmosphere due to markedly higher reactivity than O_3.

1.2.2 Comparisons to Hydroxyl Radical

The most prominent oxidizing agent in the atmosphere is hydroxyl radical ($HO\cdot$), which operates primarily during the day as it is a byproduct of the photolytic cleavage of O_3 in the presence of water vapor. Reactions of $HO\cdot$ have been exhaustively examined due to its relevance not only in the atmosphere, but because of its role as a reactive oxygen species within the body, where it is produced endogenously.[7–9] The effectiveness of $HO\cdot$ and $NO_3\cdot$ in cleansing organic pollutants from the atmosphere stems from their highly reactive oxidative ability; the aqueous one-electron reduction potential of $HO\cdot$ and $NO_3\cdot$ are 2.81 V[10] and 2.49 V,[11] respectively.

Because HO· and NO_3· are so highly electrophilic, they are able to break down several classes of organic pollutants by initiating oxidative chain reactions. The mechanisms by which initiation occurs differs depending upon the functionality of the substrate. NO_3· is often considered a less reactive version of HO· as they have overlapping roles and chemistries. For compounds with saturated aliphatic regions, such as alkanes and alcohols, hydrogen abstraction is the dominant pathway for both radicals. When unsaturation is introduced, namely as alkenes, electrophilic addition dominates. However, in aromatic compounds, the radicals undergo diverse chemistries with NO_3· reacting via hydrogen abstraction, electron-transfer, and electrophilic addition.[5,7,12]

1.2.3 Hydrogen Atom Transfer Mechanisms

The oxidation of hydrocarbons, alcohols, and ethers (which react at the α-carbon)[13,14] begins with abstraction of a hydrogen atom. These reactions are thought to occur through the classical hydrogen atom transfer (HAT) mechanism by which the radical abstracts a H-atom through a linear transition structure.

$$NO_3^{\bullet} + H{-}CH_3 \longrightarrow HNO_3 + CH_3^{\bullet} \quad (4)$$

Abstractions of hydrogen from alkanes is expected to depend on the strength of the C-H bonds which are directly related to the stability of the alkyl radical formed. The predicted reactivity trend, based upon bond strengths (kcal mol^{-1}), is therefore 3° (95) > 2° (98) > 1° (102) which matches experimental observation.[5,14] The same trend has also been identified at the α-carbon of alcohols, 3° (92) > 2° (93) > 1° (98). For ethers, the C-H bond strength (93) appears less dependent on the alkyl group, although there are fewer experimental determinations. In agreement with the bond enthalpies, gas-phase reaction rate constants for alcohols and ethers with NO_3· tend to be an order of magnitude larger than alkanes because of resonance stabilization by the non-bonding electron pair on oxygen (Figure 1.1). Reaction rate constants for

alkanes and saturated alcohols with $NO_3\cdot$ have been reported between 10^4-10^5 M^{-1} s^{-1}.[5,14,15] The rate constants for the handful of ethers that have been reported are more reactive ($\approx 10^6$ M^{-1} s^{-1}), presumably because the O-atom is able to activate additional C-H bonds.[5,16,17]

Figure 1.1. The resonance contribution from the hydroxyl group following the abstraction of hydrogen at the α-carbon of alcohols.

Reports describing the reactions of $NO_3\cdot$ with carboxylic acids are noticeably absent from the literature. Studies of $HO\cdot$ reactions with carboxylic acids have been examined in the gas-phase. Primary isotope effects ($k_{O\text{-}H}/k_{O\text{-}D} \approx 6$) have been observed for reactions with formic (HCO_2H) and acetic acid (CH_3CO_2H) at the CO_2H moiety. This suggests that the hydrogen atom abstraction breaks the stronger O-H bond (112 ± 3 kcal mol^{-1}), rather than the weaker C-H bonds (96 ± 1 kcal mol^{-1}) of HCO_2H and CH_3CO_2H.[18,19] Butkovskaya et al. analyzed reactions of $HO\cdot$ with acetic acid and found CO_2 to be a product of the reaction, i.e., abstraction of hydrogen from COO-H generates a carboxyl radical that subsequently decarboxylates.[20] These experimental findings have received computational support by Anglada who examined $HO\cdot$ reactions with HCO_2H.[21] Anglada found that abstraction from the carboxyl group proceed through a low energy intermediate (E_a = 0.51 kcal mol^{-1}) via proton-coupled electron-transfer (PCET). PCET is an alternative HAT mechanism by which electron-transfer to the radical and abstraction of the proton occur from different orbitals (Figure 1.2).

A different coupled mechanism has been proposed for reactions of carboxylic acids with *tert*-butoxyl radical. Denisov and Shestakov proposed that abstractions from RCO_2H may be coupled to C-C bond cleavage, whereby the decarboxylation products are generated with

hydrogen abstraction.[22] They suggest that these reactions are a rare example of a decrease in activation energy (compared to a step-wise process) even though more atoms are involved in the transition state.

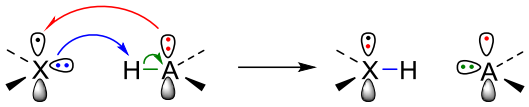

Figure 1.2. The proton transfer and electron transfer occur from different orbitals in proton-coupled electron-transfer.

For a classical HAT, Anglada also noted that abstraction from the C-H bond has a marginally higher activation energy (E_a = 1.17 kcal mol^{-1}). Follow–up ab initio calculations by Sun et al. examined HO· with valeric acid (*n*-$C_4H_9CO_2H$). The authors report that abstractions of β- and γ-hydrogens dominate the reaction pathways, and that classical HAT initiates the oxidative degradation. This change in mechanism is noted in solution and will be discussed below.

Additional HAT mechanisms exist, e.g., single electron transfer-proton transfer and sequential proton-loss electron-transfer,[23] although, there is insufficient evidence they occur for gaseous NO_3· reactions with saturated substrates.

1.2.4 Electrophilic Addition and Electron-Transfer Processes

By far the most reactive pathway for NO_3· is electrophilic addition to π-bonds, with rate constants for gas-phase reactions with unsaturated substrates (ca. 10^8 M^{-1} s^{-1}) being several orders of magnitude greater than the HAT mechanisms.

$$NO_3^{\cdot} + H_2C{=}CH_2 \longrightarrow O_2NO\text{-}CH_2\dot{C}H_2 \qquad (5)$$

The high rate constants for these reactions has drawn considerable interest and thus has been exhaustively studied. A good deal of work has also been done on reactions with aromatic

compounds that proceed primarily through an electron-transfer mechanism. Other mechanisms for aromatic compounds include electrophilic addition with phenols ($k \approx 10^8$ M^{-1} s^{-1})[12] and HAT with monoalkylbenzenes ($k \approx 10^5$ M^{-1} s^{-1}).[24]

(6)

The gas-phase represents a major component of the atmosphere, however, reactions may also occur as clouds develop, within particulate matter, and in the microreactors of rain droplets.[25] To understand these additional facets of the atmosphere, several studies have examined these reactions in solution.

1.3 Solution-Phase Reactions of NO_3·

1.3.1 Comparison to Gas-Phase

To study alkanes in solution, a solvent other than H_2O must be used due to poor hydrocarbon solubility. As a results, these are generally lacking compared to available gas-phase data. Alfassi et al. reports rate constants of 5.9×10^5 M^{-1} s^{-1} and 1.0×10^6 M^{-1} s^{-1} for NO_3· abstractions from *n*-hexane and cyclohexane, respectively, in acetonitrile (CH_3CN).[14] The authors note that NO_3· reacts with CH_3CN with a second order rate constant $\leq 10^3$ M^{-1} s^{-1}.

Reactions with alcohols have received more attention, being studied in both CH_3CN and H_2O. Reaction rate constants are on the order of $\approx 10^6$ M^{-1} s^{-1} and reactions are faster in CH_3CN than H_2O.[14,26,27] Mezyk et al. also examined reactions in *tert*-butanol with rate constants an additional order of magnitude greater than CH_3CN. The authors attribute the increase in rate across the three solvents to a "decreasing dielectric strength that allows for increase mobility of NO_3·."[26] Studies by Ito et al. and Alfassi et al. attribute the increase in rate going from H_2O to CH_3CN to the polar effect (*vide infra*), albeit for different reasons.[14,27]

In solution, there exists just three reports on the reaction of $NO_3\cdot$ with saturated carboxylic acids. Dogliotti and Hayon first report rate constants in H_2O for HCO_2H (2.1×10^5 M^{-1} s^{-1}) and CH_3CO_2H (4.6×10^4 M^{-1} s^{-1}).[28] As their study focused on generating $NO_3\cdot$ from ceric salts, they report no discussion of the chemistry involved with the substrates and provide no evidence for hydrogen abstraction. Martin, Swift, and Venable report that hydrogen abstraction by $NO_3\cdot$ from acetic and propionic acid result in decarboxylation products; their discussion is brief and only qualitative in nature with no reported rate constants.[29] Neta and Huie remeasured the rate constant for HCO_2H ($<1.0 \times 10^5$ M^{-1} s^{-1}) in H_2O, commenting only that the value is "in agreement with the high C-H bond strength of formic acid" when compared to hydrogen abstraction rate constants from alcohols.[30]

As the nature of the reaction between $NO_3\cdot$ and various carboxylic acids is relatively unexplored, a comparative analysis of the reaction of $HO\cdot$ with RCO_2H will be discussed. Taniguchi et al. examined reactions of branched carboxylic acids with $HO\cdot$ by electron spin resonance.[31] The authors found that abstractions from C-H bonds are least reactive at the α-carbon, more reactive at terminal-methyl groups, and most reactive in-between. This was attributed to the polar effect. A similar result was found by Serpone et al. who monitored aqueous reactions of unbranched carboxylic acids, chain lengths C1–C5, by high-performance liquid chromatography.[32]

1.3.2 Polarized Transition Structures

The concept of the polar effect is that the energy level of a highly polarized transition state, i.e., a transition state in which a large electronegativity difference exists across the reaction coordinate, may be altered by solvent and/or substituent effects. In a polar protic solvent, for example, hydrogen bonding to the intermediate could provide stability and lower the reaction

barrier (Figure 1.3). However, the energy level of the transition state could also increase if the substrate contains a substituent that competes for electron density, as in the case of halogens and carbonyls. Prior work in our group has shown that HO· abstractions from alkanes and the α-carbon of alcohols and ethers experience significant rate enhancement in H_2O compared to CH_3CN.[13]

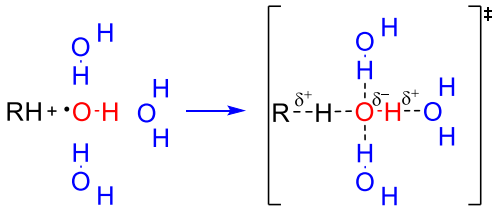

Figure 1.3. Hydrogen atom abstractions by hydroxyl radical from organic substrates leads to the formation of a polarized transition structure. In an aqueous solvent the transition structure is stabilized by H-bonding.

Ito et al. identified the development of a polar transition structure for abstraction at the α-carbon for reactions between NO_3· and alcohols.[27] However, the solvent effect noted by the authors was that rate constants for reactions in CH_3CN were higher than those in H_2O. They propose that hydrogen bonding interactions to both reactants, NO_3· and the substrate (alcohols), reduce reaction rates because the water molecules need to be displaced before the reaction can proceed. The authors also briefly suggest an interaction between the oxygen atom of H_2O and the electron-deficient oxygen radical center.

Alfassi et al. identified the same rate enhancement in CH_3CN compared to H_2O, adding that reactions with alkanes in CH_3CN occur faster than the gaseous reactions. Alfassi et al. instead suggest that the solvent effect is the result of NO_3· being less polar as a reactant, due to its high symmetry, compared to the transition state where a loss of symmetry increases the complex's polarity, thus strengthening solvation. The authors rationalize a stronger effect in

CH_3CN despite water being more polar due to the nature of solvation within each solvent; CH_3CN solvation is primarily through dipolar interactions while hydrogen bonding is the major influence on solvation in H_2O.

1.3.3 Generation of $NO_3\cdot$ in Solution

$NO_3\cdot$ is unsurprisingly generated from nitrates in solution due to their widespread commercial availability, low cost, and high solubility in polar solvents. Selection of the radical precursor is often dependent on the technique used to study the radical. Pulse radiolysis, for example, generates $NO_3\cdot$ directly from concentrated nitric acid (HNO_3) or sodium nitrate.[5] Ceric nitrate salts may also be used to obtain $NO_3\cdot$ through flash photolysis.[5,14,27] Both of these methods are also capable of indirectly forming $NO_3\cdot$ through the interconversion of other radicals, e.g. $HO\cdot$ or sulfate radical.[11,33]

1.4 Transient Absorption Spectroscopy

1.4.1 Laser Flash Photolysis

The short-lived nature of $NO_3\cdot$ makes transient absorption spectroscopy the ideal method for monitoring its reactions in solution. Laser flash photolysis (LFP) is a modular, ultrafast spectroscopic technique that was invented by George Porter who later won the 1967 Nobel Prize for its creation.[34] Principally, LFP works via laser excitation of a sample to generate a photo-active transient species that is spectroscopically monitored over its lifetime (Figure 1.4).

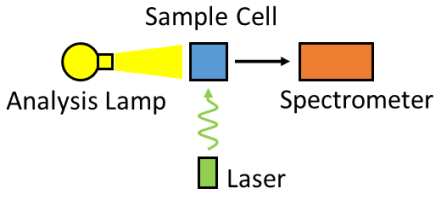

Figure 1.4. Schematic of a laser flash photolysis spectrometer.

Typically, a nitrogen or neodymium-doped yttrium aluminum garnet generates the transient species on the nanosecond timescale, however titanium sapphire lasers have been used for femtosecond LFP.[35] The transient species is then monitored by absorbance, fluorescence, or phosphorescence.

1.4.2 Spectro-Kinetic Instrumentation

Our system is comprised of an Applied Photophysics LKS.80 spectrometer that uses the third harmonic of a Continuum Surelite I-10 Nd:YAG laser (4–6 ns pulse, 355 nm). A Hewlett–Packard Infinium digital oscilloscope is used to monitor the transient signals which are analyzed using the Applied Photophysics Spectra Kinetic Workstation software (version 4.59). A VWR Scientific Products (PolyScience) variable temperature-circulating bath (model 1150-A) was connected to the sample holder. The temperature of the external walls of the cuvette were measured with a thermocouple.

1.4.3 LFP of Ceric Nitrate Salts

Ceric ammonium nitrate (CAN, $(NH_4)_2[Ce^{IV}(NO_3)_6]$) and ceric potassium nitrate (CKN, $K_2[Ce^{IV}(NO_3)_6]$) have been established as successfully generating $NO_3\cdot$ in CH_3CN and H_2O.[5,14,27,36] It should be noted that reactions of CAN in water disrupt the ceric coordination sphere and inhibit the production of $NO_3\cdot$. This is remedied either by adding HNO_3 to solution until 2 M acid is present to drive the equilibria toward $[Ce^{IV}(NO_3)_6]^{2-}$, or through the use of CKN. Upon photolysis at 355 nm, the Ce(IV) complex undergoes an intramolecular electron-transfer that results in $NO_3\cdot$ generation, observable at 600, 635 (peak), and 675 nm.[29,37] The decay profile of $NO_3\cdot$ in the absence of substrate is attributed to the back reaction of the Ce(III) complex.

$$[Ce^{IV}(NO_3)_6]^{2-} \rightleftharpoons NO_3^{\bullet} + [Ce^{III}(NO_3)_5]^{2-} \quad (7)$$

1.5 Metal Ion Complexation to Radical Clocks

1.5.1 Evidence for Rate Enhancement

The rate constants for hydrogen atom abstractions have also been measured through competition kinetics with radical clocks.[38] Radical clocks are reactions with known absolute rate constants, typically unimolecular fragmentations or rearrangements.[39] The rate constants for these reactions have long been thought to be resistant to changes in their chemical environment. Propagation rate constants for the free radical polymerization of olefins have been shown to increase in the presence of Li^+ which coordinate to the double bond and lower the activation energy.[40–43] This led Horn and Clark to hypothesize that metal ion complexation could make radical clocks run fast.[44] The authors computationally examined the cyclization of Δ^5-hexenyl radical in the presence of alkali metals in both explicit polar solvation and the gas-phase (Scheme 1.1).

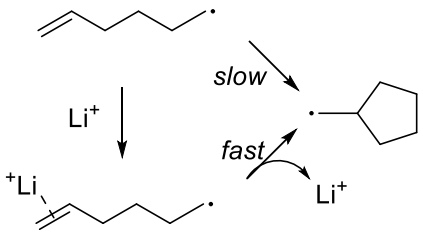

Scheme 1.1. The cyclization rate of Δ^5-hexenyl radical was predicted to increase in the presence of lithium ion that complexes with the double bond.

1.5.2 Hydrogen Abstraction Competition Kinetics

Walling et al. used the radical clock reaction of β-scission for *tert*-butoxyl radical to map the rate constants for the competing hydrogen abstraction reaction. Walling and Wagner have also proposed that the rate constant for β-scission, k_β, increases with solvent polarity due to the increase in dipole moment of the transition structure;[45] this hypothesis was later confirmed.[46–48]

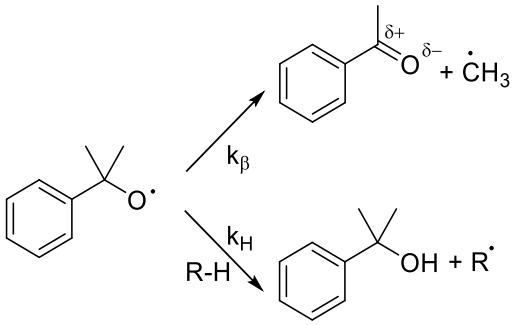

Scheme 1.2. The competing pathways of cumyloxyl radical: hydrogen abstraction from a substrate to form cumyl alcohol, the β-scission self-reaction to form acetophenone.

Cumyloxyl radical has been shown to have the same reactivity as *tert*-butoxyl radical and undergoes the same β-scission process (Scheme 1.2). Cumyloxyl radical also has a spectroscopic signature at 485 nm which allows for these reactions to be easily monitored by LFP.

1.6 Electrochemical Examination of Furan- and Bifuran-Ester Monomers

1.6.1 Commercial Feasibility of a Biosourced Polyester

One of the more commercially successful polymers, poly(ethylene terephthalate) (PET) (Figure 1.5) has seen widespread applications in single-use plastics, fibers, and composites. One of the drawbacks of PET is the modest glass transition temperature (T_g) of 76 °C which limits its use in applications where a higher heat tolerance is needed, dishwasher safe products, hot food/beverage packaging, etc. PET also suffers from a modest amount of oxygen permeability which can lead to food spoilage and oxidation of packaged materials. The biosourced polyester, poly(ethylene furanoate) (PEF) (Figure 1.5) has recently been the subject of considerable interest for replacing PET. The physical properties of these two polymers somewhat overlap, however PEF demonstrates a 10-fold decrease in oxygen permeability, and a marginally higher T_g, 85 °C.[49]

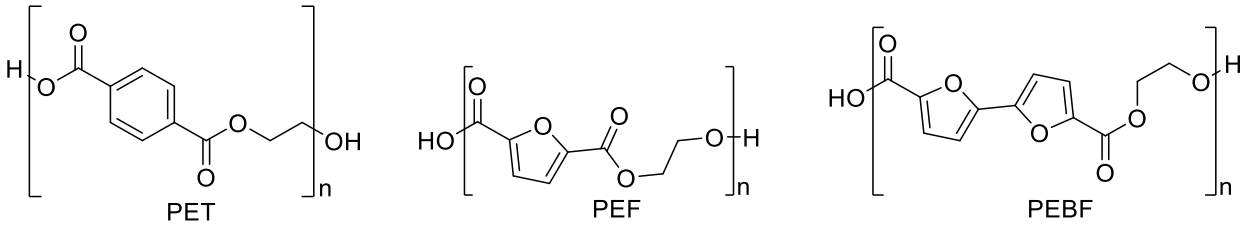

Figure 1.5. Structures of poly(ethylene terephthalate), poly(ethylene furanoate), poly(ethylene bifuranoate).

A new polyester, poly(ethylene 2,2'-bifuran-5,5'-dicarboxylate) (PEBF) (Figure 1.5) has been reported with a higher oxygen barrier, UV absorbance that protects against photodegradation, and good thermal resistance, T_g = 106 °C. However, cast and compression molded films displayed extreme brittleness.

1.6.2 Redox Stability

Early attempts at the polymerization of dimethyl-2,2'-bifuran-5,5'-dicarboxylate (BFE) via standard melt phase polycondensation conditions were observed to darken in color over time. Oxidation of the BFE monomer was suspected to be the source of the color change; the equivalent monofuran ester monomer also oxidized, albeit to a lesser visual extent. Cyclic voltammetry was employed to examine the difference in redox behavior of three furan- and bifuran-ester based monomers.

1.6.3 Electrochemical Instrumentation

Cyclic voltammetry was performed with an EG&G Princeton Applied Research Model 283 Potentiostat/Galvanostat. A five-neck electrochemical cell was outfitted with a glassy carbon working, a platinum coil auxiliary electrode, a Ag/Ag^+ reference electrode, an inlet, and an outlet for nitrogen purging. Princeton Applied Research Electrochemistry Powersuite software (version 2.58) was used for analysis.

1.7 Scope of Dissertation

This dissertation will address key features of $NO_3\cdot$ reactivity to further the fundamental understanding of the atmosphere. The polar effect was first examined for alkanes, alcohols, and ethers (Chapter 2) by expanding the availability of hydrogen abstraction rate constant data for alkanes and ethers in CH_3CN, H_2O, and solvent mixtures. The influence of the polar effect was then examined for saturated carboxylic acids (Chapter 3) where an electron-withdrawing moiety is adjacent to abstractable hydrogens for mechanistic insights. Next, this thesis will also highlight contributions on the study of metal ions complexation influence on radical clocks (Chapter 4) and the potential for rate enhancement in these otherwise chemically robust reactions. Lastly, this work features an electrochemical examination on the redox stability of furan- and bifuran-ester monomers (Chapter 5) for melt-phase polycondensation.

1.8 References

(1) Smil, V. *Energy Transitions: Global and National Perspectives*, Second Edi.; Praeger.

(2) Link, M. F.; Nguyen, T. B.; Bates, K.; Müller, J. F.; Farmer, D. K. Can Isoprene Oxidation Explain High Concentrations of Atmospheric Formic and Acetic Acid over Forests? *ACS Earth Sp. Chem.* **2020**, *4* (5), 730–740. https://doi.org/10.1021/acsearthspacechem.0c00010.

(3) Landrigan, P. J. Air Pollution and Health. *Lancet Public Health* **2017**, *2* (1), e4–e5.

(4) Friedman, B.; Link, M. F.; Fulgham, S. R.; Brophy, P.; Galang, A.; Brune, W. H.; Jathar, S. H.; Farmer, D. K. Primary and Secondary Sources of Gas-Phase Organic Acids from Diesel Exhaust. *Environ. Sci. Technol.* **2017**, *51* (18), 10872–10880. https://doi.org/10.1021/acs.est.7b01169.

(5) Wayne, R. P.; Barnes, I.; Biggs, P.; Burrows, J. P.; Canosa-Mas, C. E.; Hjorth, J.; Le Bras,

G.; Moortgat, G. K.; Perner, D.; Poulet, G.; Restelli, G.; Sidebottom, H. The Nitrate Radical: Physics, Chemistry, and the Atmosphere. *Atmos. Environ. Part A, Gen. Top.* **1991**, *25* (1), 1–203.

(6) Platt, U. F.; Winer, A. M.; Biermann, H. W.; Atkinson, R.; Pitts, J. N. *Measurement of Nitrate Radical Concentrations in Continental Air*; 1984; Vol. 18.

(7) Atkinson, R. Kinetics and Mechanisms of the Gas-Phase Reactions of the Hydroxyl Radical with Organic Compounds under Atmospheric Conditions. *Chem. Rev.* **1985**, *85*, 69–201.

(8) Rafat Husain, S.; Cillard, J.; Cillard, P. Hydroxyl Radical Scavenging Activity of Flavonoids. *Phytochemistry* **1987**, *26* (9), 2489–2491. https://doi.org/10.1016/S0031-9422(00)83860-1.

(9) Lipinski, B. Hydroxyl Radical and Its Scavengers in Health and Disease. *Oxidative Medicine and Cellular Longevity*. 2011. https://doi.org/10.1155/2011/809696.

(10) Koppenol, W. H.; Liebman, J. F. The Oxidizing Nature of the Hydroxyl Radical. A Comparison with the Ferryl Ion (FeO2+). *J. Phys. Chem.* **1984**, *88* (1), 99–101.

(11) Jiang, P. Y.; Katsumura, Y.; Ishigure, K.; Yoshidalb, Y. Reduction Potential of the Nitrate Radical in Aqueous Solution. *Inorg. Chem.* **1992**, *31* (24), 5135–5136.

(12) Nakano, Y.; Matsuda, S.; Ishiwata, T. Kinetics and Mechanism of the Gas-Phase Reaction of Nitrate Radical with Phenol. *React. Kinet. Mech. Catal.* **2016**, *118* (2), 349–363. https://doi.org/10.1007/s11144-016-1001-1.

(13) Mitroka, S.; Zimmeck, S.; Troya, D.; Tanko, J. M. How Solvent Modulates Hydroxyl Radical Reactivity in Hydrogen Atom Abstractions. *J. Am. Chem. Soc.* **2010**, *132* (9), 2907–2913.

(14) Alfassi, Z. B.; Padmaja, S.; Neta, P.; Huie, R. E. Rate Constants for Reactions of NO3• Radicals with Organic Compounds in Water and Acetonitrile. *J. Phys. Chem.* **1993**, *97* (15), 3780–3782.

(15) Aschmann, S. M.; Atkinson, R. Rate Constants for the Reactions of the NO3 Radical with Alkanes at 296 ± 2 K. *Atmos. Environ.* **1995**, *29* (17), 2311–2316.

(16) Chew, A. A.; Atkinson, R.; Aschmann, S. M. Kinetics of the Gas-Phase Reactions of NO3 Radicals with a Series of Alcohols, Glycol Ethers, Ethers and Chloroalkenes. *J. Chem. Soc. - Faraday Trans.* **1998**, *94* (8), 1083–1089. https://doi.org/10.1039/a708183i.

(17) Zhu, J.; Wang, S.; Tsona, N. T.; Jiang, X.; Wang, Y.; Ge, M.; Du, L. Gas-Phase Reaction of Methyl n-Propyl Ether with OH, NO3, and Cl: Kinetics and Mechanism. *J. Phys. Chem. A* **2017**, *121* (36), 6800–6809.

(18) Blanksby, S. J.; Ellison, G. B. Bond Dissociation Energies of Organic Molecules. *Acc. Chem. Res.* **2003**, *36* (4), 255–263.

(19) Luo, Y. R. *Comprehensive Handbook of Chemical Bond Energies*, 1st Ed.; CRC Press: Boca Raton, 2007.

(20) Butkovskaya, N. I.; Kukui, A.; Pouvesle, N.; Le Bras, G. Rate Constant and Mechanism of the Reaction of OH Radicals with Acetic Acid in the Temperature Range of 229-300 K. *J. Phys. Chem. A* **2004**, *108* (34), 7021–7026. https://doi.org/10.1021/jp048444v.

(21) Anglada, J. M. Complex Mechanism of the Gas Phase Reaction between Formic Acid and Hydroxyl Radical. Proton Coupled Electron Transfer versus Radical Hydrogen Abstraction Mechanisms. *J. Am. Chem. Soc.* **2004**, *126* (31), 9809–9820. https://doi.org/10.1021/ja0481169.

(22) Denisov, E. T.; Shestakov, A. F. Free-Radical Decarboxylation of Carboxylic Acids as a

Concerted Abstraction and Fragmentation Reaction. *Kinet. Catal.* **2013**, *54* (1), 22–33. https://doi.org/10.1134/S0023158413010059.

(23) Spiegel, M.; Andruniów, T.; Sroka, Z. Flavones' and Flavonols' Antiradical Structure-Activity Relationship-A Quantum Chemical Study. *Antioxidants* **2020**, *9*, 461–483. https://doi.org/10.3390/antiox9060461.

(24) Ma, Y.; Su, K.; Zhang, J.; Wang, Y.; Wang, X.; Liu, Y. Hydrogen Abstraction Mechanisms and Reaction Rates of Toluene+NO 3. https://doi.org/10.1007/s00894-015-2749-3.

(25) Chapleski, R. C.; Zhang, Y.; Troya, D.; Morris, J. R. Heterogeneous Chemistry and Reaction Dynamics of the Atmospheric Oxidants, O3, NO3, and OH, on Organic Surfaces. *Chem. Soc. Rev.* **2016**, *45* (13), 3731–3746.

(26) Mezyk, S. P.; Cullen, T. D.; Rickman, K. A.; Mincher, B. J. The Reactivity of the Nitrate Radical (• NO 3) in Aqueous and Organic Solutions. *Int J Chem Kinet* **2017**, *49*, 635–642. https://doi.org/10.1002/kin.21103.

(27) Ito, O.; Akiho, S.; Iino, M. Kinetic Study for Reactions of Nitrate Radical (NO3·) with Alcohols in Solutions. *Bull. Chem. Soc. Jpn.* **1989**, *62* (5), 1606–1611. https://doi.org/10.1246/bcsj.62.1606.

(28) Dogliotti, L.; Hayon, E. Transient Species Produced in the Photochemical Decomposition of Ceric Salts in Aqueous Solution. Reactivity of N03 and HS04 Free Radicals. *J. Phys. Chem.* **1967**, 71, 12, 3802–3808

(29) Martin, T. W.; Swift, L. L.; Venable, J. H. NO3 Radical: "Soft" Lattice Preparation and Pure ESR Spectrum at 88°K. *J. Chem. Phys.* **1970**, *52* (4), 2138–2143.

(30) Neta, P.; Huie, R. E. Rate Constants for Reactions of NO3 Radicals in Aqueous Solutions.

J. Phys. Chem. **1986**, *90* (19), 4644–4648. https://doi.org/10.1021/j100410a035.

(31) Taniguchi, H.; Fukui, K.; Ohnishi, S. I.; Hatano, H.; Hasegawa, H.; Maruyama, T. Free-Radical Intermediates in the Reaction of the Hydroxyl Radical with Amino Acids. *J. Phys. Chem.* **1968**, *72* (6), 1926–1931. https://doi.org/10.1021/j100852a012.

(32) Serpone, N.; Martin, J.; Horikoshi, S.; Hidaka, H. Photocatalyzed Oxidation and Mineralization of C1-C5 Linear Aliphatic Acids in UV-Irradiated Aqueous Titania Dispersions-Kinetics, Identification of Intermediates and Quantum Yields. *J. Photochem. Photobiol. A Chem.* **2005**, *169* (3), 235–251. https://doi.org/10.1016/j.jphotochem.2004.07.001.

(33) Rousse, D.; George, C. A Novel Long Path Photolysis Cell - Application to the Reactivity of Selected Organic Compounds toward the Nitrate Radical (NO3). *Phys. Chem. Chem. Phys.* **2004**, *6* (13), 3408–3414.

(34) Porter, G. Flash Photolysis and Spectroscopy A New Method for the Study of Free Radical Reactions. *Proc. R. Soc. Lond. A* **1950**, *200* (1061), 284–300.

(35) Kawai, H.; Nagamura, T. Ultrafast Dynamics of Photogenerated Styrylpyridinyl Radical and Its Dimer Radical Cation with Styrylpyridinium Cation Studied by Femtosecond Laser Ñash Photolysis. *J. Chem. Soc. Faraday Trans.* **1998**, *94*, 3581–3586.

(36) Ito, O.; Akiho, S.; Lino, M. Kinetics for Reactions of the Nitrate Radical (NO3·) with Aldehydes in Acetonitrile. *J. Phys. Chem.* **1989**, *93* (10), 4079–4083.

(37) Nathanael, J. G.; Hancock, A. N.; Wille, U. Reaction of Amino Acids, Di- and Tripeptides with the Environmental Oxidant NO3·: A Laser Flash Photolysis and Computational Study. *Chem. Asian J.* **2016**, *11* (22), 3188–3195.

(38) Walling, C.; Jacknow, B. B. Positive Halogen Compounds. I. The Radical Chain

Halogenation of Hydrocarbons by f-Butyl Hypochlorite1. *J. Am. Chem. Soc.* **1960**, *82* (23), 6108–6112.

(39) Griller, D.; Ingold, K. U. Free-Radical Clocks. *Acc. Chem. Res* **1980**, *13* (9), 317–323.

(40) Clark, T. Lithium Cation as Radical-Polymerization Catalyst. *J. Am. Chem. Soc.* **2006**, *128* (34), 11278–11285.

(41) Hirano, T.; Segata, T.; Hashimoto, J.; Miwa, Y.; Oshimura, M.; Ute, K. Syndiotactic- and Heterotactic-Specific Radical Polymerization of N-n-Propylmethacrylamide Complexed with Alkali Metal Ions. *Polym. Chem.* **2015**, *6*, 4927–4939.

(42) Noble, B. B.; Smith, L. M.; Coote, M. L. The Effect of LiNTf 2 on the Propagation Rate Coefficient of Methyl Methacrylate. *Polym. Chem.* **2014**, *5*, 4974–4983.

(43) Vyakaranam, K.; Barbour, J. B.; Michl, J. Li + -Catalyzed Radical Polymerization of Simple Terminal Alkenes. *J. Am. Chem. Soc.* **2006**, *128* (17), 5610–5611.

(44) Horn, A. H. C.; Clark, T. Does Metal Ion Complexation Make Radical Clocks Run Fast? *J. Am. Chem. Soc.* **2003**, *125* (9), 2809–2816.

(45) Walling, C.; Wagner, P. J. Positive Halogen Compounds. X. Solvent Effects in the Reactions of t-Butoxy Radicals. *J. Am. Chem. Soc.* **1964**, *86* (16), 3368–3375.

(46) Avila, D. V.; Brown, C. E.; Ingold, K. U.; Lusztyk, J. Solvent Effects on the Competitive β-Scission and Hydrogen Atom Abstraction Reactions of the Cumyloxyl Radical. Resolution of a Long-Standing Problem. *J. Am. Chem. Soc.* **1993**, *115* (2), 466–470.

(47) Baciocchi, E.; Bietti, M.; Salamone, M.; Steenken, S. Spectral Properties and Absolute Rate Constants for β-Scission of Ring-Substituted Cumyloxyl Radicals. A Laser Flash Photolysis Study. *J. Org. Chem.* **2002**, *67* (7), 2266–2270.

(48) Tsentalovich, Y. P.; Kulik, L. V.; Gritsan, N. P.; Yurkovskaya, A. V. Solvent Effect on

the Rate of β-Scission of the Tert-Butoxyl Radical. *J. Phys. Chem. A* **1998**, *102* (41), 7975–7980.

(49) Burgess, S. K.; Leisen, J. E.; Kraftschik, B. E.; Mubarak, C. R.; Kriegel, R. M.; Koros, W. J. Chain Mobility, Thermal, and Mechanical Properties of Poly(Ethylene Furanoate) Compared to Poly(Ethylene Terephthalate). *Macromolecules* **2014**, *47* (4), 1383–1391. https://doi.org/10.1021/ma5000199.

Chapter 2. Insight into Hydrogen Abstractions by Nitrate Radical: Structural, Solvent Effects, and Evidence for a Polar Transition State

2.1. Authors

Mark Paradzinsky, Diego Troya, and James M. Tanko*

Department of Chemistry, Virginia Polytechnic Institute and State University, Blacksburg, Virginia 24061

2.2. Abstract

The role of a polarized transition state and solvent effects on nitrate radical reactions was examined with a previously under-reported class of substrates, ethers, for their atmospheric implications. Absolute rate constants for hydrogen abstraction from a series of alcohols, ethers, and alkanes by nitrate radical have been measured in acetonitrile, water, and mixtures of these two solvents. Across all these classes of compounds, using a modified form of the Evans–Polanyi relationship, it is demonstrated that the observed structure/reactivity trends can be reconciled by considering the number of abstractable hydrogens, strength of the C-H bond, and ionization potential (IP) of the substate. Hydrogen abstractions by nitrate radical occur with low selectivity and are characterized by an early transition state ($\alpha \approx 0.3$). The dependence of the rate constant on IP suggests a polar transition state with some degree (<10%) of charge transfer. These conclusions stand for reactions conducted in solution (CH_3CN and H_2O) as well as gas-phase values. Because of this polar transition state, the rate constants increase going from the gas-phase to a polar solvent, and the magnitude of the increase is consistent with Kirkwood theory.

2.3. Introduction

Global warming, resulting from increased reliance on fossil fuels over the past few decades, is a known and existential threat. Globalization and industrialization are not just threatening our future, but also affecting our health in the present. Micro-scale particles generated from diesel vehicles, waste and crop burning, and coal-fired power plants make their way into the air and pose grave health risks because of their small size. The World Health Organization attributed 4.2 million premature deaths to ambient air pollution in 2015.[1] On its own, this would be the third leading cause of death in the world, and it directly contributes to leading global causes of death such as ischemic heart disease, stroke, and respiratory illnesses. Fortunately, the atmosphere has methods of self-cleansing that can break down some of these pollutants.

The primary method of breaking down organic pollutants in the atmosphere is through reactions with highly reactive oxidants.[2] These highly reactive oxidants typically have a highly positive one-electron reduction potential and remove electrons from organic molecules. Therefore, the oxidized products are more susceptible to breakdown either through cracking or hydrogen abstraction. The two major pathways for tropospheric oxidation are day-time reactions with hydroxyl radical ($HO\cdot$)[3,4] or night-time reactions with nitrate radical ($NO_3\cdot$)[5–8] which have aqueous one-electron reduction potentials of 2.81 V[9] and 2.49 V,[10] respectively. Because the concentrations of these atmospheric "detergents" are directly tied to atmospheric photon concentration, these oxidants mostly operate independently.

Scheme 2.1 shows how sunlight leads to the photogeneration of $HO\cdot$ through the breakdown of ozone into an excited oxygen atom ($O(^1D)$) and singlet dioxygen ($O_2(^1\Delta_g)$). $HO\cdot$ is formed from $O(^1D)$ in the presence of water vapor.

Scheme 2.3. The primary mechanism for $HO\cdot$ atmospheric generation

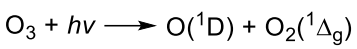

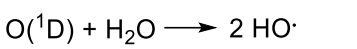

Reactions of nitrogen dioxide and ozone generate $NO_3\cdot$ during the day and at night. However, since $NO_3\cdot$ is photolyzable, daytime $NO_3\cdot$ rapidly decomposes into NO_x gases (Scheme 2.2). Consequently, the concentrations of the radicals peak asynchronously.

Scheme 2.4. The primary mechanism for $NO_3\cdot$ generation and daytime photolysis

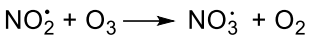

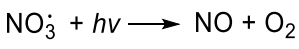

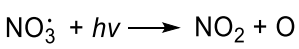

Extensive work has been done to show how each of these radicals operate in the gas-phase (Scheme 2.3). During the day, $HO\cdot$ abstracts hydrogen from alkanes, alcohols, and ethers; undergoes electrophilic addition to pi bonds; and directly reacts with alkyl aromatics through hydrogen atom abstraction or substituent elimination.[3] Mechanistically, $NO_3\cdot$ works in much the same way at night except for reactions with aromatic rings where electron transfer dominates.[5]

To fully understand the photochemical reactivity of $NO_3\cdot$ Reuveni and Luz γ-irradiated $NaNO_3$ to generate ESR spectra to understand and probe the ground state electronic configuration.[11] Subsequent work[5,12–15] helped to assign D_{3h} symmetry, supporting a Reuveni and Luz model where each oxygen nucleus carried a spin density of $\frac{1}{3}$, meaning the unpaired electron was distributed equally. Based on the ESR spectra, Reuveni and Luz also discuss a second Y-shaped geometry with two equivalent oxygen nuclei of spin density $\frac{1}{2}$, while the remaining oxygen carries no spin density. The corresponding structure would have C_{2v} symmetry and while

the literature generally accepts the D_{3h} assignment, there is computational support in the literature for C_{2v} symmetry under the basis of pseudo Jahn–Teller distortion.[14–16] Reactions in the atmosphere are not limited to the gas-phase and solution-phase reactions can be observed in cloud formation, within raindrops, and upon aerosol surfaces.[2,5]

Scheme 2.5. Common reaction pathways for HO· and NO_3· with organic substrates

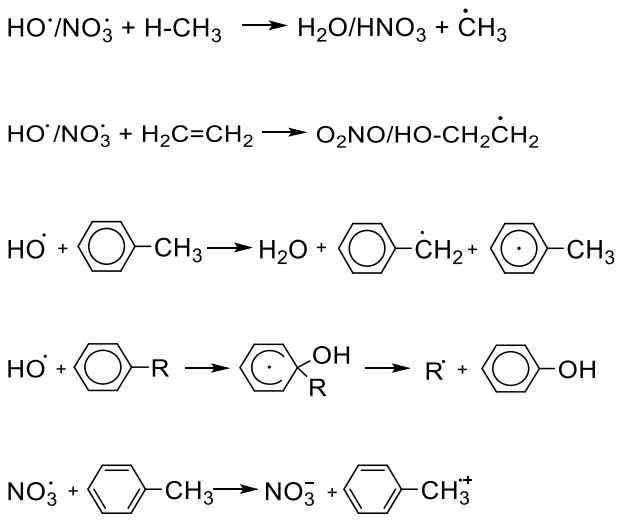

Previous work in our group has shown that the rate constants for hydrogen abstractions by HO· from various organic substrates were sensitive to solvent effects, particularly hydrogen bonding (H-bond).[4] Experimentally, it was observed that rate constants for HO· hydrogen abstractions were 1–2 orders of magnitude smaller in acetonitrile compared to water ($k_W > k_{AN}$) for the same substrates. This was attributed to the polar effect; the idea that a polarized transition state can be stabilized by H-bonding to solvent thus lowering the reaction barrier. Consider the abstraction of hydrogen from a carbon center by hydroxyl radical as in Figure 2.1. Oxygen is more electronegative than carbon and hydrogen, and as result, the transition state is highly polarized. This leads to the buildup of a partial positive charge on carbon and hydrogen as they donate electron density to oxygen, which consequently develops a partial negative charge. When water is the solvent, the transition state is stabilized via H-bonding. Computational analysis was

also performed which qualitatively and quantitatively support the polar effect and stabilization of the transition state by H-bonding.

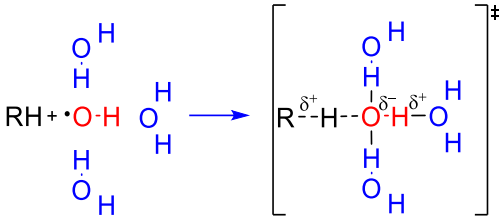

Figure 2.6. Hydrogen atom abstractions by hydroxyl radical from organic substrates leads to the formation of a polarized transition state. In an aqueous solvent the transition state is stabilized by H-bonding.

Early work by Ito et al. indicates that a polar transition state also arises for $NO_3\cdot$.[6] The authors suggest that as substrate (alcohols) ionization energy decreases, polar resonance structure contributions in the transition state increase (Figure 2.2). This leads to greater charge transfer from the alcohols to the highly electrophilic $NO_3\cdot$ ultimately decreasing the activation energy of the abstraction at the α-carbon.

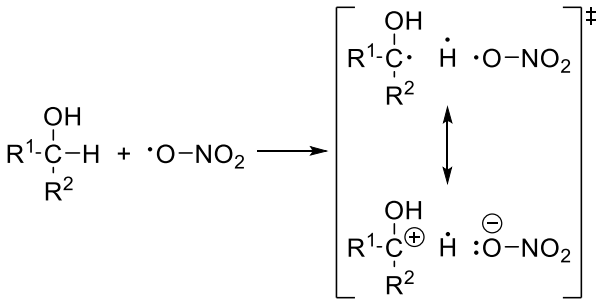

Figure 2.7. The resonance forms of the polarized transition state following hydrogen atom abstractions by $NO_3\cdot$ from alcohols.

The authors also noted a solvent effect where the rate constants were higher in acetonitrile than aqueous solution and suggested three origins for this effect. The first contribution to the solvent effect is the interaction between the acidic aqueous solvent and

attacking $NO_3\cdot$ via H-bonding. Next, they propose that the electron-deficient oxygen radical center may interact with the oxygen atom of H_2O, though the nature of this interaction is not discussed in detail. Finally, Ito suggests that H-bonding between the substrate and H_2O decreased reaction rates compared to reactions in acetonitrile[6] because the H-bonded waters must first be displaced before the reaction can proceed, as depicted in Figure 2.3.

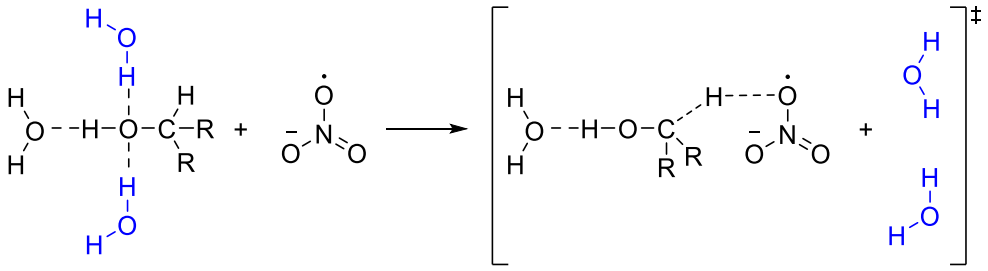

Figure 2.8. H-bonding to the substrate by the solvent must be broken to reach the transition state complex.

Investigations by Alfassi et al. expanded the work of Ito to reexamine alcohols in both acetonitrile and water. They also measured the rate constants for hydrogen abstraction from alkanes in acetonitrile and compared the results with those obtained in the gas-phase. These authors also found that hydrogen abstractions from alcohols by $NO_3\cdot$ were about an order of magnitude faster in acetonitrile than water, $k_{AN} > k_W$.[7] However, Alfassi instead offered an unusual variant of the polar transition state concept, suggesting that the primary cause of the solvent effect is decreased polarity of the symmetric reactant, $NO_3\cdot$, compared to the asymmetric activated complex. The loss of symmetry as the reaction proceeds to the transition state increases the complex's polarity and leads to stronger solvation which subsequently accelerates the reaction in polar solvents compared to the gas-phase. The authors suggest that although water is more polar than acetonitrile, this effect would be pronounced in acetonitrile which solvates

primarily through dipolar interactions and would offer only minor contributions in water because H-bonding presumably dominates solvation.

The effect of solvent on the rates of hydrogen atom abstractions by $NO_3\cdot$ appears to be complicated and unresolved. It remains unclear as to how a potentially polarized transition state, solvent interactions, and H-bonding effects explain $NO_3\cdot$ reactivity, and whether there is any comparison to $HO\cdot$. The objective of our work was to untangle these effects by examining $NO_3\cdot$ reaction rates in CH_3CN and H_2O (or CH_3CN/H_2O mixtures when solubility was an issue) and to compare these rates to gas-phase data.

The general classes of substrates examined herein include alcohols, ethers, and alkanes for the following reasons: In addition to being polar, alcohols function as both hydrogen bond donors and acceptors. While ethers are also polar and serve as hydrogen bond acceptors through the electron pair on oxygen, they are not hydrogen bond donors. Alkanes are non-polar and lack the ability to serve as hydrogen bond donors or acceptors.

2.4. Experimental Section

To carry out these experiments a nitrate radical source that can operate in both acetonitrile and aqueous solvents was needed. It has been established that commercially available ceric ammonium nitrate (CAN) generates $NO_3\cdot$ upon photolysis in acetonitrile, and is a proven method for studying $NO_3\cdot$ kinetics by laser flash photolysis (LFP).[5,7] In aqueous environments it was noted that water molecules replaced the nitrate ions in the ceric coordination sphere of CAN,[7] and as a consequence, did not produce $NO_3\cdot$ on photolysis. To combat this issue the literature suggested using ceric potassium nitrate (CKN), but procedures for synthesizing CKN were either lacking or vague.[17] The best reported procedure involves a transligation of CAN via potassium hydroxide (KOH) to yield CKN, however the product is insoluble in water

and therefore cannot be CKN. Herein, we report, to the best of our knowledge, the first unambiguous, preparation of CKN for use in LFP experiments.

2.4.1. Preparation of Ceric Potassium Nitrate

All reagents were purchased from Millipore Sigma and used as received. Typically, 1.42 g (2.6 mmol) of CAN, an orange powder, was added to 40 mL distilled water which yielded a yellow solution. A stoichiometric amount of KOH (0.29 g, 5.2 mmol) was added to the solution and vigorously mixed until opaque and yellow. The intermediate was isolated and subsequently dissolved in 2 M nitric acid to form a transparent orange solution which was evaporated down to an orange powder.

Scheme 2.6. Preparation of ceric potassium nitrate (CKN)

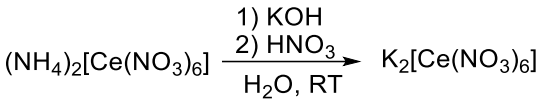

To ensure the nitrate radical could be generated from CKN prepared in this manner (Scheme 2.4), transient absorption spectroscopy (described below) was used to successfully generate a UV-visible spectra (Figure 2.4) in both acetonitrile and water that matched the reported spectrum of NO_3·.[8,13]

2.4.2. Nitrate Radical Kinetics

Rate constants were determined via laser–flash photolysis using an Applied Photophysics LKS.80 spectrometer and the third harmonic of a Continuum Surelite I-10 Nd:YAG laser (4–6 ns pulse, 355 nm). A Hewlett–Packard Infinium digital oscilloscope was used to monitor the transient signals which were analyzed using the Applied Photophysics Spectra Kinetic Workstation software (version 4.59). Samples were prepared by dissolving substrate with a stock CKN solution prepared from acetonitrile, water, or a solvent mixture. Samples were monitored at

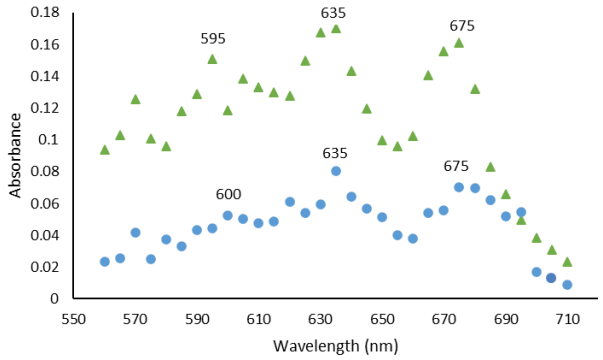

Figure 2.9. UV-Vis spectra of NO_3· generated by laser flash photolysis of ceric potassium nitrate. Spectra recorded after the laser pulse: 200 ns for acetonitrile (▲) and 2 μs for water (●).

25 °C and agitated between each subsequent flash. The NO_3· was produced from CKN by laser–flash photolysis at 355 nm and monitored at 635 nm. In the absence of added substrate, NO_3· is still observed to decay. It has been reported that NO_3· arises via an intramolecular electron transfer in the Ce(IV) complex[13] and that the disappearance of NO_3· occurs through the back reaction seen in Scheme 2.5.[6]

Scheme 2.7. Generation of NO_3· and subsequent slow back reaction in the absence of substrate

$$K_2[Ce^{IV}(NO_3)_6] \rightleftharpoons NO_3^{\bullet} + K_2[Ce^{III}(NO_3)_5]$$

In these experiments NO_3· was monitored in the presence various concentrations of substrate. For each concentration of a substrate, six transient decay signals were recorded and signal averaged as depicted in Figure 2.5. The signal averaged traces were fit with non-linear regression to extract an observed pseudo first order rate constant (k_{obs}). This was repeated in triplicate for every sample (Appendix A, Figures A.1–A.71 and Tables A.1–A.44). A plot of k_{obs} versus substrate concentration (Figure 2.6) yields the rate constant for hydrogen abstraction as shown in Eqs. 1–3.

$$-\frac{d[NO_3\cdot]}{dt} = k_{obs}[NO_3\cdot] \quad (1)$$

$$k_{obs} = k_o + k_H[Substrate\text{-}H] \quad (2)$$

$$Substrate = RH, ROH, ROR \quad (3)$$

where k_{obs} is the observed rate constant, k_o is the rate constant for any other processes that consume $NO_3\cdot$, and k_H is the hydrogen abstraction rate constant, subsequently denoted k_{AN}, k_W, or k_G to reference abstractions in acetonitrile, water, or the gas-phase, respectively.

In the acetonitrile, water, and mixed solvent systems, 3×10^{-3} mol L^{-1} CKN was used to generate $NO_3\cdot$. To push the equilibrium toward $Ce^{IV}(NO_3)_6^{2-}$ under aqueous conditions, nitric acid was added until the acid's concentration reached 2 mol L^{-1}. In cases where substrate water solubility was an issue, i.e., aliphatic ethers and hydrocarbons, acetonitrile/water mixtures were utilized. Although these mixtures do not provide the rate constants in pure water, they do set a lower limit for an aqueous rate constant which allows for limited interpretation.

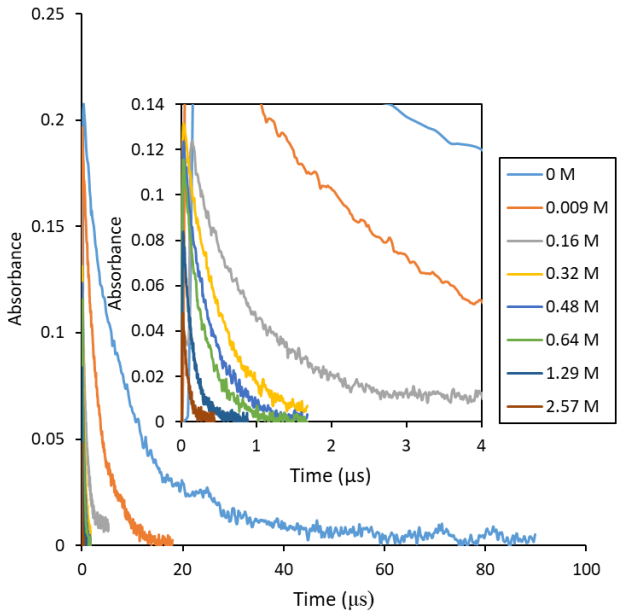

Figure 2.10. Transient traces for the decay of $NO_3\cdot$ in the presence of various concentrations of 2-propanol in acetonitrile. The inset depicts a magnified view of the decay profiles for higher concentrations of substrate.

2.5. Results and Discussion

Table 2.1 summarizes our results for the rate constants of $NO_3\cdot$ reactions with alcohols and ethers in neat acetonitrile and aqueous solvent as well as available literature data for these reactions in solution and in the gas-phase. Rate constant ratios in CH_3CN, water, and the gas-phase are also reported.

Several of the ethers were not sufficiently soluble in water at the concentrations needed for these experiments, so a mixed solvent system was used. Table 2.2 contains our results for the rate constants of $NO_3\cdot$ reactions with ethers in neat acetonitrile and mixed solvent (40% acetonitrile, 60% aqueous). Available gas-phase data for these reactions, rate constant ratios in CH_3CN and the gas-phase are reported as well.

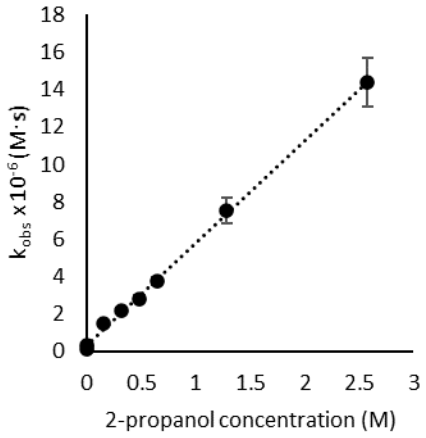

Figure 2.11. Plot of the observed rate constant for $NO_3\cdot$ vs. 2-propanol concentration in acetonitrile at 25 °C; the slope is equal to the hydrogen abstraction rate constant ($k_{AN} = 5.5 \times 10^6$ M^{-1} s^{-1}).

Table 2.1. Rate constants for hydrogen abstraction by $NO_3\cdot$ from various organic substrates in CH_3CN and H_2O at 25 °C

Substrate	k_{AN}[a]	k_W[a]	k_{AN}:k_W	k_G[a]	k_{AN}:k_W:k_G
—OH	0.6 ± 0.1 (2.1)[b,c,d]	0.3 ± 0.0 (0.30)[b,c,d,f]	2.0	(0.13)[b]	4.6 : 2.3 : 1
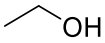	3.2 ± 5 (6.7)[b,c,d]	1.4 ± 0.2 (1.2)[b,c,d,f]	2.3	(0.54)[b]	5.9 : 2.6 : 1
	5.5 ± 0.8 (14.0)[b,c,d]	2.5 ± 0.4 (2.7)[b,c,d]	2.2	(0.14)[b,e]	39.3 : 17.9 : 1
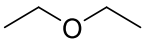	9.7 ± 1.5 (13.0)[d]	3.2 ± 0.5	3.0	(1.7)[e]	5.7 : 1.9 : 1
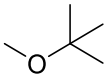	3.0 ± 0.5	0.8 ± 0.1 (0.4)[f]	3.8	-	-
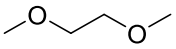	5.3 ± 0.8	1.9 ± 0.3	2.8	-	-
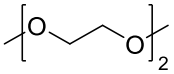	8.8 ± 1.3	3.6 ± 0.5	2.4	-	-
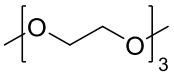	14.0 ± 2.1	5.4 ± 0.8	2.6	-	-
	29.5 ± 4.4 (54.8)[b]	12.8 ± 1.9 (12.0)[b,g]	2.7	(2.9)[b]	10.2 : 4.4 : 1
	4.6 ± 0.7	1.1 ± 0.2 (0.8)[b]	4.2	-	-
	5.0 ± 0.8	2.1 ± 0.3 (1.3)[b,g]	2.4	-	-
	0.6 ± 0.1	0.2 ± 0.0	3.0	-	-

[a] × 10^{-6} M s. k_{AN} represents the rate constant in acetonitrile, k_W in water, and k_G in the gas-phase. [b] Reference [5]. [c] Reference [6]. [d] Reference [7]. [e] Reference [23]. [f] Reference [24]. [g] Reference [25].

Solubility issues with the alkanes and some ethers in water were even more acute, requiring an even less polar solvent mixture. Results for the rate constants of NO_3· reactions with ethers and alkanes in neat acetonitrile and mixed solvent (80% acetonitrile, 20% aqueous) are reported in Table 2.3. Solution-phase and gas-phase data for these reactions and the ratios of our experimental data relative to mixed solvent and the gas-phase are also available.

Table 2.2. Rate constants for hydrogen abstraction by NO_3· from various organic substrates in CH_3CN and 4:6 CH_3CN/H_2O solvent mixtures at 25 °C

Substrate	k_{AN}[a]	$k_{AN/W(4:6)}$[a]	$k_{AN}:k_{AN/W(4:6)}$	k_G[a]	$k_{AN}:k_{AN/W(4:6)}:k_G$
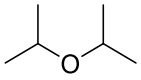	14.5 ± 2.2	7.2 ± 1.1	2.8	(2.4)[b]	6.0 : 3 : 1
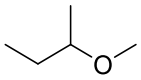	11.2 ± 1.7	6.3 ± 09	1.8	-	-
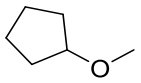	11.8 ± 1.8	8.2 ± 1.2	1.4	-	-
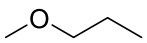	4.5 ± 0.7	3.9 ± 0.6	1.4	(1.0)[c]	4.5 : 3.9 : 1

[a] × 10^{-6} M s; $k_{AN/W(4:6)}$ is the rate constant in 4:6 acetonitrile/water. [b] Reference [23]. [c] Reference [26].

To fully resolve and separate the possible effects of a polar transition state, solvent interactions, and hydrogen bonding on the rates of these reactions, we must first reiterate that hydrogen abstraction from alcohols and ethers has been well established[4,6,7] to occur at the α-carbon and abstraction from alkanes occurs at the most substituted carbon.[5,7] This is attributable to C-H bond strength (and the stability of the resulting radical) as measured by bond dissociation energy (BDE). In terms of C-H bond strengths (kcal mol^{-1}), 1° (102) > 2° (98) > 3° (95) for the alkanes, and for alcohols, $HOCH_3$ (96) > $HOCH_2R$ (93) > $HOCHR_2$ (92). The α-C-H BDE for

ethers is ca. 93 kcal mol^{-1}, and less dependent on the alkyl substituents.[18–21] These values explain the overall observation that the rate constants for hydrogen abstraction from alcohols and ethers tend to be about an order of magnitude greater than those for alkanes as the presence of an O-atom activates the adjacent C-H bonds.

Table 2.3. Rate constants for hydrogen abstraction by NO_3· from various organic substrates in CH_3CN and 8:2 CH_3CN/H_2O solvent mixtures at 25 °C

Substrate	k_{AN}[a]	$k_{AN/W(8:2)}$[a]	k_{AN}:$k_{AN/W(8:2)}$	k_G[a]	k_{AN}:$k_{AN/W(8:2)}$:k_G
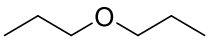	15.8 ± 2.4	14.1 ± 2.1	1.1	(3.0)[d]	5.3 : 4.7 : 1
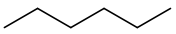	1.5 ± 0.02 (0.59)[c]	1.4 ± 0.2	1.2	(0.063)[b,c,e]	23.8 : 22.2 : 1
	1.9 ± 0.3 (1.00)[c]	3.4 ± 0.5	0.6	(0.081)[b,c,e]	23.5 : 42.0 : 1
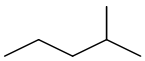	1.1 ± 0.2	1.3 ± 0.2	0.8	(0.10)[e]	11 : 13 : 1
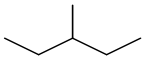	1.2 ± 0.2	1.3 ± 0.2	0.9	(0.12)[e]	10 : 10.8 : 1
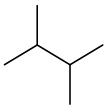	2.3 ± 0.3	1.2 ± 0.2	1.9	(0.25)[b,e]	9.2 : 4.8 : 1

[a] × 10^{-6} M s; $k_{AN/W(8:2)}$ is the rate constant in 8:2 CH_3CN/H_2O. [b] Reference [5]. [c] Reference [7]. [d] Reference [23]. [e] Reference [30].

2.5.1. Reactions of NO_3· in CH_3CN Solvent

For alcohols, Ito et al. previously noted a correlation between the rate constant, or more appropriately 2.303RT *log*(k) and the ionization potential (IP) of the substrate, *vide supra*. (IP is energy required to remove an electron from a substance.) In this work, we extend that correlation

to include ethers and alkanes (Figure 2.7) and note a similar correlation (r = 0.812). (Note: To maintain consistency of units, R = 1.99 × 10^{-3} kcal mol^{-1} K^{-1}, and IPs are in kcal mol^{-1}) However, as already noted for hydrogen abstraction reactions, the overall rate constant should also depend on the C-H BDE and the number of abstractable hydrogens. Figure 2.8 depicts 2.303RT *log*(k_H/H) vs. the BDE of the C-H bond, where k_H/H represents the rate constant for hydrogen abstraction on a per hydrogen basis, and the correlation (r = 0.721) is nearly (but not quite) as good as found for Figure 2.7. These observations suggest that in order to fully understand NO_3· reactivity, *both* factors must be taken into account: the ionization potential of the substrate, and the C-H bond strength—correcting for the number of abstractable hydrogens.

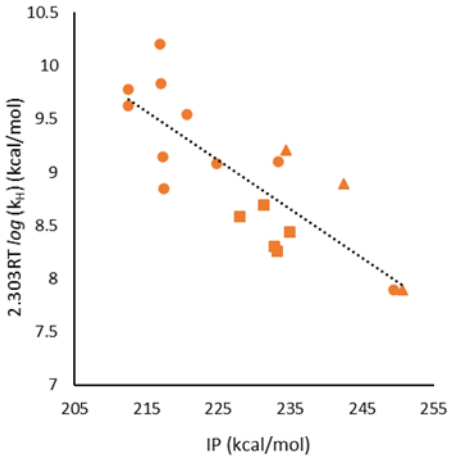

Figure 2.12. Reaction of NO_3· with ethers (●), alkanes (■), and alcohols (▲) in CH_3CN: Plot of 2.303RT l*og*(k_H) vs. the ionization potential of the substrate.

To test this hypothesis, the following analysis was applied. According to the Evans–Polanyi relationship (Eq. 4), the *log* of the rate constant for hydrogen abstraction is expected to correlate with the enthalpy of reaction (ΔH^o) and thus the C-H bond strength (since ΔH° = BDE(C-H) – BDE(H-ONO_2). The value α ($0 \leq \alpha \leq 1$) is a measure of transition state location; α

< 0.5 implies an early, reactant-like transition state, while α > 0.5 implies a later, product like transition state.[22]

$$2.303RT\ log(k) = Constant\ - \alpha \cdot BDE(C-H) \quad (4)$$

To account for both C-H bond strength, number of abstractable hydrogens, and the ionization potential, we propose a modification of the Evans–Polanyi equation (Eq. 5).

$$2.303RTlog\left(\frac{k_H}{H}\right) = Z\ - \alpha\ \cdot BDE(C-H) - \beta\ \cdot IP \quad (5)$$

where k_H/H is the rate constant for hydrogen abstraction on a per hydrogen basis, β is a measure of the sensitivity of the rate constant to the ionization potential of the substrate and *Z* is a constant.

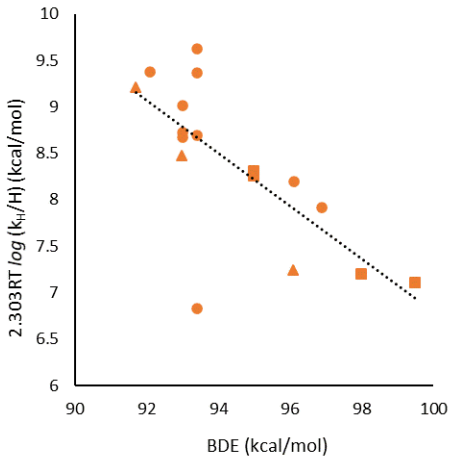

Figure 2.13. Reaction of NO_3· with ethers (●), alkanes (■), and alcohols (▲) in CH_3CN: Plot of 2.303RT *log*(k_H/H) vs. the C-H bond dissociation energy; k_H/H is the rate constant for hydrogen abstraction on a per hydrogen basis.

Using available C-H BDEs and IPs reported in the literature, the data summarized in Tables 2.1–2.3 were subjected to multiple linear regression analysis (Table A.45), yielding α = 0.26 ± 0.04, β = 0.04 ± 0.01, and as shown in Fig. 2.9, a correlation coefficient r = 0.920. This

analysis clearly shows that in order to fully understand $NO_3\cdot$ reactivity, the bond strength, number of hydrogens, and ionization potential must all be taken into account.

Based upon this modified Evans–Polanyi treatment, the observed value for a = 0.26 suggests an early transition state. As the C-H bond strengths for these substrates all fall between and 92 and 100 kcal mol^{-1}, and the H-ONO_2 bond strength is 102 kcal mol^{-1},[27] all these hydrogen abstractions by $NO_3\cdot$ are exothermic. In accordance with the Hammond postulate, an early transition state for these reactions is both reasonable and expected.

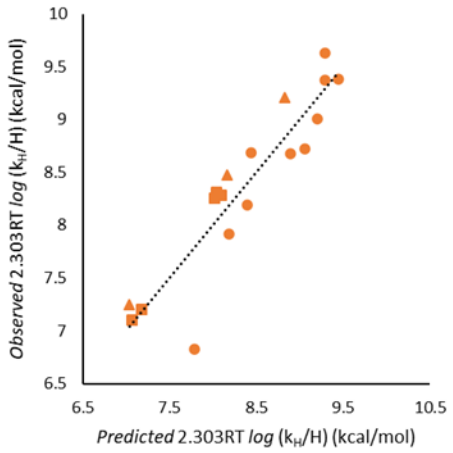

Figure 2.14. Reaction of $NO_3\cdot$ with ethers (●), alkanes (■), and alcohols (▲) in CH_3CN: Plot of the experimental vs. predicted value of 2.303RT *log*(k_H/H) on the basis of Eq. 5 (α = 0.26, β = 0.04; r = 0.920).

Because of this early transition state, the selectivity of $NO_3\cdot$ is anticipated to be low. However, estimation of the per-H selectivity is complicated by the fact the rate constants also depend on ionization potential. For the alkanes, all of which have a narrow range of ionization potentials (10 ± 0.1 eV), the selectivity order is 3° (24) > 2° (4.0) > 1° (1.0) based on these results. These values are reminiscent of *t*-butoxyl radical,[28] whose selectivity is 3° (40) > 2° (14) > 1° (1.0), and whose absolute rate constants for hydrogen abstraction from alkanes also fall in

the 10^5–10^6 $M^{-1}s^{-1}$ range in acetonitrile. $NO_3\cdot$ is more selective and less reactive than HO·, 3° (14) > 2° (1.4) > 1° (1.0), where k_H is about an order of magnitude greater, 10^7–10^8 $M^{-1}s^{-1}$ in CH_3CN.[4]

For hydrogen abstraction from the α-C-H of alcohols by $NO_3\cdot$, a similar trend can be extracted from the data, 3° (21.5) > 2° (6.5) > 1° (1.0), but the ionization potential varies by about 1 eV for the three substrates examined. Hence, we do not put much confidence in the physical interpretation of these values. Finally, for the ethers, there is not sufficient structural diversity in the substrates examined to derive any meaningful values.

As discussed, the rate constants depend on the ionization potential of the substrate. Based upon this modified Evans–Polanyi treatment, and consistent with the earlier work of Ito, et al., the observed value of $\beta = 0.04$ (Figure 2.9) suggests a modest amount of charge transfer in the transition state, consistent with a polar transition state for these hydrogen abstractions as hypothesized. However, the fact that $\beta << 1.0$ rules out any possibility that a single electron transfer process is occurring. (Electron transfer can also be ruled out based on thermodynamic arguments: the ionization potential of these substrates range from 9–11 eV, and the electron affinity of $NO_3\cdot$ is 3.94 eV,[29] which means single electron transfer is highly unfavorable.)

2.5.2. Reactions of $NO_3\cdot$ in Water as Solvent

Because of limited solubility, rate constant measurements in water were limited to only a few substrates (alcohols and a few ethers). The rate data did not correlate particularly well to the IP of the substrate (Figure A.72). However, the rate data (corrected for the number of abstractable hydrogens) did correlate well to the BDE of the substrate (Figure 2.10), with $\alpha = 0.30 \pm 0.09$ ($r = 0.857$).

Because the α value is nearly identical in both solvents (Table A.46 and Figure A.73), the same interpretation applies: NO_3· reacts through an early transition state and a low selectivity is expected. The selectivity order for NO_3· abstractions of the α-C-H in alcohols in water mirrors acetonitrile, 3° (19.0) > 2° (5.5) > 1° (1.0). We apply the same caveats here as earlier since the range of IP is quite large for the three alcohols and withhold interpretation of the other substrates on the basis of solubility.

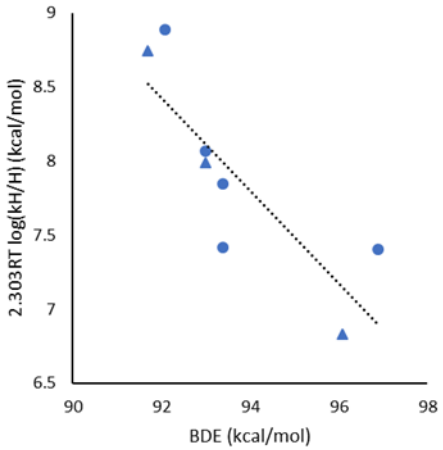

Figure 2.15. Reaction of NO_3· with ethers (●), alcohols (▲) in water: Plot of 2.303RT *log*(k_H/H) vs. the C-H bond dissociation energy. k_H/H is the rate constant for hydrogen abstraction on a per hydrogen basis.

2.5.3. Gas-phase Reactions of NO_3·

Analysis of rate constants in the gas-phase was limited to their availability in the literature: alcohols, alkanes, and a few ethers. The rate constants correlate fairly well with the IP (r = 0.736) and strongly with BDE (r = 0.893) when adjusted for the number of abstractable hydrogens (Figures A.74 and A.75). The gas-phase rate constants were subjected to the same multiple linear regression analysis (Table A.47 and Figure A.76) described above yielding α = 0.33 ± 0.05, β = 0.03 ± 0.01, and r = 0.938. Given that the α and β terms compare favorably to

the solution-phase data, we suggest that NO_3· reactions in the gas-phase proceed with low selectivity and have an early polarized transition state.

2.5.4. Solvent Effects on the Reactivity of NO_3·

The rate constants for hydrogen abstraction from all classes of substrates studied (alcohols, ethers, and hydrocarbons) are all affected by solvent to varying degrees with several trends emerging: 1) for all of these substrates, the rate constant in a polar solvent is greater than in the gas-phase (k_{AN}, $k_W > k_G$); 2) for both alcohols (as reported by Ito et al. and Alfassi et al.) and ethers, the rate constants in acetonitrile are slightly greater than those in water ($k_{AN} > k_W$); 3) for ethers with low water solubility, this trend continues—the addition of a significant amount of water (4:6 CH_3CN/H_2O mixtures) lowered the rate constant ($k_{AN} > k_{AN/W}$); 4) for hydrocarbons, which could only be studied in 8:2 CH_3CN/H_2O mixtures because of solubility, the addition of water had little effect on the rate constant ($k_{AN} \approx k_{AN/W}$).

The difference between the rate constants measured in polar solvents (CH_3CN, H_2O) vs. the gas-phase is consistent with a polar transition state for H-abstraction that can be stabilized by solvent. Activated complex theory, applied in the context of the Kirkwood equation,[31] rationalizes these observations. For the reaction, A + B → transition state → products, the rate constant varies with solvent polarity and more specifically, polarity as measured by the dielectric constant of the solvent/medium (Eq. 6), where k is the rate constant in the medium of dielectric constant $\mathcal{E}$, k_o is the rate constant in a condensed medium of dielectric constant unity, $\mu_{\ddagger}$ is the dipole moment of the activated complex, μ_A is the dipole moment of reactant A, μ_B is the dipole moment of reactant B, $r_{\ddagger}$ is the radius of the activated complex, r_A and r_B are the radii of reactants A and B respectively, $\mathcal{E}_o$ is the permittivity of vacuum, N is Avogadro's number, R is the gas constant, and T is temperature.

$$\ln k = \ln k_o + \frac{1}{4\pi\varepsilon_o}\frac{N}{RT}\left(\frac{\mu_{\ddagger}^2}{r_{\ddagger}^3} - \frac{\mu_A^2}{r_A^3} - \frac{\mu_B^2}{r_B^3}\right)\left(\frac{\varepsilon - 1}{2\varepsilon + 1}\right) \quad (6)$$

Although the dielectric constant of water (80.1) is greater than that of acetonitrile (37.5), the effect on ln(k) in CH_3CN vs. H_2O is nominal because of the $\frac{\varepsilon-1}{2\varepsilon+1}$ dependence; the predicted change in going from the gas-phase to either of these two solvents is miniscule because $\frac{\varepsilon-1}{2\varepsilon+1}$ is 0.49 and 0.48 for H_2O, CH_3CN, respectively. Aside from dielectric constant, the predicted change also depends upon the dipole moments and radii of the reactants and transition state. For reasons discussed below, we were unable to study these reactions and test these ideas using electronic structure calculations. If it is assumed that the major contribution to the solvent polarity effect comes from a polarized transition state ($\mu_{\ddagger}^2/r_{\ddagger}^3 >> \mu_A^2/r_A^3, \mu_B^2/r_B^3$), then admitted crude calculations based on Eq. 6 suggest that the observed ca. 10× rate enhancement in going from the gas-phase to acetonitrile or water is plausible, with $\mu_{\ddagger}$ ranging from 1.3–2.3 Debye (for $r_{\ddagger}$ on the order of 2–3 Angstroms) consistent with a modest degree of charge transfer, $\beta < 0.1$ in the transition state. The dipole moment of $NO_3\cdot$ is zero (assuming D_{3h} symmetry), but not if the symmetry is C_{2v} as has been suggested (which would further diminish the magnitude of the solvent effect).

Hydrogen bonding appears to have little effect on the rate constant for H-abstraction by $NO_3\cdot$ in solution, suggesting either the polar transition state is not stabilized by hydrogen bonding to the solvent, or that any stabilization of the transition state is offset by a nearly equal degree of stabilization afforded by H_2O to the reactant(s). Alcohols are both H-bond donors and acceptors while ethers are only H-bond acceptors. For both classes of substrates $k_{AN} > k_W$ (or $k_{AN} > k_{AN/W}$ in the case of CH_3CN/H_2O solvent mixtures) suggesting, perhaps, a modest degree of stabilization of these substrates via H-bonding.

Alkanes, however, are neither H-bond donors nor acceptors, and within experimental error, the rate constants in CH_3CN and CH_3CN/H_2O are nearly identical. This means that if the polar transition state is stabilized by H-bonding when water is the solvent, it must be offset by nearly the same amount of stabilization of $NO_3\cdot$ by water solvent. Hydrogen bonding to $NO_3\cdot$ by water, or possibly stabilization of $NO_3\cdot$ via interaction with an electron pair on water (as suggested by Ito) might rationalize these results. It is also conceivable that the nature of the $NO_3\cdot$ ground state (D_{3h} vs. C_{2v}) is altered by solvation.

In principle, some of these ideas pertaining to $NO_3\cdot$ reactivity could be tested using quantum-mechanical calculations. We consequently attempted to conduct electronic structure calculations (density functional theory) of the barriers for hydrogen abstraction by $NO_3\cdot$ from CH_4, CH_3OH, and CH_3OCH_3 to 1) assess whether the transition states for H-abstraction by $NO_3\cdot$ from alkanes, ethers, and alcohols were indeed polarized and whether increased solvent polarity would lower the reaction barrier, and to 2) assess whether the polarized transition state can be stabilized by H-bonding to water, and if so, whether this is offset by possible stabilizing interactions between $NO_3\cdot$ and water.

However, previous work by Anglada et al. attempting to probe the reaction $NH_2\cdot + HNO_3 \rightarrow NH_3 + NO_3\cdot$ has shown that DFT calculations involving $NO_3\cdot$ can be notoriously erratic[15]—and our experience confirms this. In our hands, the results of these calculations were meaningless, at best. To address this, high level, complete-basis-set CBS-QB3[32] calculations were conducted using Gaussian09,[33] and provided transition-state energies of 14.0, 6.4, and 5.7 kcal mol^{-1}, respectively for the reactions with CH_4, CH_3OH, and CH_3OCH_3. Unfortunately, examination of the T1 diagnostic of Lee and Taylor[34] in the CCSD(T) calculation of the CBS-QB3 method provided values suggestive of multireference character for all systems (0.022,

0.035, and 0.031 for the transition states in the $NO_3\cdot$ + CH_4, CH_3OH, and CH_3OCH_3 reactions). Even the $NO_3\cdot$ itself presents a T1 diagnostic value (0.024) outside the threshold of reliability of single-reference calculations (0.020). While we plan to conduct multireference calculations for hydrogen abstraction reactions by $NO_3\cdot$ in the future, such specialized calculations are well beyond the immediate scope of this work.

2.6. Conclusions

These results demonstrate that the rate constant for hydrogen abstraction from a large range of substrates (alcohols, ethers, and alkanes) by $NO_3\cdot$ depends on the strength of the C-H bond, number of abstractable hydrogens, and the ionization potential of the substate. The dependence on the ionization potential strongly infers these reactions proceed via polar transition state. Furthermore, in all cases, the rate constants are greater (by as much as an order of magnitude) in polar solvents compared to the gas-phase, and this rate enhancement can be readily attributed to stabilization of the transition state by the polar solvent in the context of Kirkwood theory; the transition state is more polar than the reactants, and the rate enhancement is a function of the dielectric constant of the solvent.

For alcohols and ethers, reaction rate constants were greater in acetonitrile than in water or were reduced with the addition of water to the acetonitrile. For alkanes, the addition of water to acetonitrile had no discernable effect on the rate constant. Together, these results suggest that either hydrogen-bonding to water does not stabilize the polar transition state, or that any stabilization of the transition state is offset by a nearly equivalent degree of stabilization afforded to the reactant(s). These results do not resolve this issue. These experimental results provide a fundamental understanding of $NO_3\cdot$ chemistry and will provide further insight into the mechanism by which the most abundant night-time atmospheric oxidant operates within the

atmosphere, specifically in non-gaseous environments such as raindrops, cloud formation, and upon aerosol surfaces.

2.7. References

(1) Landrigan, P. J. Air Pollution and Health. *Lancet Public Health* **2017**, *2* (1), e4–e5.

(2) Chapleski, R. C.; Zhang, Y.; Troya, D.; Morris, J. R. Heterogeneous Chemistry and Reaction Dynamics of the Atmospheric Oxidants, O3, NO3, and OH, on Organic Surfaces. *Chem. Soc. Rev.* **2016**, *45* (13), 3731–3746.

(3) Atkinson, R. Kinetics and Mechanisms of the Gas-Phase Reactions of the Hydroxyl Radical with Organic Compounds under Atmospheric Conditions. *Chem. Rev.* **1985**, *85*, 69–201.

(4) Mitroka, S.; Zimmeck, S.; Troya, D.; Tanko, J. M. How Solvent Modulates Hydroxyl Radical Reactivity in Hydrogen Atom Abstractions. *J. Am. Chem. Soc.* **2010**, *132* (9), 2907–2913.

(5) Wayne, R. P.; Barnes, I.; Biggs, P.; Burrows, J. P.; Canosa-Mas, C. E.; Hjorth, J.; Le Bras, G.; Moortgat, G. K.; Perner, D.; Poulet, G.; Restelli, G.; Sidebottom, H. The Nitrate Radical: Physics, Chemistry, and the Atmosphere. *Atmos. Environ. Part A, Gen. Top.* **1991**, *25* (1), 1–203.

(6) Ito, O.; Akiho, S.; Iino, M. Kinetic Study for Reactions of Nitrate Radical (NO3·) with Alcohols in Solutions. *Bull. Chem. Soc. Jpn.* **1989**, *62* (5), 1606–1611. https://doi.org/10.1246/bcsj.62.1606.

(7) Alfassi, Z. B.; Padmaja, S.; Neta, P.; Huie, R. E. Rate Constants for Reactions of NO3• Radicals with Organic Compounds in Water and Acetonitrile. *J. Phys. Chem.* **1993**, *97* (15), 3780–3782.

(8) Nathanael, J. G.; Hancock, A. N.; Wille, U. Reaction of Amino Acids, Di- and Tripeptides with the Environmental Oxidant NO3·: A Laser Flash Photolysis and Computational Study. *Chem. Asian J.* **2016**, *11* (22), 3188–3195.

(9) Koppenol, W. H.; Liebman, J. F. The Oxidizing Nature of the Hydroxyl Radical. A Comparison with the Ferryl Ion (FeO2+). *J. Phys. Chem.* **1984**, *88* (1), 99–101.

(10) Jiang, P. Y.; Katsumura, Y.; Ishigure, K.; Yoshidalb, Y. Reduction Potential of the Nitrate Radical in Aqueous Solution. *Inorg. Chem.* **1992**, *31* (24), 5135–5136.

(11) Reuveni, A.; Luz, Z. ESR of NO3 in Sodium Nitrate. *J. Magn. Reson.* **1976**, *23* (2), 271–274.

(12) Xiao-Yan, C.; Gong-Yi, H.; Dian-Xun, W.; Le-Min, L.; Guang-Xian, X. Density Functional Theory (DFT) Studies on the Ground State of NO3(2A'2) Radical and the First Triplet State of NO3+ Cation. *Chinese J. Chem.* **2000**, *18* (3), 267–270.

(13) Martin, T. W.; Swift, L. L.; Venable, J. H. NO3 Radical: "Soft" Lattice Preparation and Pure ESR Spectrum at 88°K. *J. Chem. Phys.* **1970**, *52* (4), 2138–2143.

(14) Eisfeld, W.; Morokuma, K. A Detailed Study on the Symmetry Breaking and Its Effect on the Potential Surface of NO3. *J. Chem. Phys.* **2000**, *113* (14), 5587–5597.

(15) Anglada, J. M.; Olivella, S.; Solé, A. Atmospheric Formation of the NO3 Radical from Gas-Phase Reaction of HNO3 Acid with the NH2 Radical: Proton-Coupled Electron-Transfer versus Hydrogen Atom Transfer Mechanisms. *Phys. Chem. Chem. Phys.* **2014**, *16* (36), 19437–19445.

(16) Kalemos, A. The Nature of the Chemical Bond in NO3, Neutral and Anion. *Theor. Chem. Acc.* **2020**, *139* (3), 50.

(17) Ito, O.; Akiho, S.; Lino, M. Kinetics for Reactions of the Nitrate Radical (NO3·) with

Aldehydes in Acetonitrile. *J. Phys. Chem.* **1989**, *93* (10), 4079–4083.

(18) Paul, S.; Deka, R. C.; Gour, N. K. Quantum Chemical Study on the Reaction Mechanism and Kinetics of Cl-Initiated Oxidation of Methyl n-Propyl Ether. *Theor. Chem. Acc.* **2018**, *137* (4), 62.

(19) Hoshino, H.; Sakakibara, K.; Watanabe, K. Autoxidation Resistant Cyclopentyl Methyl Ether. *Chem. Lett.* **2008**, *37* (7), 774–775.

(20) Przybylak, K. R.; Cronin, M. T. D. Correlation between Bond Dissociation Energies and Spin Distribution for the Radicals of Ethers: A DFT Study. *J. Mol. Struct. THEOCHEM* **2010**, *955* (1–3), 165–170.

(21) Luo, Y. R. *Comprehensive Handbook of Chemical Bond Energies*, 1st Ed.; CRC Press: Boca Raton, 2007.

(22) Russell, G. A. Reactivity, Selectivity, and Polar Effects in Hydrogen Atom Transfer Reactions. In *Free Radicals*; Vol. 1, Kochi, J. K., Eds.; John Wiley & Sons: New York, 1973; pp 275–331.

(23) Chew, A. A.; Atkinson, R.; Aschmann, S. M. Kinetics of the Gas-Phase Reactions of NO3 Radicals with a Series of Alcohols, Glycol Ethers, Ethers and Chloroalkenes. *J. Chem. Soc. - Faraday Trans.* **1998**, *94* (8), 1083–1089. https://doi.org/10.1039/a708183i.

(24) Rousse, D.; George, C. A Novel Long Path Photolysis Cell - Application to the Reactivity of Selected Organic Compounds toward the Nitrate Radical (NO3). *Phys. Chem. Chem. Phys.* **2004**, *6* (13), 3408–3414.

(25) Wan, L. K.; Peng, J.; Lin, M. Z.; Muroya, Y.; Katsumura, Y.; Fu, H. Y. Hydroxyl Radical, Sulfate Radical and Nitrate Radical Reactivity towards Crown Ethers in Aqueous Solutions. *Radiat. Phys. Chem.* **2012**, *81* (5), 524–530.

(26) Zhu, J.; Wang, S.; Tsona, N. T.; Jiang, X.; Wang, Y.; Ge, M.; Du, L. Gas-Phase Reaction of Methyl n-Propyl Ether with OH, NO3, and Cl: Kinetics and Mechanism. *J. Phys. Chem. A* **2017**, *121* (36), 6800–6809.

(27) Blanksby, S. J.; Ellison, G. B. Bond Dissociation Energies of Organic Molecules. *Acc. Chem. Res.* **2003**, *36* (4), 255–263.

(28) Finn, M.; Friedline, R.; Suleman, N. K.; Wohl, C. J.; Tanko, J. M. Chemistry of the T-Butoxyl Radical: Evidence That Most Hydrogen Abstractions from Carbon Are Entropy-Controlled. *J. Am. Chem. Soc.* **2004**, *126* (24), 7578–7584.

(29) Weaver, A.; Arnold, D. W.; Bradforth, S. E.; Neumark, D. M. Examination of the 2A′2 and 2E″ States of NO3 by Ultraviolet Photoelectron Spectroscopy of NO3-. *J. Chem. Phys.* **1991**, *94* (3), 1740–1751.

(30) Aschmann, S. M.; Atkinson, R. Rate Constants for the Reactions of the NO3 Radical with Alkanes at 296 ± 2 K. *Atmos. Environ.* **1995**, *29* (17), 2311–2316.

(31) Reichardt, C.; Welton, T. *Solvents and Solvent Effects in Organic Chemistry*, 4th ed.; Wiley-VCH Verlag & Co. KGaA: Boschstrasse 12, 69469 Weinheim, Germany, 2010.

(32) Montgomery, J. A.; Frisch, M. J.; Ochterski, J. W.; Petersson, G. A. A Complete Basis Set Model Chemistry. VII. Use of the Minimum Population Localization Method. *J. Chem. Phys.* **2000**, *112* (15), 6532–6542.

(33) Gaussian 09, Revision A.02, Frisch, M. J.; Trucks, G. W.; Schlegel, H. B.; Scuseria, G. E.; Robb, M. A.; Cheeseman, J. R.; Scalmani, G.; Barone, V.; Petersson, G. A.; Nakatsuji, H.; Li, X.; Caricato, M.; Marenich, A.; Bloino, J.; Janesko, B. G.; Gomperts, R.; Mennucci, B.; Hratchian, H. P.; Ortiz, J. V.; Izmaylov, A. F.; Sonnenberg, J. L.; Williams-Young, D.; Ding, F.; Lipparini, F.; Egidi, F.; Goings, J.; Peng, B.; Petrone, A.; Henderson, T.;

Ranasinghe, D.; Zakrzewski, V. G.; Gao, J.; Rega, N.; Zheng, G.; Liang, W.; Hada, M.; Ehara, M.; Toyota, K.; Fukuda, R.; Hasegawa, J.; Ishida, M.; Nakajima, T.; Honda, Y.; Kitao, O.; Nakai, H.; Vreven, T.; Throssell, K.; J. A. Montgomery, J.; Peralta, J. E.; Ogliaro, F.; Bearpark, M.; Heyd, J. J.; Brothers, E.; Kudin, K. N.; Staroverov, V. N.; Keith, T.; Kobayashi, R.; Normand, J.; Raghavachari, K.; Rendell, A.; Burant, J. C.; Iyengar, S. S.; Tomasi, J.; Cossi, M.; Millam, J. M.; Klene, M.; Adamo, C.; Cammi, R.; Ochterski, J. W.; Martin, R. L.; Morokuma, K.; Farkas, O.; Foresman, J. B.; Fox, D. J. Gaussian, Inc., Wallingford CT, 2016.

(34) Lee, T. J.; Taylor, P. R. A Diagnostic for Determining the Quality of Single-reference Electron Correlation Methods. *Int. J. Quantum Chem.* **1989**, *36* (23 S), 199–207.

Chapter 3. Mechanism and Kinetics of the Reaction of Nitrate Radical with Carboxylic Acids

3.1. Authors

Mark Paradzinsky, Aditya Ponukumati, and James M. Tanko*

Department of Chemistry, Virginia Polytechnic Institute and State University, Blacksburg, Virginia 24061

3.2. Introduction

Gas-phase organic acids in the atmosphere are produced by both natural sources, such as isoprene emission from broadleaf trees,[1] and artificial sources, including diesel engines emissions.[2] These organic acids pose both human health risks via pollution and particulate matter, as well as through interactions with the environment, e.g., acid rain, soil erosion, water and soil acidification. In the southeastern United States, the source of 30–50% of summertime rainwater acidity is believed to be from formic acid.[1] Studies on the removal of atmospheric pollutants have focused on hydroxyl radical (HO·) reactions due to its high reactivity. However, reactions with nitrate radical (NO_3·) also represent a major pathway for the breakdown of organic pollutants in the atmosphere. The success of NO_3· as an atmospheric "detergent" arises from its high electrophilicity. In the atmosphere, NO_3· is primarily formed through the reaction

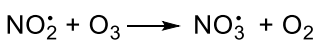

(1)

however, NO_3· is highly photolyzable and rapidly decomposes according to

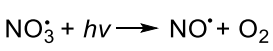

(2)

and

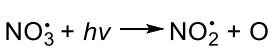

(3)

during the day. This causes the concentration of $NO_3\cdot$ to peak at night whereby it breaks down organic pollutants through electrophilic addition to π-bonds and electron-transfer with aromatic rings. In the absence of these two more reactive pathways, reactions are expected to proceed via hydrogen abstraction.[3] In solution there are a number of ways to generate $NO_3\cdot$, such as the flash photolysis of cerous nitrates, or pulse radiolysis of nitric acid.[3] The aqueous one-electron reduction potential of 2.49 V for $NO_3\cdot$ makes it a highly reactive oxidizing agent.[4]

While gas-phase studies of $NO_3\cdot$ have been the subject of much work in the literature,[3] there are no studies examining reactions with saturated carboxylic acids in the gas-phase. As $NO_3\cdot$ also operates in cloud formation, within raindrops, and upon aerosol surfaces,[5] we expanded our search to the condensed-phase and found three reports.

The first report, by Dogliotti and Hayon, broadly examined reactions of $SO_4\cdot^-$ and $NO_3\cdot$ from ceric sulfate and ceric nitrate in water with various substrates.[6] Although the authors reported rate constants of 2.1×10^5 M^{-1} s^{-1} and 4.6×10^4 M^{-1} s^{-1} for the reaction of $NO_3\cdot$ with HCO_2H and CH_3CO_2H, respectively, the focus of the paper was on cerous salts and radical generation. Because of this, the authors had no discussion about the chemistry following radical formation. In their report characterizing $NO_3\cdot$ by electron spin resonance, Martin, Swift, and Venable include a brief, qualitative, and seemingly misplaced observation that reactions of $NO_3\cdot$ with CH_3CO_2H and $CH_3CH_2CO_2H$ result in decarboxylation products;[7] though the report indicated that this would be the subject of future studies, no follow-up work was found in the literature. Neta and Huie compared their reported rate constant for reactions of $NO_3\cdot$ with HCO_2H ($<1.0 \times 10^5$ M^{-1} s^{-1})[8] in water to the hydrogen abstractions rate constants of alcohols and commented only that the value is “in agreement with the high C-H bond strength of formic acid.”

As examination of $NO_3\cdot$ reactions with saturated carboxylic acids are lacking, and the slight mechanistic insights available are conflicting, an analysis of HO· will be discussed, where appropriate, as it undergoes similar chemistries[9] and can provide a basis for the study of $NO_3\cdot$.

Hydrogen abstractions by $NO_3\cdot$ are believed to proceed through the classical hydrogen atom transfer (HAT) mechanism (Scheme 3.1),[3] in which hydrogen is abstracted through a linear transition structure. For carboxylic acids, two reaction pathways exist: abstraction from the carboxyl moiety, RCOO-H, or from the alkyl region, H-CR_2CO_2H.

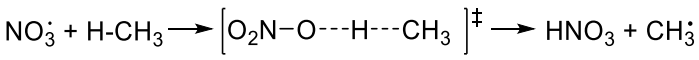

Scheme 3.8. The transition structure for $NO_3\cdot$ abstracting hydrogen from methane is linear.

There is ample experimental[10,11] and theoretical evidence[12] on reactions of branched and unbranched saturated carboxylic acids with HO·. For acids of chain length C1–C5, the reactivity at each carbon seems to increase as distance from the carbonyl increases except for the terminal methyl group, i.e., the reactivity followed the series α- < methyl < β- < γ-. The authors suggested the surprisingly low reactivity at the α-carbon suggests that the inductive effect of the carboxyl group may inhibit reactivity at the neighboring reaction center. We have previously reported that hydrogen abstractions by HO· are influenced by the polar effect, and the polar transition structure is stabilized by solvent interactions in the context of Kirkwood theory and destabilized through substituent effects that compete for electron density in the substrate. Recently we found that polar solvents stabilize the transition structure for $NO_3\cdot$ hydrogen abstractions from alkanes, ethers, and alcohols. The influence of carbonyls on abstractions of alkyl hydrogens from carboxylic acids appears unexplored (Figure 3.1).

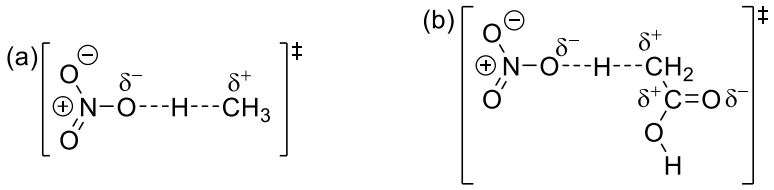

Figure 3.1. The development of a highly polarized transition state illustrated for (a) hydrogen abstraction from methane and (b) hydrogen abstraction from the α-position of acetic acid. The carbonyl dipole is hypothesized to destabilize the transition state.

Because of the low reactivity at the α-position, Singleton et al. examined the reaction of HO· with HCO_2H, DCO_2H and DCO_2D to identify which hydrogens were abstracted.[13] The authors reported kinetic isotope effects (KIE) of $k_{O\text{-}H}/k_{O\text{-}D} \approx 6$ and $k_{C\text{-}H}/k_{C\text{-}D} \approx 1$. These experiments were later expanded to CH_3CO_2H, CD_3CO_2H, and CD_3CO_2D by Singleton et al.[14] and Vimal and Stevens[15] where primary isotope effects of $k_{C\text{-}H}/k_{C\text{-}D}$ were close to unity and $k_{O\text{-}H}/k_{O\text{-}D} \approx 4$ and ≈ 7 were found, respectively. Abstractions of COO-H should generate the carboxyl radical (or bypass it; *vide infra*) which is known to subsequently decarboxylate into CO_2.[16] Butkovskaya analyzed the reaction of HO· with CH_3CO_2H for CO_2 yield, which confirmed COO-H abstraction.

These results suggesting abstraction occurs from COO-H rather than C-H were unexpected when examining bond strengths (Table 3.1). Because the bond dissociation energy (BDE) of the O-H bond of water is so high, reactions of HO· would be favorable for abstractions of both hydrogens; however, the C-H bonds are ≈ 16 kcal mol^{-1} weaker than the COO-H bond in both carboxylic acids. The Zavitsas model might explain the unusually high reactivity of the COO-H towards HO·,[19,20] despite their larger BDE. The model suggests abstraction of COO-H would result in decreased triplet-repulsion (^3E) in the linear transition state which lowers the activation energy compared to C-H abstraction. As the O-H bond in HNO_3 is considerably

weaker than H_2O, abstractions from carboxylic acids may occur from the alkyl region for reactions with $NO_3\cdot$ even with the reduced energy barrier from ^3E.

Table 3.4. Experimental bond dissociation energies for RH → R· + H· at 298 K

R-**H**	*BDE* (kcal mol^{-1})[ab]
H-OH	118.8 ± 0.1
H-ONO_2	101.7 ± 0.4
tert-C_4H_9O-**H**	106.4 ± 0.7
H-COOH	96 ± 1
HCOO-**H**	112 ± 3
H-CH_2COOH	96 ± 1
CH_3COO-**H**	112 ± 3

[a] Reference [17]. [b] Reference [18].

An alternative explanation has been suggested by Anglada who used high level quantum mechanical calculations to examine the reactivity of both the C-H and COO-H bonds of HCO_2H towards HO·.[21] He found that abstractions of COO-H begin with the development of a 5-membered pre-reactive hydrogen bond complex and proceed through a low energy intermediate (E_a = 0.51 kcal mol^{-1}) via a proton coupled electron-transfer (PCET) mechanism. PCET differs from classical HAT in that the proton-transfer and electron-transfer occur from different orbitals (Scheme 3.2).

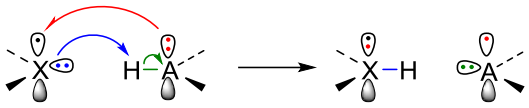

Scheme 3.9. Differing orbitals facilitate the proton- and electron-transfers in the proton coupled electron-transfer mechanism.

He also observed that reactions with the C-H bond proceed through classical HAT with only a mild increase in activation energy (E_a = 1.17, and 1.61 kcal mol^{-1}; the reactions differ in initial orientation). Anglada also investigated classical HAT for abstractions of COO-H and found a higher energy intermediate in the transition state (E_a = 3.4 kcal mol^{-1}). While he notes that BDE should dictate the reaction pathway, the "unexpected experimental observation" must be rationalized by PCET. This supports the notion that HO· reactions with carboxylic acids may be subject to a change in mechanism when the alkyl chain becomes sufficiently long. Further, PCET may be inaccessible for reactions with NO_3· as the developing O-H bond is substantially weaker making the reaction endothermic.

Computations by Denisov and Shestakov have led them to propose an alternate mechanism in the case of *tert*-butoxyl radical (*t*-BuO·), whose reaction with COO-H is also endothermic (Table 3.1).[22] The authors suggest abstractions of COO-H by *t*-BuO· would be coupled to the C-C bond cleavage step involved in decarboxylation rather than precede it; in other words, H-abstraction and decarboxylation are synchronous (Scheme 3.3). Denisov and Shestakov argue that these reactions represent "a rare instance when a lower activation energy coincides with the restructuring of orbitals of five atoms across the C-C and O-H bonds."

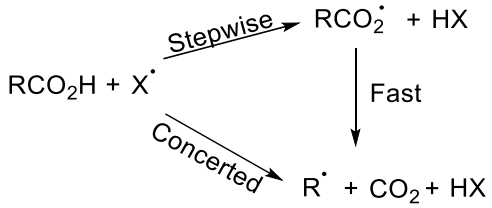

Scheme 3.10. Hydrogen abstractions from carboxylic acids can proceed either through a stepwise mechanism followed by decarboxylation or coupled to it.

For $NO_3\cdot$, the standard heats of formation (Figure 3.2) favor a concerted hydrogen abstraction-decarboxylation pathway suggesting an analogous mechanism may be plausible. Since the chemistry of $NO_3\cdot$ with RCO_2H is relatively unknown, a fundamental understanding of the nature of these reactions is needed due to their atmospheric importance.

$$NO_3^{\bullet} + CH_3CO_2H \longrightarrow HNO_3 + CH_3C(O)O^{\bullet} \qquad \Delta H^{\circ} = +7.9 \text{ kcal mol}^{-1}$$

$$NO_3^{\bullet} + CH_3CO_2H \longrightarrow HNO_3 + \dot{C}H_3 + CO_2 \qquad \Delta H^{\circ} = -5.4 \text{ kcal mol}^{-1}$$

$$NO_3^{\bullet} + CH_3CO_2H \longrightarrow HNO_3 + \dot{C}H_2C(O)OH \qquad \Delta H^{\circ} = -3.0 \text{ kcal mol}^{-1}$$

Figure 3.2. Standard heats of formation for three pathways of nitrate radical reacting with acetic acid.[23]

In this manuscript we aim to address basic features of these reactions *(Does $NO_3\cdot$ abstract hydrogen from RCO_2H, and what is the regiochemistry of this reaction? How does the reactivity change with increasing chain length, i.e., do more aliphatic hydrogens have higher reactivity? How does branching affect reactivity, that is, what if there are no α-C-H bonds? β-C-H?) How does the proximity of a carbonyl affect the development of a polarized transition state?) Are hydrogen abstraction from COO-H and decarboxylation concerted?* such that more complicated questions can be addressed in the future. Below we report the rate constants for the

reactions of $NO_3\cdot$ with several carboxylic acids in acetonitrile. To address the regiochemistry of the reaction, we used appropriately deuterated substrates to probe for a KIE. We explored changes in alkyl group reactivity of carboxylic acids by increasing chain length and differing branching patterns.

3.3. Experimental Section

Laser flash photolysis was used to monitor the kinetics of $NO_3\cdot$ reactions with carboxylic acids. The experimental setup were recently described in detail.[24] $NO_3\cdot$ was generated at 25 °C from 3×10^{-4} mol L^{-1} ceric ammonium nitrate (CAN) through excitation at 355 nm, and monitored at 635 nm in acetonitrile. All reagents were purchased from Millipore Sigma and used as received. Samples were agitated between each pulse and subjected to no more than 6 pulses before the sample was replenished. The transient traces and concentration profiles (Figures B.1–B.32, Tables B.1–B.16) may be found in Appendix B.

3.4. Results and Discussion

The rate constants for reactions of $NO_3\cdot$ with carboxylic acids in neat acetonitrile are summarized in Table 3.2, along with the number of C-H bonds. To probe the regiochemistry of abstraction, $NO_3\cdot$ was reacted with (2*d1*) and (2*d3*). A primary isotope effect $k_H/k_D \approx 7$ would be expected for abstractions from COO-H and C-H, respectively;[14,15] however, the observed KIE for both acids was ca. 1. To verify this result (2*d4*) was also examined and no difference in the rate constant was observed. Reactions of (1*d1*) also demonstrated no isotope effect. As the COO-H bond strength of (1) and (2) are the same (Table 3.1) we did not investigate HCOOD or DCOOD. The surprising lack of a KIE suggests that hydrogen abstraction is not occurring from either position, or, less likely, that hydrogen abstraction is not the rate limiting step.

Table 3.5. Rate constants for hydrogen abstraction by $NO_3\cdot$ from various carboxylic acids in CH_3CN at 25 °C.

	Substrate	$k_{AN} \times 10^{-5}$ M s		Substrate	$k_{AN} \times 10^{-5}$ M s
(1)	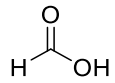	0.5 ± 0.1	(5)	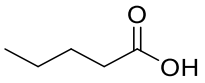	7.8 ± 1.4
(1*d*$_1$)	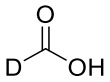	0.4 ± 0.1	(6)	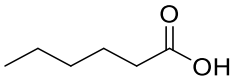	26.6 ± 4.7
(2)	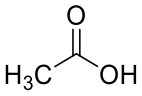	1.7 ± 0.2	(7)	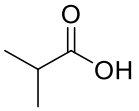	3.3 ± 0.4
(2*d*$_1$)	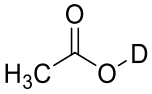	1.8 ± 0.2	(8)	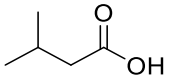	9.3 ± 1.1
(2*d*$_3$)	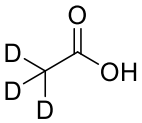	1.8 ± 0.1	(9)	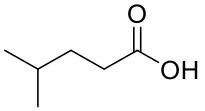	24.6 ± 5.2
(2*d*$_4$)	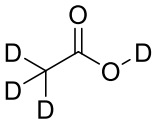	1.7 ± 0.1	(10)	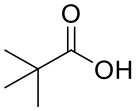	8.4 ± 0.4
(3)	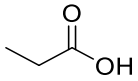	2.1 ± 0.1	(11)	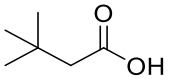	10.0 ± 1.1
(4)	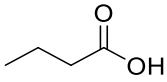	2.8 ± 0.2	(11*d*$_1$)	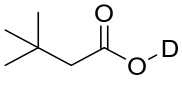	9.2 ± 1.6

A plot of the rate constants (for the non-deuterated substrates) versus the number of C-H bonds in the carboxylic acids (Figure 3.3) reveals upward curvature, suggestive of a change in mechanism for the reaction. For short chain acids, the rate constants are an order of magnitude smaller than normal aliphatic C-H bonds we have previously studied ($k_H = 10^6$ M^{-1} s^{-1})[24] despite

the α-C-H bonds of RCO_2H being weaker than alkanes by ≈ 2 kcal mol^{-1}.[18] This low reactivity could be explained by the polar effect (Figure 3.1). Because of the bond dipole moment of the carbonyl, it pulls electron density from the adjacent carbon through the inductive effect. When NO_3· approaches the already deactivated C-H bond in the transition state, the further buildup of positive charge is met with repulsion from the partial positive charge on the C-atom of the carbonyl. In the case of (1), the deactivation of the C-H bond could be even more extreme as the hydrogen is directly attached to the carbonyl.

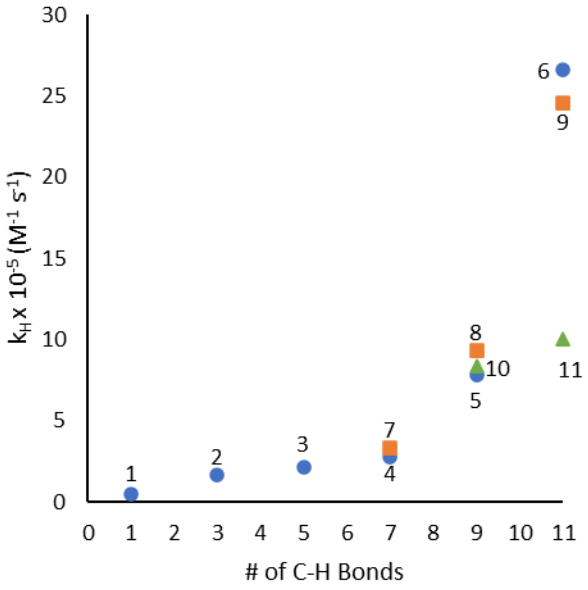

Figure 3.3. Plot of the hydrogen abstraction rate constant by NO_3· from unbranched (●), terminal iso-propyl (■), and terminal tert-butyl (▲) carboxylic acids vs. the number of C-H bonds in those acids.

As the acid chains become longer and more branched, they become more aliphatic in nature and their reactivity becomes comparable to alkanes. To determine if longer or highly branched acids were undergoing abstraction from the C-H or COO-H, (11*d1*) was examined. An analysis of the KIE ($k_{O\text{-}H}/k_{O\text{-}D}$ ≈ 1.1) indicates that these abstractions occur from the γ-carbons of

the bulky substituent. The modest increase in reactivity of (11) compared to (10) is a consequence of the lack of reactivity at the α-carbon as seen for the smaller acids.

As evidenced in the reports on HO·,[10–12] the nominal increase in rate constants between (3) and (7) could be explained by the poor reactivity of the terminal methyl groups (in addition to the polar effect at the α-carbon). Both effects could, in part, explain why the rate constant for (4) is small, as the only two abstractable hydrogens are at the β-position.

3.5. Conclusions

The rate constants for hydrogen abstraction of a series of carboxylic acids by NO_3· have been reported. No kinetic isotope effect was observed for reactions of small acids, suggesting that hydrogen abstraction is not occurring from either the COO-H or α-C-H for those acids. The reactivity of the substrates increases as they become longer and more highly branched with abstraction occurring from the alkyl region. The lack of evidence suggesting COO-H abstraction rules out the pathway of HAT coupled to decarboxylation for NO_3·. Previous reports on the low reactivity of terminal methyl groups with the more reactive HO· account for the reactivity of the other small acids. Although these studies have addressed some questions relating to NO_3· reactions with RCO_2H, many things remain unknown. *For carboxylic acids possessing only α-C-H and O-H, or in the special case of HCO_2H, what is the mechanism for these reactions? Is it addition to the carbonyl? Is it complexation follow by abstraction? Are abstractions from the alkyl region proceeding through classical HAT or PCET? Does a decrease in ^3E stabilize abstractions from COO-H? How is a polar transition state affected by changes in solvent when adjacent to a carbonyl?*

3.6. References

(1) Link, M. F.; Nguyen, T. B.; Bates, K.; Müller, J. F.; Farmer, D. K. Can Isoprene

Oxidation Explain High Concentrations of Atmospheric Formic and Acetic Acid over Forests? *ACS Earth Sp. Chem.* **2020**, *4* (5), 730–740. https://doi.org/10.1021/acsearthspacechem.0c00010.

(2) Friedman, B.; Link, M. F.; Fulgham, S. R.; Brophy, P.; Galang, A.; Brune, W. H.; Jathar, S. H.; Farmer, D. K. Primary and Secondary Sources of Gas-Phase Organic Acids from Diesel Exhaust. *Environ. Sci. Technol.* **2017**, *51* (18), 10872–10880. https://doi.org/10.1021/acs.est.7b01169.

(3) Wayne, R. P.; Barnes, I.; Biggs, P.; Burrows, J. P.; Canosa-Mas, C. E.; Hjorth, J.; Le Bras, G.; Moortgat, G. K.; Perner, D.; Poulet, G.; Restelli, G.; Sidebottom, H. The Nitrate Radical: Physics, Chemistry, and the Atmosphere. *Atmos. Environ. Part A, Gen. Top.* **1991**, *25* (1), 1–203.

(4) Jiang, P. Y.; Katsumura, Y.; Ishigure, K.; Yoshidalb, Y. Reduction Potential of the Nitrate Radical in Aqueous Solution. *Inorg. Chem.* **1992**, *31* (24), 5135–5136.

(5) Chapleski, R. C.; Zhang, Y.; Troya, D.; Morris, J. R. Heterogeneous Chemistry and Reaction Dynamics of the Atmospheric Oxidants, O3, NO3, and OH, on Organic Surfaces. *Chem. Soc. Rev.* **2016**, *45* (13), 3731–3746.

(6) Dogliotti, L.; Hayon, E. Transient Species Produced in the Photochemical Decomposition of Ceric Salts in Aqueous Solution. Reactivity of N03 and HS04 Free Radicals. *J. Phys. Chem.* **1967**, 71, 12, 3802–3808

(7) Martin, T. W.; Swift, L. L.; Venable, J. H. NO3 Radical: “Soft” Lattice Preparation and Pure ESR Spectrum at 88°K. *J. Chem. Phys.* **1970**, *52* (4), 2138–2143.

(8) Neta, P.; Huie, R. E. Rate Constants for Reactions of NO3 Radicals in Aqueous Solutions. *J. Phys. Chem.* **1986**, *90* (19), 4644–4648. https://doi.org/10.1021/j100410a035.

(9) Atkinson, R. Kinetics and Mechanisms of the Gas-Phase Reactions of the Hydroxyl Radical with Organic Compounds under Atmospheric Conditions. *Chem. Rev.* **1985**, *85*, 69–201.

(10) Taniguchi, H.; Fukui, K.; Ohnishi, S. I.; Hatano, H.; Hasegawa, H.; Maruyama, T. Free-Radical Intermediates in the Reaction of the Hydroxyl Radical with Amino Acids. *J. Phys. Chem.* **1968**, *72* (6), 1926–1931. https://doi.org/10.1021/j100852a012.

(11) Serpone, N.; Martin, J.; Horikoshi, S.; Hidaka, H. Photocatalyzed Oxidation and Mineralization of C1-C5 Linear Aliphatic Acids in UV-Irradiated Aqueous Titania Dispersions-Kinetics, Identification of Intermediates and Quantum Yields. *J. Photochem. Photobiol. A Chem.* **2005**, *169* (3), 235–251. https://doi.org/10.1016/j.jphotochem.2004.07.001.

(12) Sun, W.; Yang, L.; Yu, L.; Saeys, M. Ab Initio Reaction Path Analysis for the Initial Hydrogen Abstraction from Organic Acids by Hydroxyl Radicals. *J. Phys. Chem. A* **2009**, *113* (27), 7852–7860. https://doi.org/10.1021/jp8090792.

(13) Singleton, D. L.; Paraskevopoulos, G.; Irwin, R. S.; Jolly, G. S.; McKenney, D. J. Rate and Mechanism of the Reaction of Hydroxyl Radicals with Formic and Deuteriated Formic Acids. *J. Am. Chem. Soc.* **1988**, *110* (23), 7786–7790. https://doi.org/10.1021/ja00231a032.

(14) Singleton, D. L.; Paraskevopoulos, G.; Irwin, R. S. Rates and Mechanism of the Reactions of Hydroxyl Radicals with Acetic, Deuterated Acetic, and Propionic Acids in the Gas Phase. *J. Am. Chem. Soc.* **1989**, *111* (14), 5248–5251. https://doi.org/10.1021/ja00196a035.

(15) Vimal, D.; Stevens, P. S. Experimental and Theoretical Studies of the Kinetics of the

Reactions of OH Radicals with Acetic Acid, Acetic Acid-d 3 and Acetic Acid-d 4 at Low Pressure. *J. Phys. Chem. A* **2006**, *110* (40), 11509–11516. https://doi.org/10.1021/jp063224y.

(16) T. Michael Bockman; Stephan M. Hubig, and; Kochi*, J. K. Direct Observation of Ultrafast Decarboxylation of Acyloxy Radicals via Photoinduced Electron Transfer in Carboxylate Ion Pairs. **1997**. https://doi.org/10.1021/JO9617833.

(17) Blanksby, S. J.; Ellison, G. B. Bond Dissociation Energies of Organic Molecules. *Acc. Chem. Res.* **2003**, *36* (4), 255–263.

(18) Luo, Y. R. *Comprehensive Handbook of Chemical Bond Energies*, 1st Ed.; CRC Press: Boca Raton, 2007.

(19) Zavitsas, A. A. Activation Energy Requirements in Hydrogen Abstractions. Quantitative Description of the Causes in Terms of Bond Energies and Infrared Frequencies. *J. Am. Chem. Soc.* **1972**, *94* (8), 2779–2789. https://doi.org/10.1021/ja00763a041.

(20) Zavitsas, A. A.; Melikian, A. A. Hydrogen Abstractions by Free Radicals. Factors Controlling Reactivity. *J. Am. Chem. Soc.* **1975**, *97* (10), 2757–2763. https://doi.org/10.1021/ja00843a025.

(21) Anglada, J. M. Complex Mechanism of the Gas Phase Reaction between Formic Acid and Hydroxyl Radical. Proton Coupled Electron Transfer versus Radical Hydrogen Abstraction Mechanisms. *J. Am. Chem. Soc.* **2004**, *126* (31), 9809–9820. https://doi.org/10.1021/ja0481169.

(22) Denisov, E. T.; Shestakov, A. F. Free-Radical Decarboxylation of Carboxylic Acids as a Concerted Abstraction and Fragmentation Reaction. *Kinet. Catal.* **2013**, *54* (1), 22–33. https://doi.org/10.1134/S0023158413010059.

(23) Ruscic, B.; Bross, D. H. Active Thermochemical Tables (ATcT) values based on ver. 1.122p of the Thermochemical Network (2020); available at ATcT.anl.gov https://atct.anl.gov/Thermochemical Data/version 1.122p/index.php.

(24) Paradzinsky, M.; Troya, D.; Tanko, J. M. Insight into Hydrogen Abstractions Ny Nitrate Radical: Structural, Solvent Effects, and Evidence for a Polar Transition State. *J. Phys. Chem.* **2021**, *In Review*.

Chapter 4. Does Metal Ion Complexation Make Radical Clocks Run Fast? An Experimental Perspective

4.1. Authors

Marwa K. Abdel Latif, Jared N. Spencer, Mark Paradzinsky, James M. Tanko*

4.2. Abstract

The rate constant for the β-scission of the cumyloxyl radical (k_β) was measured in the presence of various added electrolytes in acetonitrile and DMSO solvent. The results show that in CH_3CN, k_β increases in the presence of added electrolyte, roughly paralleling the size of the cation: $Li^+ > Mg^{2+} \approx Na^+ > {}^nBu_4N^+ >$ no added electrolyte. This effect is attributable to stabilizing ion–dipole interactions in the transition state of the developing carbonyl group, a conclusion supported by MO calculations (gas-phase). Compared to the gas-phase predictions however, this effect is seriously attenuated in solution because complexation of the cation to the electrophilic alkoxyl radical (relative to the solvent, CH_3CN) is very weak. Because the interaction of Li^+ and Na^+ is much stronger with DMSO than with CH_3CN, addition of these ions has no effect on the rate of β-scission.

4.3. Introduction

Radical clocks,[1] usually based upon unimolecular fragmentations or rearrangements with known absolute rate constants, are used to measure the rate constants of competing bimolecular products through competition kinetics. The underlying assumption in these experiments is that the unimolecular rate constant for the clock reaction is constant and not affected by reaction conditions.

In 2003, Horn and Clark posed the intriguing question "*Does Metal Ion Complexation Make Radical Clocks Run Fast?*"[2] To answer this question, these workers studied,

computationally, the Δ^5-hexenyl radical rearrangement (Scheme 4.1), postulating that complexation of a metal ion to the double bond would decrease the activation energy (E_a). These authors found that cations (in general) were predicted to decrease the activation barrier to ring closure. For alkali metals, the predicted decrease in E_a paralleled the size of the ion. For Li^+, which exhibited the most dramatic effect, the barrier decreased from 8.3 to 3.2 kcal/mol (CBS-RAD-(QCISD,B3-LYP), which equates to a three order of magnitude rate acceleration in the presence of Li^+. The magnitude of this effect, of course, would likely be diminished in a polar solvent (vs. the gas-phase) but the calculations nonetheless predicted a ca. 1.7 kcal/mol reduction of the barrier in THF (obtained via explicit solvation of the reactants and transition state).[2]

Scheme 4.11. Complexation of lithium ion to the double bond of Δ^5-hexenyl radical is predicted to enhance the rate of cyclization

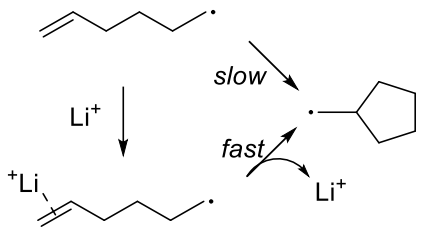

The rationale for Horn and Clark's hypothesis, *i.e.*, that Li^+ will complex to a double bond and lower the activation barrier for intermolecular radical additions, has received some experimental and computational support in the polymer literature as Li^+ complexation has been demonstrated to "catalyze" the free radical polymerization of olefins, increase the propagation rate constant, etc.[3–6] However, the original question posed about radical clocks (unimolecular reactions) in their 2003 paper remains unanswered. Moreover, questions about how metal ions might affect rates of other classes of clock reactions have yet to be addressed.

Our interest in this question comes from a slightly different perspective. Neutral free radicals can be generated by the electrochemical oxidation and reduction of anions and cations,

respectively. Because electrochemical techniques such as cyclic voltammetry can be used to measure rate constants for reactions following electron transfer (illustrated for oxidation of an anion in Scheme 4.2), and electrochemical oxidations/reductions require a supporting electrolyte, the possibility that an ion can change the rate of a neutral radical reaction becomes an important issue.

Scheme 4.12. Neutral radicals generated by the electrochemical oxidation of the corresponding anions

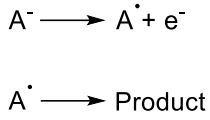

To test whether the unimolecular rate constant for a neutral radical clock reaction would vary in the presence of a cation, we examined the rate constant for β-scission of alkoxyl radicals. In work dating back to the early 1960s, Walling and co-workers used the β-scission of *t*-butoxyl radical as a free radical clock to measure the rate constants for competing hydrogen abstraction reactions (Scheme 4.3).[7] Walling and Wagner also suggested that k_β increased with solvent polarity (attributable to an increase in dipole moment of the transition structure associated with the formation of a polar carbonyl group),[8] a hypothesis that was subsequently confirmed three decades later.[9–11]

Based upon this precedent, it was quite reasonable to suspect that if the transition state for β-scission is stabilized by a polar solvent (dipole–dipole interaction), the transition state might also be stabilized by an ion–dipole interaction as well. As a test, the rate constant for β-scission of cumyloxyl radical was measured in the presence of various electrolytes typically used for electrochemical studies, as well as added water. Cumyloxyl, rather than *t*-butoxyl, radical was

used because of its characteristic absorbance at 485 nm that could be used to monitor the kinetics of the reaction.[9,10,12]

Scheme 4.13. β-Scission of *tert*-butoxyl radical is faster in polar solvents

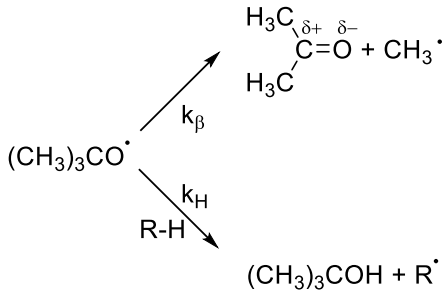

4.4. Experimental and Theoretical Methods

Dicumyl peroxide (98%), lithium perchlorate ($LiClO_4$, 99.9%), magnesium perchlorate ($Mg(ClO_4)_2$, ACS grade), and sodium perchlorate ($NaClO_4$, ACS grade) were purchased from Aldrich and used as received.

n-Tetrabutylammonium perchlorate (Bu_4NClO_4) was prepared by ion exchange reaction,[13] recrystallized 3–5 times from ethyl acetate/hexane, dried at 80 °C in a vacuum oven for 24 hours, dried over P_2O_5 in a vacuum desiccator and transferred under *vacuo* into the glovebox. D_2O (Aldrich, 99.9 atom % D) in 0.6 mL vials were purchased and used as received.

Steady-state UV-vis spectra were recorded on a Hewlett–Packard diode array UV-vis spectrophotometer (HP 8452A). Laser flash photolysis were performed with an Applied Photophysics LKS.80 spectrometer using the third harmonic of a Continuum Surelite I-10 Nd:YAG laser (4–6 ns pulse, 355 nm). Transient signals were monitored by a Hewlett–Packard Infinium digital oscilloscope and analyzed with the Applied Photophysics Spectra Kinetic Workstation software (version 4.59.) Variable temperature experiments were performed with a

jacketed cell holder connected to a VWR Scientific Products (PolyScience) variable temperature-circulating bath (model 1150-A). The cell holder was equipped with a thermocouple to measure the temperature directly adjacent to the cuvette.

Steady-state UV-Vis spectra were recorded on all solutions to verify that dicumyl peroxide was the only species absorbing at the excitation wavelength prior to photolysis. Solutions containing the cumyloxyl radical precursor (dicumyl peroxide) and desired electrolyte were prepared in acetonitrile (or DMSO) solvent and purged for 10 minutes prior to photolysis. To test for possible laser power dependence on the apparent rate constant, solutions were flashed at various laser intensities. Within experimental error, k_β was constant, verifying that no other second order competing side reactions were occurring (*e.g.*, dimerization.)

For the variable temperature work, to minimize thermal decomposition of the peroxide, multiple samples were prepared and only exposed to high temperatures during the actual laser flash experiment. Samples were thermally equilibrated prior to photolysis by placing the cuvettes in a tray in the circulating bath for 10 min. Afterward, the samples were placed in the spectrometer and equilibrated for an additional 5 min. Temperature dependent studies were performed over the range –11 to 75 °C.

Calculations were performed using the Gaussian 09 computational software package.[14] Conformational analysis was performed at the B3LYP/6-31G* level of theory and basis set. All optimized reactant, transition state, and product structures, as well as potential energy surface profiles, were obtained at the B3LYP/6-311+(3df,2pd) level of theory and basis set (where the unrestricted method was used for open-shell systems). All optimized structures were verified and thermochemical corrections to the electronic energies were obtained from frequency jobs at the same theory and basis set. Single point energies for all optimized structures were obtained with

the CCSD(T)/Aug-CC-pVTZ theory and basis set. Thermochemical corrections from the lower level frequency jobs were applied to the single point energies from the CCSD jobs to obtain the thermochemical data presented in Tables 3 and 4. For $M^+ = {}^nBu_4N^+$, the optimization and frequency jobs were only performed at the B3LYP/6-31G* level of theory and basis set and the single point energies were obtained with the CCSD/ 6-31G* theory and basis as the large size of the cation made more expensive methods unfeasible. Additionally, the convergence criteria for the single point job of the parent cumyloxyl radical/${}^nBu_4N^+$ structure had to be reduced by one significant figure in order to achieve convergence. The visualization software MOLDEN was used to visualize the Gaussian output files.[15]

4.5. Results and Discussion

Cumyloxyl radical (**1**) was generated by flash photolysis of dicumyl peroxide at 355 nm in acetonitrile, and its characteristic absorption at *ca.* 485 nm was used to follow the kinetics.[9,10,12] Rate constants measured in the presence of various electrolytes (that were sufficiently soluble in CH_3CN) are summarized in Table 4.1. We also determined the rate constant in the presence of H_2O, D_2O, and in the presence of electrolyte plus water. These results are summarized in the Supporting Information.

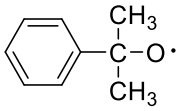

1

Arrhenius parameters for β-cleavage in CH_3CN with added electrolyte, H_2O, and D_2O were determined via non-linear regression analysis in accordance with the Arrhenius equation (Eq 1); reported errors are based upon 95% confidence limits. The results are summarized in Table 4.2.

Table 4.6. Rate constants for the β-cleavage of cumyloxyl radical in the presence of various electrolytes in CH_3CN at 25 °C

[Electrolyte]	$k_\beta/10^5$ s^{-1}			
(mol·L^{-1})	$LiClO_4$	$NaClO_4$	*n*-Bu_4NClO_4	$Mg(ClO_4)_2$
0	8.1 (0.2)			
0.08	9.2 (0.2)	8.4 (0.2)	8.2 (0.2)	8.3 (0.3)
0.15	10.1 (0.2)	8.6 (0.2)	8.6 (0.2)	9.5 (0.3)
0.23	10.0 (0.2)	9.0 (0.2)	8.7 (0.2)	9.7 (0.3)
0.31	11.5 (0.3)	9.4 (0.2)	9.1 (0.3)	9.2 (0.3)
0.39	12.6 (0.2)	10.2 (0.2)	9.5 (0.3)	
0.62	16.4 (0.3)	11.2 (0.2)	10.5 (0.3)	
0.77	19.2 (0.8)	11.9 (0.2)	10.7 (0.3)	
1.15			11.8 (0.4)	
1.54			12.8 (0.5)	

$$k = Ae^{-E_a/RT} \quad (1)$$

To obtain further insight, the free energy of activation for the β-cleavage of the tbutoxyl radical (complexed to Li^+, Na^+, K^+, and $^nBu_4N^+$) were obtained through molecular orbital calculations (gas-phase, Table 4.3). To assess the relative binding affinity of the cations (M^+) to t-butoxyl radical relative to the solvent (CH_3CN), ΔG for the following exchange reaction was determined: $CH_3CN/M^+ + {}^tBuO\bullet \rightarrow CH_3CN + {}^tBuO\bullet/M^+$; the results are summarized in Table 4.4.

In all cases, the addition of electrolyte increased the rate constant for β-scission of the cumyloxyl radical (Table 4.1; Figure 4.1) in the order $Li^+ > Mg^{2+} \approx Na^+ > {}^nBu_4N^+$; for clarity, the results for $Mg(ClO_4)_2$ were omitted from the figure. The magnitude of the effect increased with

increasing electrolyte concentration. This study was somewhat limited by the solubility of the electrolyte in CH_3CN solvent; *e.g.*, $KClO_4$ was not sufficiently soluble.

Table 4.7. Arrhenius parameters for the β-cleavage of cumyloxyl radical in the presence of various additives (M) in CH_3CN

M	[M]/mol·L^{-1}	log(A/s^{-1})	E_a/kcal·mol^{-1}	k_β /10^5 s^{-1} at 30 °C
None	0.00	11.5 (0.2)	7.7 (0.7)	11.2 (0.6)
$LiClO_4$	0.23	11.5 (0.2)	7.5 (0.3)	14.4 (0.5)
	0.39	11.6 (0.4)	7.5 (0.5)	17.6 (0.7)
	0.77	11.6 (0.9)	7.4 (0.7)	21.8 (0.7)
$NaClO_4$	0.39	11.1 (0.2)	7.0 (0.6)	13.7 (0.8)
$^nBu_4NClO_4$	0.39	11.2 (0.6)	7.2 (0.6)	12.8 (0.9)
$MgClO_4$	0.39	11.5 (0.2)	7.5 (0.7)	12.7 (0.9)
H_2O	2.1	11.3 (0.20	7.1 (0.3)	14.0 (0.6)
D_2O	2.1	11.5 (0.2)	7.4 (0.2)	13.2 (0.4)

The activation energy for β-scission was also examined in the presence and absence of electrolyte (Table 4.2). Although the results seem to suggest a lowering of the barrier when M^+ is present, the effect is too small to be detected (*i.e.*, for all the cations, differences in the measured activation energies are within experimental uncertainty). Consequently, to further probe whether the observed trend was consistent with the hypothesis that cation complexation with the developing C=O in the transition state was responsible for the observed rate enhancement, MO calculations (gas-phase) were performed to model the effect of cations on the analogous β-scission of t-butoxyl radical. The results are summarized in Table 4.3.

Table 4.8. Calculated (CCSD(T)/uB3LYP) activation free energies for β-scission of *t*-butoxyl radical complexed to a cation in the gas-phase

M^+	$\Delta G^{\ddagger}$/kcal·mol^{-1}
None	13.8
K^+	7.6
Na^+	5.8
Li^+	2.8
$^{n}Bu_4N^+$	14.0[a]

[a]Obtained from CCSD/uB3LYP theory and 6-31G* basis set. See note in **4.4. Experimental and theoretical methods**. The values above are calculated on the basis of

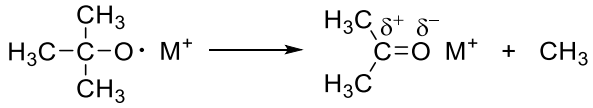

Although *qualitatively* consistent with the notion that complexation of M^+ to an alkoxyl radical will lower the barrier to β-cleavage, the most striking result from the gas-phase calculations is that the effect is predicted to be much greater than what was experimentally observed. Almost certainly, the explanation is that in solution, complexation of M^+ to an electron deficient species such as an alkoxyl radical is strongly disfavored (relative to complexation to the solvent, CH_3CN). The calculations summarized in Table 4.4 clearly support this interpretation.

Table 4.9. Calculated (CCSD/B3LYP) ΔG for binding of *tert*-butoxyl radical to cations (relative to CH_3CN) in the gas-phase

M^+	ΔG/kcal·mol^{-1}
K^+	4.0

Na^+	5.5
Li^+	5.3
$^nBu_4N^+$	2.91[a]

[a]ΔE obtained from B3LYP/6-31G* theory and basis set. See note in **4.4. Experimental and theoretical methods**. The values above are calculated on the basis of $CH_3CN/M^+ + {}^tBuO\cdot \rightarrow CH_3CN + {}^tBuO\cdot/M^+$

A reviewer of this manuscript suggested that these conclusions might be further amplified by performing these experiments in an additional solvent, and in response, some of these experiments were repeated in DMSO with $LiClO_4$ and $NaClO_4$ (two of the electrolytes that exhibited the largest effect in acetonitrile). Cumyloxyl radical is known to abstract hydrogen from DMSO ($k_H = 1.8\ (\pm\ 0.1) \times 10^4\ M^{-1}s^{-1}$),[16] but this competing pathway constitutes less than 10% of the observed rate constant, and is easily corrected for ($k_\beta = k_{obs} - k_H[DMSO]$.)

As shown in Figure 4.1, over the same range of concentrations, added Li^+ or Na^+ has no effect on the rate constant for β-scission when DMSO is the solvent. This result makes perfect sense because Li^+ and Na^+ are much more strongly solvated by DMSO compared to CH_3CN; the free energies of transfer from $CH_3CN \rightarrow$ DMSO are –14.9 and –5.9 kcal/mol, respectively.[17]

We also examined whether k_β would be lowered with the addition of water, perhaps as a result of hydrogen bonding to the developing C=O in the transition state. As shown in Figure 4.2, in the presence and absence of electrolyte ($^nBu_4NClO_4$), k_β increased modestly with increased water concentration (CH_3CN solvent.)

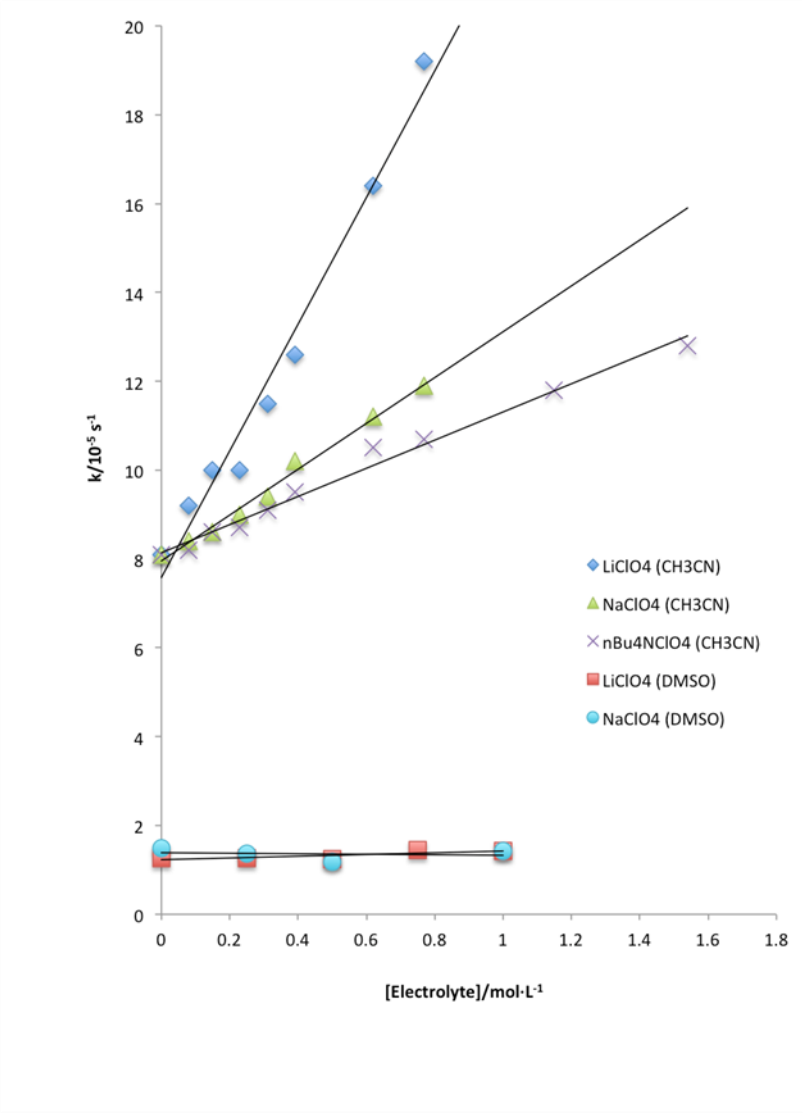

Figure 4.16. Rate constants for the β-scission of cumyloxyl radical in the presence of added electrolytes (CH_3CN and/or DMSO solvent, ambient temperature).

It was also thought that if H-bonding to the transition state were important, the system might exhibit a modest secondary kinetic isotope effect. Within experimental error however, there was no significant difference between H_2O and D_2O in either the observed rate constants or activation parameters (Table 4.2). To the extent there was an isotope effect, these measurements were not sensitive enough to detect it. Hence, these results do not reveal whether the rate increases

because the transition state is stabilized by H-bonding to water, or simply because the solvent polarity increases with water addition.

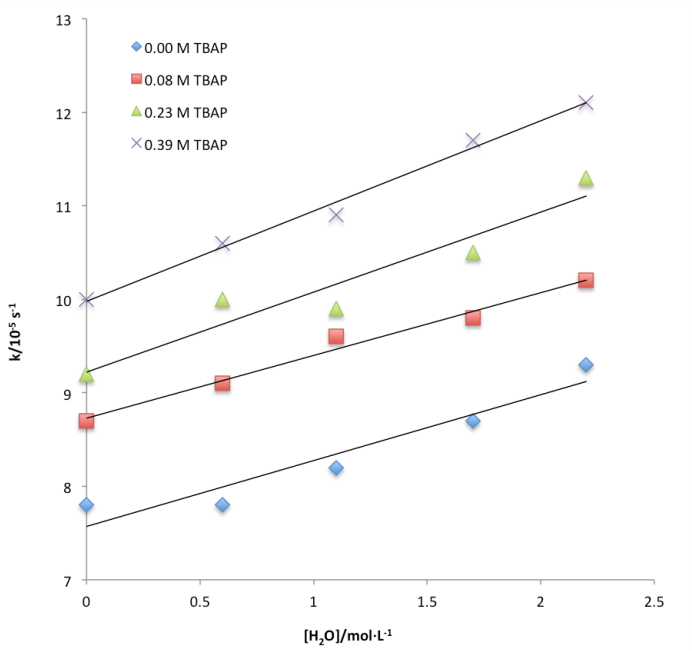

Figure 4.17. Combined effect of electrolyte ($^{n}Bu_4NClO_4$) and water on the rate constant for β-scission of *t*-butoxyl radical (CH_3CN solvent, ambient temperature).

4.6. Conclusions

The results demonstrate that through complexation, the absolute rate constants for radical clock reactions such as the β-scission of alkoxyl radicals are influenced by cations ($Li^+ > Mg^{2+} \approx Na^+ > {}^{n}Bu_4N^+$). This effect is attributable to stabilizing ion–dipole interactions in the transition state of the developing carbonyl group, a conclusion supported by MO calculations. In solution however, this effect is seriously attenuated because complexation of the cation to the electrophilic alkoxyl radical (relative to the solvent, CH_3CN) is very weak. Presumably the effect would be greater in a non-polar solvent, but this would be difficult to test experimentally because of

solubility issues. In DMSO, which binds Li^+ and Na^+ more tightly, this effect is not observed. Addressing the original question posed by Horn and Clark, yes, metal ion complexation can cause radical clocks to run fast—and for reasons that make sense based on fundamental principles. However, these results also go one step further by showing that that even if the complexation between the radical and ion is unfavorable, a significant effect can be observed if, in cases such as studied herein, there is an increase in dipole moment going from reactant → transition state.

4.7. References

(1) Griller, D.; Ingold, K. U. Free-Radical Clocks. *Acc. Chem. Res* **1980**, *13* (9), 317–323.

(2) Horn, A. H. C.; Clark, T. Does Metal Ion Complexation Make Radical Clocks Run Fast? *J. Am. Chem. Soc.* **2003**, *125* (9), 2809–2816.

(3) Clark, T. Lithium Cation as Radical-Polymerization Catalyst. *J. Am. Chem. Soc.* **2006**, *128* (34), 11278–11285.

(4) Hirano, T.; Segata, T.; Hashimoto, J.; Miwa, Y.; Oshimura, M.; Ute, K. Syndiotactic- and Heterotactic-Specific Radical Polymerization of N-n-Propylmethacrylamide Complexed with Alkali Metal Ions. *Polym. Chem.* **2015**, *6*, 4927–4939.

(5) Noble, B. B.; Smith, L. M.; Coote, M. L. The Effect of LiNTf 2 on the Propagation Rate Coefficient of Methyl Methacrylate. *Polym. Chem.* **2014**, *5*, 4974–4983.

(6) Vyakaranam, K.; Barbour, J. B.; Michl, J. Li + -Catalyzed Radical Polymerization of Simple Terminal Alkenes. *J. Am. Chem. Soc.* **2006**, *128* (17), 5610–5611.

(7) Walling, C.; Jacknow, B. B. Positive Halogen Compounds. I. The Radical Chain Halogenation of Hydrocarbons by f-Butyl Hypochlorite1. *J. Am. Chem. Soc.* **1960**, *82* (23), 6108–6112.

(8) Walling, C.; Wagner, P. J. Positive Halogen Compounds. X. Solvent Effects in the Reactions of t-Butoxy Radicals. *J. Am. Chem. Soc.* **1964**, *86* (16), 3368–3375.

(9) Avila, D. V.; Brown, C. E.; Ingold, K. U.; Lusztyk, J. Solvent Effects on the Competitive β-Scission and Hydrogen Atom Abstraction Reactions of the Cumyloxyl Radical. Resolution of a Long-Standing Problem. *J. Am. Chem. Soc.* **1993**, *115* (2), 466–470.

(10) Baciocchi, E.; Bietti, M.; Salamone, M.; Steenken, S. Spectral Properties and Absolute Rate Constants for β-Scission of Ring-Substituted Cumyloxyl Radicals. A Laser Flash Photolysis Study. *J. Org. Chem.* **2002**, *67* (7), 2266–2270.

(11) Tsentalovich, Y. P.; Kulik, L. V.; Gritsan, N. P.; Yurkovskaya, A. V. Solvent Effect on the Rate of β-Scission of the Tert-Butoxyl Radical. *J. Phys. Chem. A* **1998**, *102* (41), 7975–7980.

(12) Avila, D. V.; Ingold, K. U.; Di Nardo, A. A.; Zgierski, M. Z.; Lusztyk, J.; Zerbetto, F. Electronic Absorption Spectra of Some Alkoxyl Radicals. An Experimental and Theoretical Study. *J. Am. Chem. Soc.* **1995**, *117* (10), 2711–2718.

(13) House, H. O.; Gall, M.; Olmstead, H. D.; House, H. O. The Chemistry of Carbanions. XIX. The Alkylation of Enolates from Unsymmetrical Ketones. *J. Org. Chem.* **1971**, *36* (16), 2361–2371.

(14) Gaussian 09, Revision A.02, Frisch, M. J.; Trucks, G. W.; Schlegel, H. B.; Scuseria, G. E.; Robb, M. A.; Cheeseman, J. R.; Scalmani, G.; Barone, V.; Petersson, G. A.; Nakatsuji, H.; Li, X.; Caricato, M.; Marenich, A.; Bloino, J.; Janesko, B. G.; Gomperts, R.; Mennucci, B.; Hratchian, H. P.; Ortiz, J. V.; Izmaylov, A. F.; Sonnenberg, J. L.; Williams-Young, D.; Ding, F.; Lipparini, F.; Egidi, F.; Goings, J.; Peng, B.; Petrone, A.; Henderson, T.; Ranasinghe, D.; Zakrzewski, V. G.; Gao, J.; Rega, N.; Zheng, G.; Liang, W.; Hada, M.; Ehara, M.; Toyota, K.; Fukuda, R.; Hasegawa, J.; Ishida, M.; Nakajima, T.; Honda, Y.; Kitao, O.; Nakai, H.; Vreven, T.; Throssell, K.; J. A. Montgomery, J.; Peralta, J. E.; Ogliaro, F.; Bearpark, M.; Heyd, J. J.; Brothers, E.; Kudin, K. N.; Staroverov, V. N.; Keith, T.; Kobayashi, R.; Normand, J.; Raghavachari, K.; Rendell, A.; Burant, J. C.; Iyengar, S. S.; Tomasi, J.; Cossi, M.; Millam, J. M.; Klene, M.;

Adamo, C.; Cammi, R.; Ochterski, J. W.; Martin, R. L.; Morokuma, K.; Farkas, O.; Foresman, J. B.; Fox, D. J. Gaussian, Inc., Wallingford CT, 2009.

(15) Schaftenaar, G.; Noordik, J. H. Molden: A Pre- and Post-Processing Program for Molecular and Electronic Structures. *J. Comput. Aided. Mol. Des.* **2000**, *14* (2), 123–134.

(16) Salamone, M.; Dilabio, G. A.; Bietti, M. Reactions of the Cumyloxyl and Benzyloxyl Radicals with Strong Hydrogen Bond Acceptors. Large Enhancements in Hydrogen Abstraction Reactivity Determined by Substrate/Radical Hydrogen Bonding. *J. Org. Chem.* **2012**, *77* (23), 10479–10487.

(17) Hörzenberger, F.; Gritzner, G. Gibbs Energies, Entropies and Enthalpies of Transfer for Monovalent Cations from Acetonitrile to Several Solvents. *J. Chem. Soc. Faraday Trans.* **1993**, *89* (19), 3557–3564.

Chapter 5. High Barrier Biosourced Polyester from Dimethyl [2,2'-bifuran]-5,5'-dicarboxylate

5.1. Authors

H. Eliot Edling [a], Hua Sun [b], Edward Paschke [c], David A. Schiraldi [b], James M. Tanko [d], Mark Paradzinsky [d], S. Richard Turner [a,*]

[a] Macromolecules Innovation Institute, Department of Chemistry, Virginia Tech, Blacksburg, VA, 24061, USA

[b] Department of Macromolecular Science and Engineering, Case Western Reserve University, 10900 Euclid Avenue, Cleveland, OH, 44106, USA

[c] 4 Hearthstone Path, Galena, IL, 61038, USA

[d] Department of Chemistry, Virginia Tech, Blacksburg, VA, 24061, USA

5.2. Abstract

Poly(ethylene 2,2'-bifuran-5,5'dicarboxylate) (PEBF) is a new biosourced polyester recently reported to have significant enhancement of oxygen barrier properties and glass transition temperature when compared to poly(ethylene terephthalate). We report herein our independent studies on the polymerization and properties of this new polyester. Our findings are contrasted to an earlier report. While the T_g of 106–108 °C was confirmed to be consistent with the early data, we observed crystallization on both cooling and heating cycles in the DSC which were not previously observed, higher tensile elongation to break values, and significantly lower oxygen permeabilities compared to the earlier report. Preliminary uniaxial orientation experiments indicate that this polymer is a good candidate for biaxial orientation processing. We discovered that both the monomer, dimethyl-2,2'-bifuran-5,5'-dicarboxylate (BFE), and the polymer are subject to thermal oxidation which was explored with cyclic voltammetry on the

monomer. Experiments with added antioxidant during the polycondensation show marked reduction in the thermal oxidation as observed by color reduction and enhanced stability to melt processing.

5.3. Introduction

Poly(ethylene terephthalate) (PET) is a ubiquitous commercial polymer with major applications in food/beverage packaging, fibers, and composites. These enormously successful applications render PET to be one of the world's most important and highest production volume commercial polymers. These applications result from a myriad of excellent properties and process characteristics of PET. PET can be processed to a clear, colorless plastic that can be oriented to give good gas barrier properties for food packaging and excellent strength for fibers. PET has very low organoleptics and can readily be reprocessed and has the highest recycle rate of any of the commodity plastics. However, PET possesses a modest T_g of 76 °C which prohibits use in various applications that require higher heat resistance such as dishwasher safe products, hot fill food packaging, etc. The modest barrier to oxygen also limits food packaging application of materials with oxygen sensitivity. In addition, there is a strong interest in finding new biosourced monomers for many PET applications for environmental reasons.

Poly(ethylene furanoate), PEF, for example, has received considerable interest the last few years as a biosourced (2,5-furandicarboxylic acid) polyester to replace PET. A few important references are listed, but this paper does not provide a list of the many recent papers published on PEF.[1–4] The physical properties of PEF somewhat mirror PET except it exhibits a 10X oxygen barrier enhancement vs. PET. It also has a marginally higher T_g—85 °C vs. PET ca. 76 °C.[5] PEF made from biosourced ethylene glycol (EG) results in a highly touted food

packaging polyester.[6] The food packaging industry has considerable interest in providing "sustainable/green" bottles and other food packaging materials for their products.

Recently a new polyester poly(ethylene 2,2'-bifuran-5,5'dicarboxylate) (PEBF) was reported in the literature.[7] PEBF was reported to have significantly enhanced oxygen barrier to PET, a marginally higher tensile modulus compared to PET and UV absorbance as a result of the bifuran structure which could be useful to protect UV sensitive cargo in a package. However, cast and compression molded films were extremely brittle, perhaps due to the abnormally high catalyst level used in the melt-phase polymer synthesis. This polymer exhibited a significantly enhanced T_g of 106 °C however this reported PEBF did not show a melting peak in the reheat cycle of a DSC and thus would not be expected to be orientable. It was also reported to be extremely brittle with tensile elongations of ca. 5%. This report summarizes our independent studies, which were in progress at the time of the first publication of PEBF, of the synthesis and property evaluation of PEBF. In our studies we have used standard melt-phase polyesterification chemistry, with significantly lower catalyst levels than in the previous report on PEBF, employing both melt-phase polycondensation to high molecular weight PEBF and also with a combination melt-phase solid state polymerization. Using these polycondensation techniques we have obtained PEBF with significantly enhanced thermal and mechanical properties in comparison to the earlier PEBF report. We have also discovered that the BFE monomer and PBEF polyester exhibit significant degradation in oxygen at high temperatures.

5.4. Experimental

5.4.1. Materials

Dimethyl-2,2'-bifuran-5,5'-dicarboxylate (BFE) was prepared via a similar route to that reported in the literature.[7,8] Bis (2-hydroxyethoxy) 2,2'-bifuran-5,5'-dicarboxylate (HBEBF) was

prepared from the acid chloride of the BFE diacid reacted with ethylene glycol. [2,2'-bifuran]-5,5'-diylbis(methylene) diacetate or 2, 2'-bifuran-5,5'-dimethanol diacetate (BFDMA) were prepared by a similar metal catalyzed coupling reaction and the diol was reacted with acetic anhydride to form the diacetate for cyclic voltammetry experiments. All monomers were dried in a vacuum oven overnight at 35 °C and stored in a dry box before using. Ethylene glycol (EG, 99%) was obtained from Sigma Aldrich and used as received. Dichloroacetic acid (99%) (DCA) was obtained from Alpha Aesar and used as received. Pentaerythritol tetrakis[3-[3,5-di-*tert*-butyl-4-hydroxyphenyl]propionate 98%) (Irganox® 1010, 98%) and antimony (III) oxide (99%) and titanium (IV) butoxide (97%) were purchased from Sigma Aldrich. 1-Butanol (99.9%) was purchased from Fisher Scientific and dried over magnesium sulfate. A titanium catalyst solution (ca. 0.02 g/mL) was prepared by placing 0.2 g titanium (IV) butoxide into 10 mL volumetric flask and diluting to the calibration line with 1-butanol. The titanium solution was then transferred to a sealed container and purged with nitrogen for 10 min. Antimony (III) oxide was made into a slurry (ca. 0.02 g/mL) by adding 0.2 g with antimony (III) oxide to a 10 mL volumetric flask and diluting to the calibration line with EG. The zinc (II) diacetate and manganese (II) diacetate solutions were prepared by adding 0.14 or 0.2 g respectively to a 10 mL volumetric flask, diluting to the calibration line with methanol and allowing to dissolve overnight. Trifluoroacetic acid-*d* (TFA-d, 99.5 atom % D) was obtained from Sigma Aldrich. Chloroform-*d* ($CDCl_3$, 99.8% atom D þ 0.05% V/V TMS) was obtained from Cambridge Isotope Laboratories, Inc.

5.4.2. Characterization Methods

^{1}H NMR analysis was performed by using a Varian Unity 400 MHz spectrometer with at least 32 scans at 23 °C on polymer samples (ca. 50 mg) dissolved in a binary mixture of TFA-

d:$CDCl_3$ (10/90). Inherent viscosity (η_{inh}) was measured in DCA[9] following a procedure adapted from ASTM method D4603 by using a Cannon Type B glass capillary viscometer. Thermogravimetric analysis (TGA) was performed by using a TA Instruments Q500 starting at 25 °C and proceeding to 600 °C with a 10 °C/min heating rate under nitrogen. Differential scanning calorimetry (DSC) was performed on 5–8 mg polymer samples by using a TA Instruments Q2000 under nitrogen with 10 °C/min heating and cooling rates. Glass transitions temperatures (T_gs) were determined from the midpoint of the transition inflection point on the second heating ramp. Tensile testing of copolyesters was performed on dogbone specimens cut from 0.25 mm thick compression molded films. Dogbones were cut using a Cricut Explore One™ cutting machine into dimensions specified in the ASTM D638 procedure. An Instron 5500R machine was used for testing punched dogbone tensile specimens at a crosshead motion rate of 10 mm/min and an initial grip separation of 25.4 ± 2.0 mm. A MOCON® OX-TRAN 2/21 (Minneapolis, MN) measured oxygen flux *J(t)* for compression molded films made at 23 °C, 0% relative humidity and 1 atm pressure. Specimens were cut from the center of compressed films, placed in a test cell and conditioned until a steady baseline was reached, at which point oxygen was introduced to the test cell. As the oxygen concentration reached a constant distribution, the flux reached steady state value J_0. A Mitutoyo digimatic micrometer measured test film thickness in nine discrete locations, from which the average thickness was calculated. Oxygen permeabilities $P(O_2)$ were calculated based on steady state flux J_0, average thickness l, and the permeant gas pressure drop across the specimen Δp (Equation 1).

$$P = J_0 \frac{l}{\Delta p} \quad (1)$$

Uniaxial orientation was accomplished on dogbone specimens cut from compression molded films and stretched 4 × 1 at 100 °C in an Instron testing machine.

5.4.3. Cyclic Voltammetry

Cyclic voltammetry (CV) was performed with an EG&G Princeton Applied Research Model 283 Potentiostat/Galvanostat and analyzed with the Princeton Applied Research Electrochemistry Powersuite software (version 2.58). CV was carried out in a five-neck electrochemical cell. A 3.2 mm diameter glassy carbon (GC) electrode was used as the working electrode with a measured active surface area of 0.18 cm^2. A platinum coil was used as an auxiliary electrode. The reference electrode was Ag/Ag^+ (0.1 M in CH_3CN, 0.337 V vs. SCE). Prior to use, the GC electrode was sanded and polished with alumina slurry (Buehler) in the decreasing order of 1.0 μM, 0.3 μM, and 0.05 μM on a micro-cloth. The electrode was then rinsed with an isopropanol and DI water. Monomer (5 mM) was dissolved in supporting electrolyte consisting of tetra-*n*-butylammonium hexafluorophosphate ($TBAPF_6$) thrice recrystallized from absolute ethanol with distilled acetonitrile as solvent. All CVs were performed with 95% IR compensation. Scan rates varied from 0.025 to 1 V/s. All experiments were conducted in a nitrogen atmosphere.

5.4.4. Synthesis of PEBF from BFE via Melt Phase with Titanium Catalyst

Polymerization was performed in a dry 100 mL round bottom flask equipped with an overhead stirrer, a distillation arm and a nitrogen inlet. EG (5.16 g, 2 mol eq.) and BFE (10.08 g, 1 mol eq.) were charged into the flask along with titanium butoxide solution (150 ppm Ti to the theoretical yield). Reactions were degassed with vacuum and purged with nitrogen three times to remove oxygen. The reaction flask was submerged in a metal bath and stirred at 170 °C for 1 h, then 180 °C for 1 h, then 190 °C for 2 h, all while continually purging with nitrogen and stirring at 200 rpm. The temperature of the metal bath was increased to 275 °C while vacuum was then slowly applied over the course of 20 min until a pressure of 0.1–0.3 mmHg was reached. The

stirring speed was reduced to 30–40 rpm and stirring was allowed to continue under vacuum for 1 h. The polymer was then removed from the flask by breaking the flask. The light amber colored polyester was removed from the stir rod with hammer, chisel, and snips and then broken up and/or ground, then rinsed with DI water, and vacuum dried overnight at 120 °C. The yield of isolated polymer was 85% of theoretical with losses due to polymer remaining on the stirrer and flask walls. An inherent viscosity of 0.91 dL/g in DCA was measured.

5.4.5. Synthesis of PFE with Antimony, Zinc, and Manganese Catalyst

The polycondensation was performed with the same monomer charges and same reactor set up as in the preceding example. The catalyst system was changed to an antimony, zinc, manganese system with 250 ppm Sb, 100 ppm zinc, and 100 ppm Mn from the respective catalyst solutions. The reaction flask was submerged in a metal bath and stirred at 180 °C for 1 h, then 200 °C for 2 h, 220 °C for 2 h. During this time the polymerization was purged with nitrogen and stirred with the overhead stirrer. The polycondensation was then ramped to 260 °C during a 15–min period while gradually increasing the vacuum. This was followed by holding, while slowly stirring (stirring speed was reduced to 30–40 rpm) the viscous melt, at 260 °C and 0.2 Torr for 50 min. On cooling and removal from the stir rod, a light tan polymer with an IV of 0.81 dL/g with a DEG level measured by NMR of 2.2% was obtained.

5.4.6. Synthesis of PEBF from HBEBF with Irganox® 1010

A typical synthesis is as follows (Scheme 5.1b): The polycondensation reactor set up is as described earlier. HBEBF (62.5 g, 0.0.20 mol) was charged into a 100–mL round bottom flask along with 1000 ppm Irganox® 1010 and enough catalyst solution to equal 250 ppm Sb (III) metal by mass of the theoretical yield. Oxygen and moisture were removed from the flask with vacuum and purging with nitrogen three times. Stirring rate was set to 200 rpm and the flask was

submerged into a 230 °C metal bath for 1 h under continual nitrogen purge. The temperature was then ramped to 270 °C while slowly applying vacuum over 15 min.

The polycondensation step was then carried out with a 30 rpm stirring rate under decreased pressure (≤ 0.2 Torr) for 15 min. The flask was then removed from the metal bath and allowed to cool to room temperature. The polyester was isolated by breaking the flask and then removing the polyester from the stir rod by using a hammer, chisel and end nippers. The light tan colored polymer that was obtained was rinsed with DI water and then dried overnight under vacuum at 120 °C. An inherent viscosity of 0.60 dL/g was measured in DCA. NMR showed a DEG level of 0.4 mol %.

Scheme 5.14. Synthesis schemes for PEBF from BFE and HBEBF using antimony-based catalysts

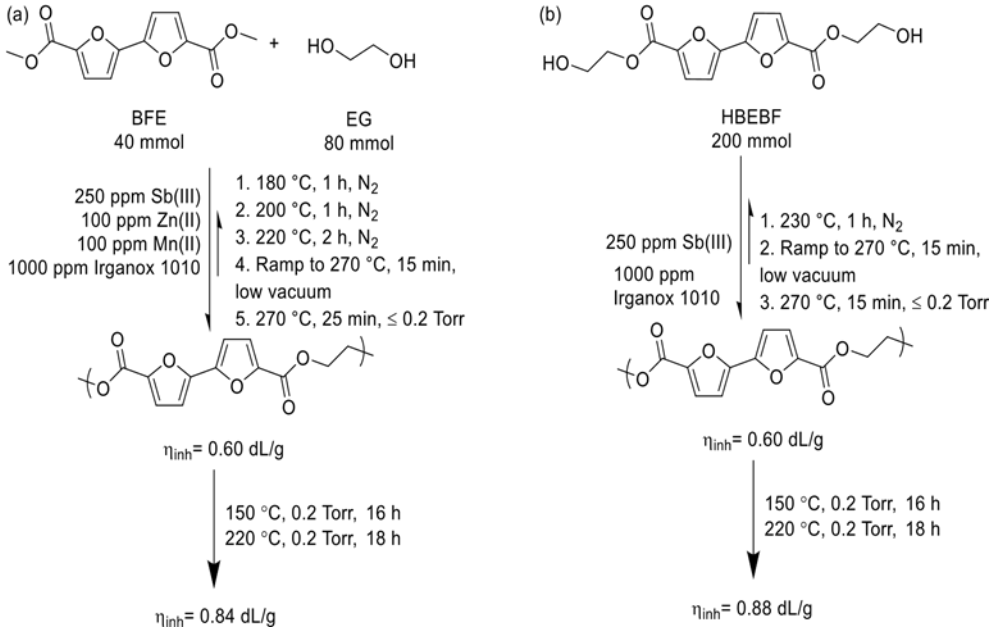

5.4.7. Solid State of Polymerization of PEBF

The isolated and dried polyester was ground into pellets using a Cumberland 6508 Beside-The Press Granulator equipped with a 4.76 mm mesh screen. Pellets with diameters between 2 and 3 mm were selected by sifting with 2- and 3-mm mesh screens and placed into a 100 mL round bottom flask, which was then attached to a rotary evaporator equipped with an oil bath. The pellets were dried by submerging the flask into a 150 °C bath and rotating for 16 h at 0.2 Torr. The temperature was then increased to 220 °C and the pellets were allowed to rotate for an additional 18 h at 0.2.

5.4.8. Compression Molded Copolyester Films

Thoroughly dried polyester particles were melt pressed into films by using a PHI Q-230H hydraulic press heated to 280 °C. Samples (4–5 g) were sandwiched between two aluminum plates, each with a layer of Kapton® film coated with Rexco Partall® Powder Glossy Liquid mold release agent to prevent sticking. Aluminum shims inserted between the aluminum plates controlled thickness. To press films, samples were placed inside the press on top of a Kapton® layered aluminum plate until the sample started to melt (1–3 min), at which point a shim and the second layer of Kapton® and aluminum were added. The plates were then moved to the center of the press, which was lightly closed until complete melting of sample (ca. 2 min). Three press-release cycles (30 s each) were completed at 5 tons of force, followed by pressing once at 10 tons of force. After pressing, samples were immediately transferred to an ice water bath to quench the samples. Films were subsequently removed from the Kapton® and dried in a 40 °C vacuum oven overnight. Samples for tensile analysis were compression molded by using a 0.30 mm shim, which produced 0.25 mm films. IVs after melt pressing generally exhibited modest decreases of 0.1–0.2 IV units.

5.5. Results and Discussion

5.5.1. Synthesis and Structural Characterization

High molecular weight PEBF (IVs from 0.7 to 0.9) was readily synthesized using conventional melt phase polycondensation conditions with modest levels of titanium or antimony catalysts. Diethylene glycol levels of 2–4 mol% were typically observed in these polycondensations. Melt phase transesterification of the dimethyl ester was facilitated by zinc and manganese catalysts when antimony was used as the catalyst. The zinc and manganese catalysts are known to promote initial transesterification reactions to convert the methyl ester ends to hydroxyethoxy end groups. As shown in Fig. 5.1, the ^{1}H NMR confirmed the expected polyester structure. Evaluation of the physical properties of these samples was challenging due to formation of bubbles during the melt pressing process. Due to issues with the thermal/oxidative stability of polyesters produced with bifuran structures (as discussed below), Irganox® 1010 was added during synthesis to minimize degradation. (Scheme 5.1).

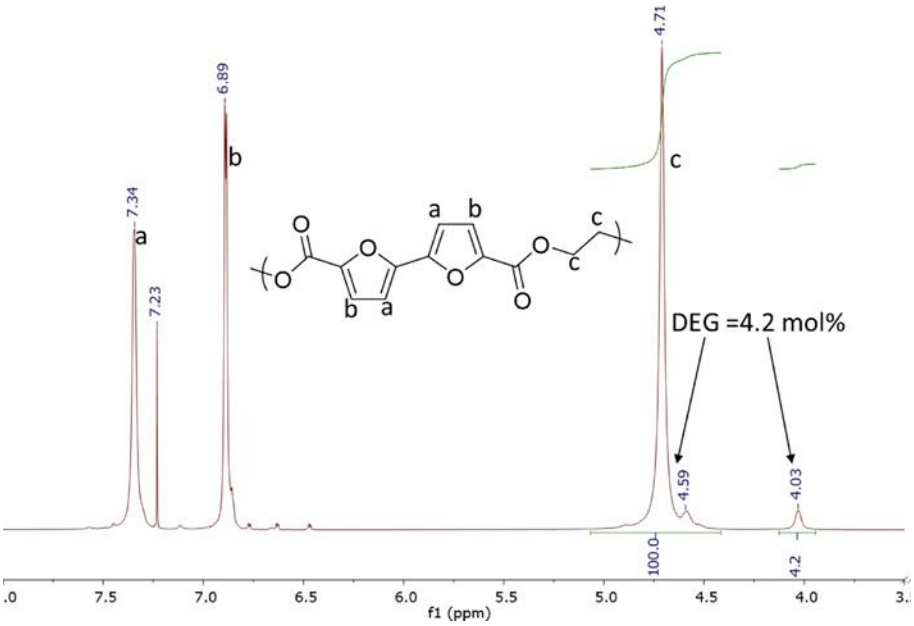

Figure 5.18. ^{1}H NMR of PEBF produced from BFE and EG.

For the BFE polymerization shown in Scheme 5.1a, the polymerization mixture was stirred under nitrogen for 4 h at temperatures of 180–220 °C which produced a yellow amber melt and allowed the removal of methanol condensate via distillation. Polycondensation of both polyesters was facilitated by antimony catalyst to achieve high molecular weight polyesters. Typically, a transesterification step is required before melt polycondensation to allow for the exchange of EG and removal of methanol (Scheme 5.1a). This transesterification step was not necessary for HBEBF (Scheme 5.1b) since the EG moiety was already present instead of the methyl ester. The time needed for complete transesterification of BFE was determined by monitoring the methyl ends using ^{1}H NMR (Fig. D.1) at intervals during the transesterification steps. Polycondensation was carried out with a stirring rate of 30 rpm so as to prevent significant wrapping at higher viscosities. Reduced pressure was used to remove excess diol and increase molecular weight to a level that permitted subsequent solid-state polymerization to achieve high molecular weights. Both reactions turned light yellow in the melt within 15 min of submerging into the metal bath and slightly darker still after increasing the temperature to 270 °C. The polyester produced from HBEBF was lighter in color, possibly from it experiencing less time in the melt under at high temperature. ^{1}H NMR analysis confirmed complete integration of the monomers into the polyester (Fig. 5.1 and Fig. D.2). Polyesters synthesized with HBEBF typically have lower concentrations of DEG in the final polymer. This is likely due to both shorter melt phase reaction times since it is well known that DEG forms more readily at high temperatures and the lack of excess EG in the polycondensation melt.

Polyesters were insoluble in solvents used in typical size exclusion chromatography (SEC). Inherent viscosity (η_{inh}) was measured by preparing 0.5 g/mL solutions of PEBF in dichloroacetic acid.[9] The Mark–Houwink–Sakurada parameters for PET in dichloroacetic acid

were used to estimate M_v from η_{inh} with Equation 2.[10] Using this equation, the estimated M_v for synthesized copolyesters an η_{inh} values of 0.80 dL/g is 26,600 g/mol.

$$[\eta_{inh}] = 1.7 \times 10^{-4}(M_v)^{0.83} \quad (2)$$

Results for structural and thermal characterization are detailed in Table 5.1 for polyesters synthesized without Irganox® 1010.

5.5.2. Thermal Properties

The thermal properties between PEBF synthesized from BFE and HBEBF are significantly different (Table 5.1). Polyesters from BFE showed a lower temperature single step weight loss in TGA—362 °C vs. 381 °C for the HBEBF polyester. This could result from the longer melt phase condensation times for the BFE polyester and/or the zinc and manganese catalysts that are present in the BFE polyester. The higher Tg of the HBEBF polyester (109 °C vs. 105 °C) is likely a result of the lower DEG level of 0.4 mol % vs. 4.1 mol %. The higher molecular weight of the HBEBF polyester could be responsible for the lower enthalpy of fusion since high molecular weight is known to decrease the rate of crystallization. A careful study using DSC of the melting behavior of the polyesters would be needed to confirm this conclusion.

5.5.3. Cyclic Voltammetry

Our initial attempts to polymerize BFE under standard melt phase polycondensation conditions with a titanium isopropoxide catalyst at 100 ppm concentration resulted in high molecular weight PEBF but the melt was observed to darken to a dark brown over the course of the polycondensation. PET polymerized under similar conditions, from DMT, exhibited only the characteristic yellowish color always seen with a simple titanium catalyzed system. Polymerization of FE under similar conditions resulted in a light tan polymer. These results suggested to us that the BFE is more easily oxidized than FE and certainly DMT when subjected

to the high temperature melt phase. It is known that linked furan units lead to chemical structures that can readily be oxidized to radical cations (higher ionization potentials and small HOMO–LUMO gaps).[11] Therefore, we employed cyclic voltammetry to study the difference in the redox behavior of FE and BFE. Figs. D.3, D.4, and D.5 show the cyclic voltammograms of BFE, BE and BFDMA.

Table 5.10. Thermal and structural analysis of PEBF polyesters from BFE and HBEF synthesized without Irganox® 1010

PEBF monomer(s)	$T_{d,5\%}$ (°C)	T_g (°C)	T_m (°C)	T_c (°C)	T_{cc} (°C)	ΔH (J/g)	η_{inh} (dL/g)	M_v (g/mol)	DEG level (mol%)
HBEBF (ssp)	381	109	256	179	199	27.7	0.88	29,800	0.4
BFE and EG (all melt phase)	362	105	254	179	185	42.8	0.75	24,600	4.1

The summary of the oxidation and reduction potentials is shown in Table 5.2 and these results clearly show that BFE is readily oxidized to its radical cation while FE and DMT (not shown) do not show this oxidation. BFDMA, where the electron withdrawing ester carbonyl on the furan ring is replaced by methylene, was even more easily oxidized. All three samples showed reduction reversible reduction peaks in the CV scans. Attempted polycondensation of BFDMA with ethylene glycol under our standard melt phase polycondensation conditions (100 ppm Ti catalyst 270 °C poly-condensation temperature) gave a very brittle black product likely due to the oxidative instability of this monomer.

Table 5.11. Cyclic voltammetry results

Compound	Reduction (E_{pc}, V)	Oxidation (E_{pa}, V)
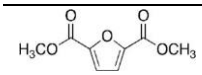	–2.686, –2.456, –2.058	–
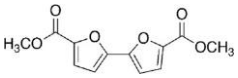	–2.757, –2.438, –2.314, –2.093	+1.429
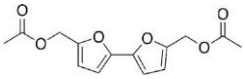	–2.962	+1.011

Scans taken at 100 mV s ^{1} Ag/Agþ (0.1 M in CH_3CN, 0.337 V vs. SCE)

As a result of the CV data, we studied the thermal oxidative stability of PEBF samples and as described earlier added Irganox® 1010 to the initial monomer charge in the polymerizations (Table 5.3). The polyester thermal oxidative characteristics were probed by placing PEBF samples into glass vials and heating at 280 °C for 1 h. PEBF in air with or without antioxidant showed significant color darkening consistent with oxidative degradation. A combination of antioxidant and inert atmosphere exhibited little apparent visible degradation. PEBF without the antioxidant showed significantly more weight loss in an isothermal TGA experiment at 300 °C for 2 h than a PET control (2.3% compared to 5%).

5.5.4. Mechanical Properties

Tensile testing was performed on polyester samples synthesized from BFE and EG. Films were measured to have an η_{inh} of 0.75 dL/g after compression molding. Table 5.4 summarizes tensile analysis results and compares them to results reported in the literature.[7] Modulus and yield stress values are nearly twice that of amorphous polyethylene terephthalate (PET) polyester samples.

Table 5.12. Results of thermal oxidative study on PEBF polyester.[a]

Air	Nitrogen
Sample 1. Without Irganox® 1010. Sample turned black with significant bubbling observed during heating process.	Sample 3. Without Irganox® 1010. Sample turned dark brown with bubbling observed during heating process.
Sample 2. With Irganox® 1010. Sample turned brown with little bubbling observed.	Sample 4. With Irganox® 1010. Very slight increase in tan color with no bubbling observed.

[a] Samples heated 280 °C for 1 h in sealed vials. Nitrogen blanketed samples were in vials purged with nitrogen and evacuated three times before sealing. Irganox®1010 was added at 1000 ppm level.

Table 5.13. Mechanical properties of compression molded PEBF and PET dogbone specimens

	Melt Pressed PEBF (0.25 mm)	Melt Pressed PEBF (0.1 mm)[a]	Lab synthesized PET (0.55 mm)
Yield Stress (MPa)	158 ± 6	–	55.7 ± 2.7
Tensile at Break (MPa)	102 ± 4	12 ± 1	52.7 ± 0.4
Break Strain (%)	20 ± 10	0.50 ± 0.05	316 ± 4
Young's Modulus (MPa)	3200 ± 100	2453 ± 140	1576 ± 41

[a] Comparative data from Reference 7.

5.5.5. Permeability

The oxygen permeability of amorphous PEBF films synthesized from HBEBF is presented in Table 5.5 and compared to other polyesters. PEBF exhibits a very low permeability relative to commercial polyesters known for having good permeability such a poly(ethylene 2,6-

naphthalenedicarboxylate) (PEN) and PET. The oxygen permeability observed in these experiments is over 2× lower than the previous report for PEBF and is even lower than amorphous PEN. PEF however exhibits a lower oxygen permeability. Monomers such as isophthalic acid are known to impart a kink to the polymer backbone have been shown to be effective in decreasing the permeability of polyester materials[12] which is believed to be the result of reduced mobility in the polymer backbone. The low oxygen permeability of PEF was also shown to be a result of low chain segment mobility from hindered furan ring flipping which is signified by the low value of the diffusion coefficient as shown in Table 5.5.[5] Likewise, PEBF exhibits a low diffusion coefficient relative to PET and thus reduced oxygen permeability due to reduced segment mobility of the polymer chain. Consistent with the PEF studies, the nonlinear structure of the bifuran units inhibits molecular motions and reduces the permeability of the PEBF.[5]

Table 5.14. Oxygen permeability comparisons at 23 °C

Polyester	Oxygen Permeability (cc[STP]·cm/m^2·day·atm	Diffusivity (10^{-10} cm^2/s)	Solubility (cm^3[STP]/ cm^{3}atm)
PEBF	0.110	8.4	0.154
PEBF[a]	0.269	ND[b]	ND[b]
PEF[c]	0.070	6.5	0.118
PET[d]	0.462	53	0.101
PEN[e]	0.167	15.1	0.127

[a] Data from Reference 7. [b] No data reported in Reference 7. [c] PEF data at 23 °C estimated at 35 °C extrapolated to 23 °C from PET temperature data. [d] Amorphous PET compression model at 280 °C and quenched in an ice bath. [e] Data from Reference 13.

5.5.6. Biaxial Orientation Studies

Preliminary studies on compression molded films of PEBF prepared from HBEFB show that this polyester is a promising candidate for biaxial orientation. Successful uniaxial orientation was achieved at 100 °C with a 4 × 1 stretch in an Instron. (Fig. D.6). WAXS confirmed orientation was achieved during this experiment (Fig. D.7). Future research should include a complete biaxial orientation study on this polyester and the effect of biaxial orientation on the barrier properties of the polyester.

5.6. Conclusions

We describe in this report high molecular weight PEBF prepared by standard melt phase and melt phase solid state polycondensation procedures. We discovered properties significantly different than those in an early report on this polyester. In our study tensile mechanical properties were significantly enhanced as exemplified by elongations to break of ca. 20+% (40x the previous report). The PEBF from our study exhibited classical crystallization exotherms (in both DSC heating and cooling) in contrast to the previous publication where the crystallization on heating and cooling was not observed. Samples were able to be uniaxially oriented. Oxygen barrier properties were also enhanced (ca. 2× previous report). Cyclic voltammetry revealed that BFE is relatively easily oxidized compared to FE and DMT. A thermal oxidative stability study of PEBF showed that the polymer is oxidatively unstable, however the use of an antioxidant, Irganox® 1010, led to significant reduction in visible oxidative degradation. The use of the hydroxyethoxy substituted monomer, HBEF, with the addition of Irganox® 1010 addition to the

monomer charge led to low color polyester that appeared to have much better stability during melt processing. The combination of the biosourced monomer, high T_g and crystallization behavior, along with enhanced oxygen barrier suggest this polyester could be a potential higher performance polyester resin for food packaging and other applications. These initial polymer properties should encourage further studies on this system. The thermal oxidative stability of the monomer and polymer will be a major issue that will need to be addressed.

5.7. References

(1) Gandini, A.; Silvestre, A. J. D.; Neto, C. P.; Sousa, A. F.; Gomes, M. The Furan Counterpart of Poly(Ethylene Terephthalate): An Alternative Material Based on Renewable Resources. *J. Polym. Sci. Part A Polym. Chem.* **2009**, *47* (1), 295–298. https://doi.org/10.1002/pola.23130.

(2) De Jong, E.; Dam, M. A.; Sipos, L.; Gruter, G. J. M. Furandicarboxylic Acid (FDCA), A Versatile Building Block for a Very Interesting Class of Polyesters. In *ACS Symposium Series*; American Chemical Society, 2012; Vol. 1105, pp 1–13. https://doi.org/10.1021/bk-2012-1105.ch001.

(3) Knoop, R. J. I.; Vogelzang, W.; van Haveren, J.; van Es, D. S. High Molecular Weight Poly(Ethylene-2,5-Furanoate); Critical Aspects in Synthesis and Mechanical Property Determination. *J. Polym. Sci. Part A Polym. Chem.* **2013**, *51* (19), 4191–4199. https://doi.org/10.1002/pola.26833.

(4) Burgess, S. K.; Karvan, O.; Johnson, J. R.; Kriegel, R. M.; Koros, W. J. Oxygen Sorption and Transport in Amorphous Poly(Ethylene Furanoate). *Polymer (Guildf).* **2014**, *55* (18), 4748–4756. https://doi.org/10.1016/j.polymer.2014.07.041.

(5) Burgess, S. K.; Leisen, J. E.; Kraftschik, B. E.; Mubarak, C. R.; Kriegel, R. M.; Koros, W.

J. Chain Mobility, Thermal, and Mechanical Properties of Poly(Ethylene Furanoate) Compared to Poly(Ethylene Terephthalate). *Macromolecules* **2014**, *47* (4), 1383–1391. https://doi.org/10.1021/ma5000199.

(6) YXY® Technology https://www.avantium.com/technologies/yxy/.

(7) Kainulainen, T. P.; Sirviö, J. A.; Sethi, J.; Hukka, T. I.; Heiskanen, J. P. UV-Blocking Synthetic Biopolymer from Biomass-Based Bifuran Diester and Ethylene Glycol. *Macromolecules* **2018**, *51* (5), 1822–1829. https://doi.org/10.1021/acs.macromol.7b02457.

(8) Kandel, K.; Cohn, Stephen, T.; Salciccioli, M.; Atienza, Crisita, C. H.; Galuska, Alan, A. Functionalized Bifuran and Synthesis Thereof. WO/2019/182693, September 26, 2019.

(9) Mourey, T. H.; Bryan, T. G.; Greener, J. Size-Exclusion Chromatography of Poly(Ethylene Terephthalate) and Related Polymers in Methylene Chloride-Dichloroacetic Acid. *J. Chromatogr. A* **1993**, *657* (2), 377–385. https://doi.org/10.1016/0021-9673(93)80293-H.

(10) Ma, H.; Hibbs, M.; Collard, D. M.; Kumar, S.; Schiraldi, D. A. Fiber Spinning, Structure, and Properties of Poly(Ethylene Terephthalate-Co-4,4′-Bibenzoate) Copolyesters. *Macromolecules* **2002**, *35* (13), 5123–5130. https://doi.org/10.1021/ma012245h.

(11) Sharma, S.; Bendikov, M. α-Oligofurans: A Computational Study. *Chem. - A Eur. J.* **2013**, *19* (39), 13127–13139. https://doi.org/10.1002/chem.201300257.

(12) Polyakova, A.; Stepanov, E. V.; Sekelik, D.; Schiraldi, D. A.; Hiltner, A.; Baer, E. Effect of Crystallization on Oxygen-Barrier Properties of Copolyesters Based on Ethylene Terephthalate. *J. Polym. Sci. Part B Polym. Phys.* **2001**, *39* (16), 1911–1919. https://doi.org/10.1002/polb.1165.

(13) Liu, R. Y. F.; Schiraldi, D. A.; Hiltner, A.; Baer, E. Oxygen-Barrier Properties of Cold-Drawn Polyesters. *J. Polym. Sci. Part B Polym. Phys.* **2002**, *40* (9), 862–877. https://doi.org/10.1002/polb.10149.

Chapter 6: Conclusions and Future Outlook

Chapter 2

Here, we began our examination of $NO_3\cdot$ hydrogen atom abstractions. We reported absolute rate constants for a substrate that was previously under-reported. These reactions were shown to depend on the bond strength of the substrate, the number of available hydrogens suitable for abstraction, and the ionization potential of the substrate. The rate constants for reactions in solution were greater than the gas-phase, as predicted by the Kirkwood equation, symbolic of a polarized transition state. This conclusion is furthered by aforementioned dependence on ionization potential. The rate constants in water were lower than those of acetonitrile (or were reduced by the addition of water) for alcohols and ethers. This effect was not observed for alkanes and suggests that hydrogen bonding to water either a) does not stabilize the polar transition state, or b) is offset by an equal degree of stability provided to the reactant(s).

To further this work, a more in depth look at cyclic substrates should be examined. The high rate constant observed for THF compared to the extremely low rate constant for 1,3,5-trioxane suggest that the resonance stability afforded to the radical intermediates by the lone pair on oxygen can be counteracted. The presence of additional adjacent oxygens may cause a development of positive charge on the α-carbons through differences in electronegativity. These net–dipoles may reduce the polarizability of the transition state, similar to the effect observed by carbonyls in Chapter 3.

Additional work could also be done for this project computationally. As discussed above, the multireference character of the $NO_3\cdot$ and abstractions from CH_4, CH_3OH, and CH_3OCH_3 resulted in meaningless single reference calculations. When conducted, the multireference calculations could assess the level of polarization in the transition state. These calculations could

also evaluate the impact of solvent, whether from changes in polarity or hydrogen bonding, on the polarized transition state.

Chapter 3

In this chapter we expanded our investigations of $NO_3\cdot$ to carboxylic acids. The lack of a kinetic isotope effect for small carboxylic acids suggested that direct hydrogen abstraction was not occurring for these reactions. For larger carboxylic acids, abstraction was shown to occur from the alkyl region following a change in mechanism for the reaction. Together, these results suggest that there is no evidence for a concerted hydrogen abstraction with C-C bond cleavage for these reactions.

Future work would focus on the mechanism of reaction with small carboxylic acids. These reactions could still proceed through a hydrogen abstraction mechanism, so long as it is preceded by a rate limiting step. As pointed out by Anglada, in the case of $HO\cdot$, these reactions could proceed through a complexation prior to abstraction. It is also possible that these reactions undergo an initial, slow addition to the carbonyl that ultimately results in abstraction. Another avenue to be explored would be examining how the polar transition state is influenced by solvent effects and whether these effects diminish as the alkyl region becomes longer and/or more branched and more aliphatic in nature.

The role of the carbonyl can also be studied in the future by examining their effects on reactions of aldehydes, esters and organocarbonates. By extending into these classes of substrates, the effects of the carbonyl on the α-carbon can be systematically examined. This would provide key experimental insight that could be supported by computational studies, and, presumably, could map out the reactive pathways of formic and acetic acid in the absence of computation.

Chapter 4

This chapter addressed the question originally posed by Horn and Clark, whether metal ion complexation can cause radical clocks to run fast. We have shown that the absolute rate constants for the β-scission of alkoxyl radicals are influenced by cations, particularly in the case of Li^+. The stabilization of the transition state has been previously attributed to ion–dipole interactions with the developing carbonyl, which has been supported by MO calculations. Additionally, this effect has been shown to be largely diminished in solution as the cation only weakly complexes to the radical rather than the solvent. Compared to CH_3CN, metal ion complexation is not observed in DMSO, which binds the cations more tightly.

Chapter 5

In this chapter we synthesized PEBF of a high molecular weight and remedied the brittleness that has been previously reported for the polymer by reducing the amount of catalyst required using melt polycondensation. These samples displayed enhanced mechanical properties compared to those made by cast or compression molding. Cyclic voltammetry revealed that BFE is relatively easily oxidized compared to FE and dimethyl terephthalate. While the thermal oxidative stability of PEBF was enhanced with the addition of Irganox® 1010, it will be a major obstacle for widespread application. The combination of mechanical properties (high T_g, crystalline behavior, enhanced oxygen barrier) along with the monomer being biosourced should lead to continued investigations on this polyester for use in food packaging and other applications.

Appendix A

Insight into Hydrogen Abstractions by Nitrate Radical: Structural, Solvent Effects, and Evidence for a Polar Transition State

*Mark Paradzinsky, Diego Troya, and James M. Tanko**

Contents

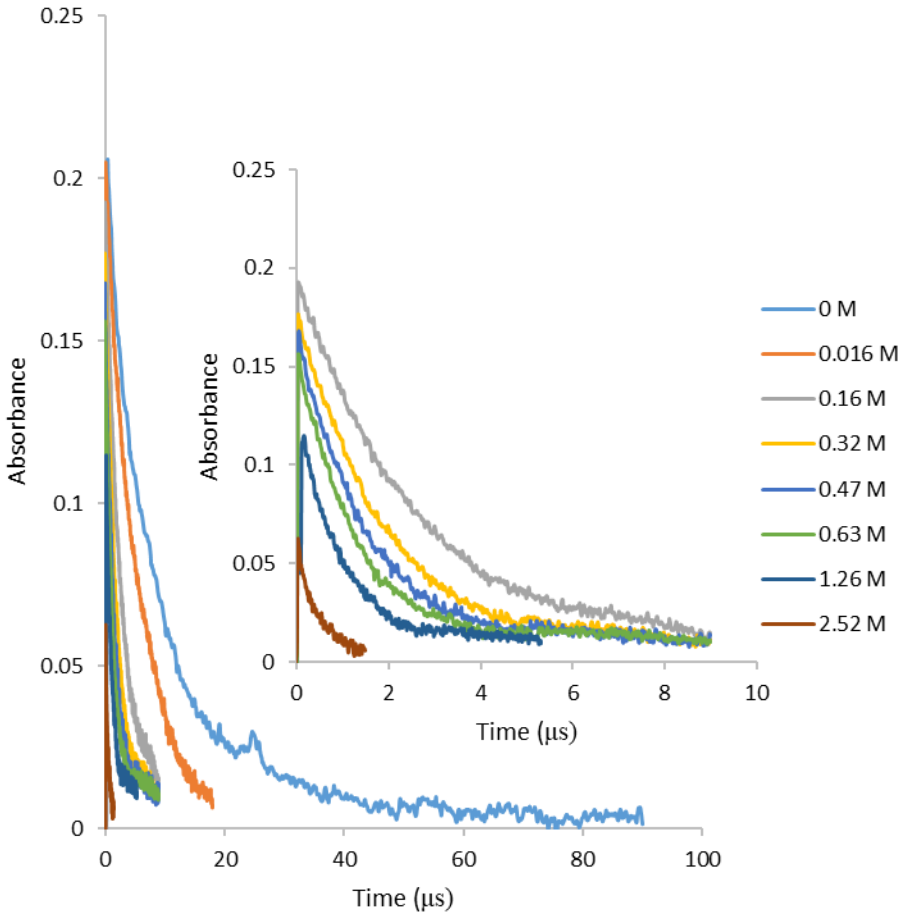

Figure A.1. Transient signal for the decay of $NO_3\cdot$ at 635 nm in the presence of methanol in neat CH_3CN generated by laser flash photolysis of 3×10^{-3} mol L^{-1} CKN. The inset depicts a magnified view of the decay profiles for higher concentrations of substrate.

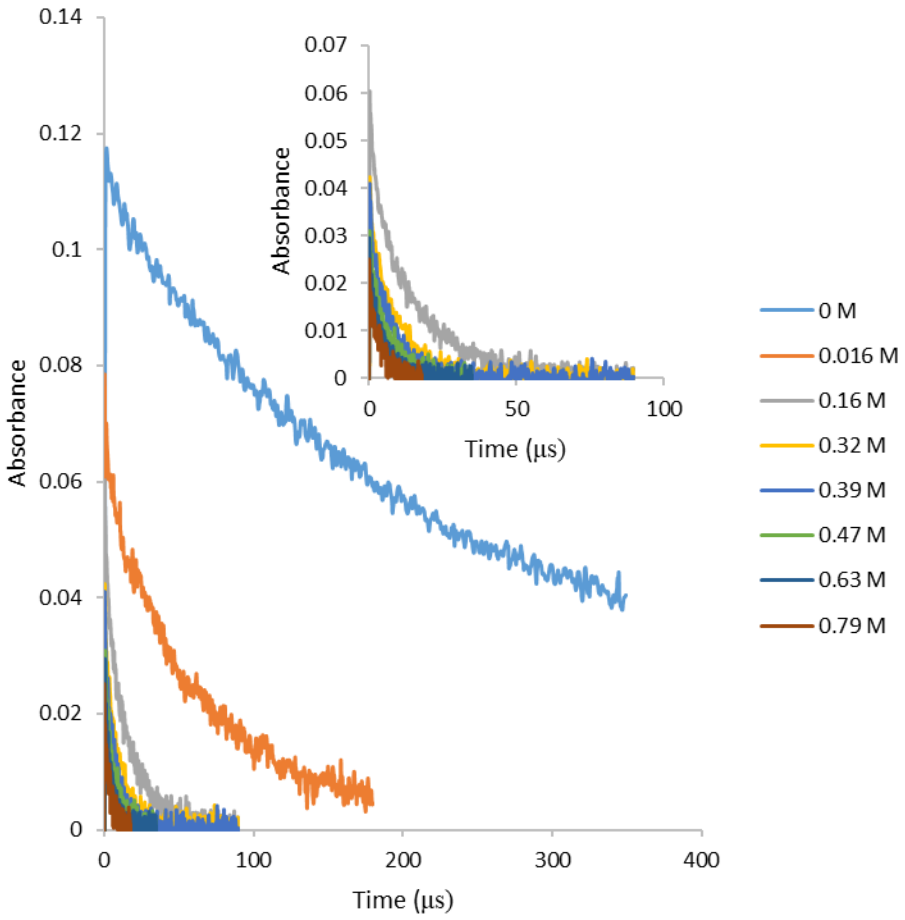

Figure A.2. Transient signal for the decay of $NO_3\cdot$ at 635 nm in the presence of methanol in H_2O generated by laser flash photolysis of 3×10^{-3} mol L^{-1} CKN. The inset depicts a magnified view of the decay profiles for higher concentrations of substrate.

Table A.15. Observed rate constants for hydrogen abstraction by $NO_3\cdot$ from various concentrations of methanol in CH_3CN at 25 °C

[methanol], M (CH_3CN)	$k_{obs} \times 10^{-6}$ s
0	0.11 ± 0.02
0.02	0.18 ± 0.01
0.26	0.41 ± 0.03
0.53	0.58 ± 0.05
0.79	0.70 ± 0.05
1.05	0.85 ± 0.04
2.10	1.49 ± 0.09
3.36	2.27 ± 0.02

Table A.2. Observed rate constants for hydrogen abstraction by $NO_3\cdot$ from various concentrations of methanol in H_2O at 25 °C

[methanol], M (H_2O)	$k_{obs} \times 10^{-5}$ s
0	0.05 ± 0.00
0.02	0.19 ± 0.04
0.16	0.72 ± 0.03
0.32	1.09 ± 0.06
0.39	1.34 ± 0.07
0.47	1.71 ± 0.13
0.63	2.22 ± 0.10
0.79	2.71 ± 0.12

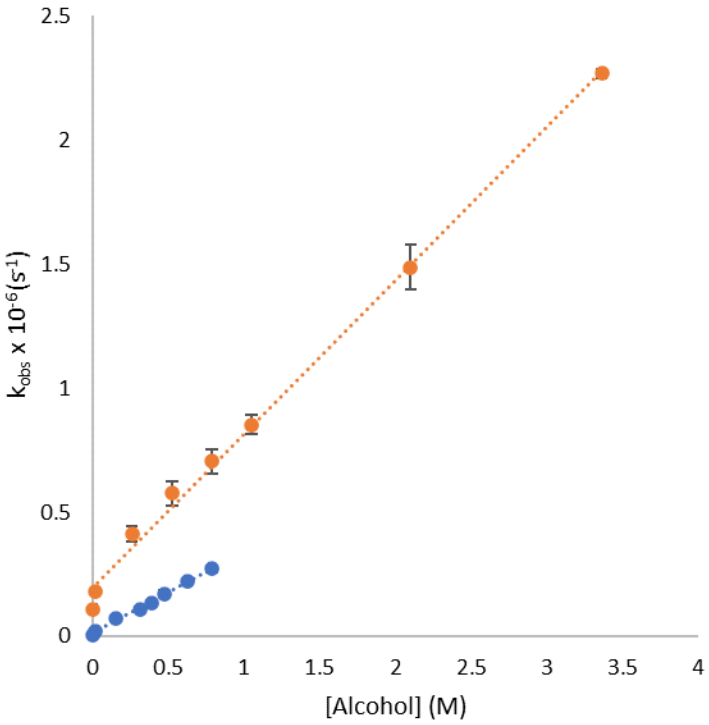

Figure A.3. Plot of the observed rate constant for $NO_3\cdot$ vs. methanol concentration in CH_3CN (●) and H_2O (●) at 25 °C; the slope is equal to the hydrogen abstraction rate constant ($k_{AN} = 0.6 \times 10^6$ $M^{-1}s^{-1}$, $k_W = 0.3 \times 10^6$ $M^{-1}s^{-1}$).

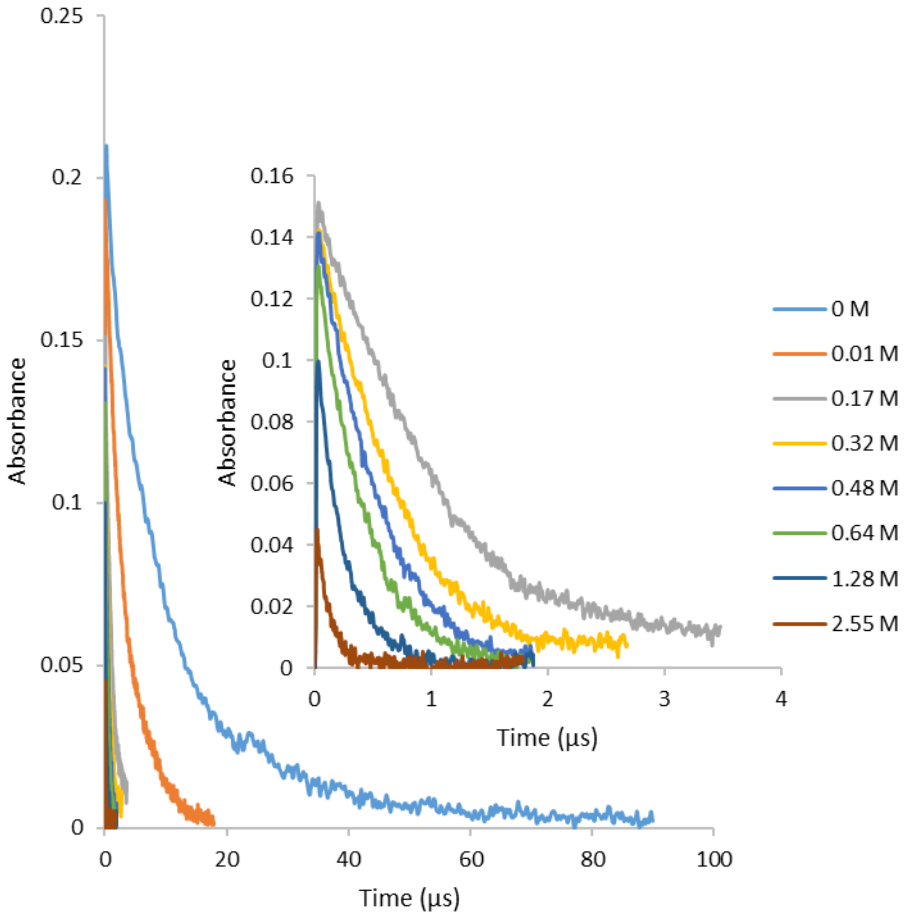

Figure A.4. Transient signal for the decay of $NO_3\cdot$ at 635 nm in the presence of ethanol in neat CH_3CN generated by laser flash photolysis of 3×10^{-3} mol L^{-1} CKN. The inset depicts a magnified view of the decay profiles for higher concentrations of substrate.

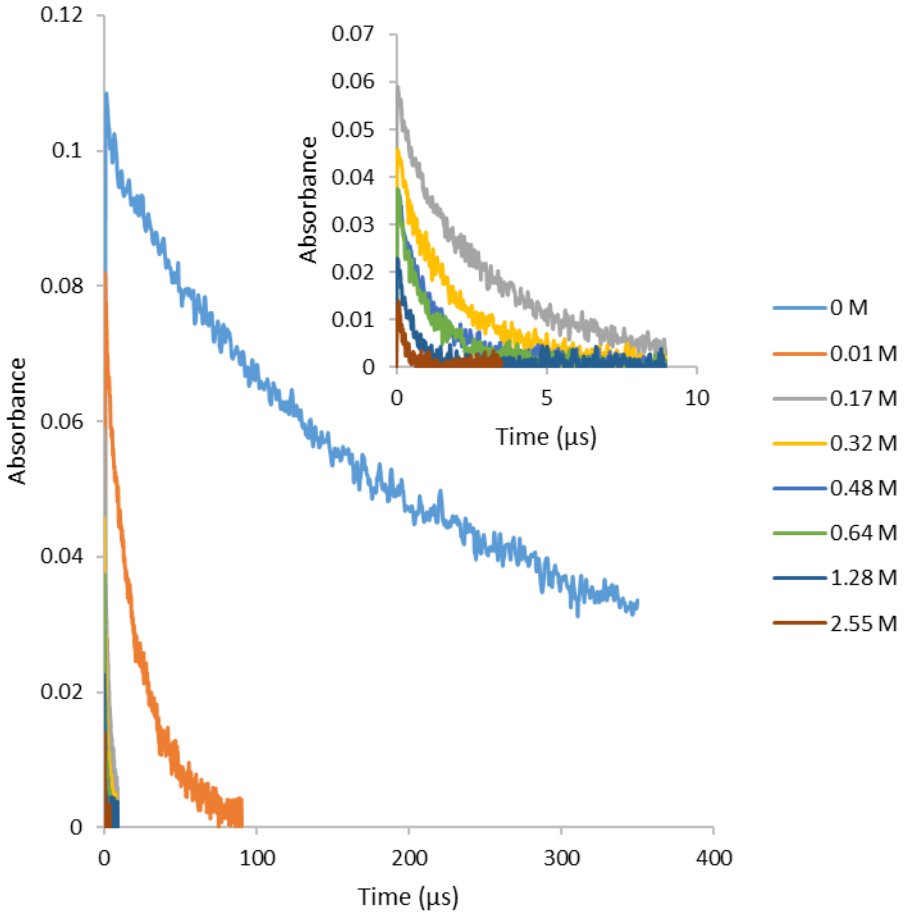

Figure A.5. Transient signal for the decay of $NO_3\cdot$ at 635 nm in the presence of ethanol in H_2O generated by laser flash photolysis of 3×10^{-3} mol L^{-1} CKN. The inset depicts a magnified view of the decay profiles for higher concentrations of substrate.

Table A.3. Observed rate constants for hydrogen abstraction by $NO_3\cdot$ from various concentrations of ethanol in CH_3CN at 25 °C

[ethanol], M (CH_3CN)	$k_{obs} \times 10^{-6}$ s
0	0.09 ± 0.00
0.011	0.31 ± 0.03
0.17	1.01 ± 0.04
0.32	1.64 ± 0.09
0.48	1.91 ± 0.09
0.64	2.31 ± 0.11
1.28	4.05 ± 0.20
2.55	8.55 ± 0.20

Table A.4. Observed rate constants for hydrogen abstraction by $NO_3\cdot$ from various concentrations of ethanol in H_2O at 25 °C

[ethanol], M (H_2O)	$k_{obs} \times 10^{-5}$ s
0	0.05 ± 0.00
0.011	0.48 ± 0.04
0.17	3.77 ± 0.14
0.32	5.85 ± 0.26
0.48	8.68 ± 0.70
0.64	11.0 ± 1.61
1.28	19.6 ± 1.88
2.55	37.0 ± 1.94

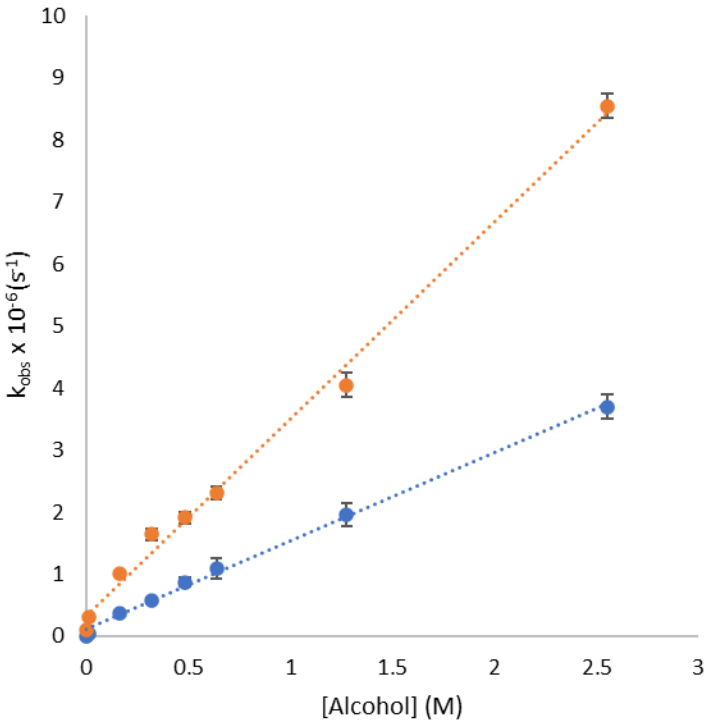

Figure A.6. Plot of the observed rate constant for $NO_3\cdot$ vs. ethanol concentration in CH_3CN (●) and H_2O (●) at 25 °C; the slope is equal to the hydrogen abstraction rate constant ($k_{AN} = 3.2 \times 10^6$ $M^{-1}s^{-1}$, $k_W = 1.4 \times 10^6$ $M^{-1}s^{-1}$).

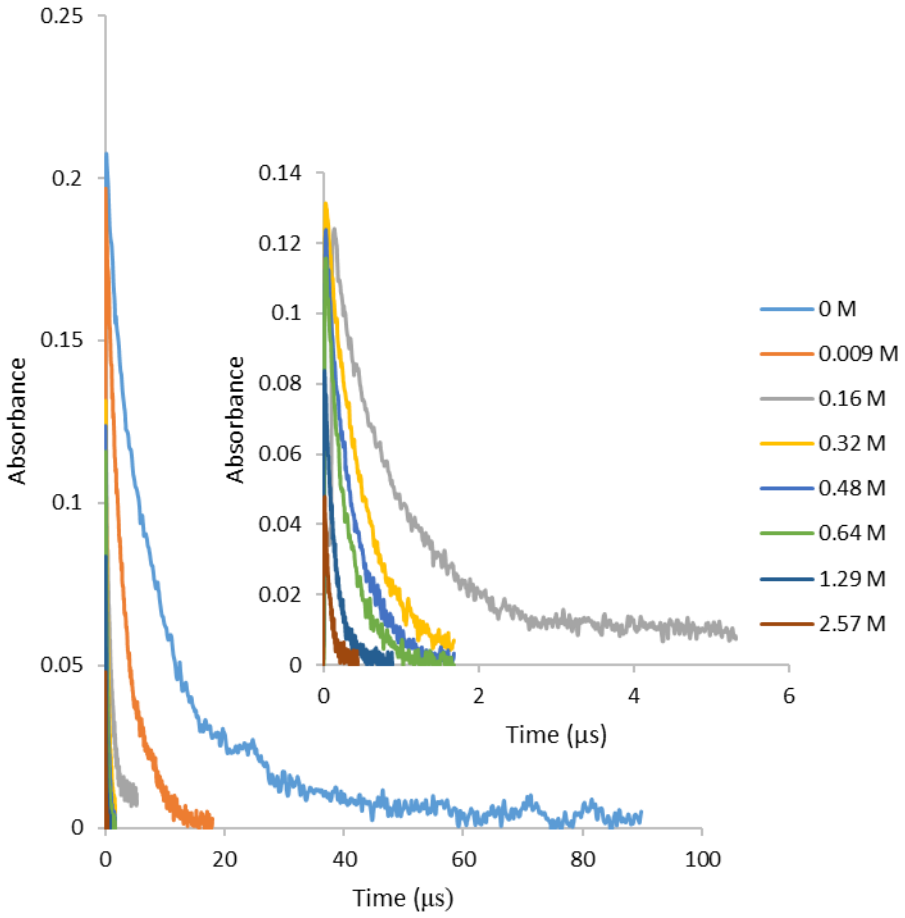

Figure A.7. Transient signal for the decay of $NO_3\cdot$ at 635 nm in the presence of 2-propanol in neat CH_3CN generated by laser flash photolysis of 3×10^{-3} mol L^{-1} CKN. The inset depicts a magnified view of the decay profiles for higher concentrations of substrate.

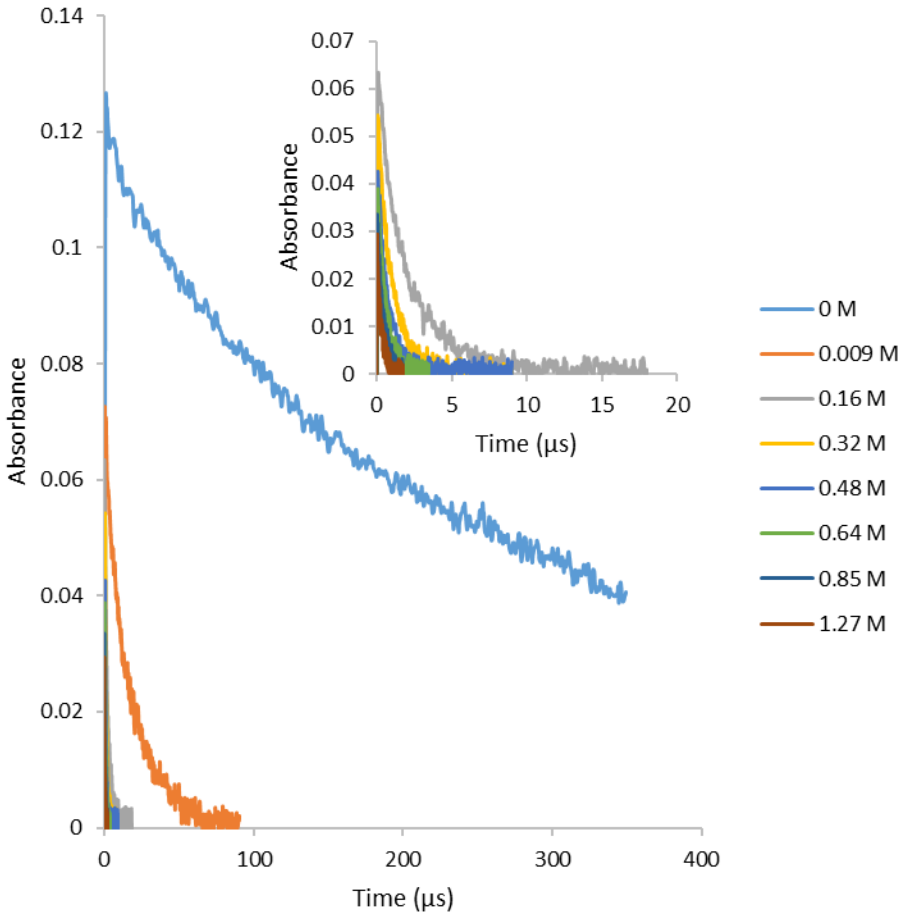

Figure A.8. Transient signal for the decay of $NO_3\cdot$ at 635 nm in the presence of 2-propanol in H_2O generated by laser flash photolysis of 3×10^{-3} mol L^{-1} CKN. The inset depicts a magnified view of the decay profiles for higher concentrations of substrate.

Table A.5. Observed rate constants for hydrogen abstraction by $NO_3\cdot$ from various concentrations of 2-propanol in CH_3CN at 25 °C

[2-propanol], M (CH_3CN)	$k_{obs} \times 10^{-6}$ s
0	0.10 ± 0.01
0.008	0.33 ± 0.02
0.16	1.48 ± 0.12
0.32	2.17 ± 0.11
0.48	2.82 ± 0.20
0.64	3.74 ± 0.20
1.29	7.52 ± 0.66
2.57	14.37 ± 1.31

Table A.6. Observed rate constants for hydrogen abstraction by $NO_3\cdot$ from various concentrations of 2-propanol in H_2O at 25 °C

[2-propanol], M (H_2O)	$k_{obs} \times 10^{-5}$ s
0	0.05 ± 0.00
0.008	0.60 ± 0.04
0.16	5.21 ± 0.18
0.32	10.11 ± 0.95
0.48	14.00 ± 1.42
0.64	18.24 ± 0.42
0.85	24.09 ± 1.15
1.27	31.07 ± 1.21

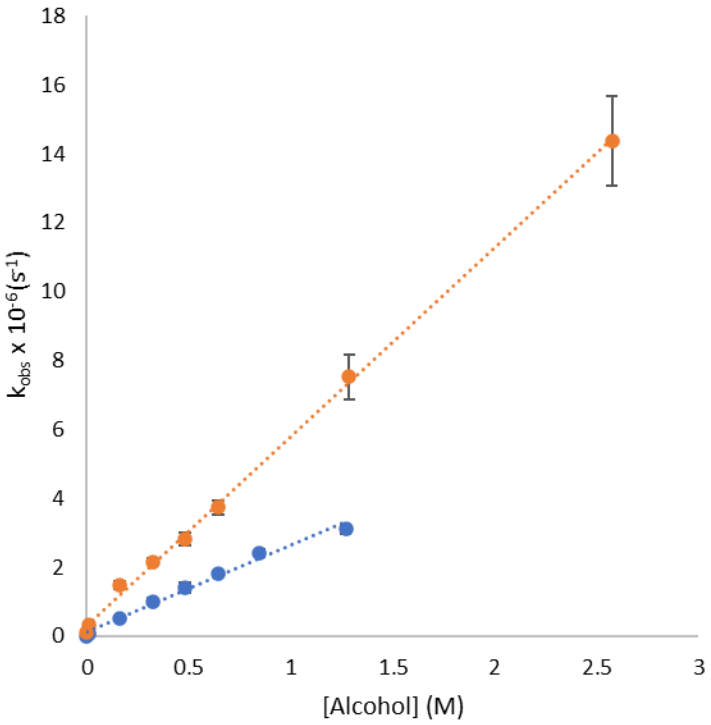

Figure A.9. Plot of the observed rate constant for $NO_3\cdot$ vs. 2-propanol concentration in CH_3CN (●) and H_2O (●) at 25 °C; the slope is equal to the hydrogen abstraction rate constant (k_{AN} = 5.5 × 10^6 $M^{-1}s^{-1}$, k_W = 2.5 × 10^6 $M^{-1}s^{-1}$).

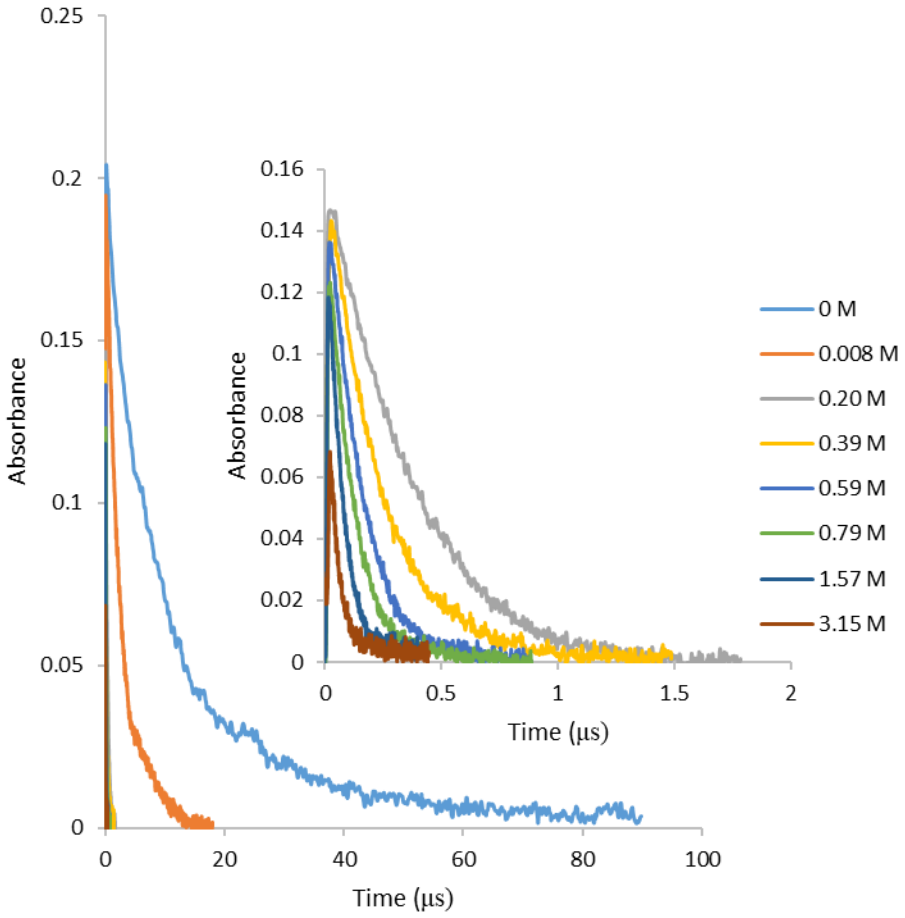

Figure A.10. Transient signal for the decay of $NO_3\cdot$ at 635 nm in the presence of diethyl ether in neat CH_3CN generated by laser flash photolysis of 3×10^{-3} mol L^{-1} CKN. The inset depicts a magnified view of the decay profiles for higher concentrations of substrate.

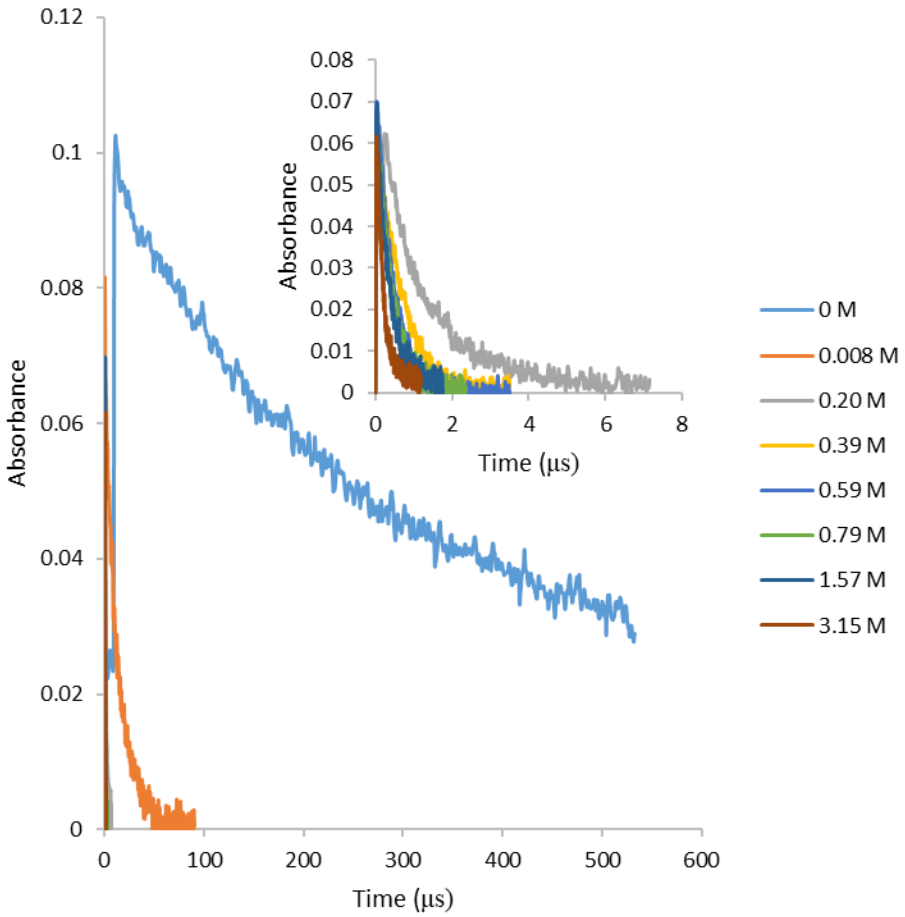

Figure A.11. Transient signal for the decay of $NO_3\cdot$ at 635 nm in the presence of diethyl ether in H_2O generated by laser flash photolysis of 3×10^{-3} mol L^{-1} CKN. The inset depicts a magnified view of the decay profiles for higher concentrations of substrate.

Table A.7. Observed rate constants for hydrogen abstraction by $NO_3\cdot$ from various concentrations of diethyl ether in CH_3CN at 25 °C

[diethyl ether], M (CH_3CN)	$k_{obs} \times 10^{-6}$ s
0	0.10 ± 0.01
0.008	0.41 ± 0.02
0.20	2.69 ± 0.01
0.39	4.80 ± 0.04
0.59	6.87 ± 0.05
0.79	8.95 ± 0.11
1.57	15.31 ± 0.23
3.15	22.74 ± 2.31

Table A.8. Observed rate constants for hydrogen abstraction by $NO_3\cdot$ from various concentrations of diethyl ether in H_2O at 25 °C

[diethyl ether], M (H_2O)	$k_{obs} \times 10^{-5}$ s
0	0.05 ± 0.00
0.008	0.76 ± 0.05
0.20	9.17 ± 0.53
0.39	15.67 ± 1.00
0.59	22.64 ± 0.83
0.79	27.26 ± 1.63
1.57	50.30 ± 0.40
3.15	68.98 ± 0.90

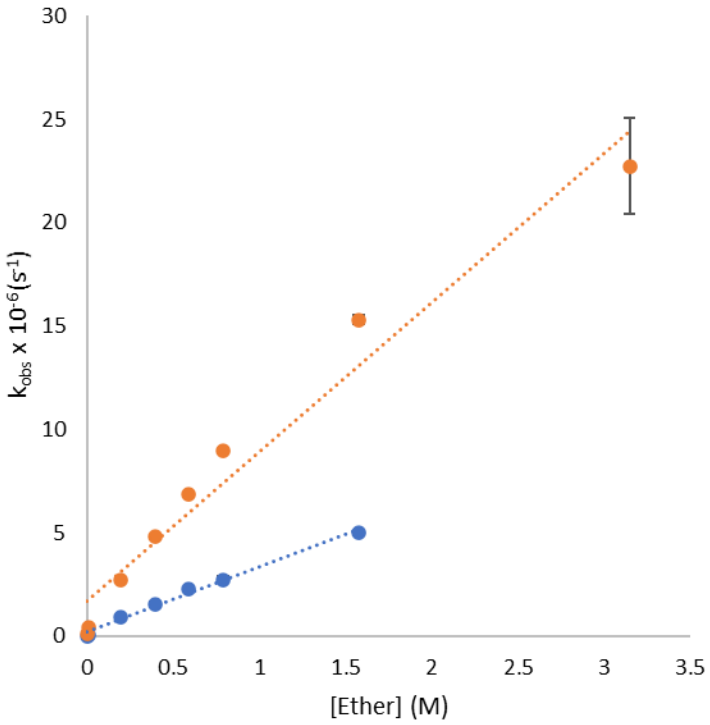

Figure A.12. Plot of the observed rate constant for $NO_3\cdot$ vs. diethyl ether concentration in CH_3CN (●) and H_2O (●) at 25 °C; the slope is equal to the hydrogen abstraction rate constant (k_{AN} = 9.7 × 10^6 $M^{-1}s^{-1}$, k_W = 3.2 × 10^6 $M^{-1}s^{-1}$).

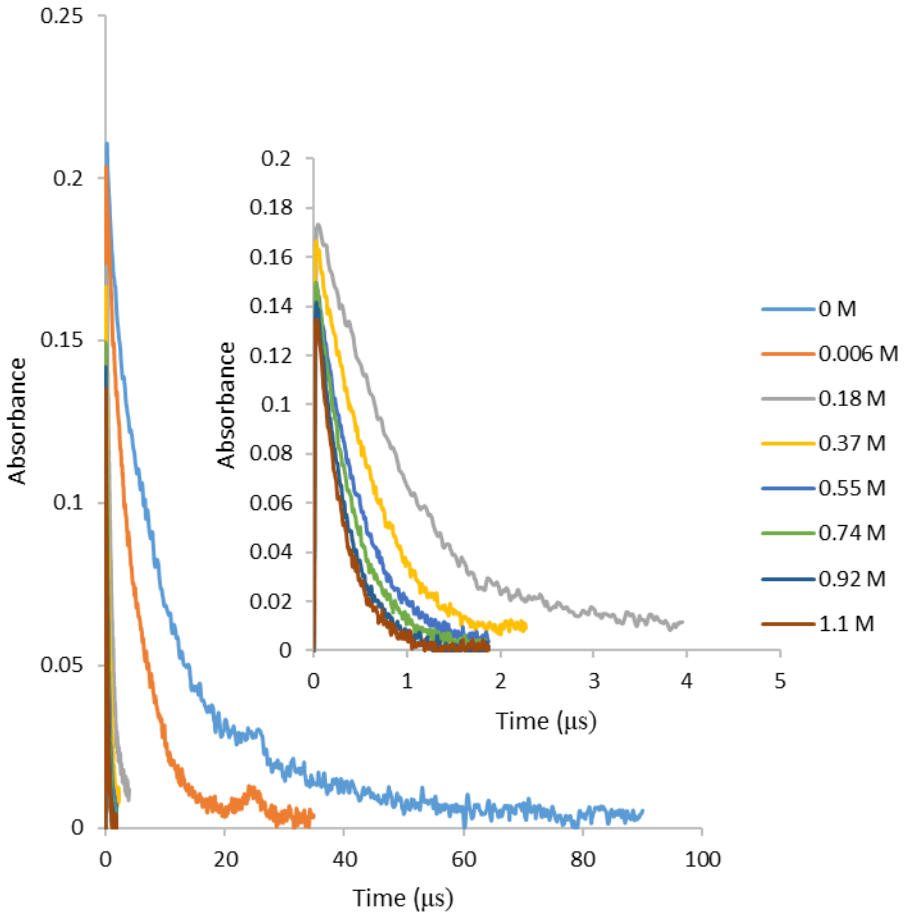

Figure A.13. Transient signal for the decay of $NO_3\cdot$ at 635 nm in the presence of *tert*-butyl methyl ether in neat CH_3CN generated by laser flash photolysis of 3×10^{-3} mol L^{-1} CKN. The inset depicts a magnified view of the decay profiles for higher concentrations of substrate.

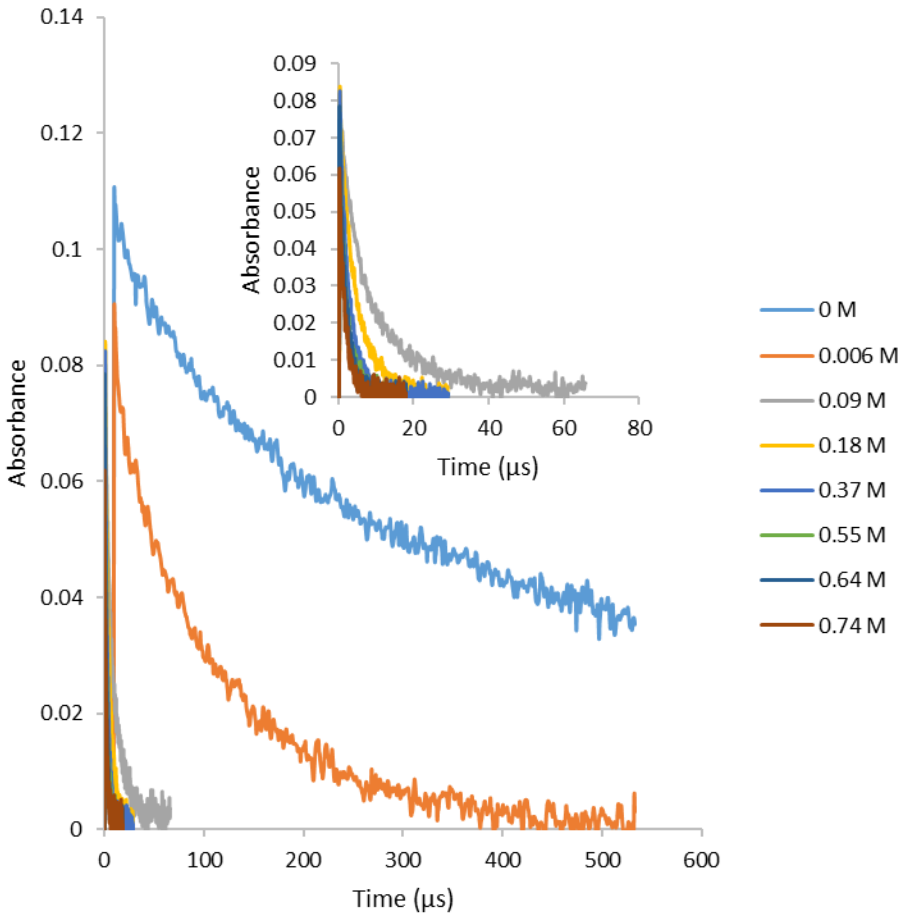

Figure A.14. Transient signal for the decay of $NO_3\cdot$ at 635 nm in the presence of *tert*-butyl methyl ether in H_2O generated by laser flash photolysis of 3×10^{-3} mol L^{-1} CKN. The inset depicts a magnified view of the decay profiles for higher concentrations of substrate.

Table A.9. Observed rate constants for hydrogen abstraction by $NO_3\cdot$ from various concentrations of *tert*-butyl methyl ether in CH_3CN at 25 °C

[*tert*-butyl methyl ether], M (CH_3CN)	$k_{obs} \times 10^{-6}$ s
0	0.09 ± 0.00
0.006	0.19 ± 0.02
0.18	1.12 ± 0.06
0.37	1.57 ± 0.18
0.55	1.89 ± 0.05
0.74	2.32 ± 0.14
0.92	3.05 ± 0.35
1.10	3.54 ± 0.49

Table A.10. Observed rate constants for hydrogen abstraction by $NO_3\cdot$ from various concentrations of *tert*-butyl methyl ether in H_2O at 25 °C

[*tert*-butyl methyl ether], M (H_2O)	$k_{obs} \times 10^{-5}$ s
0	0.06 ± 0.00
0.006	0.15 ± 0.02
0.09	1.08 ± 0.05
0.18	2.13 ± 0.24
0.37	3.39 ± 0.10
0.55	4.87 ± 0.16
0.64	5.72 ± 0.03
0.74	6.25 ± 0.08

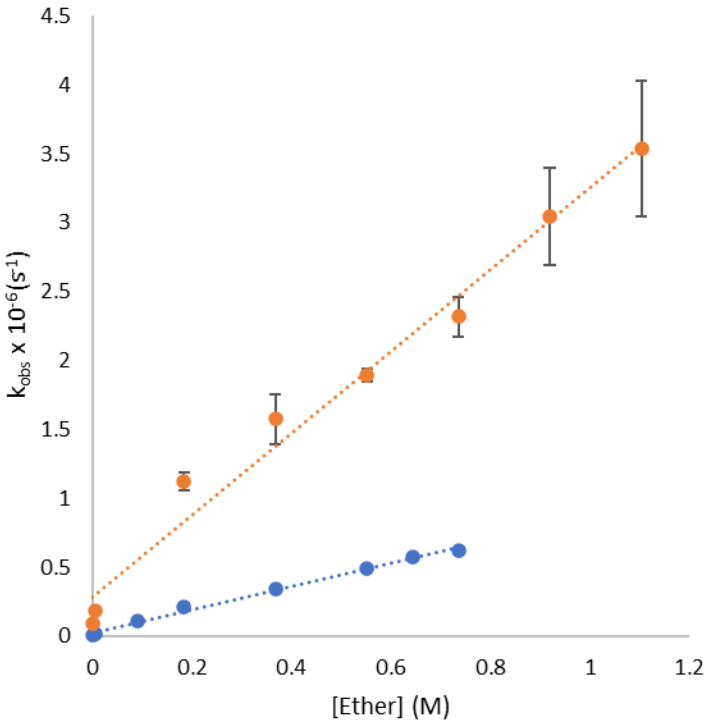

Figure A.15. Plot of the observed rate constant for $NO_3\cdot$ vs. *tert*-butyl methyl ether concentration in CH_3CN (●) and H_2O (●) at 25 °C; the slope is equal to the hydrogen abstraction rate constant ($k_{AN} = 3.0 \times 10^6\ M^{-1}s^{-1}$, $k_W = 0.8 \times 10^6\ M^{-1}s^{-1}$).

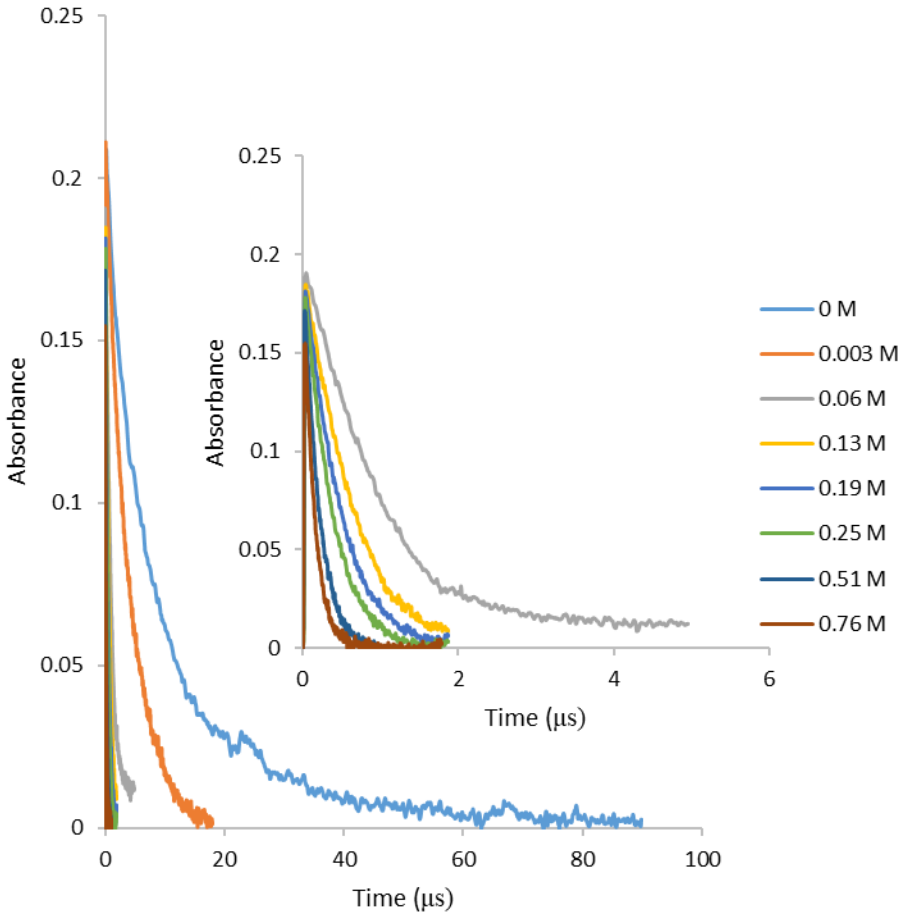

Figure A.16. Transient signal for the decay of $NO_3\cdot$ at 635 nm in the presence of 1,2-dimethoxyethane in neat CH_3CN generated by laser flash photolysis of 3×10^{-3} mol L^{-1} CKN. The inset depicts a magnified view of the decay profiles for higher concentrations of substrate.

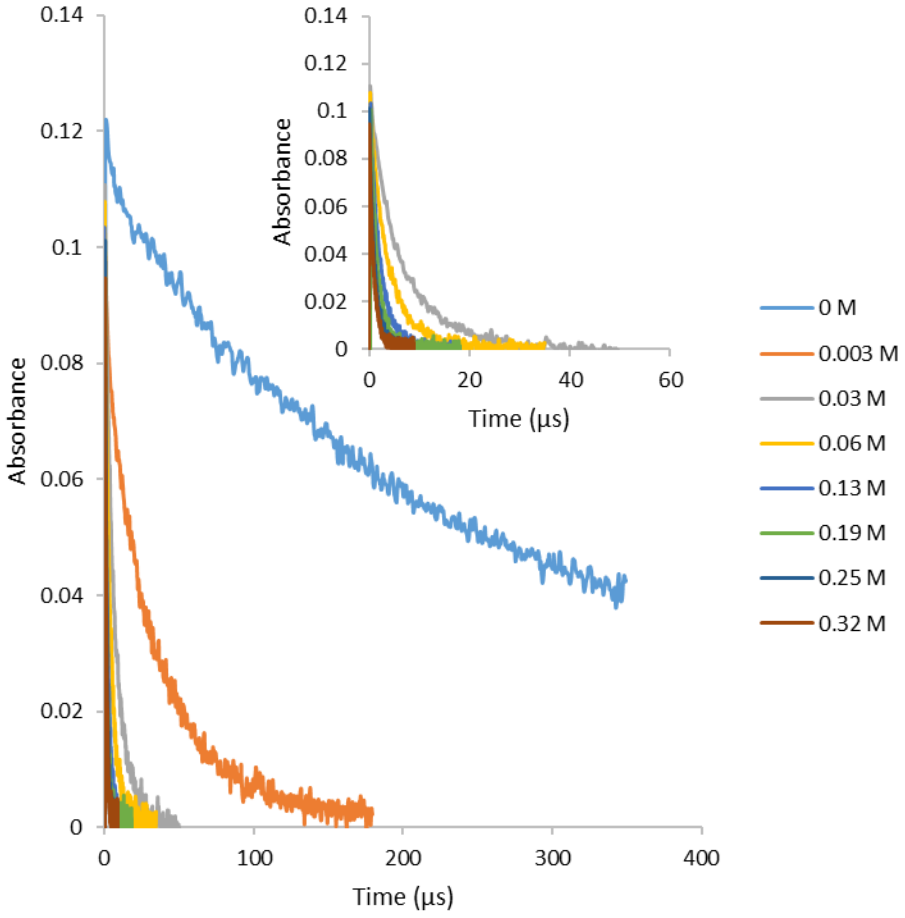

Figure A.17. Transient signal for the decay of $NO_3\cdot$ at 635 nm in the presence of 1,2-dimethoxyethane in H_2O generated by laser flash photolysis of 3×10^{-3} mol L^{-1} CKN. The inset depicts a magnified view of the decay profiles for higher concentrations of substrate.

Table A.11. Observed rate constants for hydrogen abstraction by $NO_3\cdot$ from various concentrations of 1,2-dimethoxyethane in CH_3CN at 25 °C

[1,2-dimethoxyethane], M (CH_3CN)	$k_{obs} \times 10^{-6}$ s
0	0.09 ± 0.00
0.005	0.22 ± 0.00
0.10	1.01 ± 0.01
0.20	1.53 ± 0.02
0.31	1.84 ± 0.02
0.41	2.33 ± 0.02
0.82	4.69 ± 0.04
1.23	6.65 ± 0.03

Table A.12. Observed rate constants for hydrogen abstraction by $NO_3\cdot$ from various concentrations of 1,2-dimethoxyethane in H_2O at 25 °C

[1,2-dimethoxyethane) ether], M (H_2O)	$k_{obs} \times 10^{-5}$ s
0	0.05 ± 0.00
0.005	0.29 ± 0.01
0.03	0.70 ± 0.01
0.05	1.29 ± 0.04
0.08	1.82 ± 0.09
0.10	2.26 ± 0.04
0.15	2.92 ± 0.01
0.20	4.06 ± 0.18

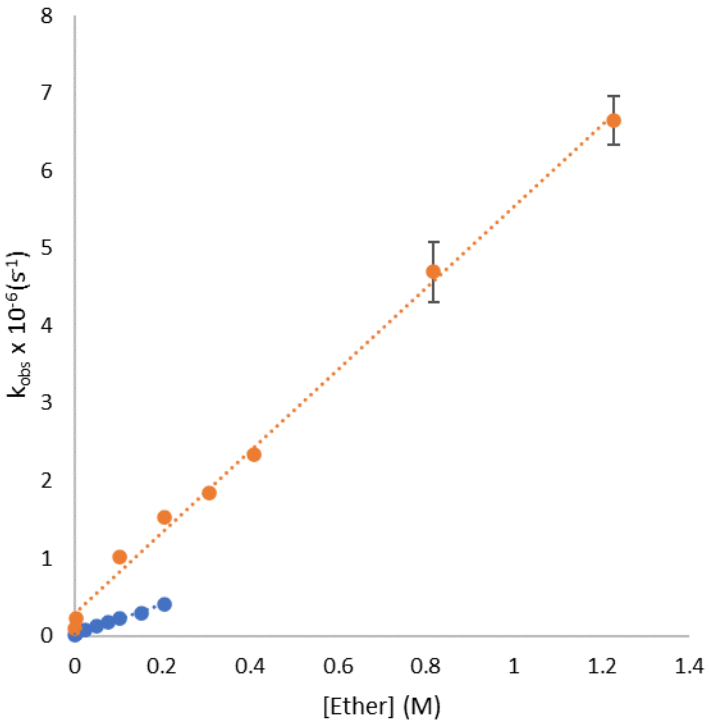

Figure A.18. Plot of the observed rate constant for $NO_3\cdot$ vs. 1,2-dimethoxyethane concentration in CH_3CN (●) and H_2O (●) at 25 °C; the slope is equal to the hydrogen abstraction rate constant ($k_{AN} = 5.3 \times 10^6\ M^{-1}s^{-1}$, $k_W = 1.9 \times 10^6\ M^{-1}s^{-1}$).

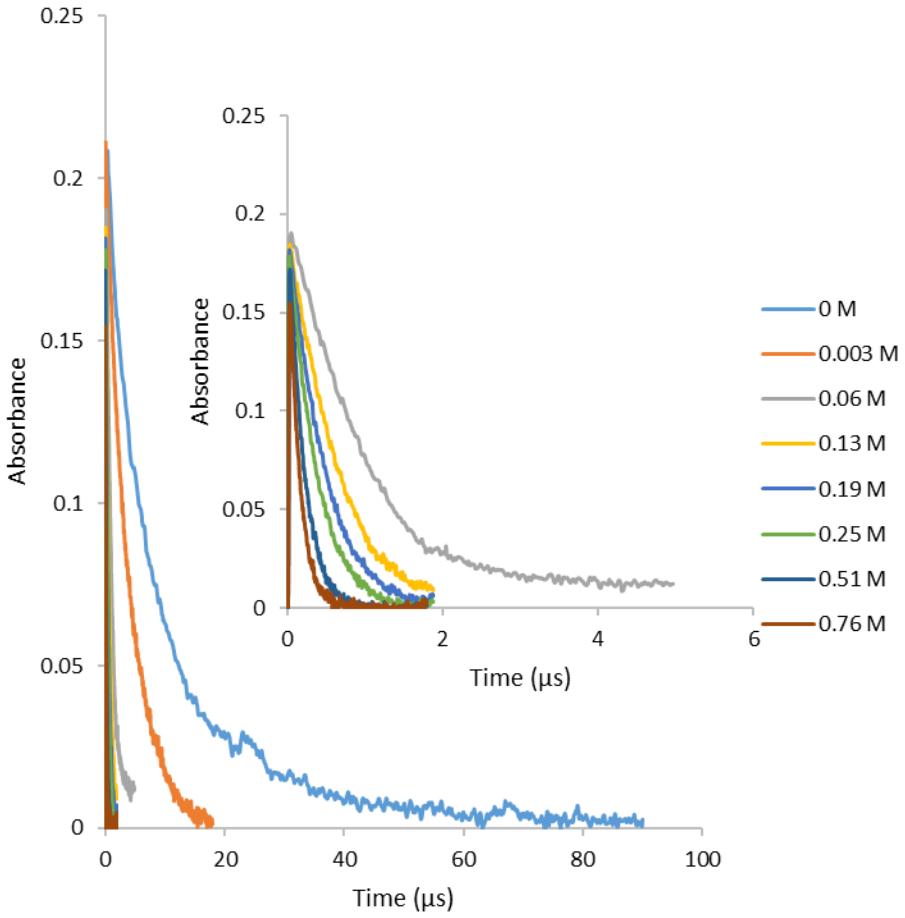

Figure A.19. Transient signal for the decay of $NO_3\cdot$ at 635 nm in the presence of bis(2-methoxyethyl) ether in neat CH_3CN generated by laser flash photolysis of 3×10^{-3} mol L^{-1} CKN. The inset depicts a magnified view of the decay profiles for higher concentrations of substrate.

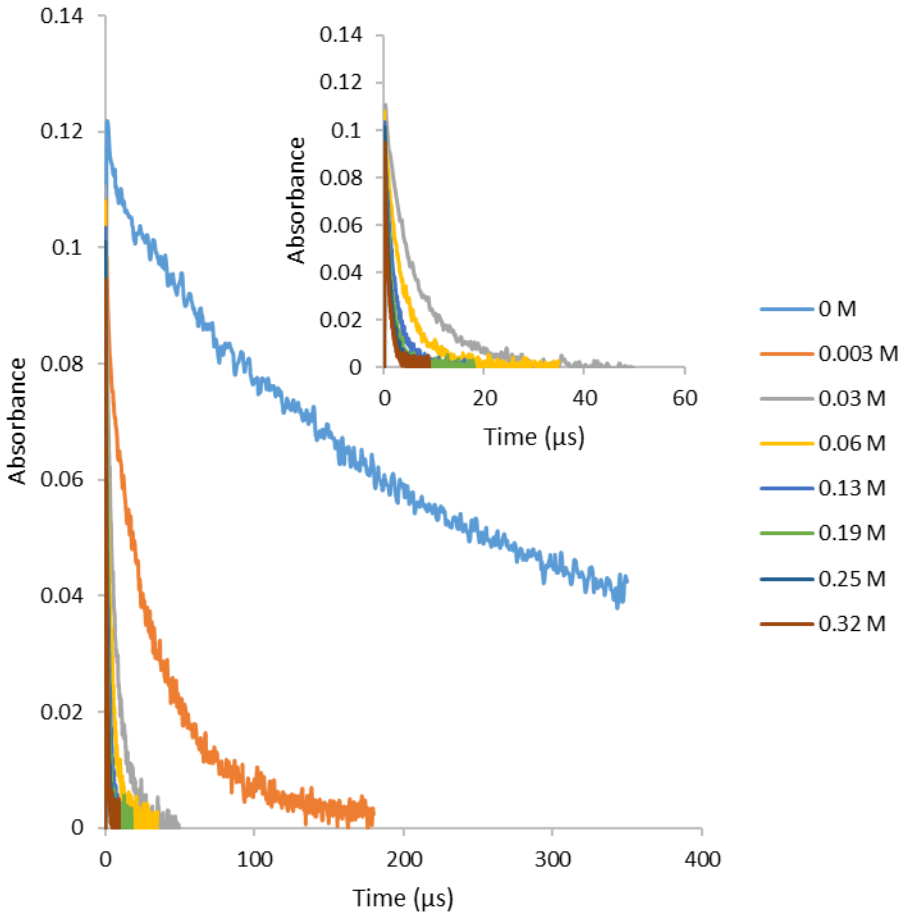

Figure A.20. Transient signal for the decay of $NO_3\cdot$ at 635 nm in the presence of bis(2-methoxyethyl) ether in H_2O generated by laser flash photolysis of 3×10^{-3} mol L^{-1} CKN. The inset depicts a magnified view of the decay profiles for higher concentrations of substrate.

Table A.13. Observed rate constants for hydrogen abstraction by $NO_3\cdot$ from various concentrations of bis(2-methoxyethyl) ether in CH_3CN at 25 °C

[bis(2-methoxyethyl) ether], M (CH_3CN)	$k_{obs} \times 10^{-6}$ s
0	0.11 ± 0.01
0.003	0.25 ± 0.01
0.06	1.17 ± 0.02
0.13	1.70 ± 0.28
0.19	1.90 ± 0.29
0.25	2.72 ± 0.03
0.51	4.96 ± 0.01
0.76	6.98 ± 0.12

Table A.14. Observed rate constants for hydrogen abstraction by $NO_3\cdot$ from various concentrations of bis(2-methoxyethyl) ether in H_2O at 25 °C

[bis(2-methoxyethyl) ether], M (H_2O)	$k_{obs} \times 10^{-5}$ s
0	0.05 ± 0.00
0.003	0.33 ± 0.09
0.03	1.42 ± 0.02
0.06	2.60 ± 0.11
0.13	4.84 ± 0.03
0.19	6.79 ± 0.22
0.25	9.49 ± 0.12
0.32	11.44 ± 0.16

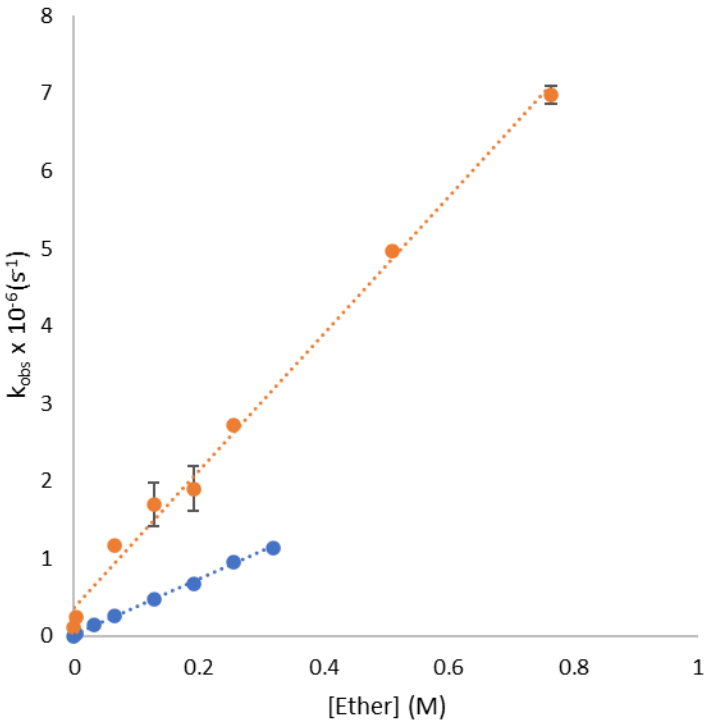

Figure A.21. Plot of the observed rate constant for $NO_3\cdot$ vs. bis(2-methoxyethyl) ether concentration in CH_3CN (●) and H_2O (●) at 25 °C; the slope is equal to the hydrogen abstraction rate constant ($k_{AN} = 8.8 \times 10^6\ M^{-1}s^{-1}$, $k_W = 3.6 \times 10^6\ M^{-1}s^{-1}$).

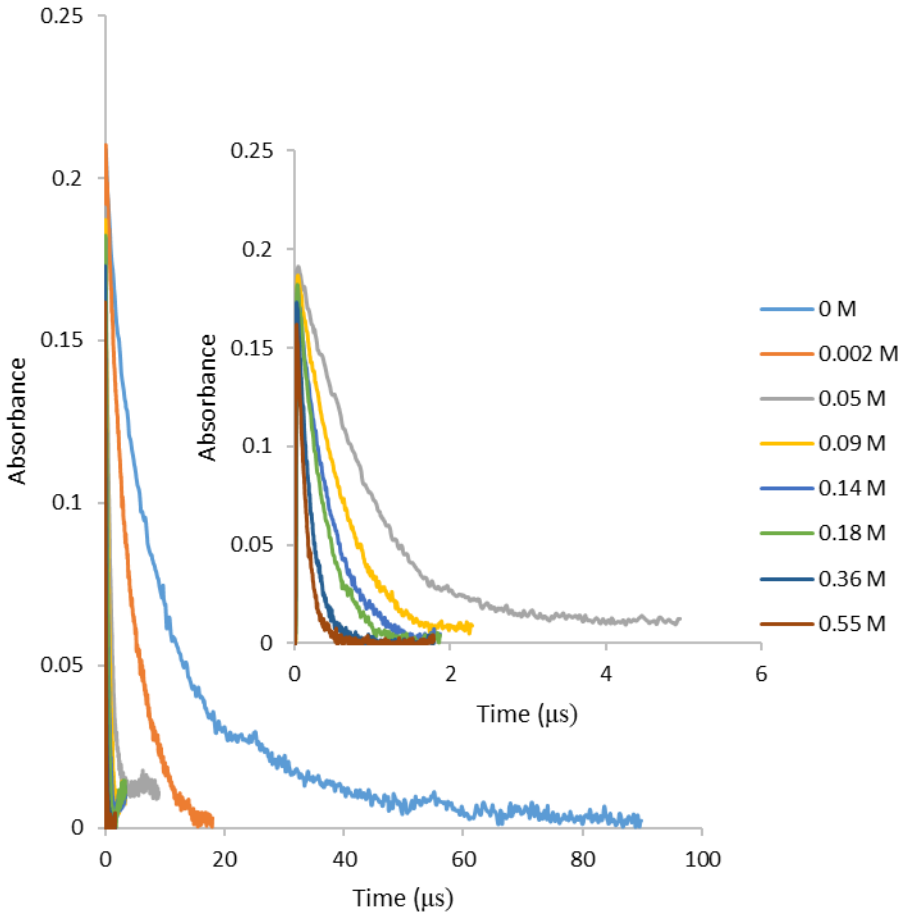

Figure A.22. Transient signal for the decay of $NO_3\cdot$ at 635 nm in the presence of 1,2-bis(2-methoxyethoxy)ethane in neat CH_3CN generated by laser flash photolysis of 3×10^{-3} mol L^{-1} CKN. The inset depicts a magnified view of the decay profiles for higher concentrations of substrate.

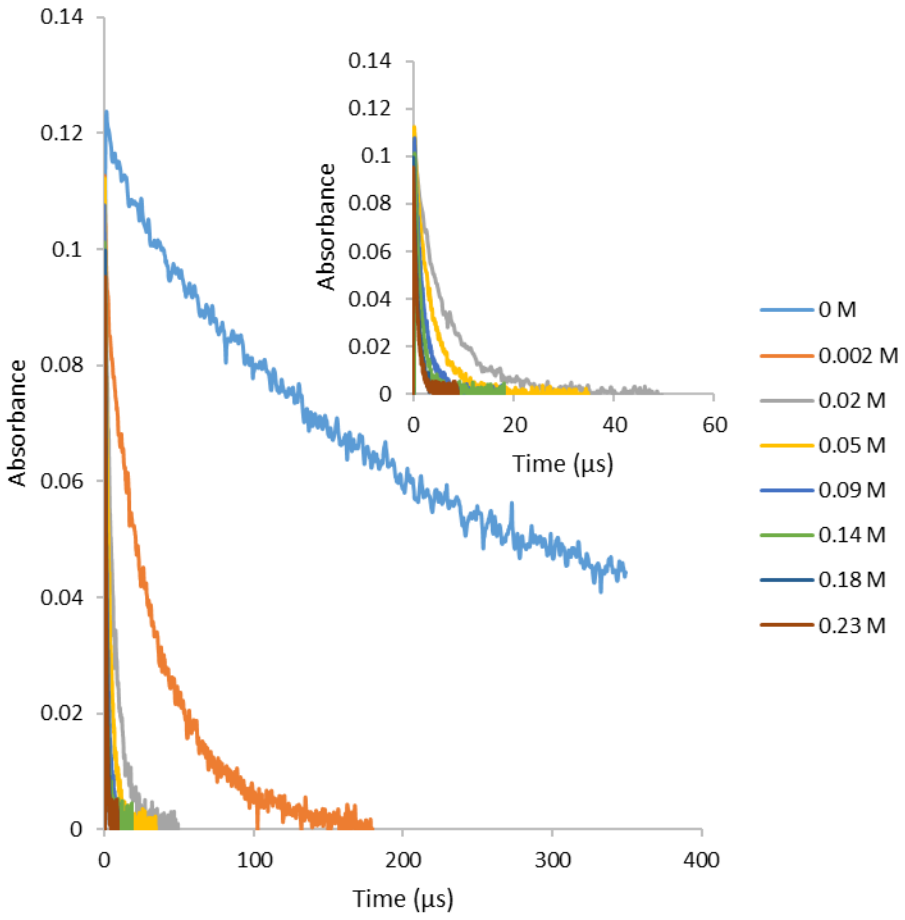

Figure A.23. Transient signal for the decay of $NO_3\cdot$ at 635 nm in the presence of 1,2-bis(2-methoxyethoxy)ethane in H_2O generated by laser flash photolysis of 3×10^{-3} mol L^{-1} CKN. The inset depicts a magnified view of the decay profiles for higher concentrations of substrate.

Table A.15. Observed rate constants for hydrogen abstraction by $NO_3\cdot$ from various concentrations of 1,2-bis(2-methoxyethoxy)ethane in CH_3CN at 25 °C

[1,2-bis(2-methoxyethoxy)ethane], M (CH_3CN)	$k_{obs} \times 10^{-6}$ s
0	0.10 ± 0.00
0.002	0.24 ± 0.01
0.05	1.20 ± 0.03
0.09	1.58 ± 0.02
0.14	2.31 ± 0.01
0.18	2.92 ± 0.02
0.36	5.52 ± 0.05
0.55	7.85 ± 0.08

Table A.16. Observed rate constants for hydrogen abstraction by $NO_3\cdot$ from various concentrations of 1,2-bis(2-methoxyethoxy)ethane in H_2O at 25 °C

[1,2-bis(2-methoxyethoxy)ethane], M (H_2O)	$k_{obs} \times 10^{-5}$ s
0	0.05 ± 0.00
0.002	0.30 ± 0.05
0.02	1.52 ± 0.07
0.05	2.81 ± 0.09
0.09	5.24 ± 0.08
0.14	7.37 ± 0.14
0.18	10.32 ± 0.23
0.23	12.33 ± 0.13

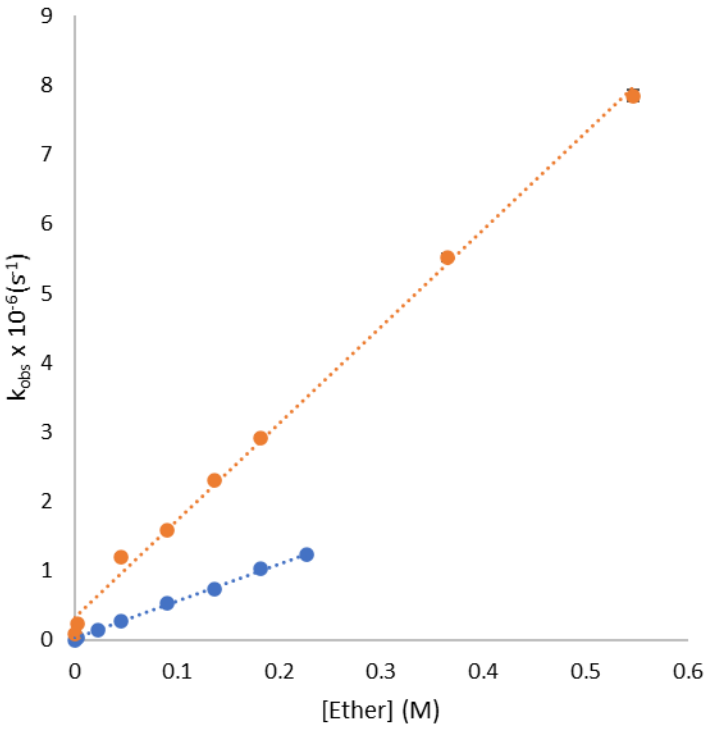

Figure A.24. Plot of the observed rate constant for $NO_3\cdot$ vs. 1,2-bis(2-methoxyethoxy)ethane concentration in CH_3CN (●) and H_2O (●) at 25 °C; the slope is equal to the hydrogen abstraction rate constant ($k_{AN} = 14.0 \times 10^6\ M^{-1}s^{-1}$, $k_W = 5.4 \times 10^6\ M^{-1}s^{-1}$).

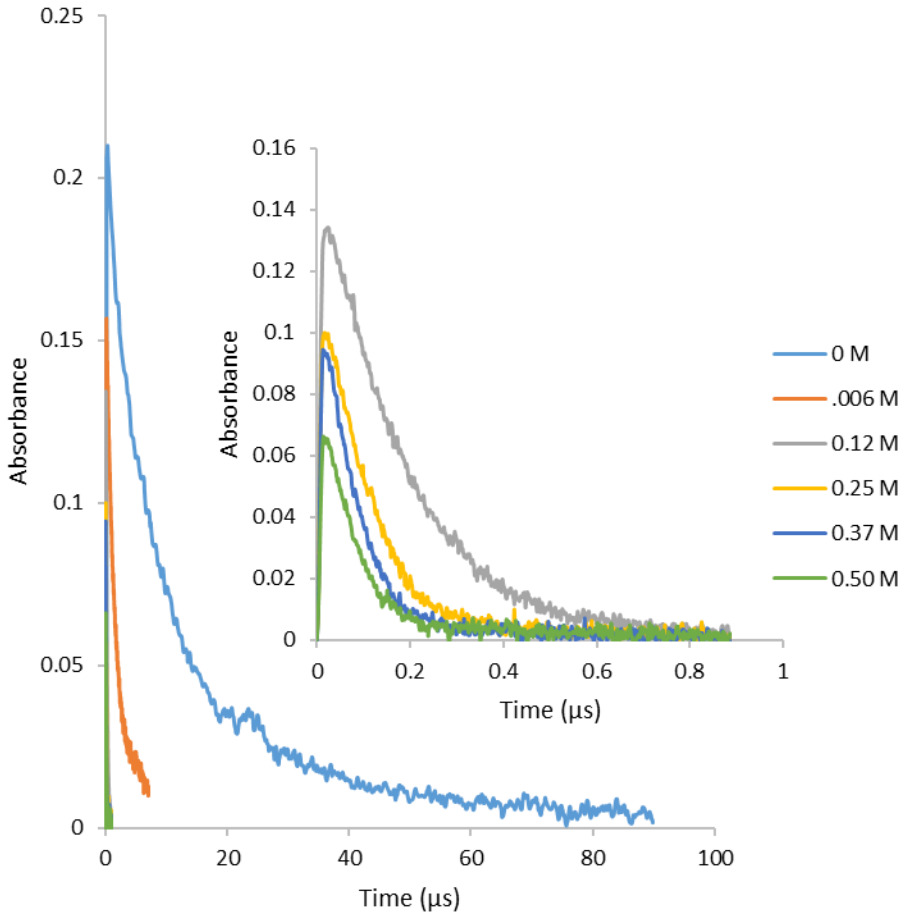

Figure A.25. Transient signal for the decay of $NO_3\cdot$ at 635 nm in the presence of tetrahydrofuran in neat CH_3CN generated by laser flash photolysis of 3×10^{-3} mol L^{-1} CKN. The inset depicts a magnified view of the decay profiles for higher concentrations of substrate.

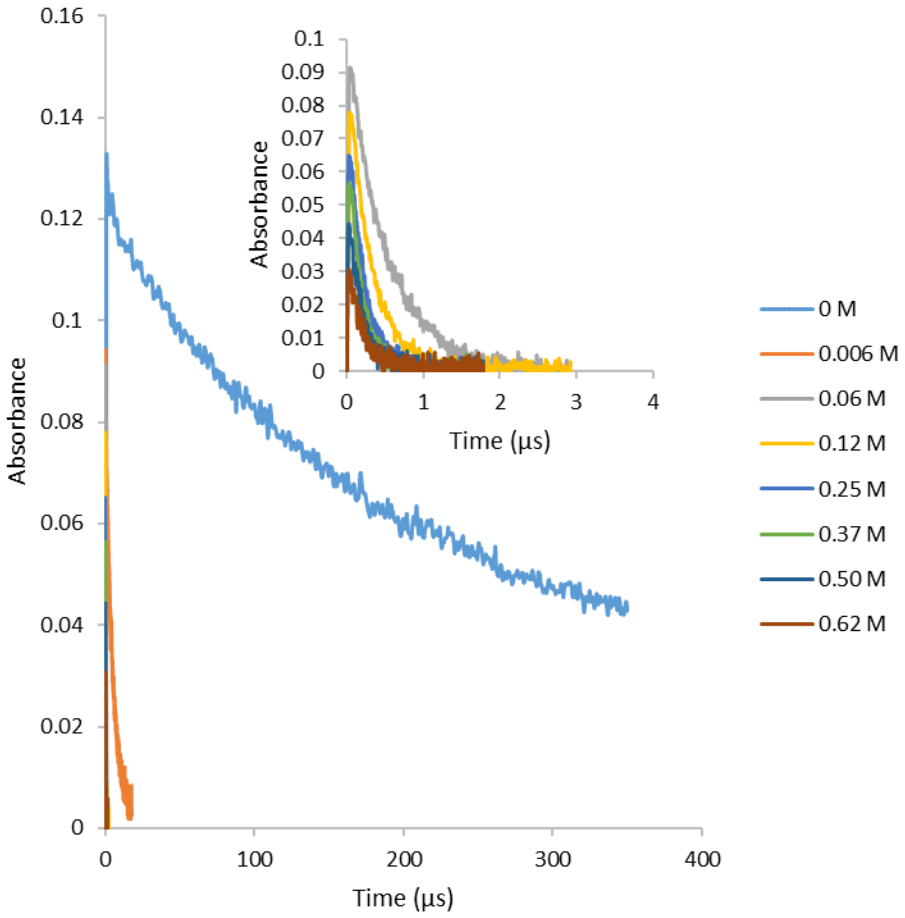

Figure A.26. Transient signal for the decay of $NO_3\cdot$ at 635 nm in the presence of tetrahydrofuran in H_2O generated by laser flash photolysis of 3×10^{-3} mol L^{-1} CKN. The inset depicts a magnified view of the decay profiles for higher concentrations of substrate.

Table A.17. Observed rate constants for hydrogen abstraction by $NO_3\cdot$ from various concentrations of tetrahydrofuran in CH_3CN at 25 °C

[tetrahydrofuran], M (CH_3CN)	$k_{obs} \times 10^{-6}$ s
0	0.09 ± 0.00
0.006	0.77 ± 0.03
0.12	5.52 ± 0.10
0.25	9.64 ± 0.45
0.37	12.84 ± 1.31
0.50	14.40 ± 1.61

Table A.18. Observed rate constants for hydrogen abstraction by $NO_3\cdot$ from various concentrations of tetrahydrofuran in H_2O at 25 °C

[tetrahydrofuran], M (H_2O)	$k_{obs} \times 10^{-5}$ s
0	0.05 ± 0.00
0.006	2.19 ± 0.08
0.062	18.20 ± 0.20
0.12	29.21 ± 3.09
0.24	41.58 ± 2.00
0.37	54.82 ± 6.34
0.50	63.50 ± 10.62

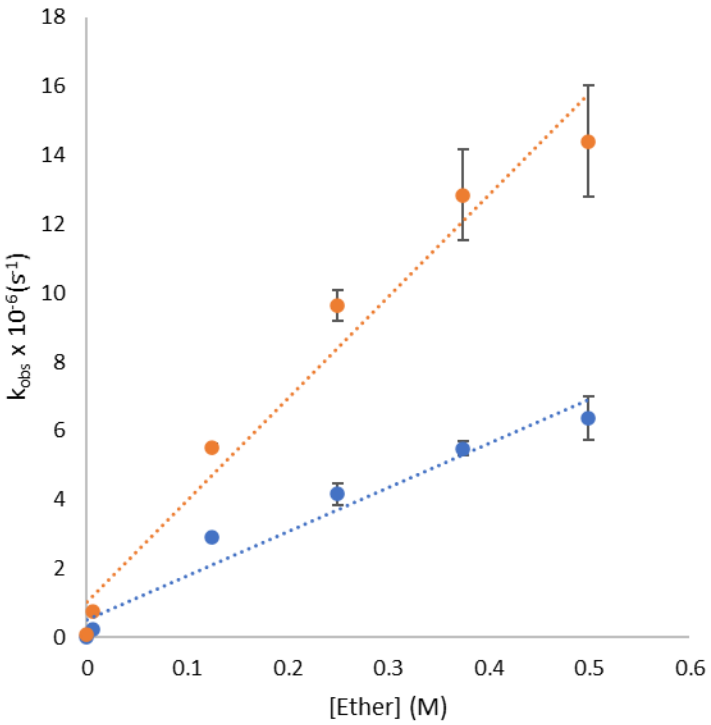

Figure A.27. Plot of the observed rate constant for $NO_3\cdot$ vs. tetrahydrofuran concentration in CH_3CN (●) and H_2O (●) at 25 °C; the slope is equal to the hydrogen abstraction rate constant (k_{AN} = 29.5 × 10^6 $M^{-1}s^{-1}$, k_W = 12.8 × 10^6 $M^{-1}s^{-1}$).

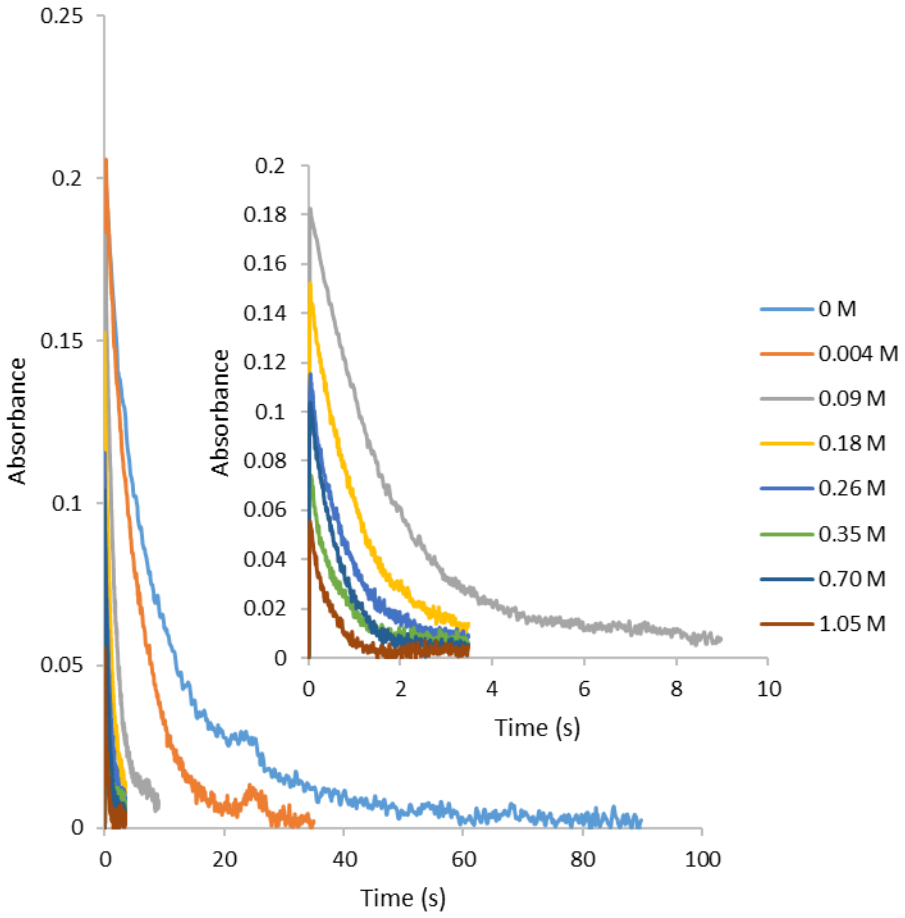

Figure A.28. Transient signal for the decay of $NO_3\cdot$ at 635 nm in the presence of 1,3-dioxane in neat CH_3CN generated by laser flash photolysis of 3×10^{-3} mol L^{-1} CKN. The inset depicts a magnified view of the decay profiles for higher concentrations of substrate.

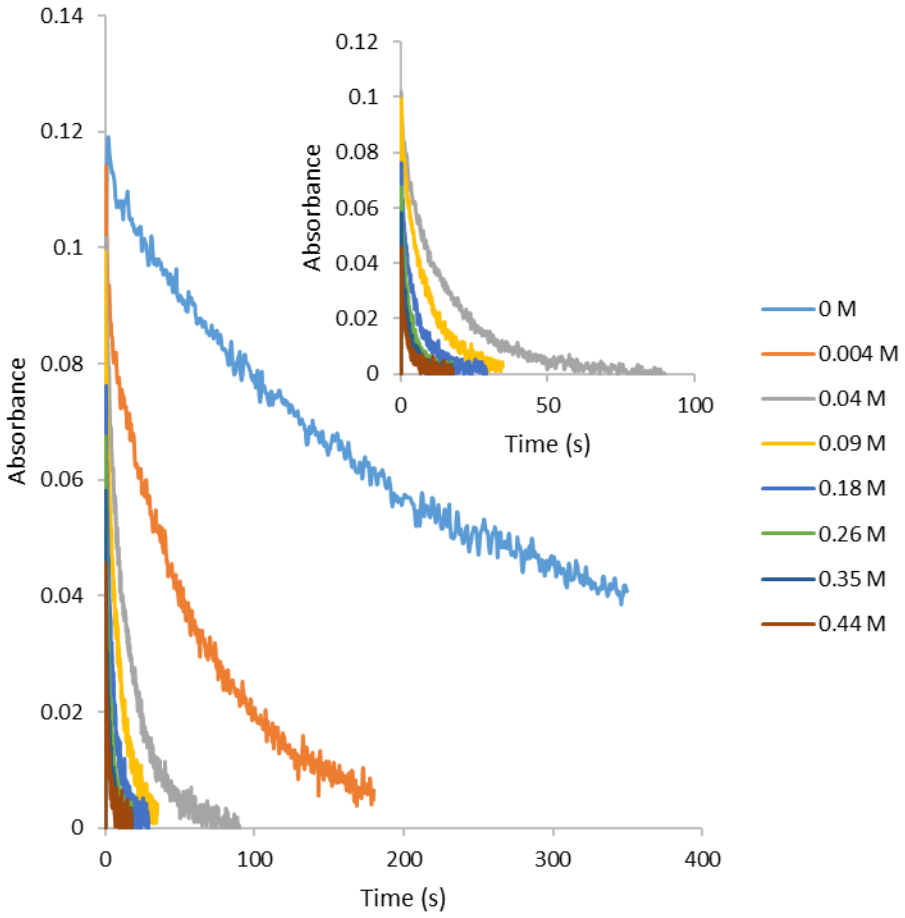

Figure A.29. Transient signal for the decay of $NO_3\cdot$ at 635 nm in the presence of 1,3-dioxane in H_2O generated by laser flash photolysis of 3×10^{-3} mol L^{-1} CKN. The inset depicts a magnified view of the decay profiles for higher concentrations of substrate.

Table A.19. Observed rate constants for hydrogen abstraction by $NO_3\cdot$ from various concentrations of 1,3-dioxane in CH_3CN at 25 °C

[1,3-dioxane], M (CH_3CN)	$k_{obs} \times 10^{-6}$ s
0	0.10 ± 0.00
0.004	0.18 ± 0.01
0.09	0.65 ± 0.02
0.18	0.99 ± 0.06
0.26	1.29 ± 0.00
0.35	1.81 ± 0.05

Table A.20. Observed rate constants for hydrogen abstraction by $NO_3\cdot$ from various concentrations of 1,3-dioxane in H_2O at 25 °C

[1,3-dioxane], M (H_2O)	$k_{obs} \times 10^{-5}$ s
0	0.05 ± 0.00
0.004	0.16 ± 0.00
0.04	0.65 ± 0.01
0.09	1.21 ± 0.02
0.18	2.18 ± 0.18
0.26	3.25 ± 0.05

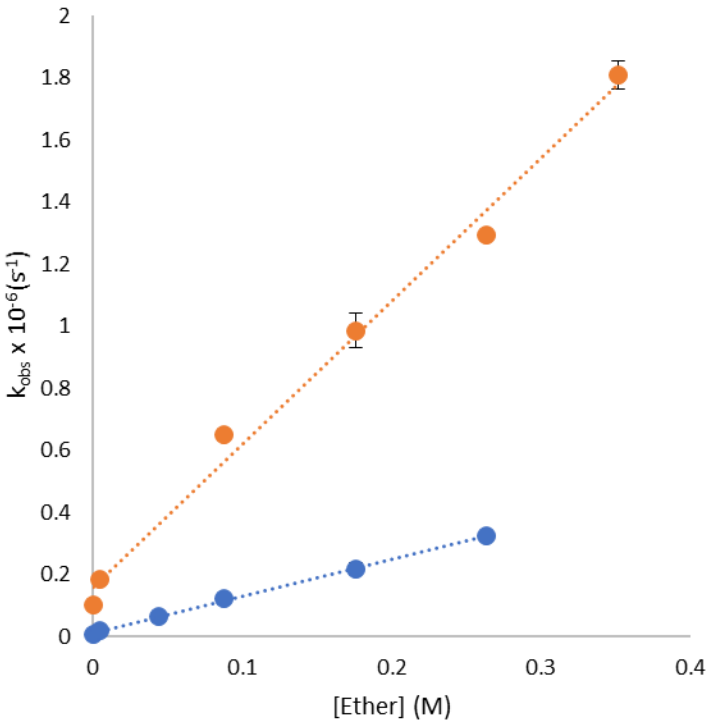

Figure A.30. Plot of the observed rate constant for $NO_3\cdot$ vs. 1,3-dioxane concentration in CH_3CN (●) and H_2O (●) at 25 °C; the slope is equal to the hydrogen abstraction rate constant (k_{AN} = 4.6 × 10^6 $M^{-1}s^{-1}$, k_W = 1.1 × 10^6 $M^{-1}s^{-1}$).

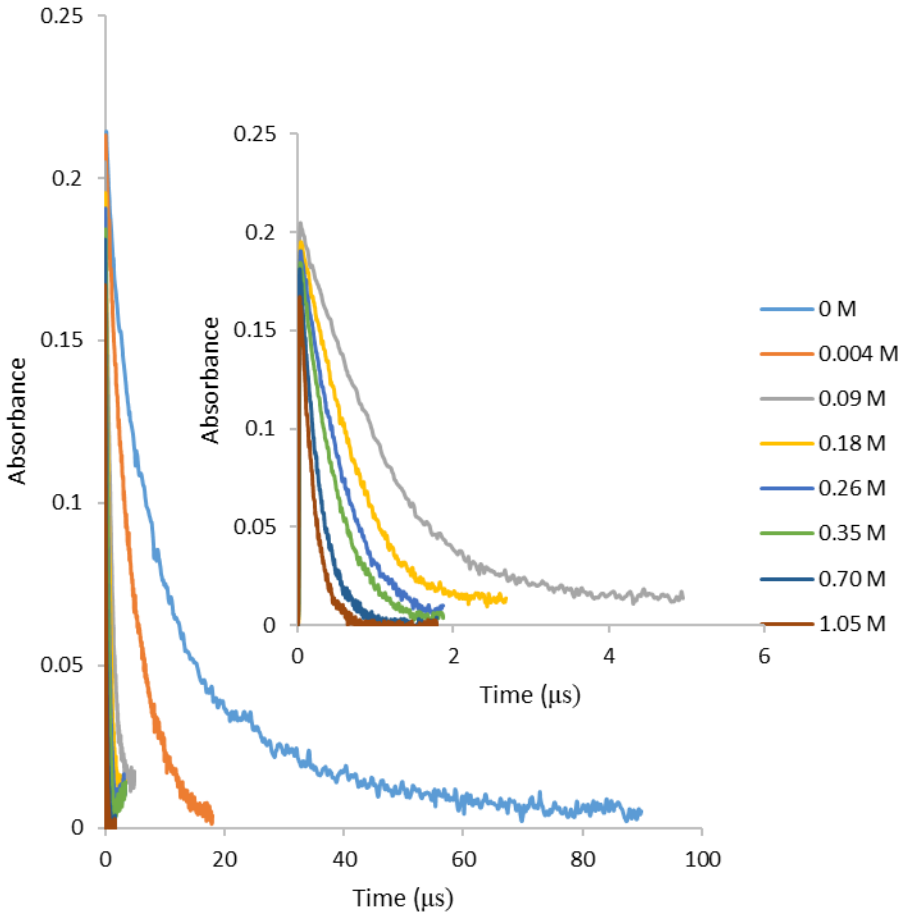

Figure A.31. Transient signal for the decay of $NO_3\cdot$ at 635 nm in the presence of 1,4-dioxane in neat CH_3CN generated by laser flash photolysis of 3×10^{-3} mol L^{-1} CKN. The inset depicts a magnified view of the decay profiles for higher concentrations of substrate.

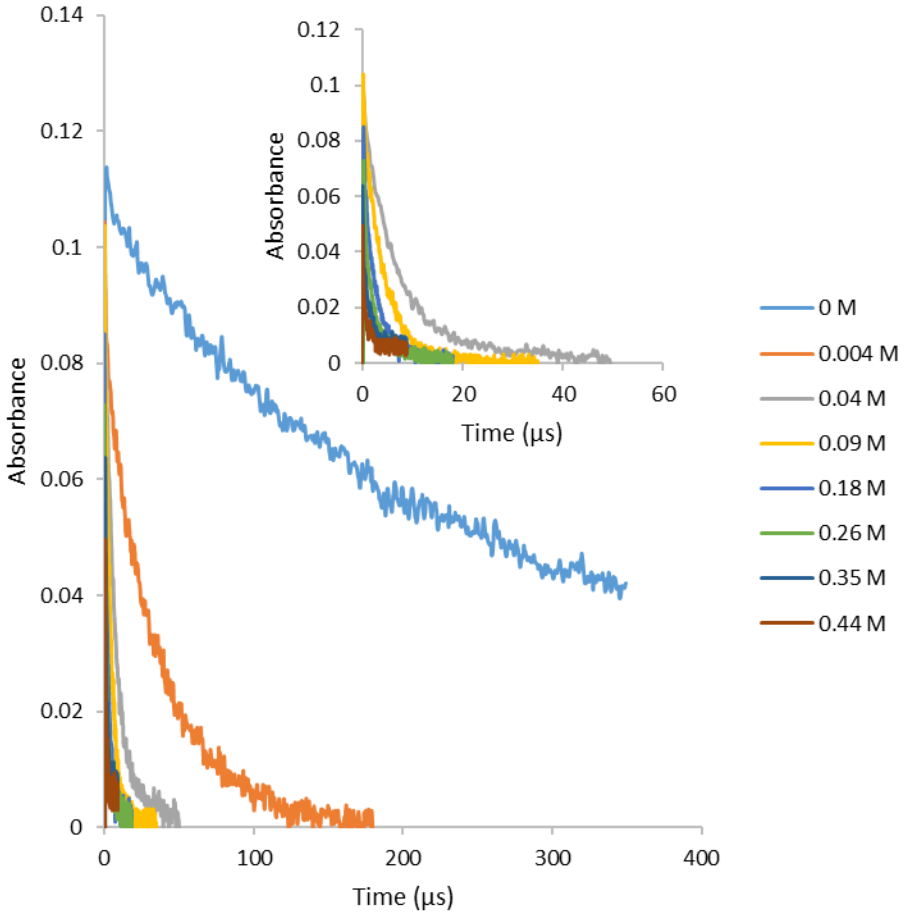

Figure A.32. Transient signal for the decay of $NO_3\cdot$ at 635 nm in the presence of 1,4-dioxane in H_2O generated by laser flash photolysis of 3×10^{-3} mol L^{-1} CKN. The inset depicts a magnified view of the decay profiles for higher concentrations of substrate.

Table A.21. Observed rate constants for hydrogen abstraction by $NO_3\cdot$ from various concentrations of 1,4-dioxane in CH_3CN at 25 °C

[1,4-dioxane], M (CH_3CN)	$k_{obs} \times 10^{-6}$ s
0	0.09 ± 0.00
0.004	0.22 ± 0.01
0.09	0.99 ± 0.02
0.18	1.50 ± 0.04
0.26	1.66 ± 0.01
0.35	2.13 ± 0.01
0.70	3.89 ± 0.05
1.05	5.50 ± 0.05

Table A.22. Observed rate constants for hydrogen abstraction by $NO_3\cdot$ from various concentrations of 1,4-dioxane in H_2O at 25 °C

[1,4-dioxane], M (H_2O)	$k_{obs} \times 10^{-5}$ s
0	0.05 ± 0.00
0.004	0.29 ± 0.04
0.04	1.34 ± 0.01
0.09	2.39 ± 0.04
0.18	4.17 ± 0.14
0.26	5.59 ± 0.09
0.35	10.53 ± 0.30
0.44	17.83 ± 0.61

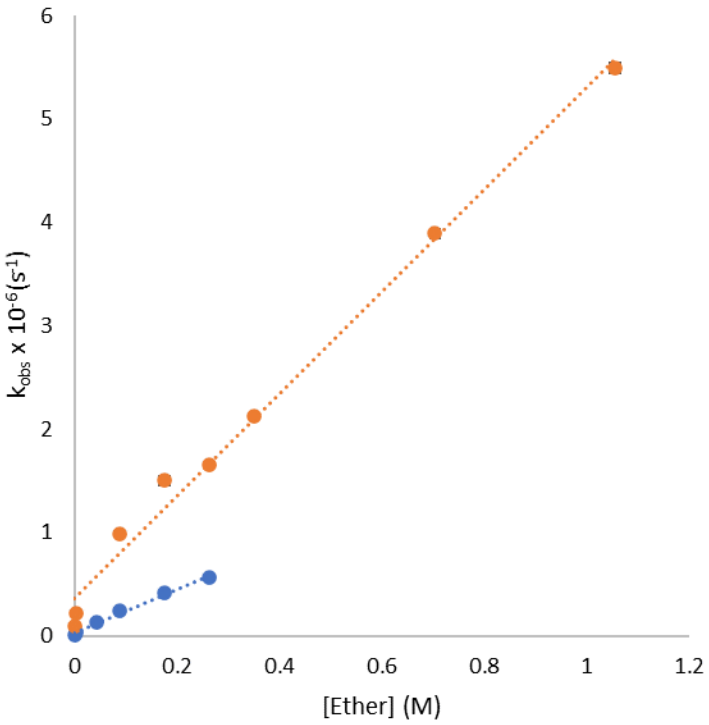

Figure A.33. Plot of the observed rate constant for $NO_3\cdot$ vs. 1,4-dioxane concentration in CH_3CN (●) and H_2O (●) at 25 °C; the slope is equal to the hydrogen abstraction rate constant (k_{AN} = 5.0 × 10^6 $M^{-1}s^{-1}$, k_W = 2.1 × 10^6 $M^{-1}s^{-1}$).

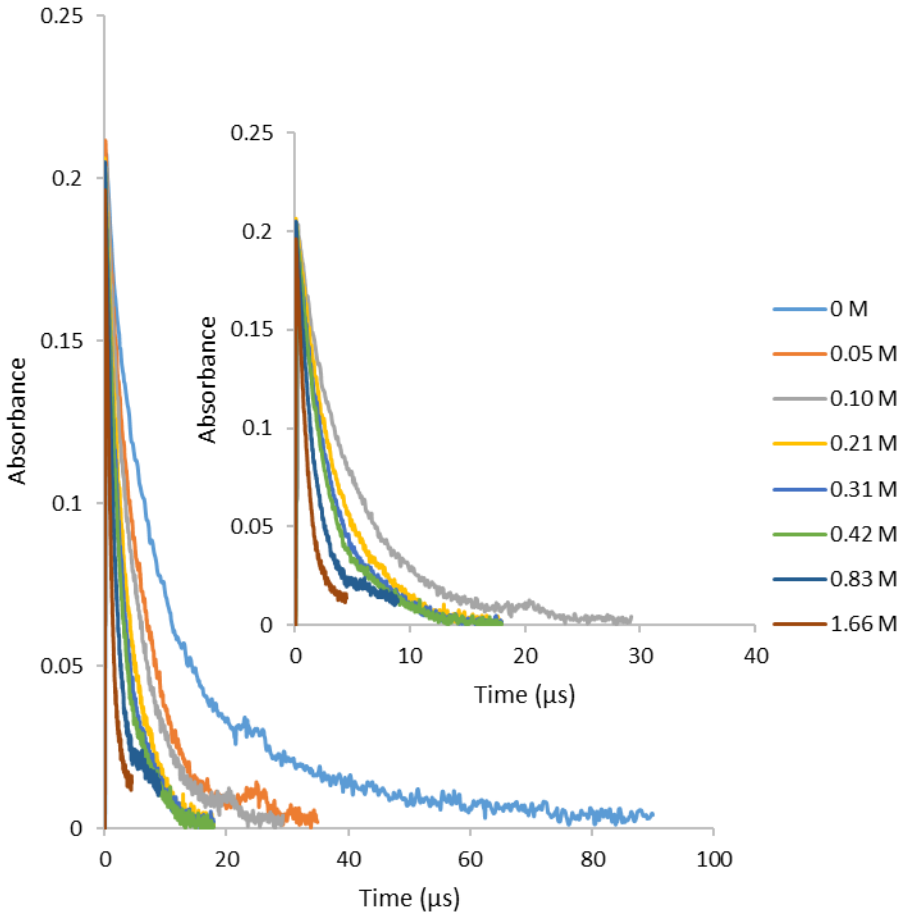

Figure A.34. Transient signal for the decay of $NO_3\cdot$ at 635 nm in the presence of 1,3,5-trioxane in neat CH_3CN generated by laser flash photolysis of 3×10^{-3} mol L^{-1} CKN. The inset depicts a magnified view of the decay profiles for higher concentrations of substrate.

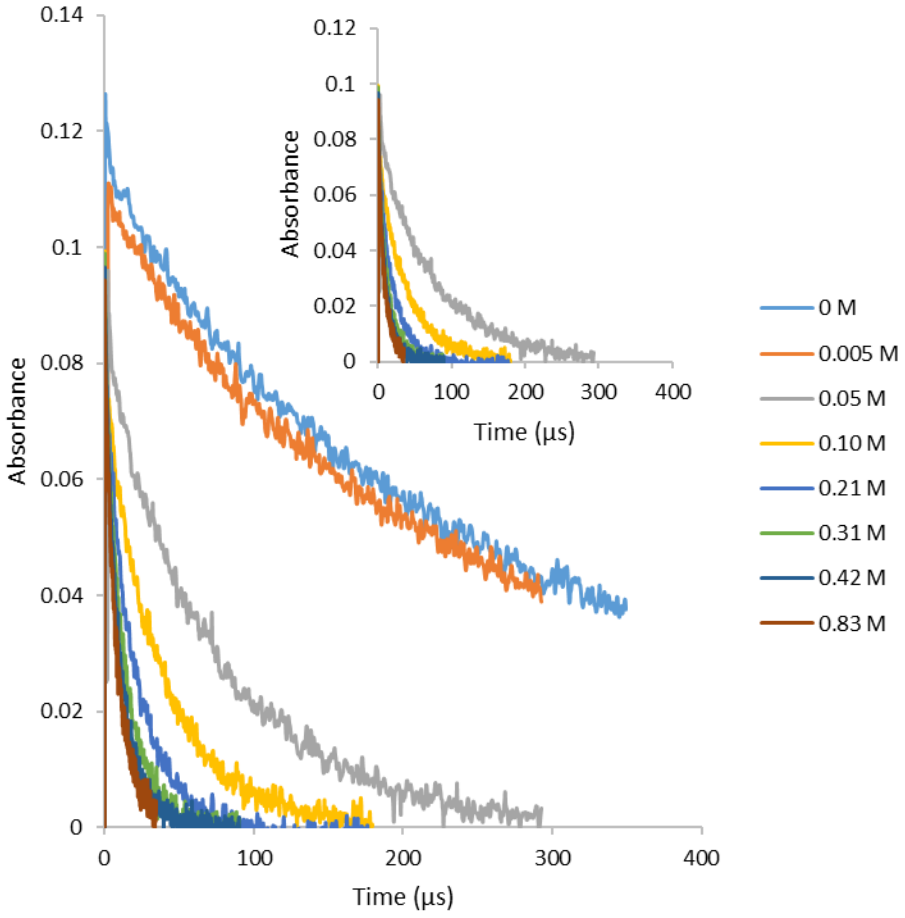

Figure A.35. Transient signal for the decay of $NO_3\cdot$ at 635 nm in the presence of 1,3,5-trioxane in H_2O generated by laser flash photolysis of 3×10^{-3} mol L^{-1} CKN. The inset depicts a magnified view of the decay profiles for higher concentrations of substrate.

Table A.23. Observed rate constants for hydrogen abstraction by $NO_3\cdot$ from various concentrations of 1,3,5-trioxane in CH_3CN at 25 °C

[1,3,5-trioxane], M (CH_3CN)	$k_{obs} \times 10^{-6}$ s
0	0.10 ± 0.00
0.05	0.17 ± 0.00
0.10	0.21 ± 0.01
0.20	0.28 ± 0.01
0.31	0.33 ± 0.00
0.41	0.37 ± 0.00
0.81	0.66 ± 0.01
1.67	1.06 ± 0.01

Table A.24. Observed rate constants for hydrogen abstraction by $NO_3\cdot$ from various concentrations of 1,3,5-trioxane in H_2O at 25 °C

[1,3,5-trioxane], M (H_2O)	$k_{obs} \times 10^{-5}$ s
0	0.05 ± 0.00
0.005	0.06 ± 0.01
0.05	0.14 ± 0.01
0.10	0.35 ± 0.09
0.21	0.49 ± 0.03
0.31	0.77 ± 0.08
0.41	0.91 ± 0.05
0.51	1.24 ± 0.01

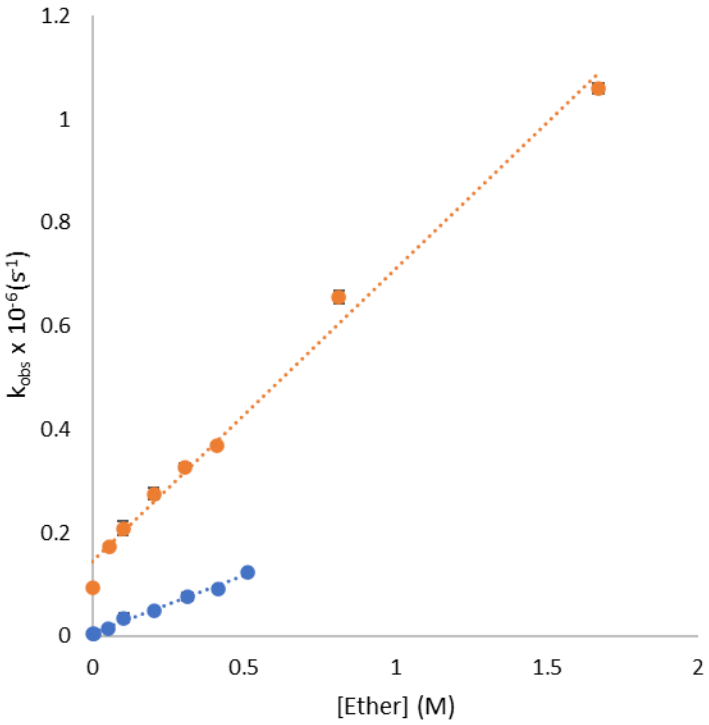

Figure A.36. Plot of the observed rate constant for $NO_3\cdot$ vs. 1,3,5-trioxane concentration in CH_3CN (●) and H_2O (●) at 25 °C; the slope is equal to the hydrogen abstraction rate constant (k_{AN} = 0.6 × 10^6 $M^{-1}s^{-1}$, k_W = 0.2 × 10^6 $M^{-1}s^{-1}$).

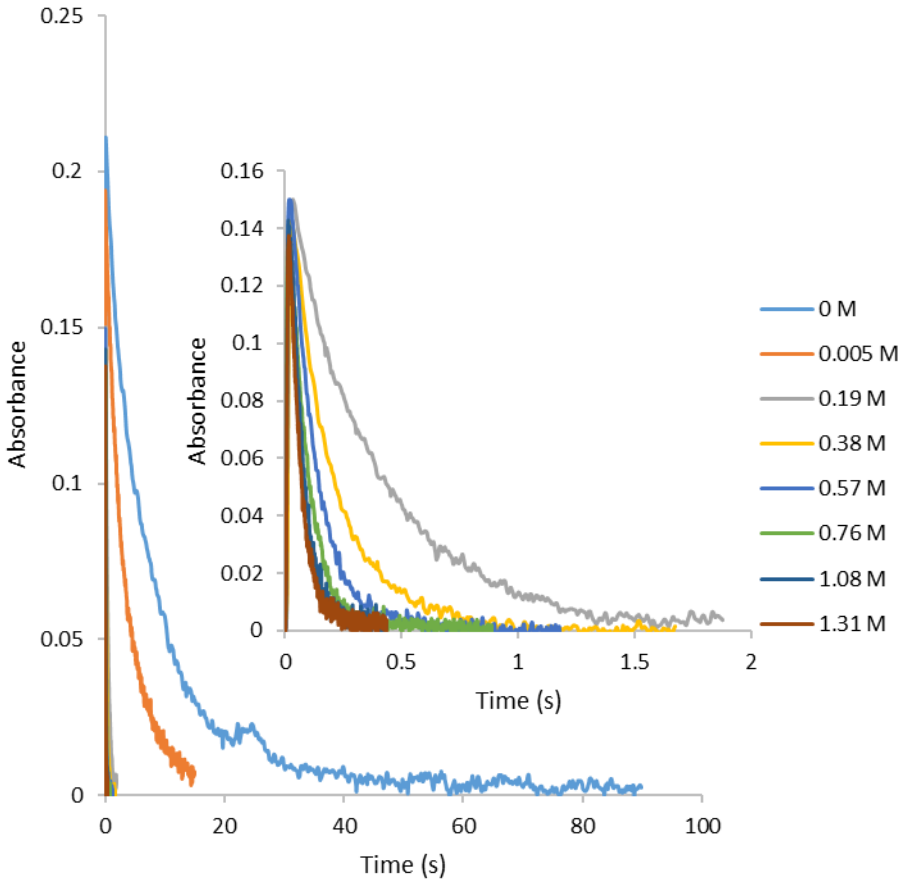

Figure A.37. Transient signal for the decay of $NO_3\cdot$ at 635 nm in the presence of diisopropyl ether in neat CH_3CN generated by laser flash photolysis of 3×10^{-3} mol L^{-1} CKN. The inset depicts a magnified view of the decay profiles for higher concentrations of substrate.

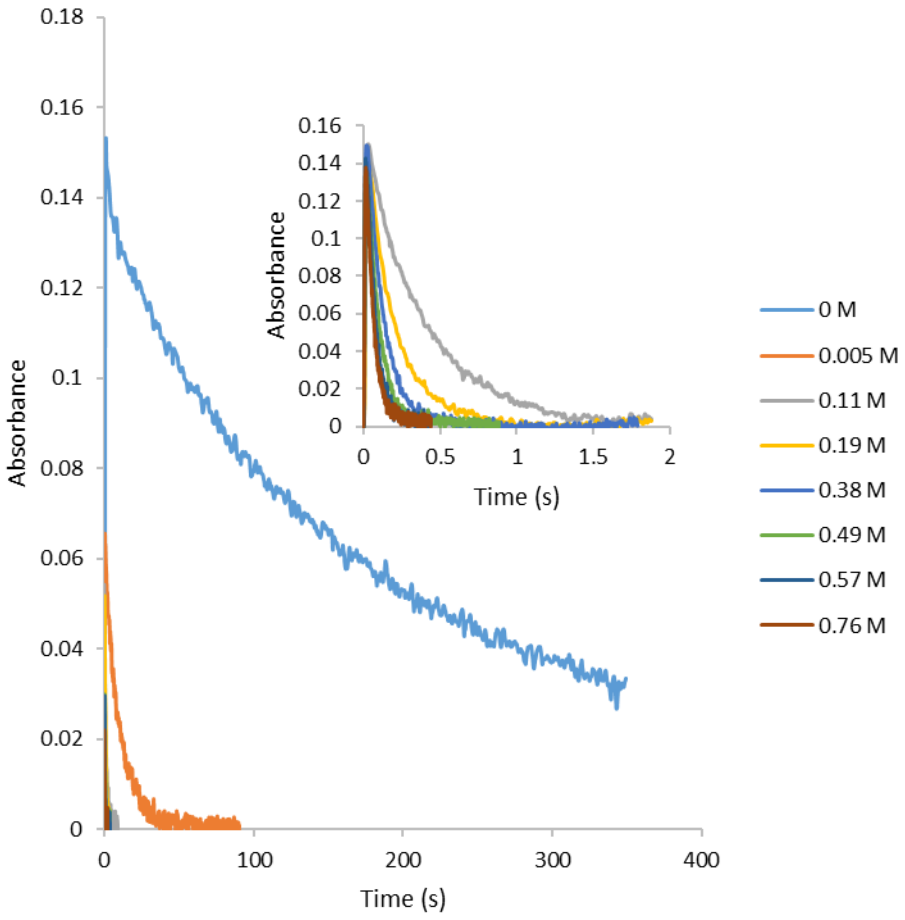

Figure A.38. Transient signal for the decay of $NO_3\cdot$ at 635 nm in the presence of diisopropyl ether in 4:6 CH_3CN/H_2O generated by laser flash photolysis of 3×10^{-3} mol L^{-1} CKN. The inset depicts a magnified view of the decay profiles for higher concentrations of substrate.

Table A.25. Observed rate constants for hydrogen abstraction by $NO_3\cdot$ from various concentrations of diisopropyl ether in CH_3CN at 25 °C

[diisopropyl ether], M (CH_3CN)	$k_{obs} \times 10^{-6}$ s
0	0.13 ± 0.02
0.005	0.33 ± 0.07
0.19	2.57 ± 0.03
0.38	5.23 ± 0.39
0.57	8.70 ± 0.58
0.76	11.80 ± 0.81
1.08	15.66 ± 0.56
1.31	18.80 ± 0.96

Table A.26. Observed rate constants for hydrogen abstraction by $NO_3\cdot$ from various concentrations of diisopropyl ether in 4:6 CH_3CN/H_2O at 25 °C

[diisopropyl ether], M (4:6 CH_3CN/H_2O)	$k_{obs} \times 10^{-5}$ s
0	0.06 ± 0.00
0.005	1.02 ± 0.13
0.11	8.50 ± 0.55
0.19	14.28 ± 0.95
0.38	26.89 ± 4.71
0.49	36.84 ± 5.11
0.57	40.76 ± 9.59
0.76	44.87 ± 1.22

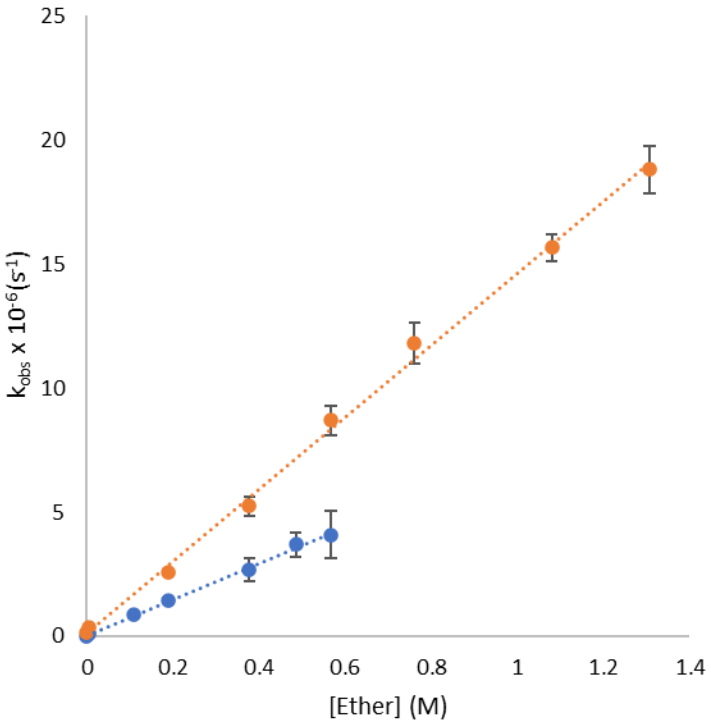

Figure A.39. Plot of the observed rate constant for $NO_3\cdot$ vs. diisopropyl ether concentration in CH_3CN (●) and 4:6 CH_3CN/H_2O (●) at 25 °C; the slope is equal to the hydrogen abstraction rate constant ($k_{AN} = 14.5 \times 10^6\ M^{-1}s^{-1}$, $k_W = 7.2 \times 10^6\ M^{-1}s^{-1}$).

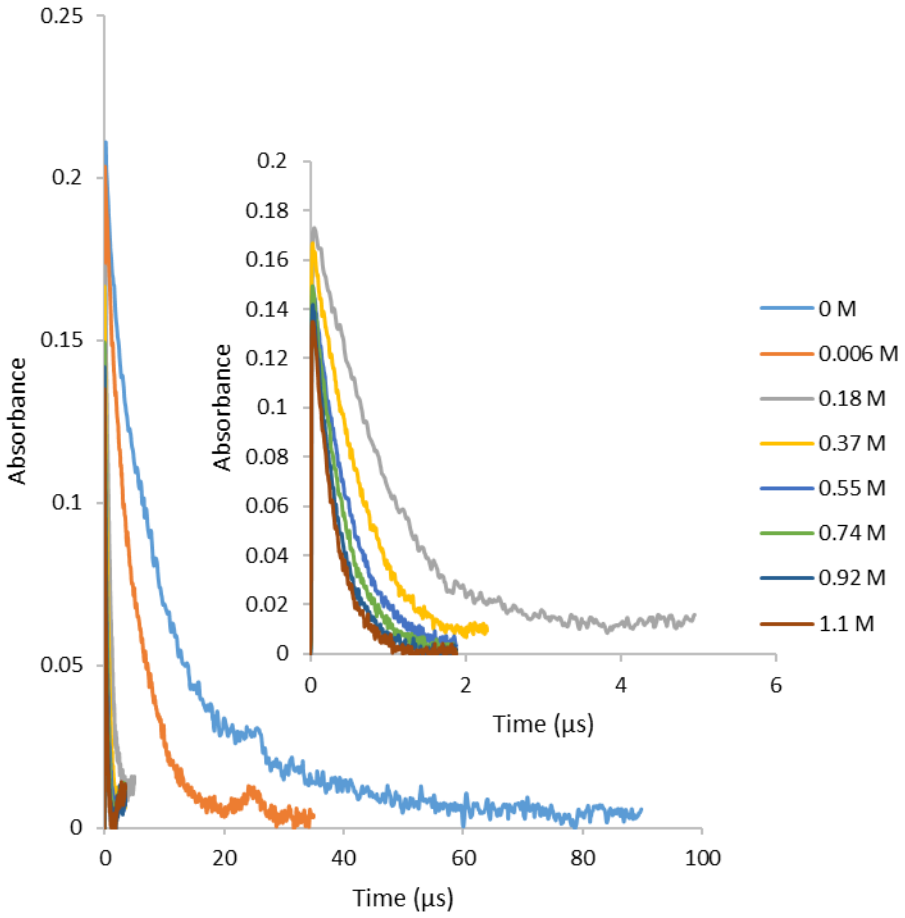

Figure A.40. Transient signal for the decay of $NO_3\cdot$ at 635 nm in the presence of *sec*-butyl methyl ether in neat CH_3CN generated by laser flash photolysis of 3×10^{-3} mol L^{-1} CKN. The inset depicts a magnified view of the decay profiles for higher concentrations of substrate.

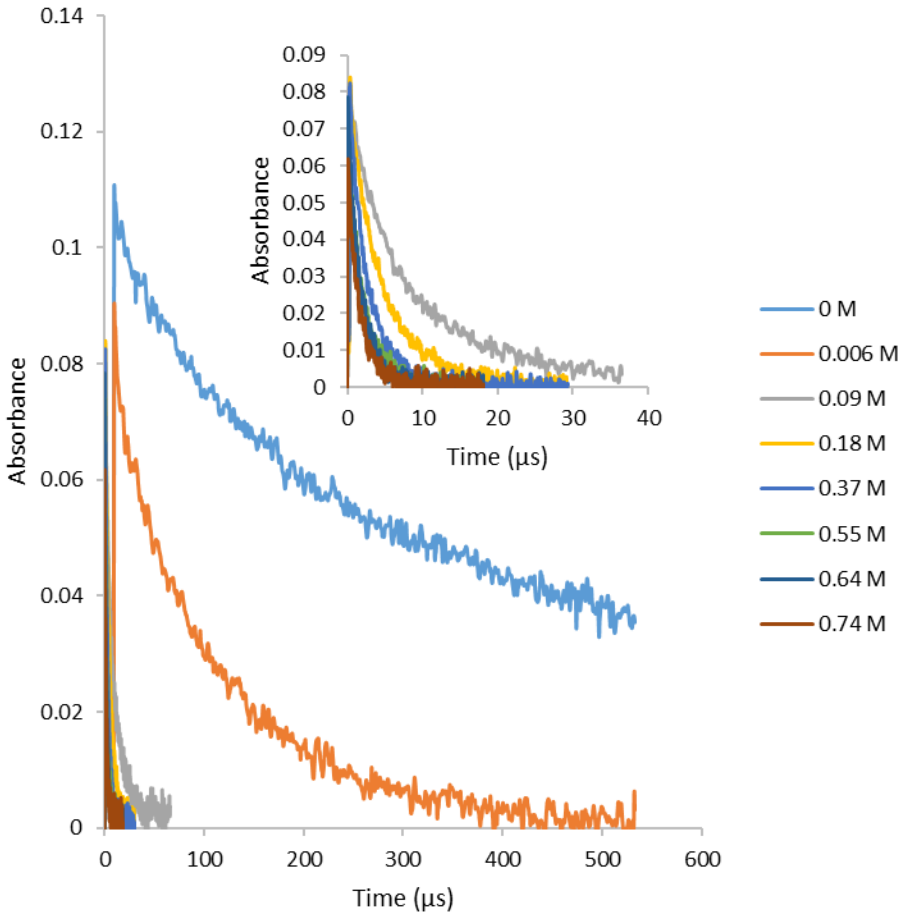

Figure A.41. Transient signal for the decay of $NO_3\cdot$ at 635 nm in the presence of *sec*-butyl methyl ether in 4:6 CH_3CN/H_2O generated by laser flash photolysis of 3×10^{-3} mol L^{-1} CKN. The inset depicts a magnified view of the decay profiles for higher concentrations of substrate.

Table A.27. Observed rate constants for hydrogen abstraction by $NO_3\cdot$ from various concentrations of *sec*-butyl methyl ether in CH_3CN at 25 °C

[*sec*-butyl methyl ether], M (CH_3CN)	$k_{obs} \times 10^{-6}$ s
0	0.10 ± 0.01
0.006	0.27 ± 0.02
0.18	1.92 ± 0.15
0.37	3.50 ± 0.30
0.55	5.86 ± 0.34
0.73	8.69 ± 0.69
1.47	19.56 ± 0.58

Table A.28. Observed rate constants for hydrogen abstraction by $NO_3\cdot$ from various concentrations of *sec*-butyl methyl ether in 4:6 CH_3CN/H_2O at 25 °C

[*sec*-butyl methyl ether], M (4:6 CH_3CN/H_2O)	$k_{obs} \times 10^{-5}$ s
0	0.06 ± 0.01
0.006	0.72 ± 0.11
0.092	4.67 ± 0.09
0.18	8.02 ± 1.63
0.37	22.24 ± 1.38
0.55	33.42 ± 3.56
0.73	46.62 ± 9.36

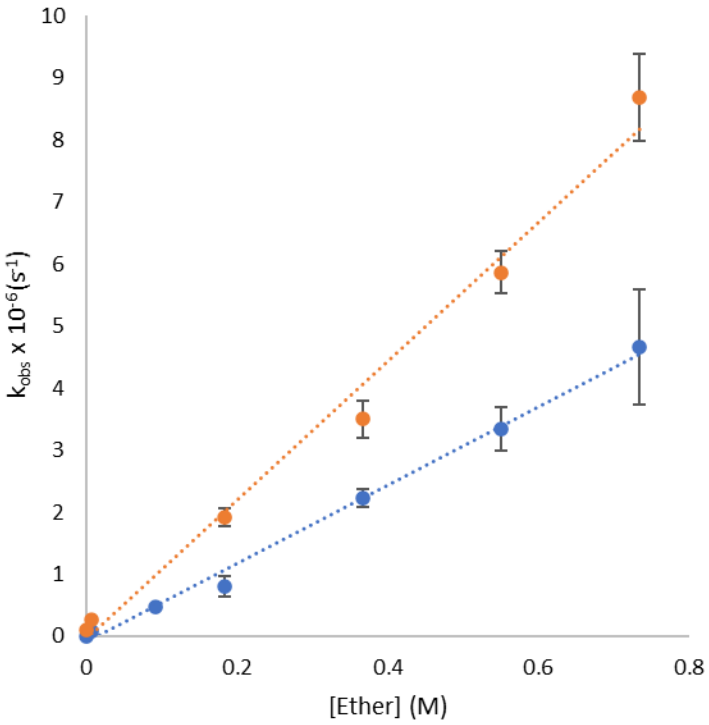

Figure A.42. Plot of the observed rate constant for $NO_3\cdot$ vs. *sec*-butyl methyl ether concentration in CH_3CN (●) and 4:6 CH_3CN/H_2O (●) at 25 °C; the slope is equal to the hydrogen abstraction rate constant ($k_{AN} = 11.2 \times 10^6\ M^{-1}s^{-1}$, $k_W = 6.3 \times 10^6\ M^{-1}s^{-1}$).

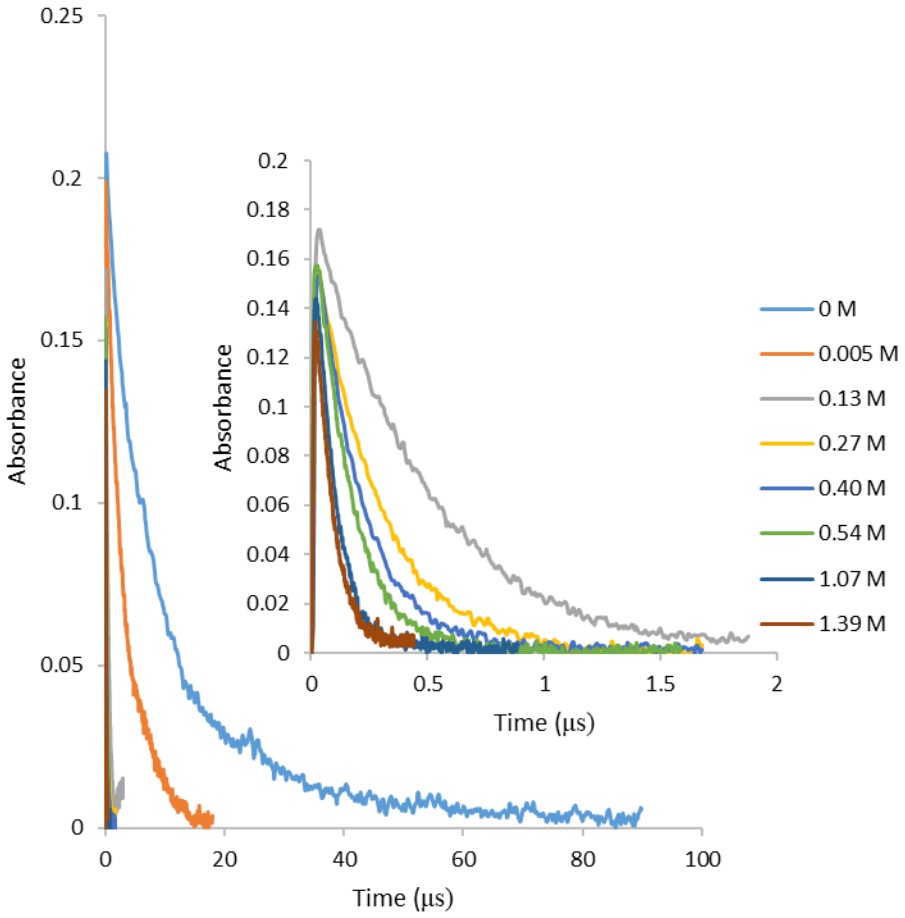

Figure A.43. Transient signal for the decay of $NO_3\cdot$ at 635 nm in the presence of cyclopentyl methyl ether in neat CH_3CN generated by laser flash photolysis of 3×10^{-3} mol L^{-1} CKN. The inset depicts a magnified view of the decay profiles for higher concentrations of substrate.

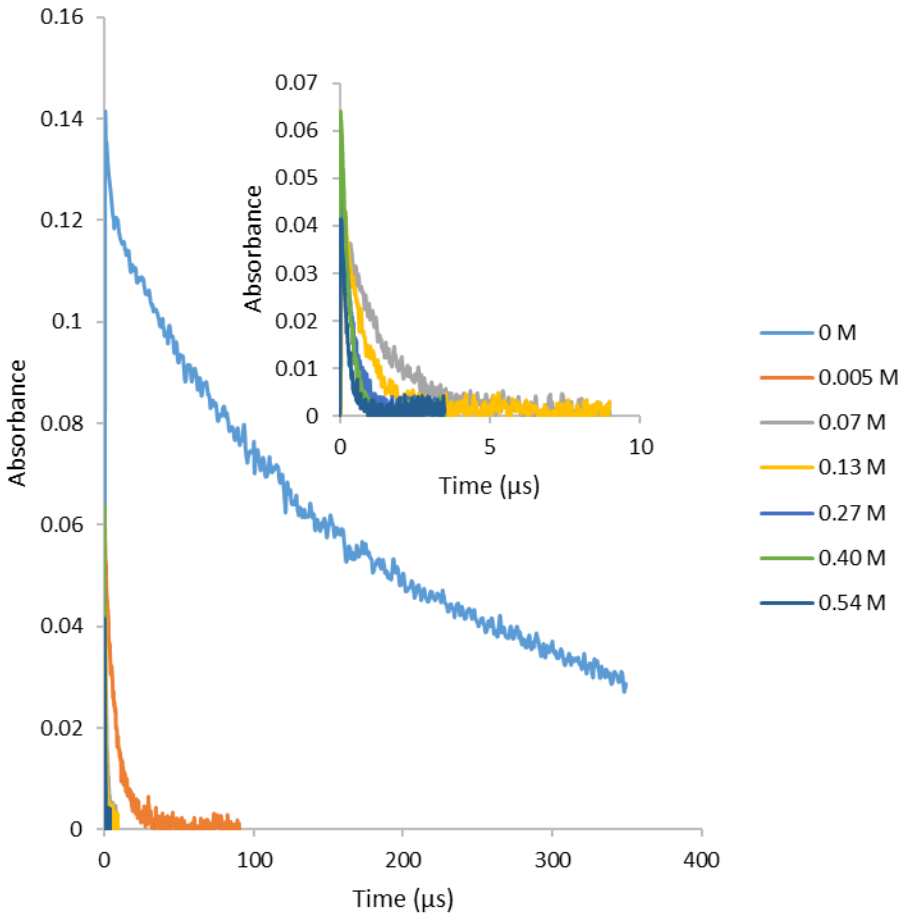

Figure A.44. Transient signal for the decay of $NO_3\cdot$ at 635 nm in the presence of cyclopentyl methyl ether in 4:6 CH_3CN/H_2O generated by laser flash photolysis of 3×10^{-3} mol L^{-1} CKN. The inset depicts a magnified view of the decay profiles for higher concentrations of substrate.

Table A.29. Observed rate constants for hydrogen abstraction by $NO_3\cdot$ from various concentrations of cyclopentyl methyl ether in CH_3CN at 25 °C

[cyclopentyl methyl ether], M (CH_3CN)	$k_{obs} \times 10^{-6}$ s
0	0.11 ± 0.02
0.005	0.31 ± 0.04
0.13	2.03 ± 0.17
0.27	3.65 ± 0.14
0.40	5.10 ± 0.20
0.54	6.46 ± 0.28
1.07	11.52 ± 0.46
1.39	12.80 ± 0.32

Table A.30. Observed rate constants for hydrogen abstraction by $NO_3\cdot$ from various concentrations of cyclopentyl methyl ether in 4:6 CH_3CN/H_2O at 25 °C

[cyclopentyl methyl ether], M (4:6 CH_3CN/H_2O)	$k_{obs} \times 10^{-5}$ s
0	0.06 ± 0.00
0.005	1.23 ± 0.02
0.07	7.57 ± 0.02
0.14	10.60 ± 0.44
0.27	25.50 ± 0.11
0.41	36.04 ± 0.26
0.55	44.44 ± 0.26

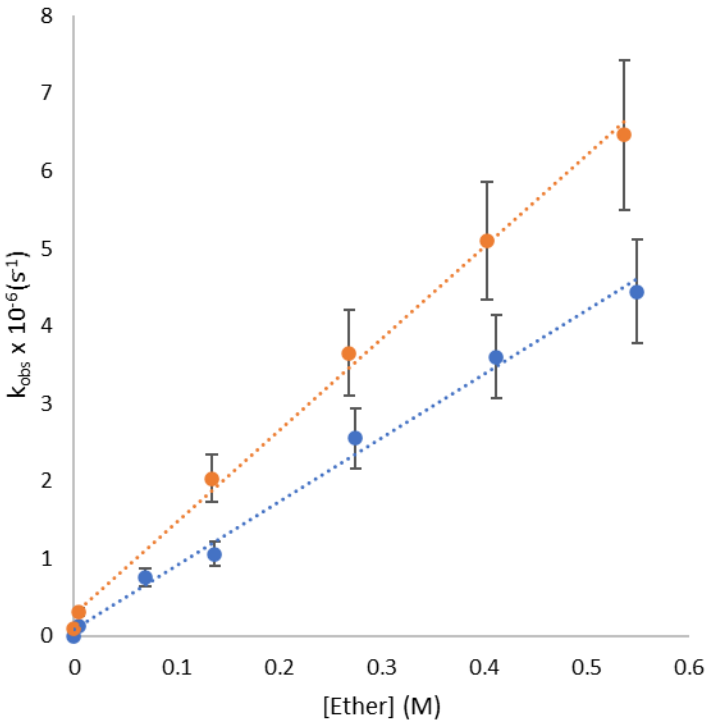

Figure A.45. Plot of the observed rate constant for $NO_3\cdot$ vs. cyclopentyl methyl ether concentration in CH_3CN (●) and 4:6 CH_3CN/H_2O (●) at 25 °C; the slope is equal to the hydrogen abstraction rate constant ($k_{AN} = 11.8 \times 10^6\ M^{-1}s^{-1}$, $k_W = 8.2 \times 10^6\ M^{-1}s^{-1}$).

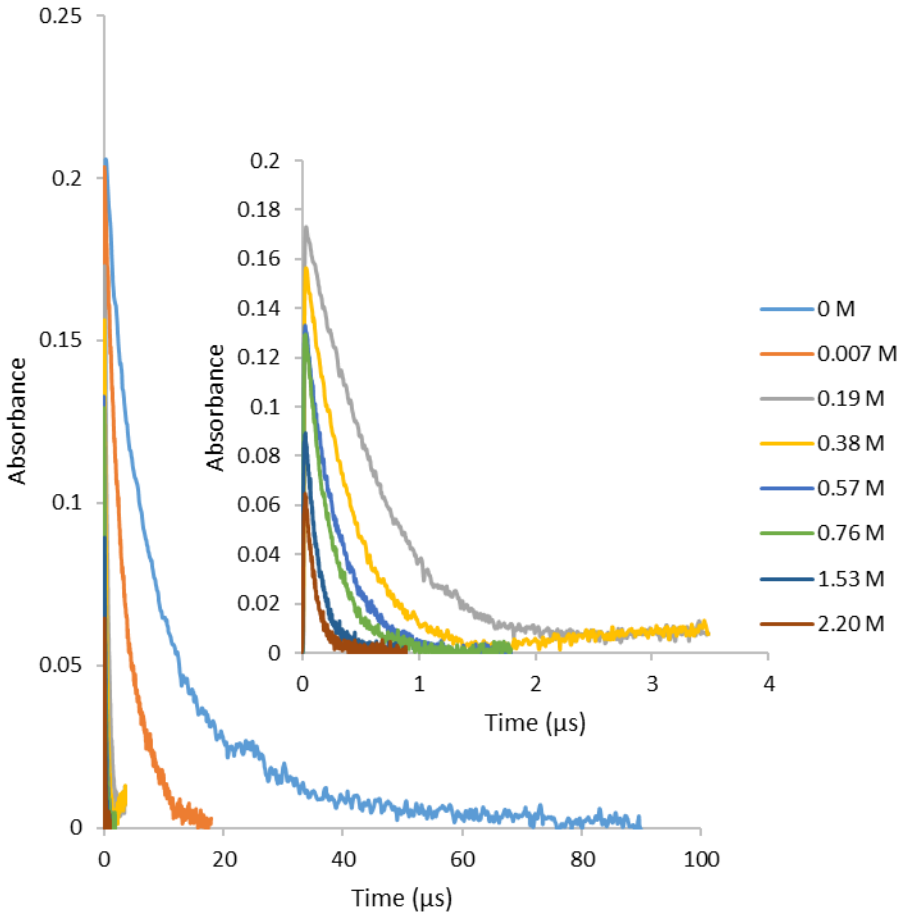

Figure A.46. Transient signal for the decay of $NO_3\cdot$ at 635 nm in the presence of 1-methoxypropane in neat CH_3CN generated by laser flash photolysis of 3×10^{-3} mol L^{-1} CKN. The inset depicts a magnified view of the decay profiles for higher concentrations of substrate.

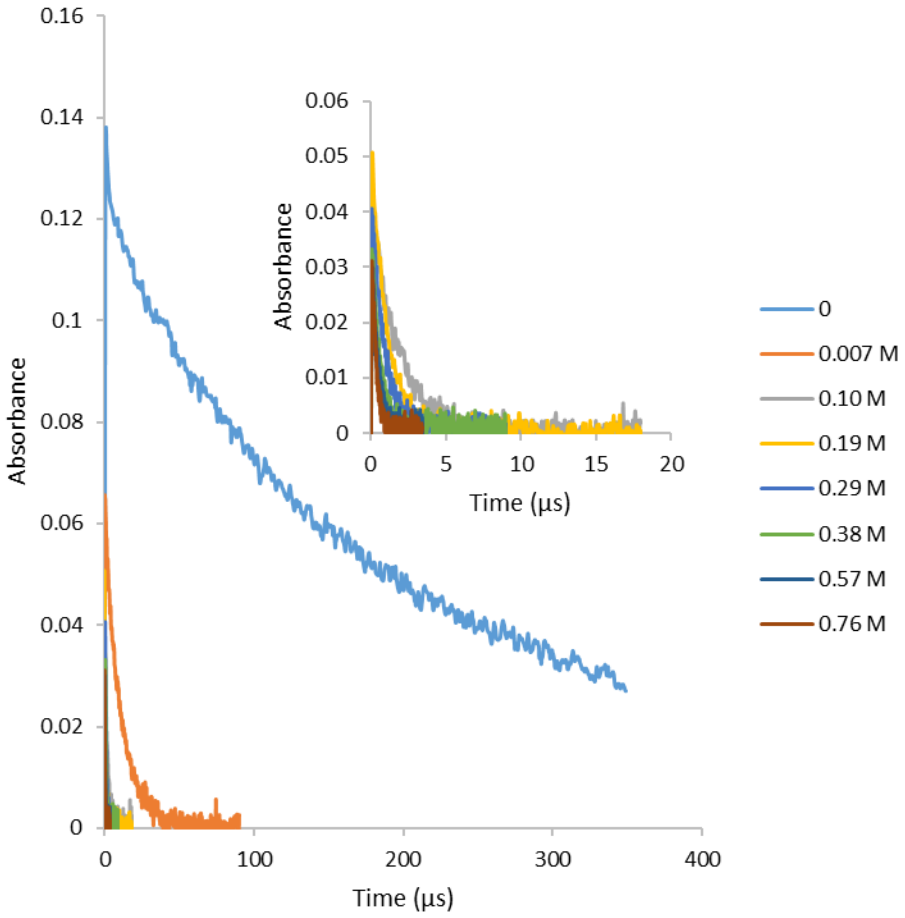

Figure A.47. Transient signal for the decay of $NO_3\cdot$ at 635 nm in the presence of 1-methoxypropane in 4:6 CH_3CN/H_2O generated by laser flash photolysis of 3×10^{-3} mol L^{-1} CKN. The inset depicts a magnified view of the decay profiles for higher concentrations of substrate.

Table A.31. Observed rate constants for hydrogen abstraction by $NO_3\cdot$ from various concentrations of 1-methoxypropane in CH_3CN at 25 °C

[1-methoxypropane], M (CH_3CN)	$k_{obs} \times 10^{-6}$ s
0	0.11 ± 0.01
0.007	0.29 ± 0.20
0.19	1.67 ± 0.62
0.38	2.57 ± 0.21
0.57	3.46 ± 0.23
0.76	4.55 ± 0.43
1.53	7.80 ± 0.53
2.20	10.17 ± 0.31

Table A.32. Observed rate constants for hydrogen abstraction by $NO_3\cdot$ from various concentrations of 1-methoxypropane in 4:6 CH_3CN/H_2O at 25 °C

[1-methoxypropane], M (4:6 CH_3CN/H_2O)	$k_{obs} \times 10^{-5}$ s
0	0.06 ± 0.00
0.007	0.91 ± 0.08
0.10	5.57 ± 0.28
0.19	9.28 ± 0.64
0.29	12.17 ± 1.02
0.38	19.07 ± 1.64
0.57	24.64 ± 2.31
0.76	29.00 ± 2.25

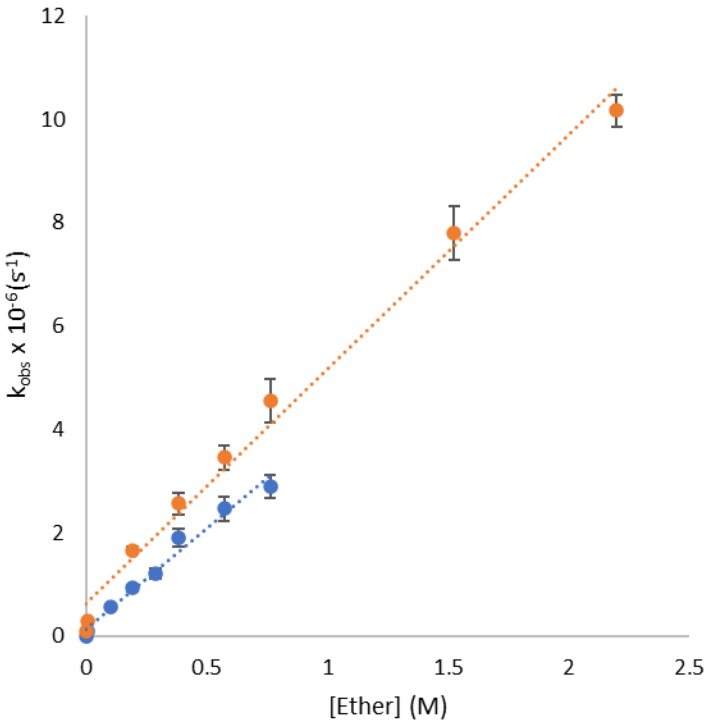

Figure A.48. Plot of the observed rate constant for $NO_3\cdot$ vs. 1-methoxypropane concentration in CH_3CN (●) and 4:6 CH_3CN/H_2O (●) at 25 °C; the slope is equal to the hydrogen abstraction rate constant ($k_{AN} = 4.5 \times 10^6\ M^{-1}s^{-1}$, $k_W = 3.9 \times 10^6\ M^{-1}s^{-1}$).

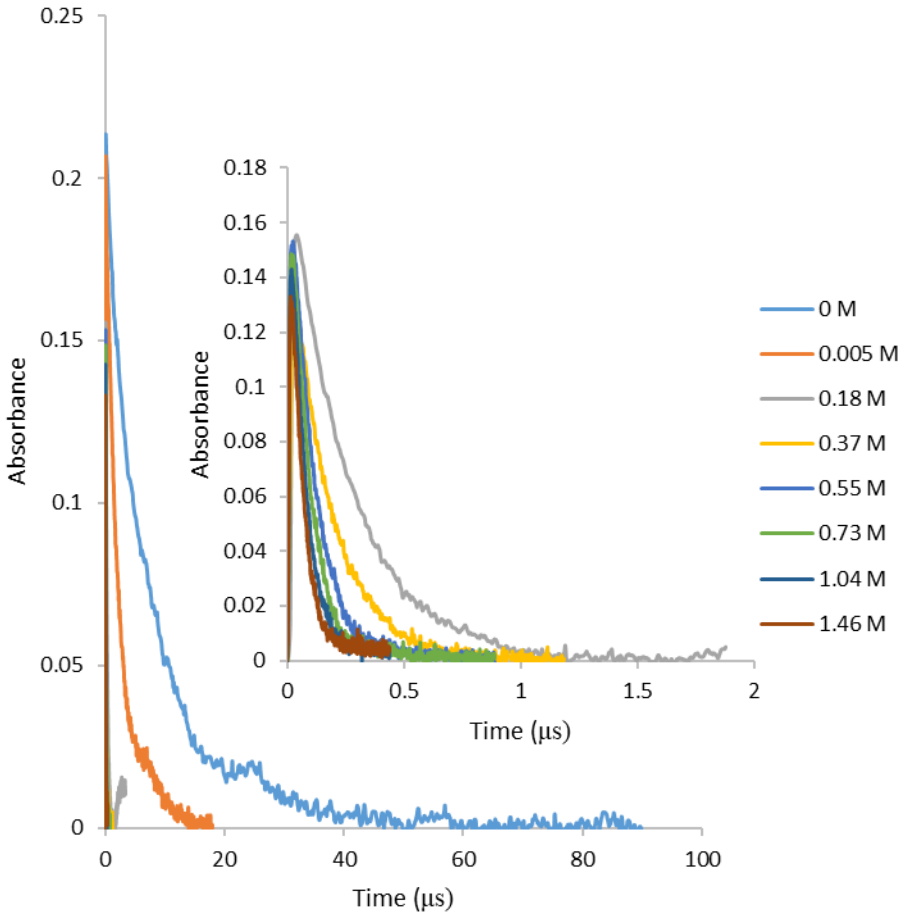

Figure A.49. Transient signal for the decay of $NO_3\cdot$ at 635 nm in the presence of dipropyl ether in neat CH_3CN generated by laser flash photolysis of 3×10^{-3} mol L^{-1} CKN. The inset depicts a magnified view of the decay profiles for higher concentrations of substrate.

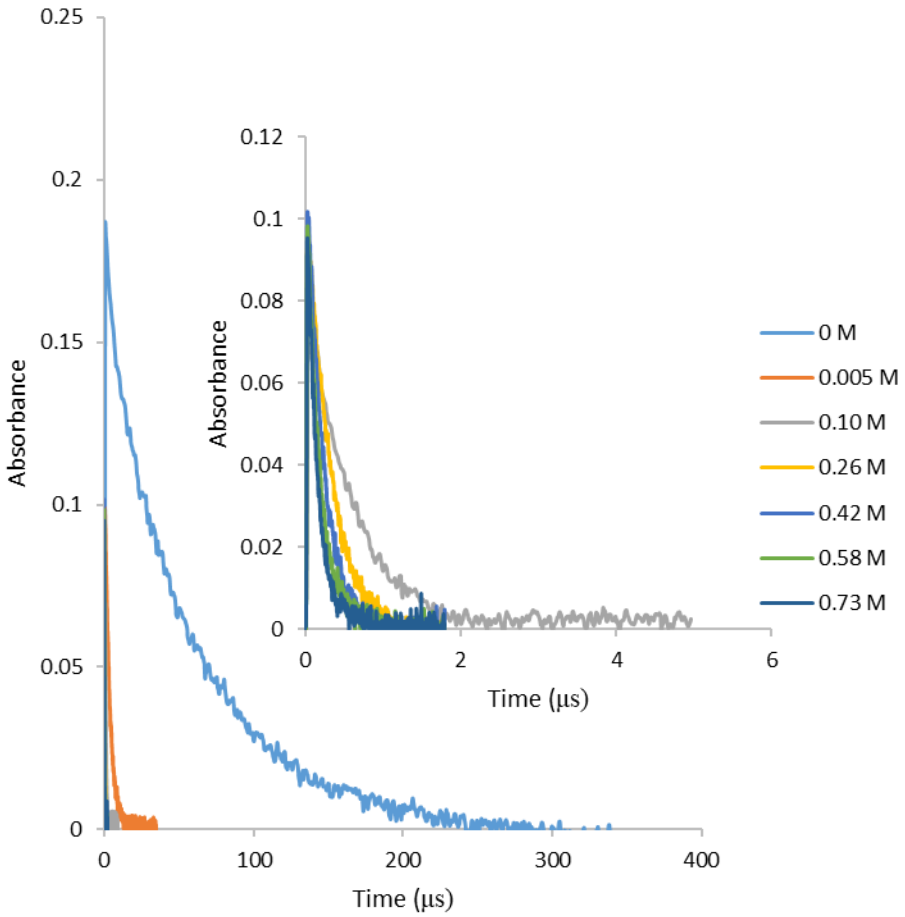

Figure A.50. Transient signal for the decay of $NO_3\cdot$ at 635 nm in the presence of dipropyl ether in 8:2 CH_3CN/H_2O generated by laser flash photolysis of 3×10^{-3} mol L^{-1} CKN. The inset depicts a magnified view of the decay profiles for higher concentrations of substrate.

Table A.33. Observed rate constants for hydrogen abstraction by $NO_3\cdot$ from various concentrations of dipropyl ether in CH_3CN at 25 °C

[dipropyl ether], M (CH_3CN)	$k_{obs} \times 10^{-6}$ s
0	0.13 ± 0.03
0.005	0.45 ± 0.02
0.18	3.66 ± 0.03
0.37	6.70 ± 0.24
0.55	9.32 ± 0.17
0.73	11.57 ± 0.28
1.04	14.15 ± 0.73
1.46	17.10 ± 1.02

Table A.34. Observed rate constants for hydrogen abstraction by $NO_3\cdot$ from various concentrations of dipropyl ether in 8:2 CH_3CN/H_2O at 25 °C

[dipropyl ether], M (8:2 H_3CN/H_2O)	$k_{obs} \times 10^{-6}$ s
0	0.17 ± 0.01
0.005	0.27 ± 0.16
0.07	1.68 ± 0.55
0.16	3.14 ± 0.54
0.28	4.65 ± 2.49
0.40	6.00 ± 1.30
0.52	7.51 ± 2.53

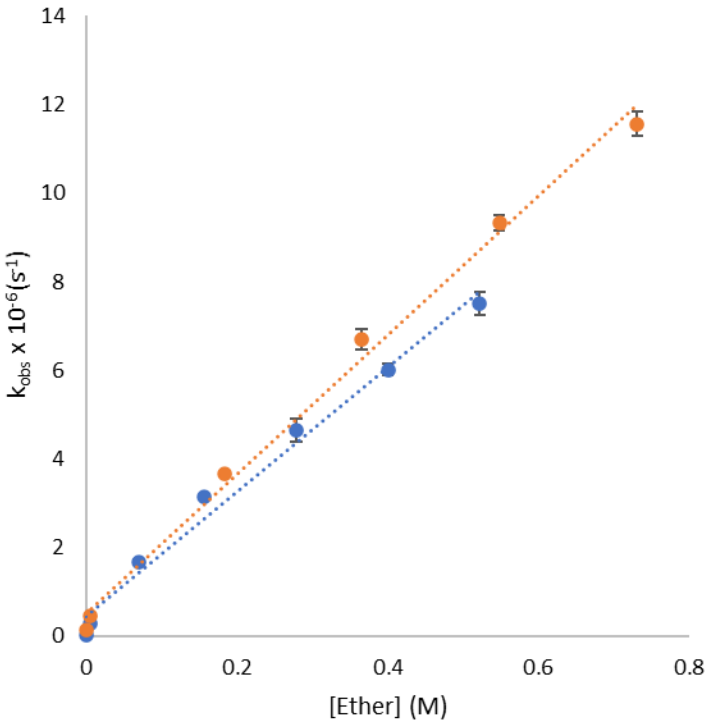

Figure A.51. Plot of the observed rate constant for $NO_3\cdot$ vs. dipropyl ether concentration in CH_3CN (●) and 8:2 CH_3CN/H_2O (●) at 25 °C; the slope is equal to the hydrogen abstraction rate constant ($k_{AN} = 15.8 \times 10^6\ M^{-1}s^{-1}$, $k_W = 14.1 \times 10^6\ M^{-1}s^{-1}$).

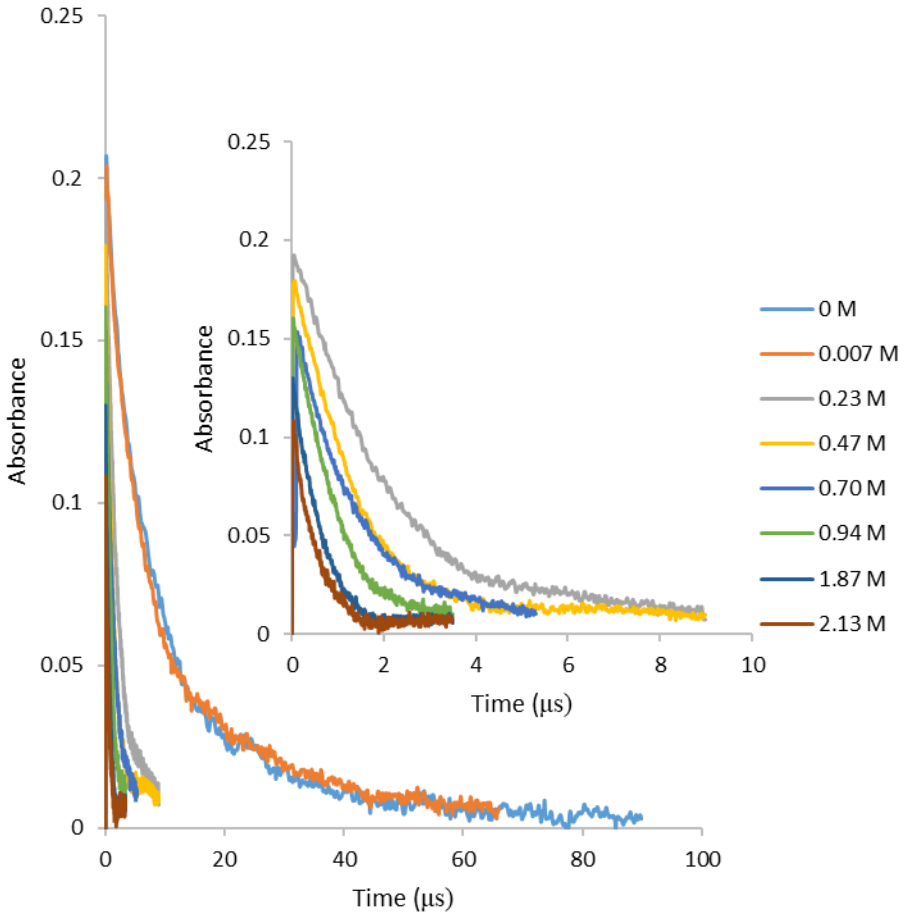

Figure A.52. Transient signal for the decay of $NO_3\cdot$ at 635 nm in the presence of n-hexane in neat CH_3CN generated by laser flash photolysis of 3×10^{-3} mol L^{-1} CKN. The inset depicts a magnified view of the decay profiles for higher concentrations of substrate.

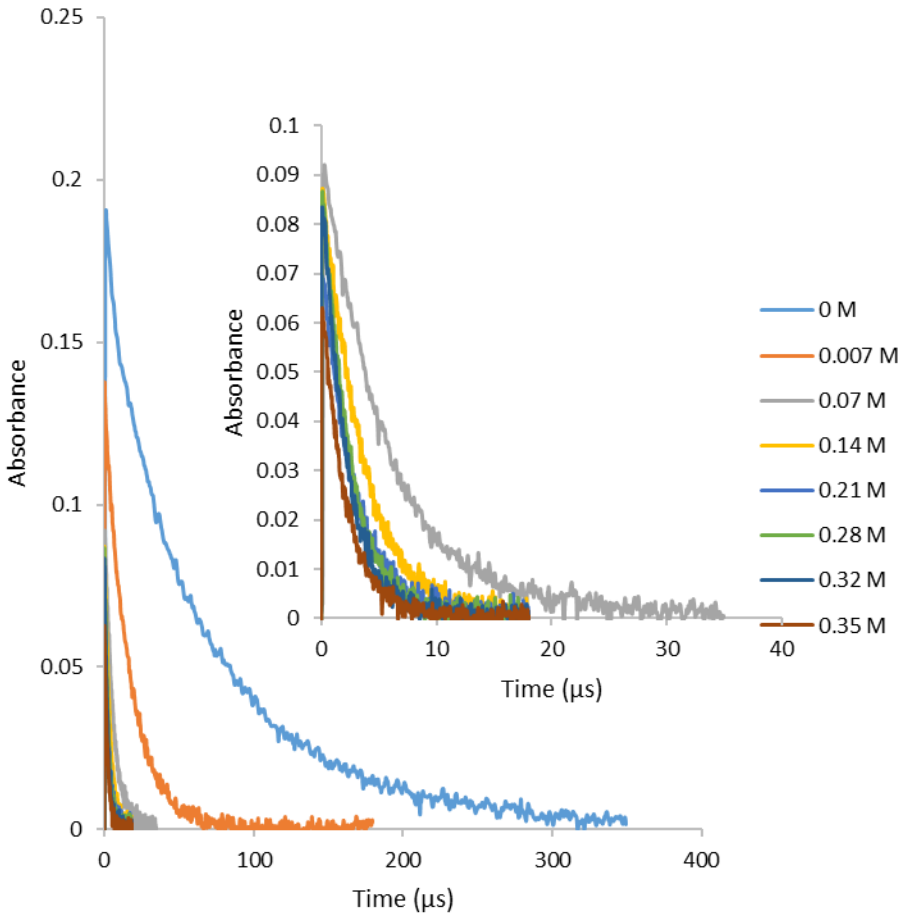

Figure A.53. Transient signal for the decay of $NO_3\cdot$ at 635 nm in the presence of n-hexane in 8:2 CH_3CN/H_2O generated by laser flash photolysis of 3×10^{-3} mol L^{-1} CKN. The inset depicts a magnified view of the decay profiles for higher concentrations of substrate.

Table A.35. Observed rate constants for hydrogen abstraction by $NO_3\cdot$ from various concentrations of n-hexane in CH_3CN at 25 °C

[hexane], M (CH_3CN)	$k_{obs} \times 10^{-6}$ s
0	0.11 ± 0.02
0.007	0.15 ± 0.01
0.17	0.55 ± 0.04
0.34	0.81 ± 0.04
0.52	0.96 ± 0.11
0.69	1.13 ± 0.10

Table A.36. Observed rate constants for hydrogen abstraction by $NO_3\cdot$ from various concentrations of n-hexane in 8:2 CH_3CN/H_2O at 25 °C

[hexane], M (8:2 CH_3CN/H_2O)	$k_{obs} \times 10^{-5}$ s
0	0.16 ± 0.01
0.007	0.57 ± 0.03
0.07	1.72 ± 0.03
0.14	2.75 ± 0.12
0.21	3.53 ± 0.06
0.28	4.11 ± 0.13
0.32	4.57 ± 0.12

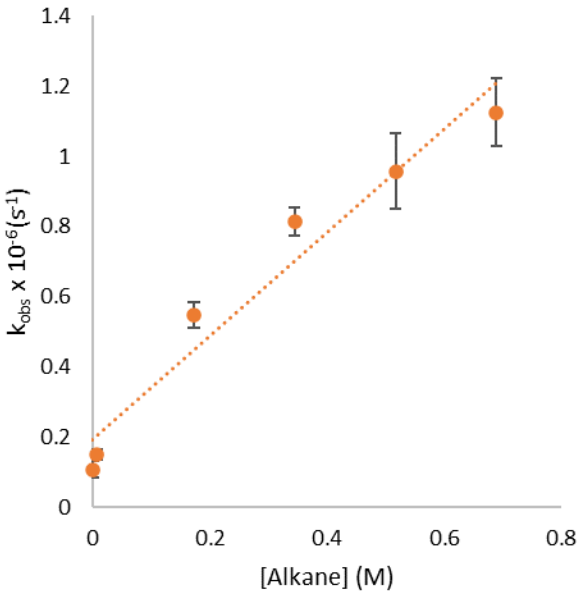

Figure A.54. Plot of the observed rate constant for $NO_3\cdot$ vs. n-hexane concentration in CH_3CN at 25 °C; the slope is equal to the hydrogen abstraction rate constant ($k_{AN} = 1.5 \times 10^6$ $M^{-1}s^{-1}$).

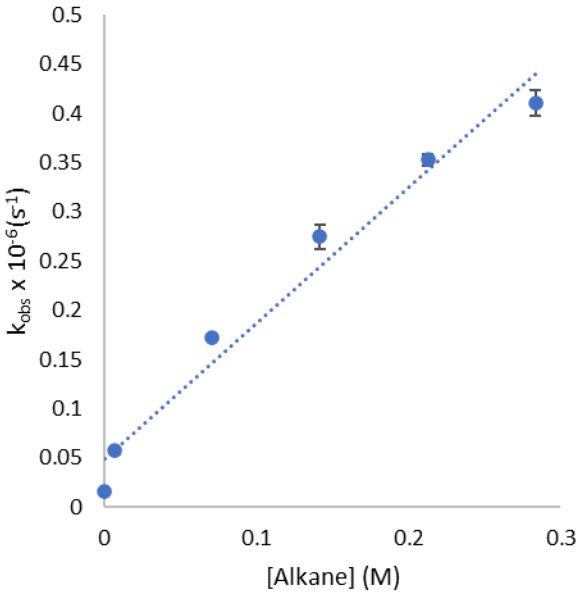

Figure A.55. Plot of the observed rate constant for $NO_3\cdot$ vs. n-hexane concentration in 8:2 CH_3CN/H_2O at 25 °C; the slope is equal to the hydrogen abstraction rate constant ($k_W = 1.4 \times 10^6$ $M^{-1}s^{-1}$).

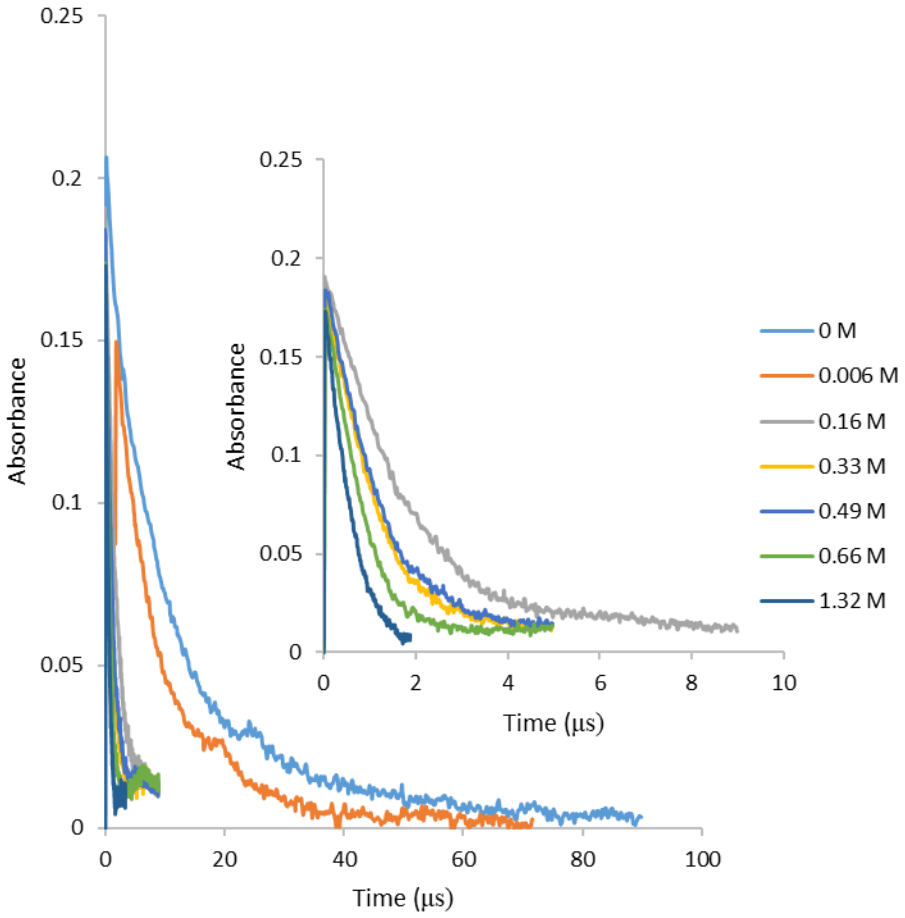

Figure A.56. Transient signal for the decay of $NO_3\cdot$ at 635 nm in the presence of cyclohexane in neat CH_3CN generated by laser flash photolysis of 3×10^{-3} mol L^{-1} CKN. The inset depicts a magnified view of the decay profiles for higher concentrations of substrate.

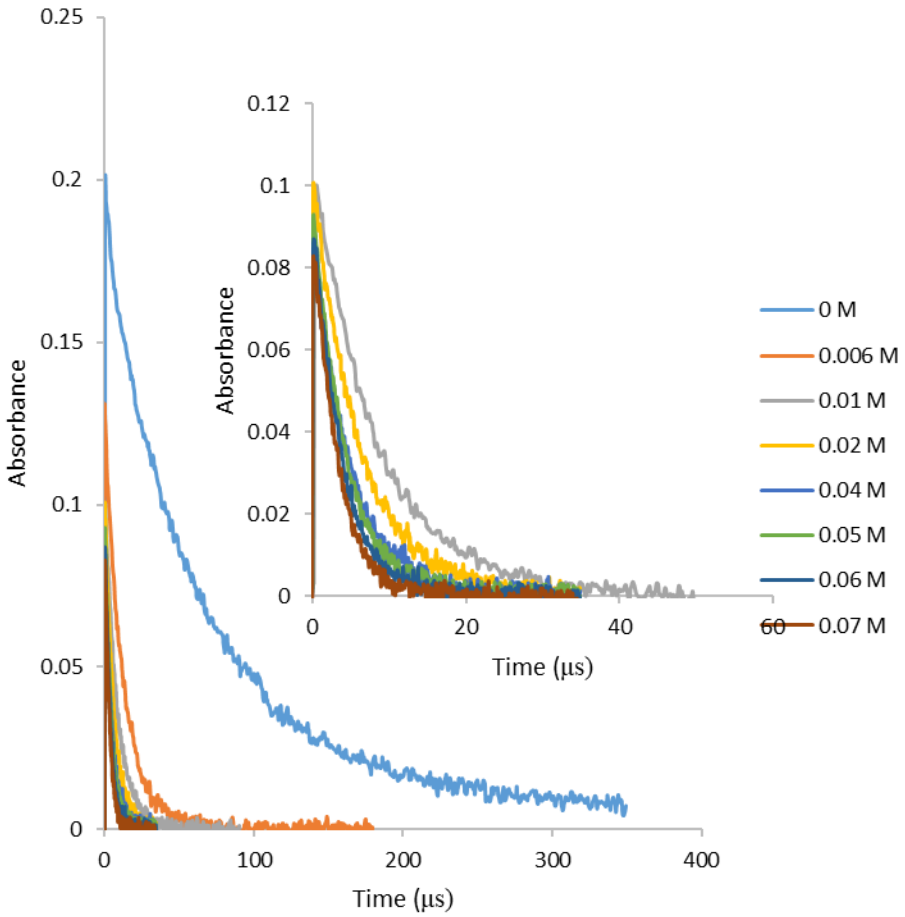

Figure A.57. Transient signal for the decay of $NO_3\cdot$ at 635 nm in the presence of cyclohexane in 8:2 CH_3CN/H_2O generated by laser flash photolysis of 3×10^{-3} mol L^{-1} CKN. The inset depicts a magnified view of the decay profiles for higher concentrations of substrate.

Table A.37. Observed rate constants for hydrogen abstraction by $NO_3\cdot$ from various concentrations of cyclohexane in CH_3CN at 25 °C

[cyclohexane], M (CH_3CN)	$k_{obs} \times 10^{-6}$ s
0	0.09 ± 0.00
0.006	0.16 ± 0.10
0.16	0.61 ± 0.10
0.33	0.89 ± 0.12
0.49	1.10 ± 0.18
0.66	1.34 ± 0.33

Table A.38. Observed rate constants for hydrogen abstraction by $NO_3\cdot$ from various concentrations of cyclohexane in 8:2 CH_3CN/H_2O at 25 °C

[cyclohexane], M (8:2 CH_3CN/H_2O)	$k_{obs} \times 10^{-5}$ s
0	0.15 ± 0.00
0.006	0.79 ± 0.12
0.012	1.11 ± 0.07
0.024	1.58 ± 0.12
0.037	1.91 ± 0.12
0.049	2.28 ± 0.13
0.061	2.53 ± 0.09
0.073	2.83 ± 0.06

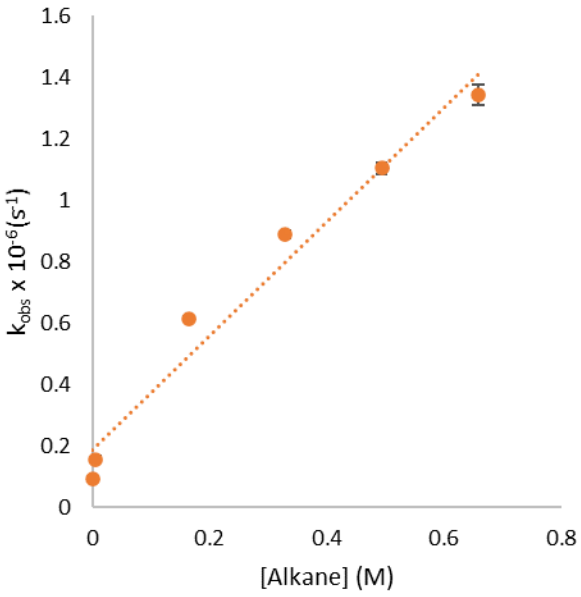

Figure A.58. Plot of the observed rate constant for $NO_3\cdot$ vs. cyclohexane concentration in CH_3CN at 25 °C; the slope is equal to the hydrogen abstraction rate constant ($k_{AN} = 1.9 \times 10^6$ $M^{-1}s^{-1}$).

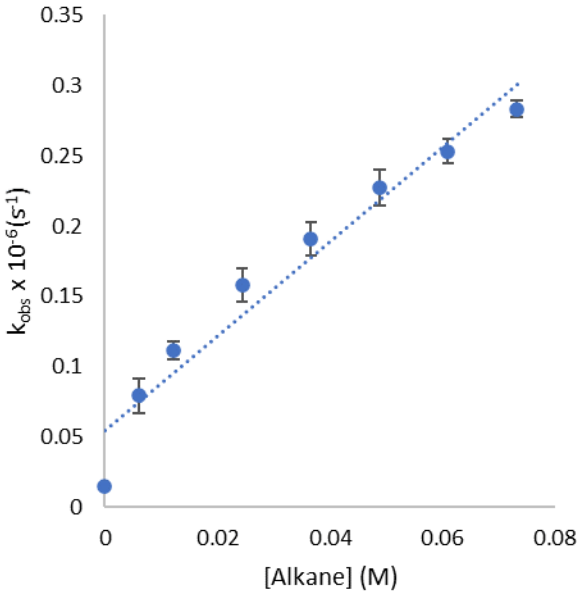

Figure A.59. Plot of the observed rate constant for $NO_3\cdot$ vs. cyclohexane concentration in 8:2 CH_3CN/H_2O at 25 °C; the slope is equal to the hydrogen abstraction rate constant ($k_W = 3.4 \times 10^6$ $M^{-1}s^{-1}$).

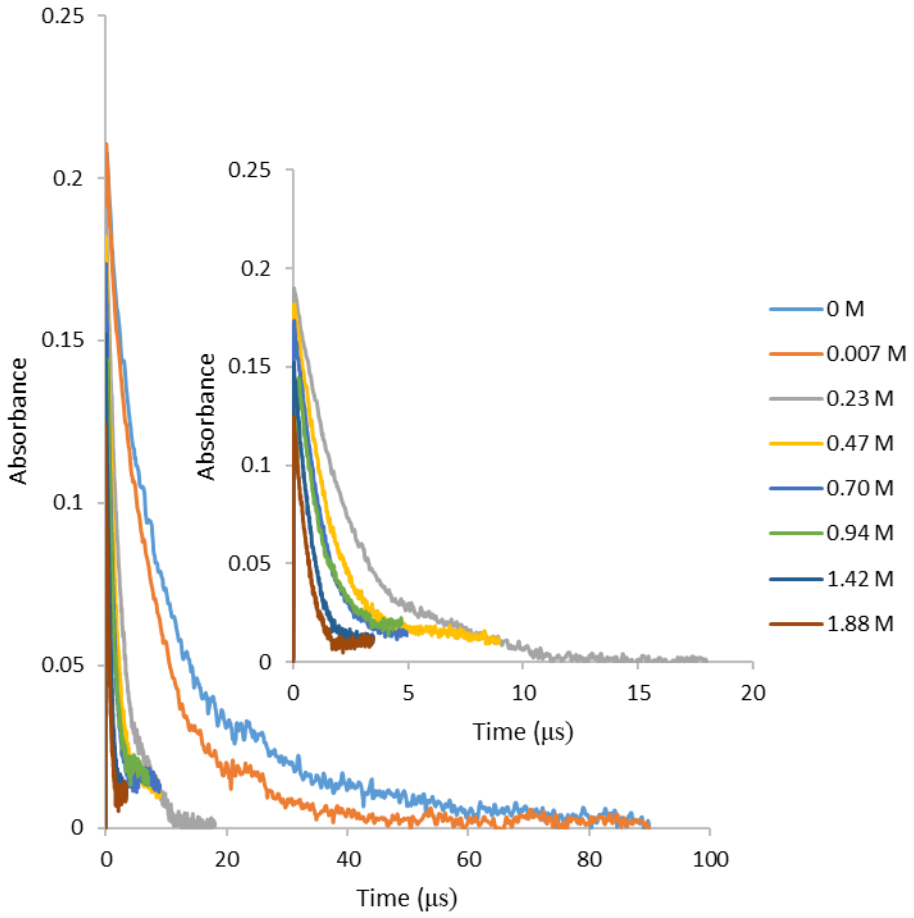

Figure A.60. Transient signal for the decay of $NO_3\cdot$ at 635 nm in the presence of 2-methylpentane in neat CH_3CN generated by laser flash photolysis of 3×10^{-3} mol L^{-1} CKN. The inset depicts a magnified view of the decay profiles for higher concentrations of substrate.

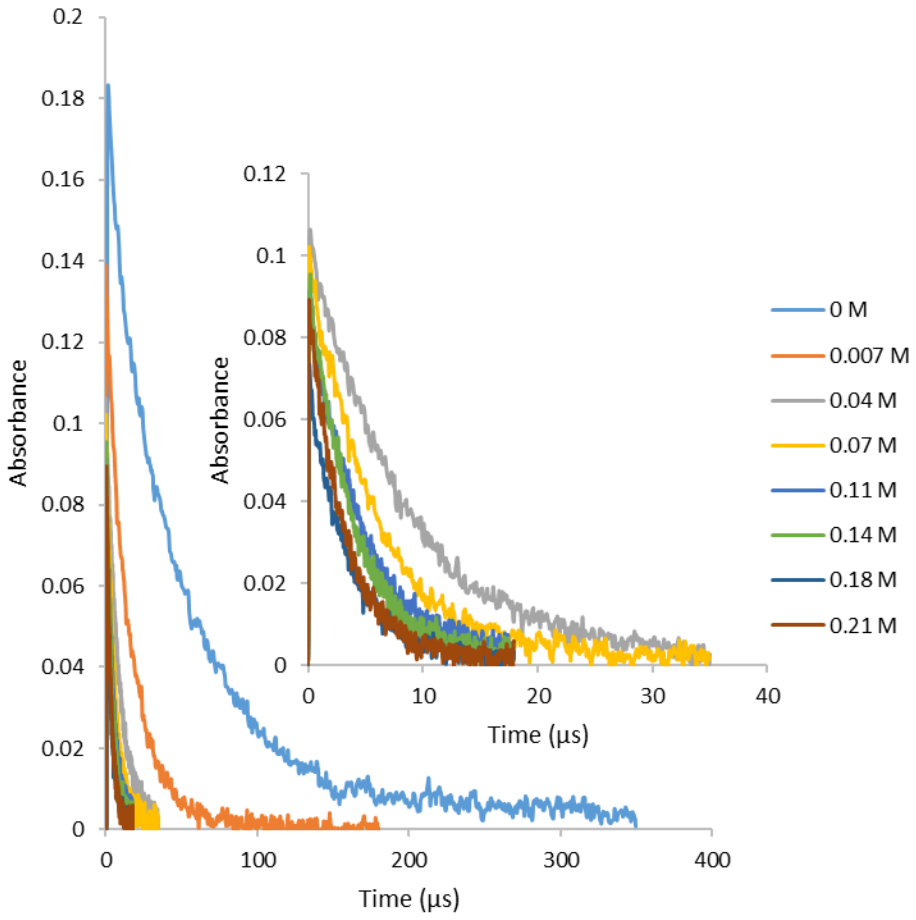

Figure A.61. Transient signal for the decay of $NO_3\cdot$ at 635 nm in the presence of 2-methylpentane in 8:2 CH_3CN/H_2O generated by laser flash photolysis of 3×10^{-3} mol L^{-1} CKN. The inset depicts a magnified view of the decay profiles for higher concentrations of substrate.

Table A.39. Observed rate constants for hydrogen abstraction by $NO_3\cdot$ from various concentrations of 2-methylpentane in CH_3CN at 25 °C

[2-methylpentane], M (CH_3CN)	$k_{obs} \times 10^{-6}$ s
0	0.09 ± 0.00
0.007	0.12 ± 0.01
0.23	0.39 ± 0.02
0.47	0.70 ± 0.02
0.70	0.93 ± 0.02
0.94	1.08 ± 0.04

Table A.40. Observed rate constants for hydrogen abstraction by $NO_3\cdot$ from various concentrations of 2-methylpentane in 8:2 CH_3CN/H_2O at 25 °C

[2-methylpentane], M (8:2 CH_3CN/H_2O)	$k_{obs} \times 10^{-5}$ s
0	0.21 ± 0.01
0.007	0.61 ± 0.06
0.04	1.16 ± 0.01
0.07	1.71 ± 0.07
0.11	2.16 ± 0.21
0.14	2.51 ± 0.11
0.18	2.84 ± 0.11
0.21	3.17 ± 0.12

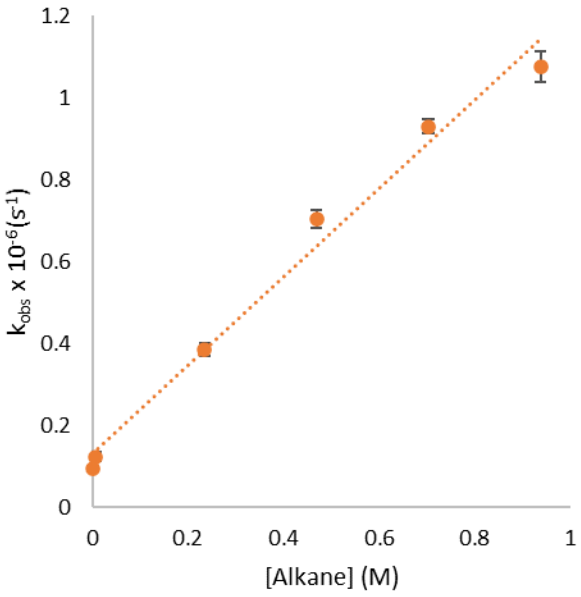

Figure A.62. Plot of the observed rate constant for $NO_3\cdot$ vs. 2-methylpentane concentration in CH_3CN at 25 °C; the slope is equal to the hydrogen abstraction rate constant ($k_{AN} = 1.1 \times 10^6$ $M^{-1}s^{-1}$).

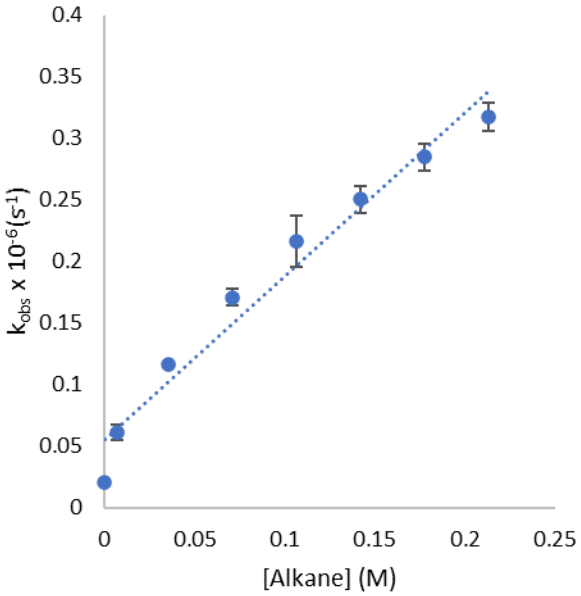

Figure A.63. Plot of the observed rate constant for $NO_3\cdot$ vs. 2-methylpentane concentration in 8:2 CH_3CN/H_2O at 25 °C; the slope is equal to the hydrogen abstraction rate constant ($k_W = 1.3 \times 10^6$ $M^{-1}s^{-1}$).

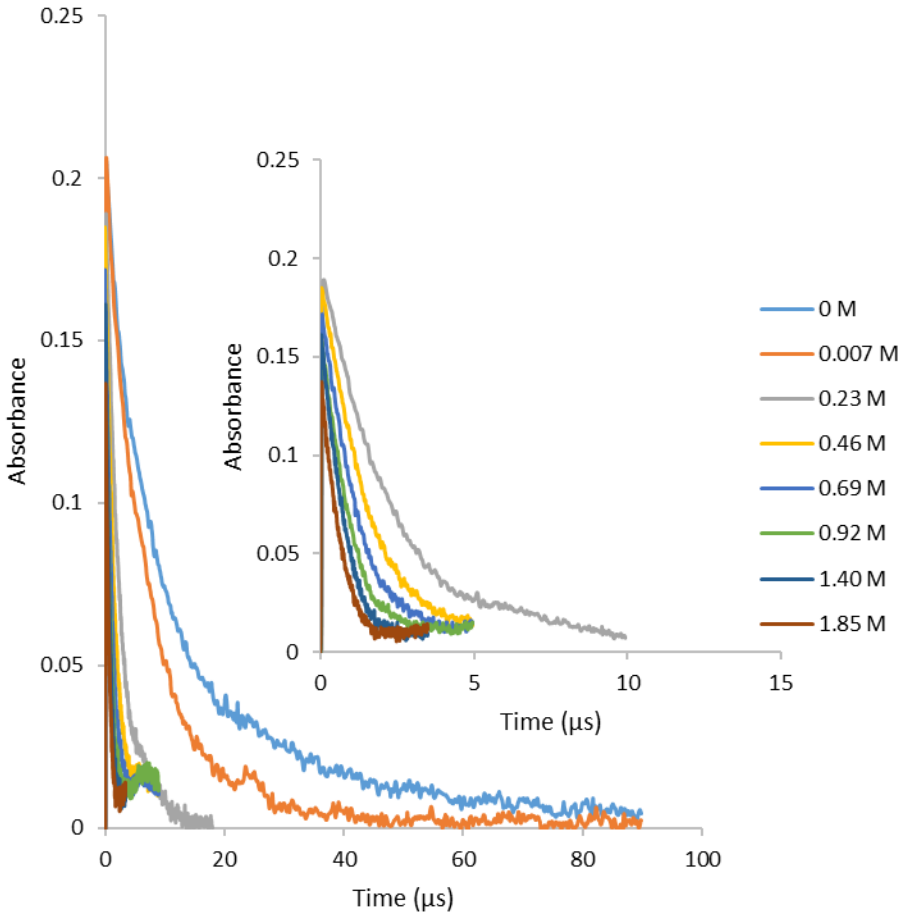

Figure A.64. Transient signal for the decay of $NO_3\cdot$ at 635 nm in the presence of 3-methylpentane in neat CH_3CN generated by laser flash photolysis of 3×10^{-3} mol L^{-1} CKN. The inset depicts a magnified view of the decay profiles for higher concentrations of substrate.

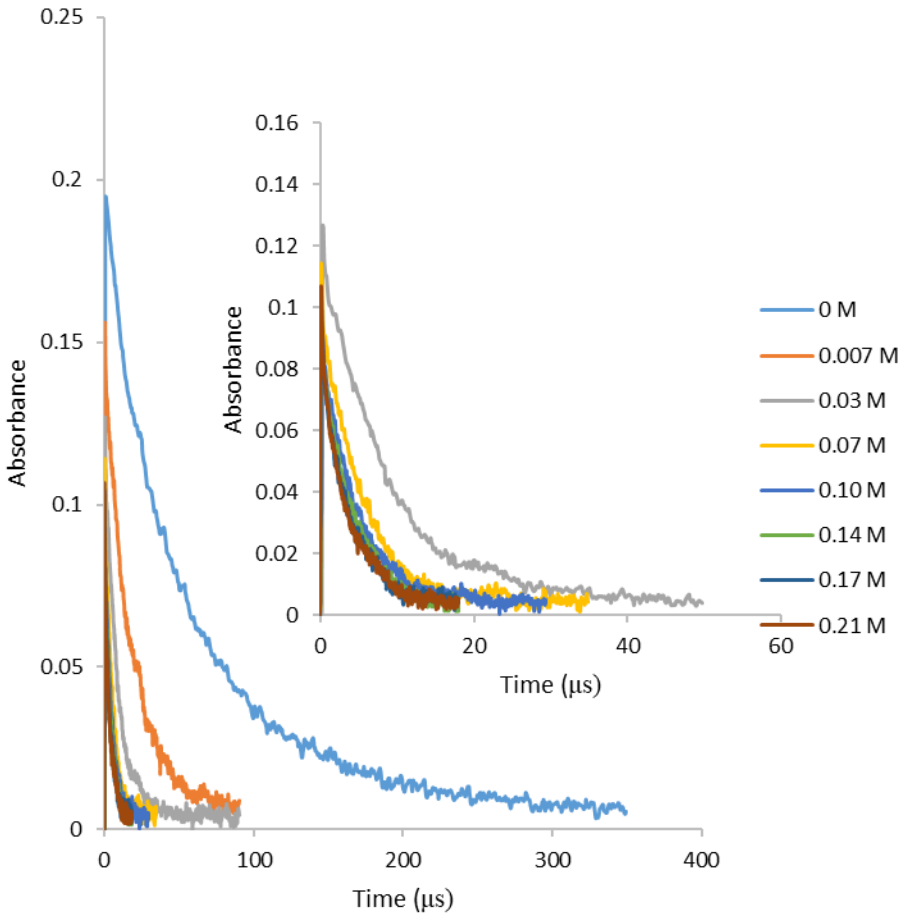

Figure A.65. Transient signal for the decay of $NO_3\cdot$ at 635 nm in the presence of 3-methylpentane in 8:2 CH_3CN/H_2O generated by laser flash photolysis of 3×10^{-3} mol L^{-1} CKN. The inset depicts a magnified view of the decay profiles for higher concentrations of substrate.

Table A.41. Observed rate constants for hydrogen abstraction by $NO_3\cdot$ from various concentrations of 3-methylpentane in CH_3CN at 25 °C

[3-methylpentane], M (CH_3CN)	$k_{obs} \times 10^{-6}$ s
0	0.09 ± 0.00
0.007	0.13 ± 0.00
0.23	0.41 ± 0.02
0.46	0.74 ± 0.05
0.69	0.94 ± 0.03
0.92	1.19 ± 0.03

Table A.42. Observed rate constants for hydrogen abstraction by $NO_3\cdot$ from various concentrations of 3-methylpentane in 8:2 CH_3CN/H_2O at 25 °C

[3-methylpentane], M (8:2 CH_3CN/H_2O)	$k_{obs} \times 10^{-5}$ s
0	0.18 ± 0.03
0.007	0.56 ± 0.05
0.03	1.14 ± 0.07
0.07	1.88 ± 0.12
0.10	2.32 ± 0.07
0.14	2.40 ± 0.26
0.17	2.92 ± 0.20
0.21	2.99 ± 0.39

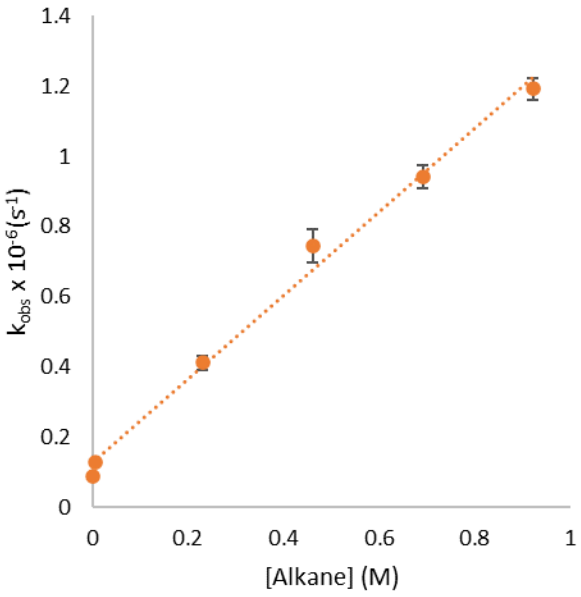

Figure A.66. Plot of the observed rate constant for $NO_3\cdot$ vs. 3-methylpentane concentration in CH_3CN at 25 °C; the slope is equal to the hydrogen abstraction rate constant ($k_{AN} = 1.2 \times 10^6$ $M^{-1}s^{-1}$).

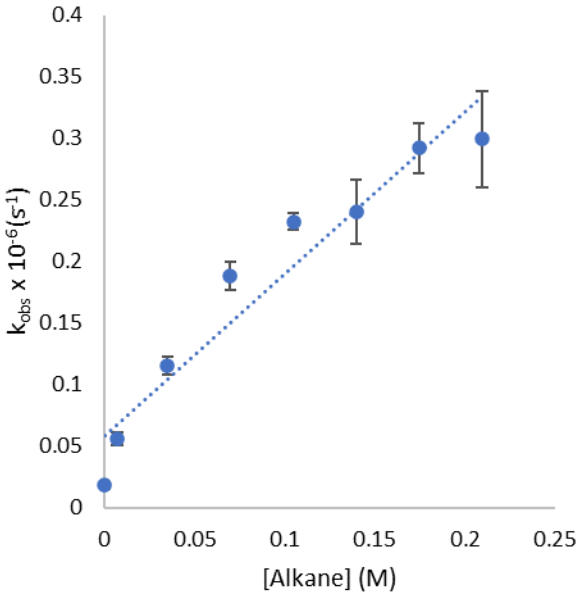

Figure A.67. Plot of the observed rate constant for $NO_3\cdot$ vs. 3-methylpentane concentration in 8:2 CH_3CN/H_2O at 25 °C; the slope is equal to the hydrogen abstraction rate constant ($k_W = 1.3 \times 10^6$ $M^{-1}s^{-1}$).

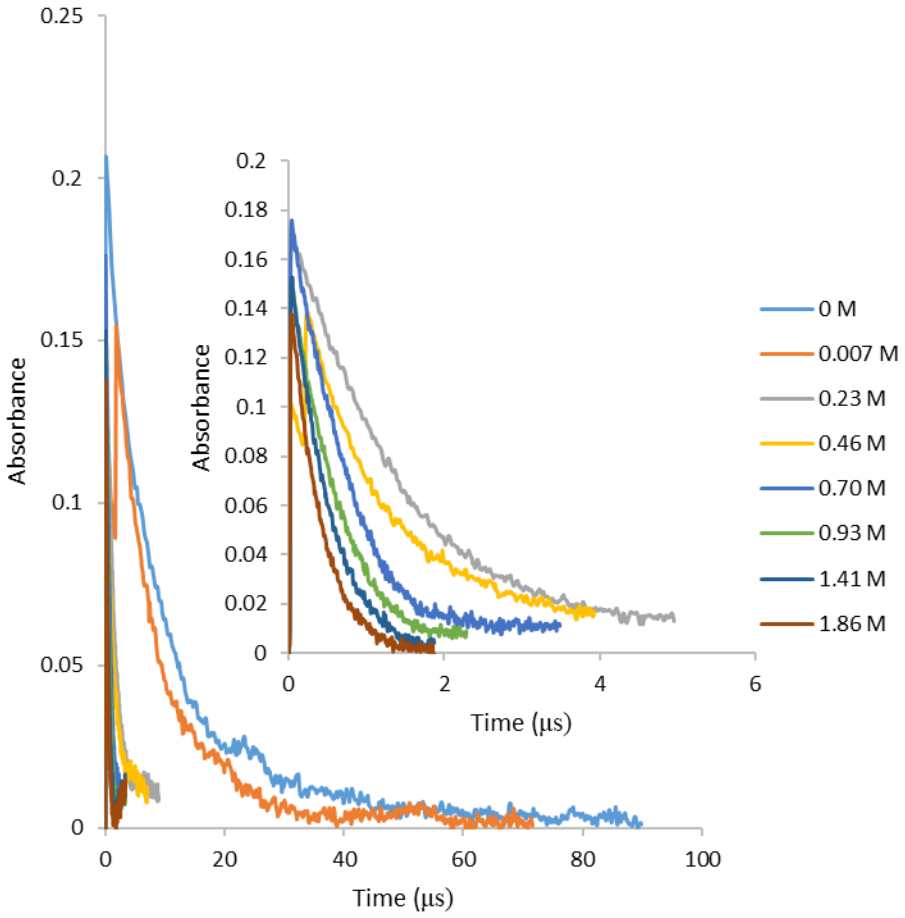

Figure A.68. Transient signal for the decay of $NO_3\cdot$ at 635 nm in the presence of 2,3-dimethylbutane in neat CH_3CN generated by laser flash photolysis of 3×10^{-3} mol L^{-1} CKN. The inset depicts a magnified view of the decay profiles for higher concentrations of substrate.

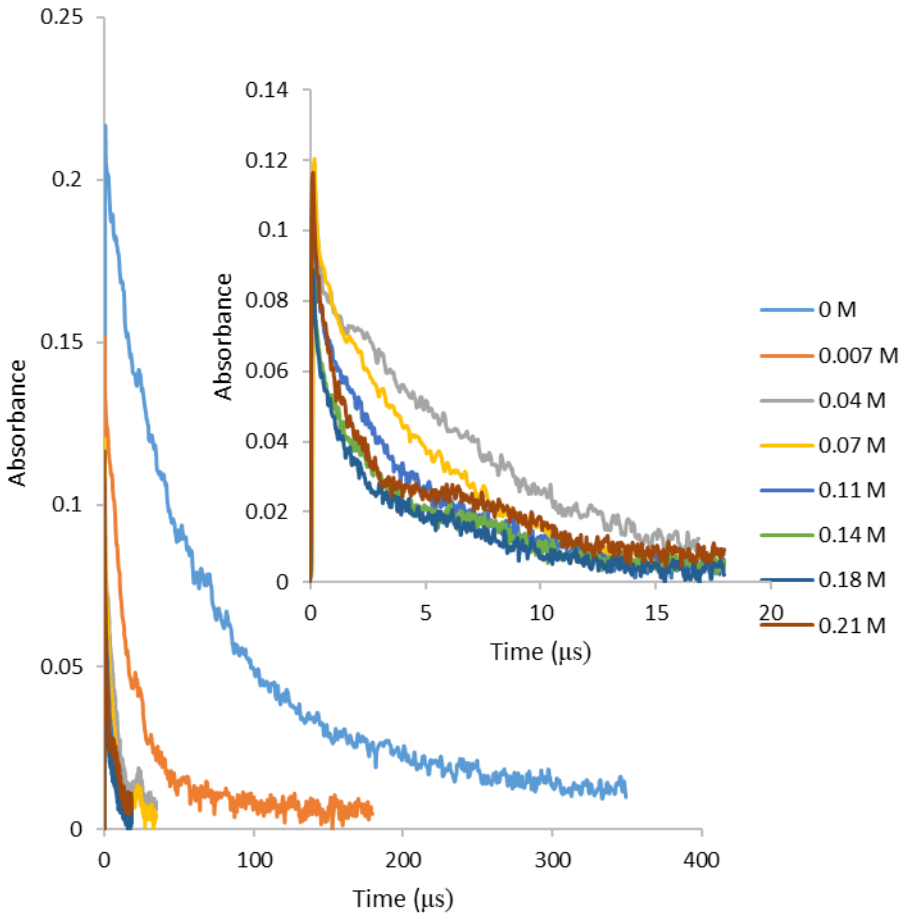

Figure A.69. Transient signal for the decay of $NO_3\cdot$ at 635 nm in the presence of 2,3-dimethylbutane in 8:2 CH_3CN/H_2O generated by laser flash photolysis of 3×10^{-3} mol L^{-1} CKN. The inset depicts a magnified view of the decay profiles for higher concentrations of substrate.

Table A.43. Observed rate constants for hydrogen abstraction by $NO_3\cdot$ from various concentrations of 2,3-dimethylbutane in CH_3CN at 25 °C

[2,3-dimethylbutane], M (CH_3CN)	$k_{obs} \times 10^{-6}$ s
0	0.11 ± 0.02
0.007	0.16 ± 0.02
0.17	0.77 ± 0.02
0.34	1.11 ± 0.07
0.51	1.44 ± 0.03
0.68	1.70 ± 0.08

Table A.44. Observed rate constants for hydrogen abstraction by $NO_3\cdot$ from various concentrations of 2,3-dimethylbutane in 8:2 CH_3CN/H_2O at 25 °C

[2,3-dimethylbutane], M (8:2 CH_3CN/H_2O)	$k_{obs} \times 10^{-5}$ s
0	0.16 ± 0.02
0.007	0.65 ± 0.11
0.06	1.59 ± 0.07
0.12	2.23 ± 0.26
0.22	2.91 ± 0.36
0.33	4.26 ± 1.04
0.43	4.92 ± 1.27
0.54	7.61 ± 1.89

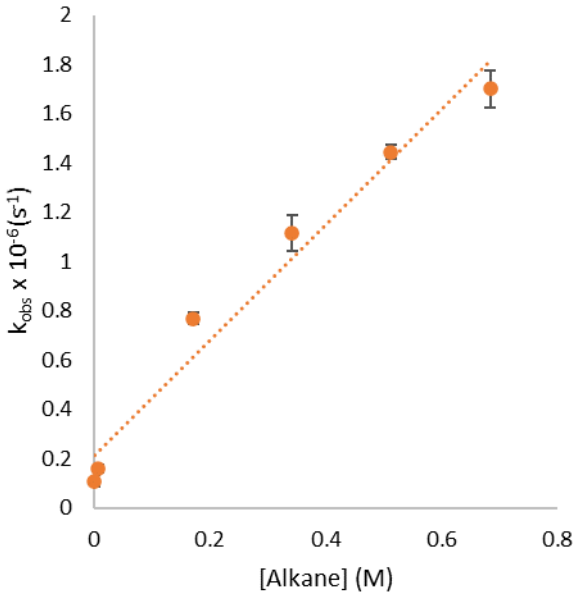

Figure A.70. Plot of the observed rate constant for $NO_3\cdot$ vs. 2,3-dimethylbutane concentration in CH_3CN at 25 °C; the slope is equal to the hydrogen abstraction rate constant ($k_{AN} = 2.3 \times 10^6$ $M^{-1}s^{-1}$).

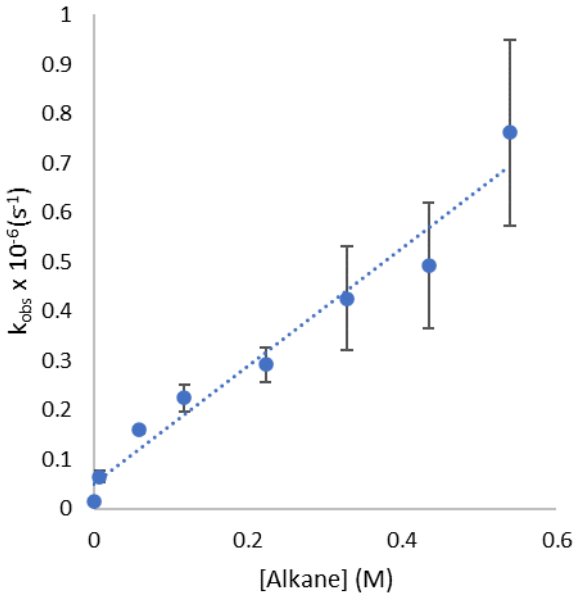

Figure A.71. Plot of the observed rate constant for $NO_3\cdot$ vs. 2,3-dimethylbutane concentration in 8:2 CH_3CN/H_2O at 25 °C; the slope is equal to the hydrogen abstraction rate constant ($k_W = 1.2 \times 10^6$ $M^{-1}s^{-1}$).

Table A.45. The organic solvent rate constant and per-H partial rate constant parameters, the ionization potential, the C-H bond dissociation energies, and the prediction of the rate constant parameter by the modified Evans–Polanyi relationship (Eqn. 2.5); the multiple linear regression analysis of 2.303RT *log*(k_{AN}/H) vs. IP and BDE yielded $\alpha = 0.26 \pm 0.04$, $\beta = 0.04 \pm 0.01$, and $R = 0.920$

Substrate	2.303RT *log* (k_{AN})	2.303RT *log* (k_{AN}/H)	IP (kcal mol^{-1})	α-C-H BDE (kcal mol^{-1})	2.303RT *log* (k_{pred})
Methanol	7.9	7.2	250.6[a]	96.1[b]	7.0
Ethanol	8.9	8.5	242.6[a]	93.0[c]	8.2
Isopropanol	9.2	9.2	234.5[a]	91.7[b]	8.8
Hexane	8.4	7.2	235.0[a]	98.0[b]	7.2
Cyclohexane	8.6	7.1	228.1[a]	99.5[b]	7.1
2-Methylpentane	8.3	8.3	233.3[a]	95.0[b]	8.0
3-Methylpentane	8.3	8.3	232.8[a]	95.0[b]	8.0
2,3-Dimethylbutane	8.7	8.3	231.5[a]	95.0[b]	8.1
Diethyl ether	9.5	8.7	220.6[a]	93.0[b]	9.1
Dipropyl ether	9.8	9.0	217.0[a]	93.0[b]	9.2
Diisopropyl ether	9.8	9.4	212.5[a]	93.4[d]	9.3
Methyl n-propyl ether	9.1	8.7	224.8[a]	93.0[b]	8.9
sec-Butyl methyl ether	9.6	9.6	212.5[a]	93.4	9.3
tert-Butyl methyl ether	8.8	8.2	217.4[a]	95.3[d]	8.4
Tetrahydrofuran	10.2	9.4	216.9[a]	92.1[b]	9.4
1,3-Dioxane	9.1	8.7	233.3[a]	93.4[e]	8.4
1,4-Dioxane	9.1	7.9	217.3[a]	96.9[e]	8.2
1,3,5-Trioxane	7.9	6.8	249.5[a]	93.4[e]	7.8

[a] Reference 1, [b] Reference 2, [c] Reference 3, [d] Reference 4, [e] Reference 5

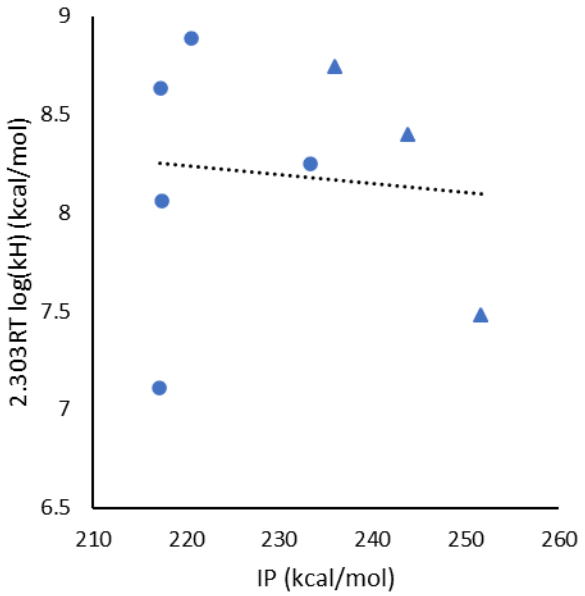

Figure A.72. Reaction of $NO_3\cdot$ with ethers and alcohols in H_2O: Plot of 2.303RT *log*(k_H) vs. the ionization potential of the substrate; ethers (●) and alcohols (▲) by $NO_3\cdot$.

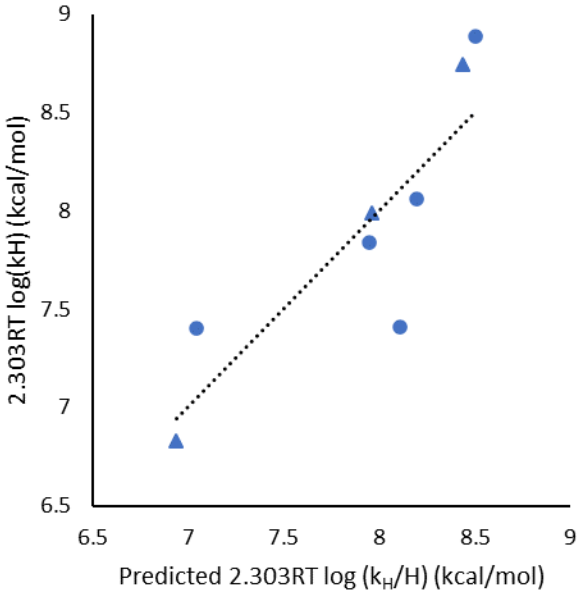

Figure A.73. Reaction of $NO_3\cdot$ with ethers and alcohols in H_2O: Plot of the experimental vs. predicted value of 2.303RT *log*(k_H/H) on the basis of Eq. 5 (a = 0.26, b = 0.04; R = 0.920); ethers (●) and alcohols (▲).

Table A.46. The aqueous rate constant and per-H partial rate constant parameters, the ionization potential, the C-H bond dissociation energies, and the prediction of the rate constant parameter by the modified Evans–Polanyi relationship (Eqn. 5); the multiple linear regression analysis of 2.303RT *log*(k_W/H) vs. IP and BDE yielded $\alpha = 0.30 \pm 0.09$, $\beta = 0.01 \pm 0.01$, and $R = 0.857$

Substrate	2.303RT *log* (k_W)	2.303RT *log* (k_W/H)	IP (kcal mol^{-1})	α-C-H BDE (kcal mol^{-1})	2.303RT *log* (k_{pred})
Methanol	7.5	6.8	250.6[a]	96.1[b]	6.9
Ethanol	8.4	8.0	242.6[a]	93.0[c]	8.0
Isopropanol	8.7	8.7	234.5[a]	91.7[b]	8.4
Diethyl ether	8.9	8.1	220.6[a]	93.0[b]	8.2
tert-Butyl methyl ether	8.1	7.4	217.4[a]	96.1[d]	8.1
Tetrahydrofuran	9.7	8.9	216.9[a]	92.1[b]	8.5
1,3-Dioxane	8.3	7.8	233.3[a]	93.4[e]	7.9
1,4-Dioxane	8.6	7.4	217.3[a]	96.9[e]	7.0

[a] Reference 1, [b] Reference 2, [c] Reference 3, [d] Reference 4, [e] Reference 5

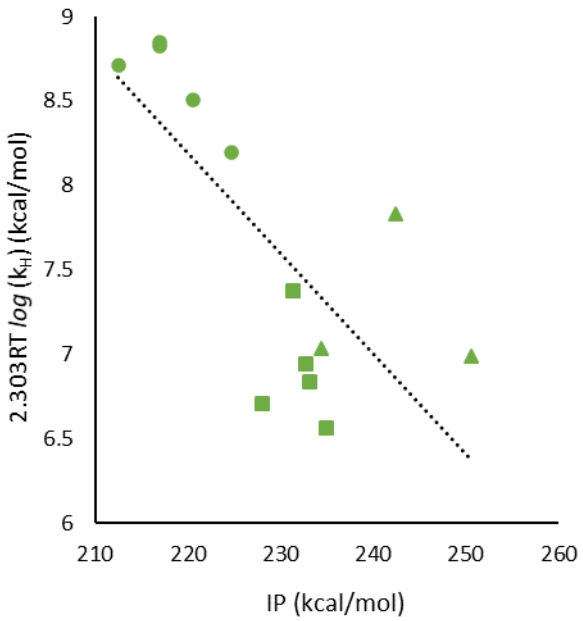

Figure A.74. Reaction of $NO_3\cdot$ with ethers, alkanes, and alcohols in the gas-phase:[6–10] Plot of 2.303RT *log*(k_H) vs. the ionization potential of the substrate; ethers (●), alkanes (■), and alcohols (▲) by $NO_3\cdot$.

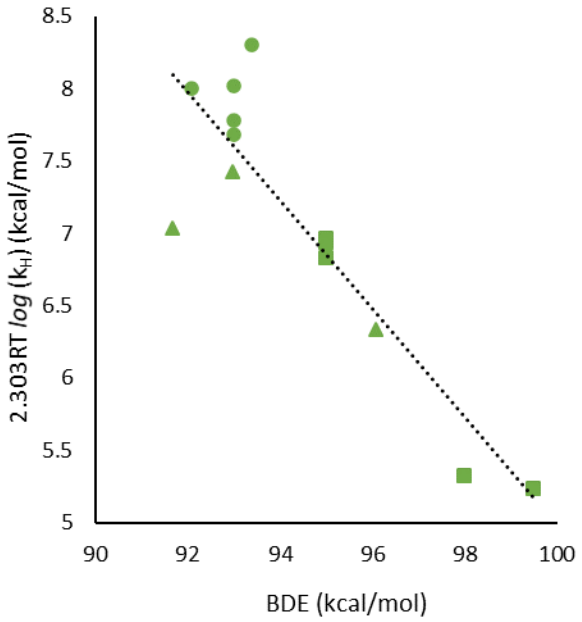

Figure A.75. Reaction of $NO_3\cdot$ with ethers, alkanes, and alcohols in the gas-phase:[6–10] Plot of 2.303RT *log*(k_H/H) vs. the C-H bond dissociation energy. k_H/H is the rate constant for hydrogen abstraction on a per hydrogen basis; ethers (●), alkanes (■), and alcohols (▲).

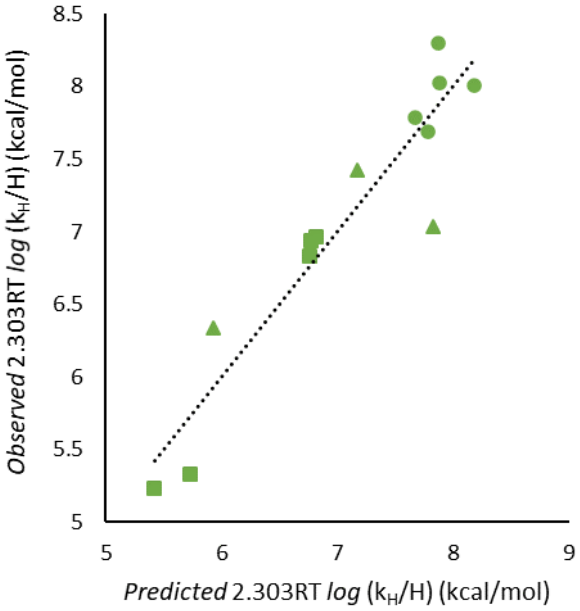

Figure A.76. Reaction of $NO_3\cdot$ with ethers, alkanes, and alcohols in the gas-phase:[6–10] Plot of the experimental vs. predicted value of 2.303RT *log*(k_H/H) on the basis of Eq. 5 (a = 0.30, b = 0.03; R = 0.938); ethers (●), alkanes (■), and alcohols (▲).

Table A.47. The gaseous rate constant and per-H partial rate constant parameters, the ionization potential, the C-H bond dissociation energies, and the prediction of the rate constant parameter by the modified Evans–Polanyi relationship (Eqn. 5); the multiple linear regression analysis of 2.303RT *log*(k_G/H) vs. IP and BDE yielded $\alpha = 0.33 \pm 0.05$, $\beta = 0.03 \pm 0.01$, and R = 0.938

Substrate	2.303RT *log* (k_G)	2.303RT *log* (k_G/H)	IP (kcal mol^{-1})	α-C-H BDE (kcal mol^{-1})	2.303RT *log* (k_{pred})
Methanol	7.0	6.3	250.6[a]	96.1[b]	7.0
Ethanol	7.8	7.4	242.6[a]	93.0[c]	8.2
Isopropanol	7.0	7.0	234.5[a]	91.7[b]	8.8
Hexane	8.5	7.7	235.0[a]	98.0[b]	7.2
Cyclohexane	8.8	8.0	228.1[a]	99.5[b]	7.1
2-Methylpentane	8.2	7.8	233.3[a]	95.0[b]	8.0
3-Methylpentane	8.7	8.3	232.8[a]	95.0[b]	8.0
2,3-Dimethylbutane	8.8	8.0	231.5[a]	95.0[b]	8.1
Diethyl ether	6.6	5.3	220.6[a]	93.0[b]	9.1
Dipropyl ether	6.7	5.2	217.0[a]	93.0[b]	9.2
Diisopropyl ether	6.8	6.8	212.5[a]	93.4[d]	9.3
Methyl n-propyl ether	6.9	6.9	224.8[a]	93.0[b]	8.9
Tetrahydrofuran	7.4	7.0	216.9[a]	92.1[b]	9.4

[a] Reference 1, [b] Reference 2, [c] Reference 3, [d] Reference 4, [e] Reference 6, [f] Reference 7, [g] Reference 8, [h] Reference 9, [I] Reference 10

References

(1) Lias, S. G.; Bartmess, J. E.; Liebman, J. F.; Holmes, J. L.; Levin, R. D.; Mallard, W. G. "Ion Energetics Data." In *NIST Chemistry WebBook NIST Standard Reference Database Number 69*; Linstrom, P. J., Mallard, W. G., Eds.; Gaithersburg MD, 20899. https://doi.org/10.18434/T4D303.

(2) Luo, Y. R. *Comprehensive Handbook of Chemical Bond Energies*, 1st Ed.; CRC Press: Boca Raton, 2007. https://doi.org/10.1201/9781420007282.

(3) Alfassi, Z. B.; Golden, D. M. The Bond Dissociation Energy of the C-H Bond in Ethanol. A Kinetic Study of the Reaction I2 + Ethanol. *J. Phys. Chem.* **1972**, *76* (23), 3314–3319.

(4) Hoshino, H.; Sakakibara, K.; Watanabe, K. Autoxidation Resistant Cyclopentyl Methyl Ether. *Chem. Lett.* **2008**, *37* (7), 774–775.

(5) Przybylak, K. R.; Cronin, M. T. D. Correlation between Bond Dissociation Energies and Spin Distribution for the Radicals of Ethers: A DFT Study. *J. Mol. Struct. THEOCHEM* **2010**, *955* (1–3), 165–170.

(6) Wayne, R. P.; Barnes, I.; Biggs, P.; Burrows, J. P.; Canosa-Mas, C. E.; Hjorth, J.; Le Bras, G.; Moortgat, G. K.; Perner, D.; Poulet, G.; Restelli, G.; Sidebottom, H. The Nitrate

Radical: Physics, Chemistry, and the Atmosphere. *Atmos. Environ. Part A, Gen. Top.* **1991**, *25* (1), 1–203.

(7) Alfassi, Z. B.; Padmaja, S.; Neta, P.; Huie, R. E. Rate Constants for Reactions of NO3• Radicals with Organic Compounds in H2O and CH3CN. *J. Phys. Chem.* **1993**, *97* (15), 3780–3782.

(8) Atkinson, R.; Aschmann, S. M.; Goodman, M. A. Kinetics of the Gas-phase Reactions of NO3 Radicals with a Series of Alkynes, Haloalkenes, and α,B-unsaturated Aldehydes. *Int. J. Chem. Kinet.* **1987**, *19* (4), 299–307.

(9) Zhu, J.; Wang, S.; Tsona, N. T.; Jiang, X.; Wang, Y.; Ge, M.; Du, L. Gas-Phase Reaction of Methyl n-Propyl Ether with OH, NO3, and Cl: Kinetics and Mechanism. *J. Phys. Chem. A* **2017**, *121* (36), 6800–6809.

(10) Aschmann, S. M.; Atkinson, R. Rate Constants for the Reactions of the NO3 Radical with Alkanes at 296 ± 2 K. *Atmos. Environ.* **1995**, *29* (17), 2311–2316.

Appendix B

Mechanism and Kinetics of the Reaction of Nitrate Radical with Caroboxylic Acids
*Mark Paradzinsky, Aditya Ponukumati, and James M. Tanko**

Contents

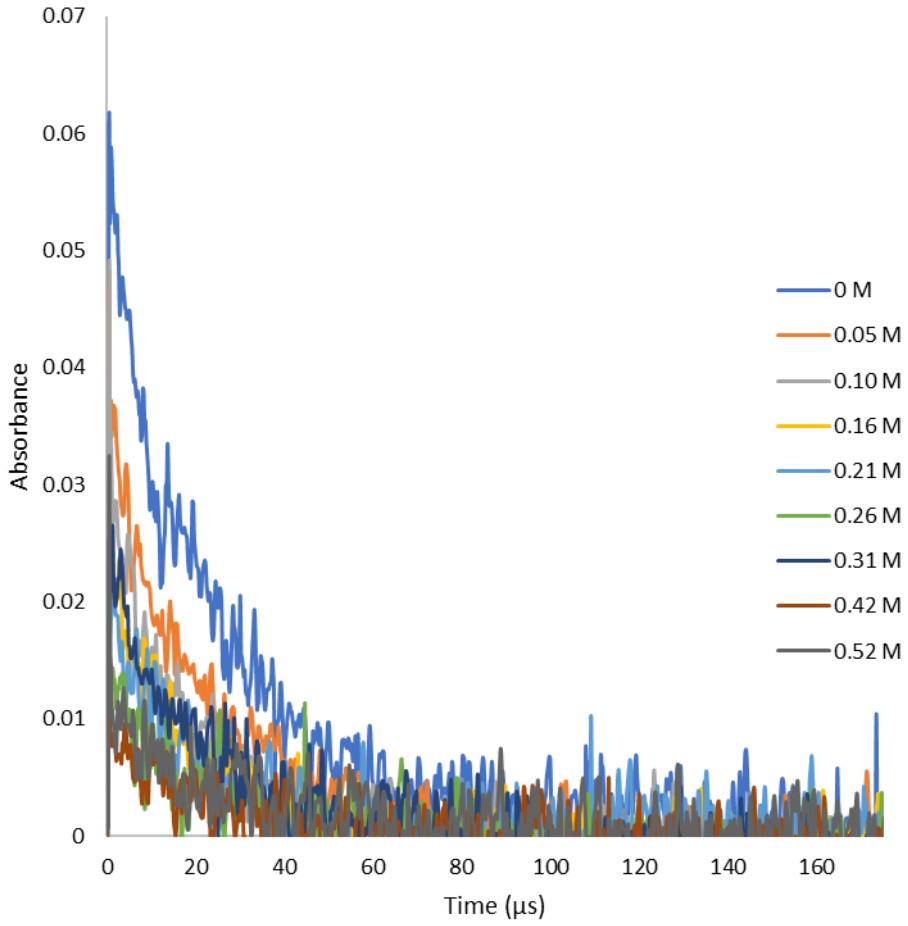

Figure B.19. Transient signal for the decay of $NO_3\cdot$ at 635 nm in the presence formic-d_1 acid in neat CH_3CN generated by laser flash photolysis of 3×10^{-4} mol L^{-1} CAN.

Table B.16. Observed rate constants for hydrogen abstraction by $NO_3\cdot$ from various concentrations of formic-d_1 acid in CH_3CN at 25 °C

[formic-d_1 acid], M (CH_3CN)	$k_{obs} \times 10^{-4}$ s
0	4.19
0.05	4.14
0.10	5.49
0.16	4.32
0.21	5.06
0.26	3.90
0.31	3.74
0.42	3.50
0.52	3.63

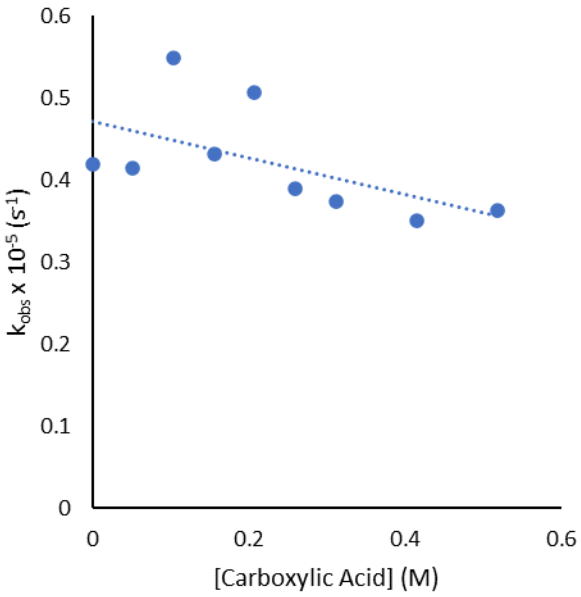

Figure B.20. Plot of the observed rate constant for $NO_3\cdot$ vs. formic–d_1 acid concentration in CH_3CN at 25 °C ($k_{AN} = 0.4 \times 10^{-5}$ M s).

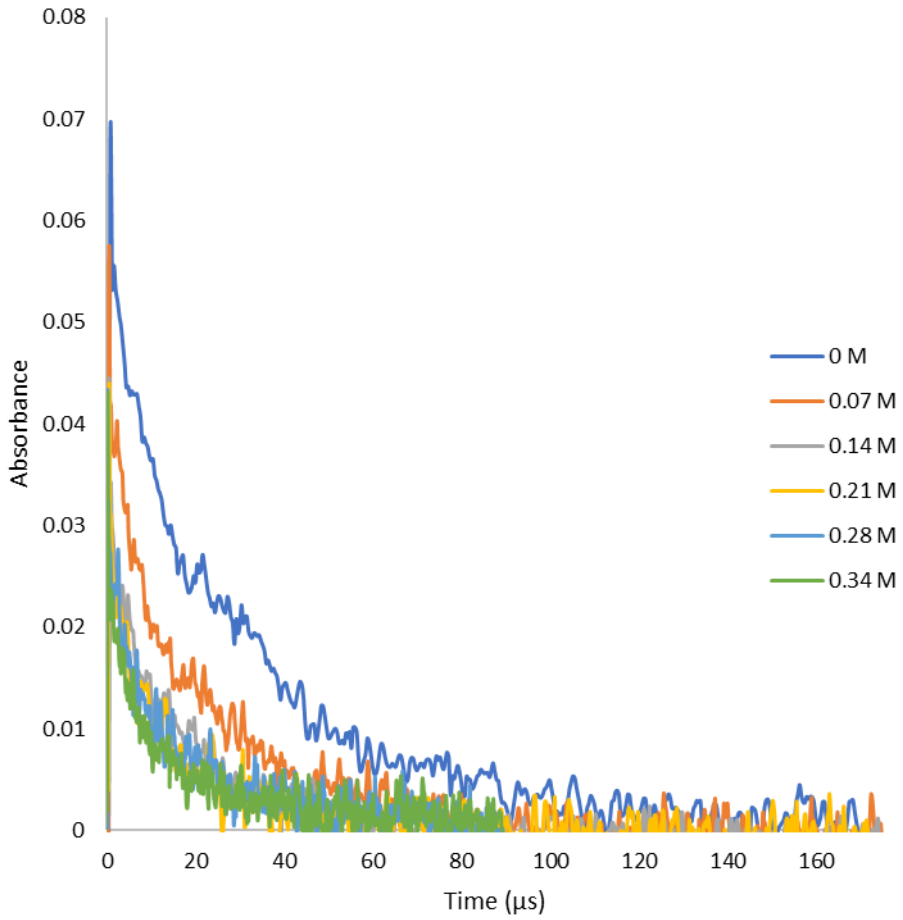

Figure B.21. Transient signal for the decay of $NO_3\cdot$ at 635 nm in the presence of acetic acid–d_1 in neat CH_3CN generated by laser flash photolysis of 3×10^{-4} mol L^{-1} CAN.

Table B.17. Observed rate constants for hydrogen abstraction by $NO_3\cdot$ from various concentrations of acetic acid–d_1 in CH_3CN at 25 °C

[acetic acid–d_1], M (CH_3CN)	$k_{obs} \times 10^{-4}$ s
0	2.96 ± 0.27
0.07	4.57 ± 0.61
0.14	5.55 ± 0.41
0.21	6.16 ± 0.39
0.28	7.75 ± 0.68
0.34	9.77 ± 1.62

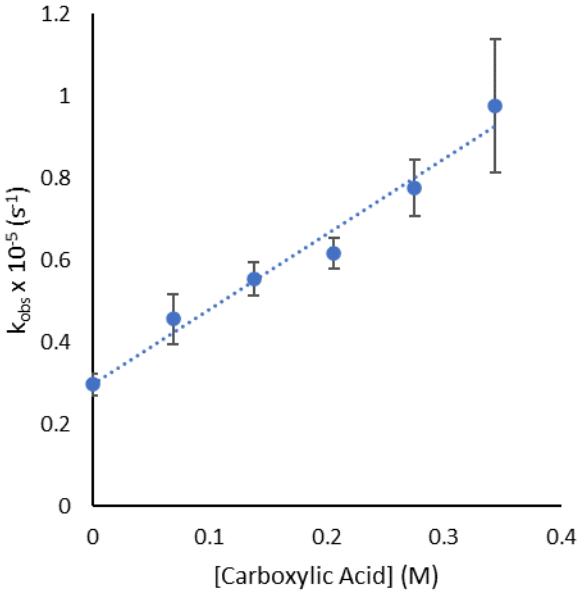

Figure B.22. Plot of the observed rate constant for $NO_3\cdot$ vs. acetic acid–d_3 concentration in CH_3CN at 25 °C ($k_{AN} = 1.8 \times 10^{-5}$ M s).

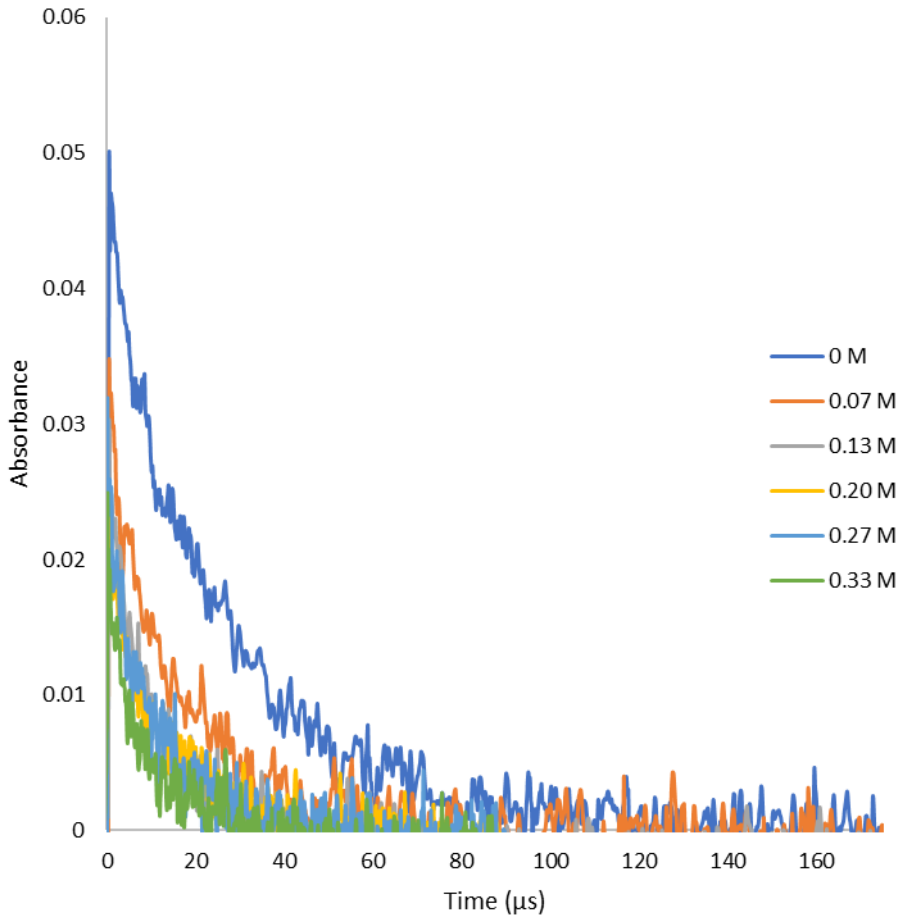

Figure B.23. Transient signal for the decay of $NO_3\cdot$ at 635 nm in the presence of acetic-2,2,2–d_3 acid in neat CH_3CN generated by laser flash photolysis of 3×10^{-4} mol L^{-1} CAN.

Table B.18. Observed rate constants for hydrogen abstraction by $NO_3\cdot$ from various concentrations of acetic-2,2,2–d_3 acid in CH_3CN at 25 °C

[acetic-2,2,2–d_3 acid], M (CH_3CN)	$k_{obs} \times 10^{-4}$ s
0	3.73 ± 0.45
0.07	5.24 ± 0.75
0.13	6.16 ± 1.16
0.20	6.89 ± 0.52
0.27	8.87 ± 0.72
0.33	9.59 ± 0.62

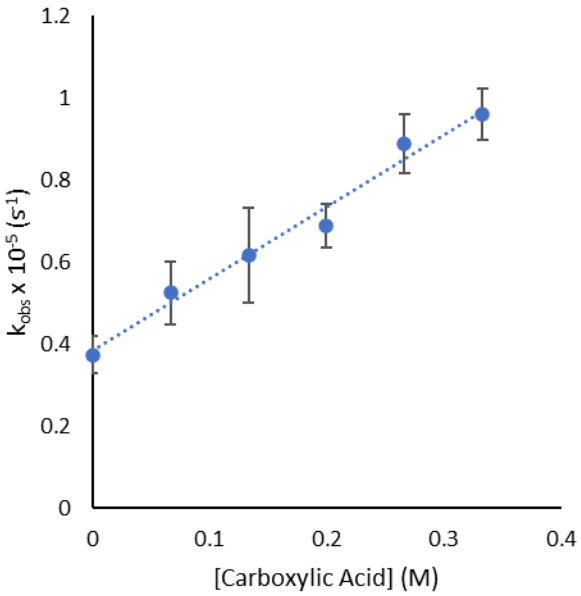

Figure B.24. Plot of the observed rate constant for $NO_3\cdot$ vs. acetic-2,2,2–d_3 acid concentration in CH_3CN at 25 °C ($k_{AN} = 1.8 \times 10^{-5}$ M s).

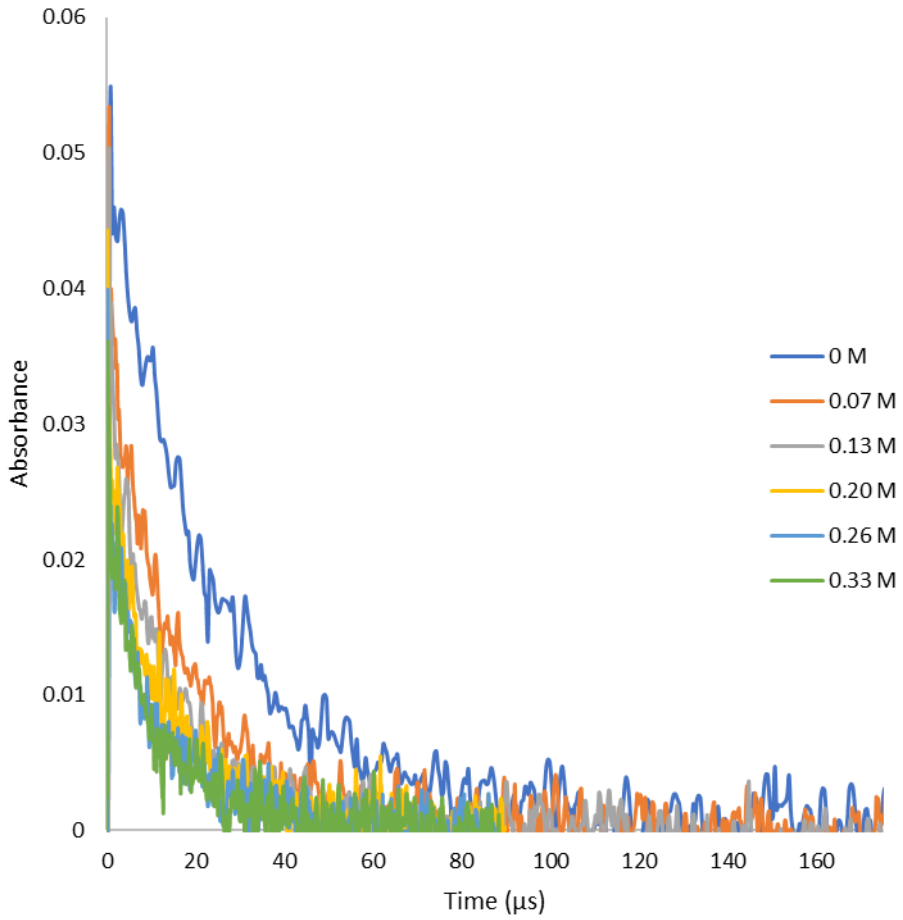

Figure B.25. Transient signal for the decay of $NO_3\cdot$ at 635 nm in the presence of acetic acid–d_4 in neat CH_3CN generated by laser flash photolysis of 3×10^{-4} mol L^{-1} CAN.

Table B.19. Observed rate constants for hydrogen abstraction by $NO_3\cdot$ from various concentrations of acetic acid–d_4 in CH_3CN at 25 °C

[acetic acid–d_4], M (CH_3CN)	$k_{obs} \times 10^{-4}$ s
0	4.15 ± 0.54
0.07	5.98 ± 0.24
0.13	6.99 ± 0.69
0.20	8.26 ± 0.59
0.26	8.70 ± 0.18
0.33	10.15 ± 0.67

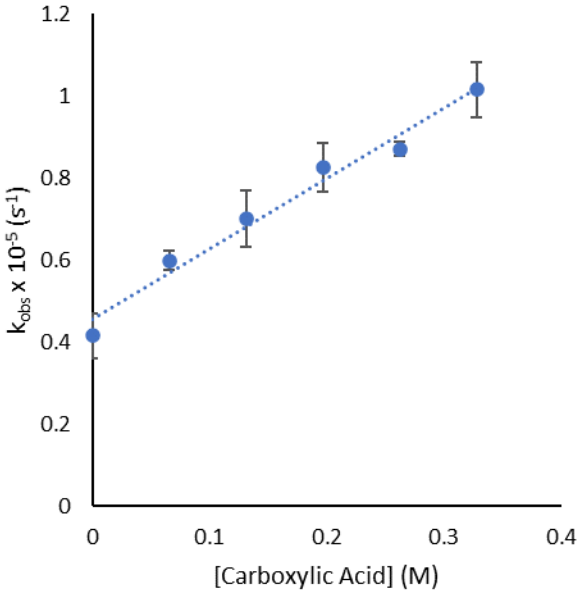

Figure B.26. Plot of the observed rate constant for $NO_3\cdot$ vs. acetic acid–d_4 concentration in CH_3CN at 25 °C ($k_{AN} = 1.7 \times 10^{-5}$ M s).

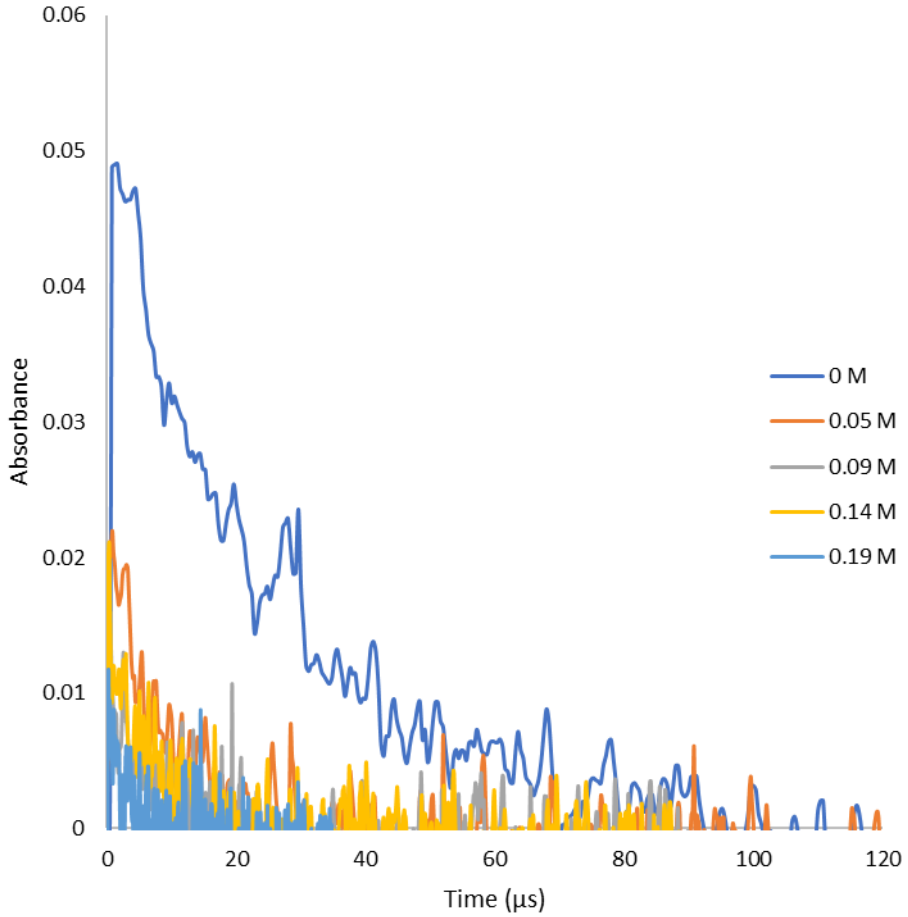

Figure B.27. Transient signal for the decay of $NO_3\cdot$ at 635 nm in the presence 3,3-dimethylbutyric acid–d_1 in neat CH_3CN generated by laser flash photolysis of 3×10^{-4} mol L^{-1} CAN.

Table B.20. Observed rate constants for hydrogen abstraction by $NO_3\cdot$ from various concentrations of 3,3-dimethylbutyric acid–d_1 in CH_3CN at 25 °C

[3,3-dimethylbutyric acid–d_1], M (CH_3CN)	$k_{obs} \times 10^{-4}$ s
0	2.79
0.05	7.15
0.09	10.13
0.14	11.99
0.19	21.80

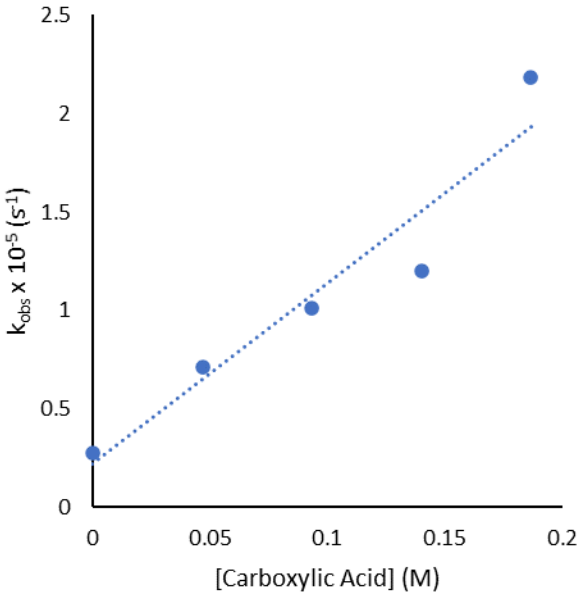

Figure B.28. Plot of the observed rate constant for $NO_3\cdot$ vs. 3,3-dimethylbutyric acid–d_1 concentration in CH_3CN at 25 °C; the slope is equal to the hydrogen abstraction rate constant ($k_{AN} = 9.2 \times 10^{-5}$ M s).

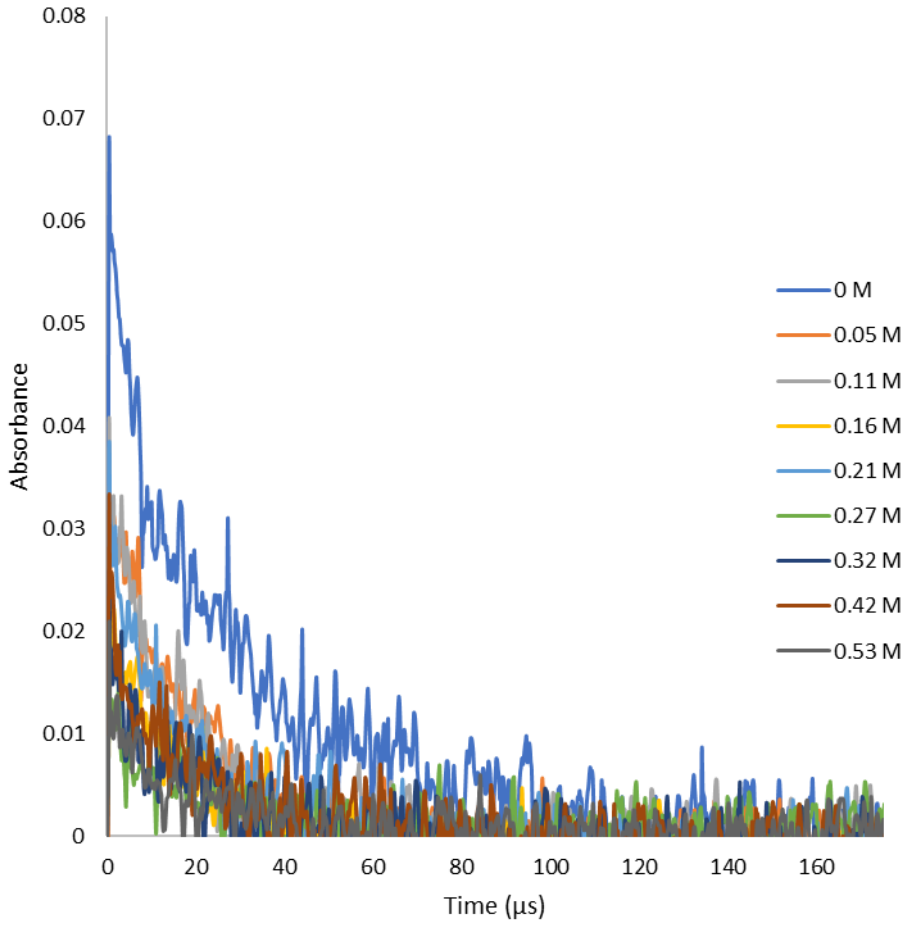

Figure B.29. Transient signal for the decay of $NO_3\cdot$ at 635 nm in the presence formic acid in neat CH_3CN generated by laser flash photolysis of 3×10^{-4} mol L^{-1} CAN.

Table B.21. Observed rate constants for hydrogen abstraction by $NO_3\cdot$ from various concentrations of formic acid in CH_3CN at 25 °C

[formic acid], M (CH_3CN)	$k_{obs} \times 10^{-4}$ s
0	3.47
0.05	4.63
0.11	5.31
0.16	5.14
0.21	4.76
0.27	5.54
0.32	4.59
0.42	4.54
0.53	5.77

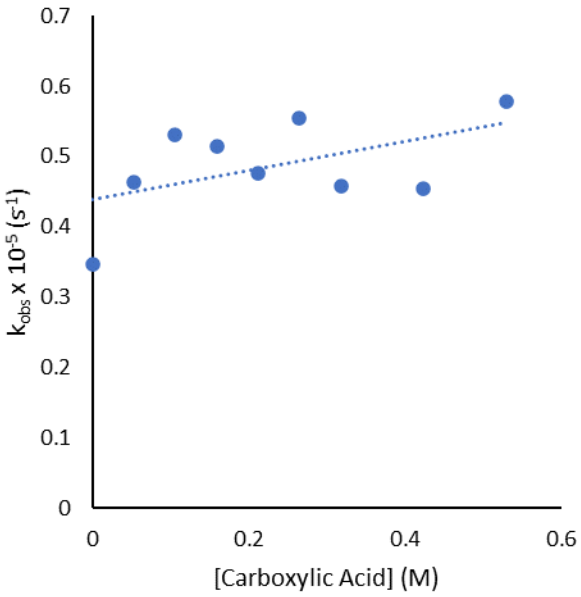

Figure B.30. Plot of the observed rate constant for $NO_3\cdot$ vs. formic acid concentration in CH_3CN at 25 °C ($k_{AN} = 0.5 \times 10^{-5}$ M s).

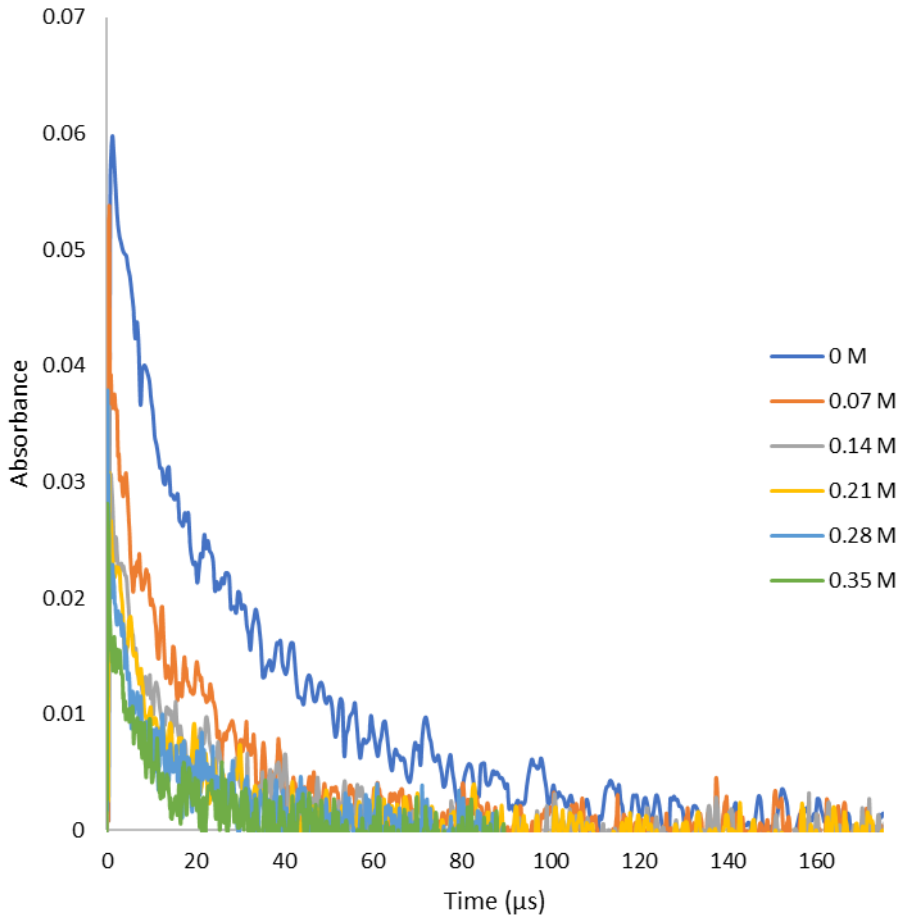

Figure B.31. Transient signal for the decay of $NO_3\cdot$ at 635 nm in the presence of acetic acid in neat CH_3CN generated by laser flash photolysis of 3×10^{-4} mol L^{-1} CAN.

Table B.22. Observed rate constants for hydrogen abstraction by $NO_3\cdot$ from various concentrations of acetic acid in CH_3CN at 25 °C

[acetic acid], M (CH_3CN)	$k_{obs} \times 10^{-4}$ s
0	2.86 ± 0.47
0.07	5.44 ± 0.26
0.14	5.92 ± 0.35
0.21	6.61 ± 0.36
0.28	8.04 ± 0.89
0.35	9.40 ± 0.11

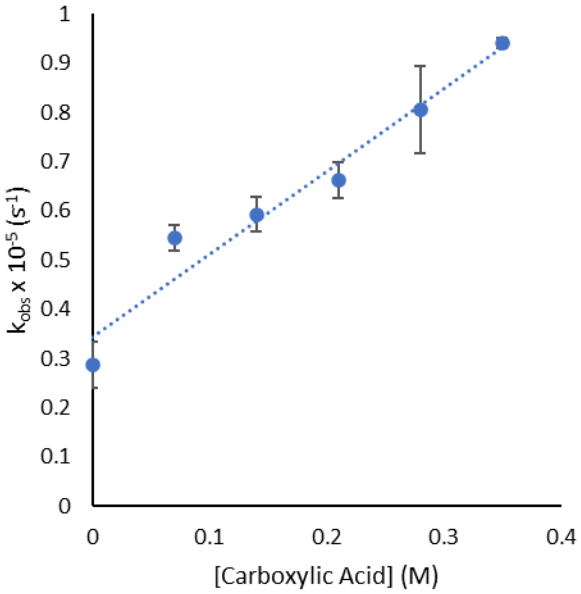

Figure B.32. Plot of the observed rate constant for $NO_3\cdot$ vs. acetic acid concentration in CH_3CN at 25 °C ($k_{AN} = 1.7 \times 10^{-5}$ M s).

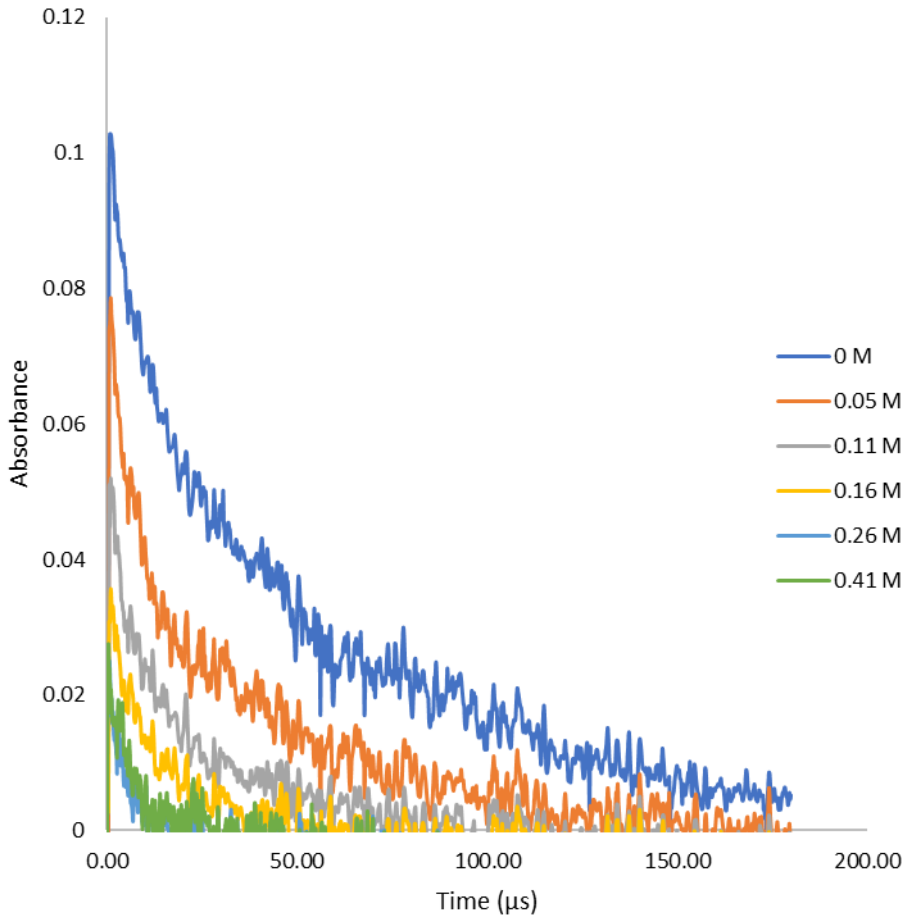

Figure B.33. Transient signal for the decay of $NO_3\cdot$ at 635 nm in the presence propionic acid in neat CH_3CN generated by laser flash photolysis of 3×10^{-4} mol L^{-1} CAN.

Table B.23. Observed rate constants for hydrogen abstraction by $NO_3\cdot$ from various concentrations of propionic acid in CH_3CN at 25 °C

[propionic acid], M (CH_3CN)	$k_{obs} \times 10^{-4}$ s
0	2.13 ± 0.04
0.05	3.61 ± 0.09
0.11	4.77 ± 0.12
0.16	5.58 ± 0.16
0.26	7.12 ± 0.27
0.41	11.42 ± 0.48

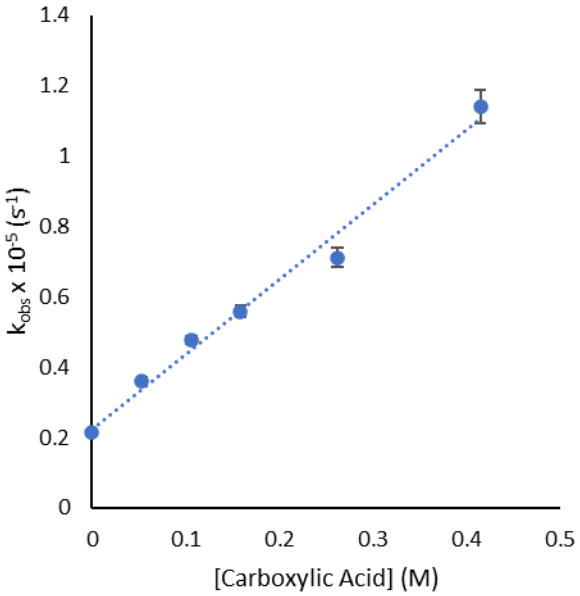

Figure B.34. Plot of the observed rate constant for $NO_3\cdot$ vs. propionic acid concentration in CH_3CN at 25 °C; the slope is equal to the hydrogen abstraction rate constant ($k_{AN} = 2.1 \times 10^{-5}$ M s).

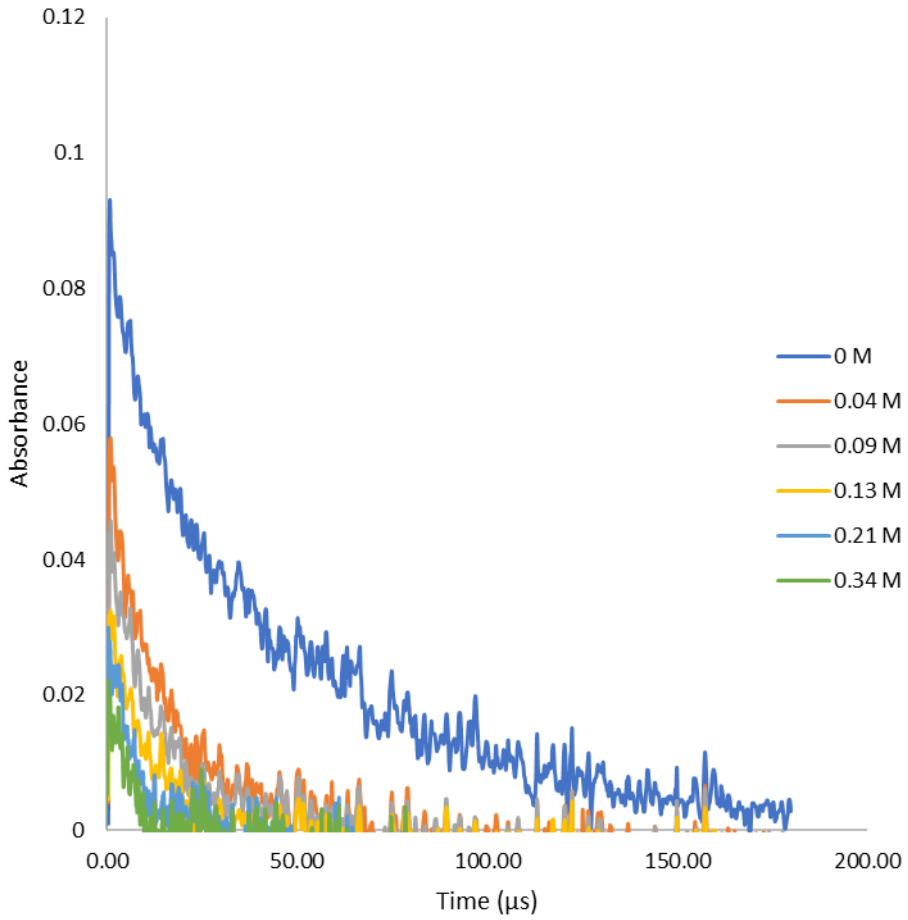

Figure B.35. Transient signal for the decay of $NO_3\cdot$ at 635 nm in the presence butyric acid in neat CH_3CN generated by laser flash photolysis of 3×10^{-4} mol L^{-1} CAN.

Table B.24. Observed rate constants for hydrogen abstraction by $NO_3\cdot$ from various concentrations of butyric acid in CH_3CN at 25 °C

[butyric acid], M (CH_3CN)	$k_{obs} \times 10^{-4}$ s
0	2.47 ± 0.05
0.04	5.45 ± 0.12
0.09	5.76 ± 0.15
0.13	7.08 ± 0.22
0.21	9.46 ± 0.29
0.34	12.47 ± 0.86

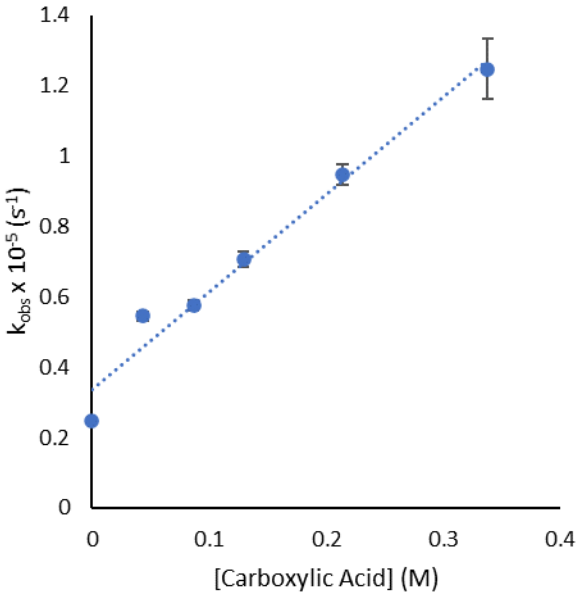

Figure B.36. Plot of the observed rate constant for $NO_3\cdot$ vs. butyric acid concentration in CH_3CN at 25 °C; the slope is equal to the hydrogen abstraction rate constant ($k_{AN} = 2.8 \times 10^{-5}$ M s).

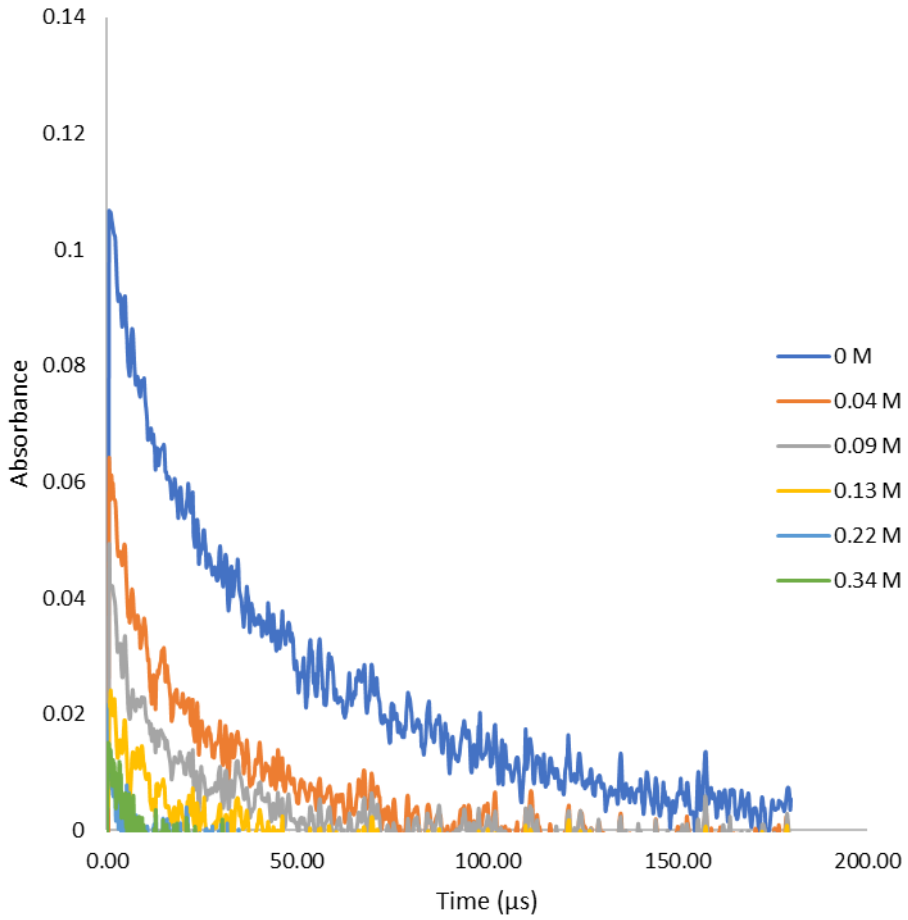

Figure B.37. Transient signal for the decay of $NO_3\cdot$ at 635 nm in the presence 2-methylpropanoic acid in neat CH_3CN generated by laser flash photolysis of 3×10^{-4} mol L^{-1} CAN.

Table B.25. Observed rate constants for hydrogen abstraction by $NO_3\cdot$ from various concentrations of 2-methylpropanoic acid in CH_3CN at 25 °C

[2-methylpropanoic acid], M (CH_3CN)	$k_{obs} \times 10^{-4}$ s
0	2.59 ± 0.05
0.04	3.77 ± 0.09
0.09	5.17 ± 0.13
0.13	7.10 ± 0.16
0.22	7.55 ± 0.25
0.34	14.39 ± 0.54

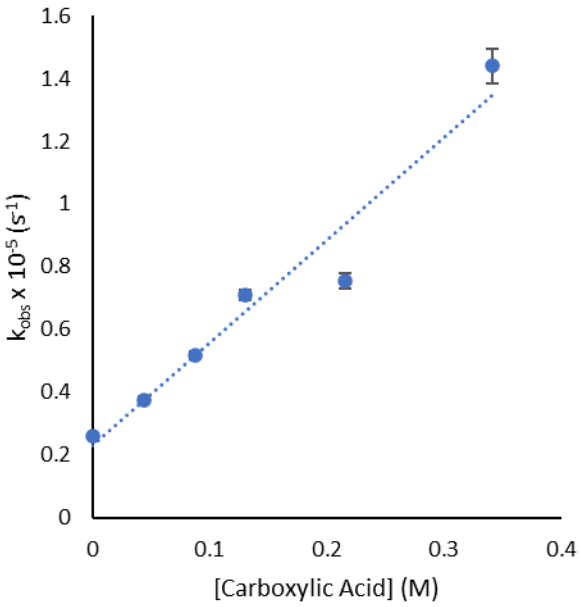

Figure B.38. Plot of the observed rate constant for $NO_3\cdot$ vs. 2-methylpropanoic acid concentration in CH_3CN at 25 °C; the slope is equal to the hydrogen abstraction rate constant ($k_{AN} = 3.3 \times 10^{-5}$ M s).

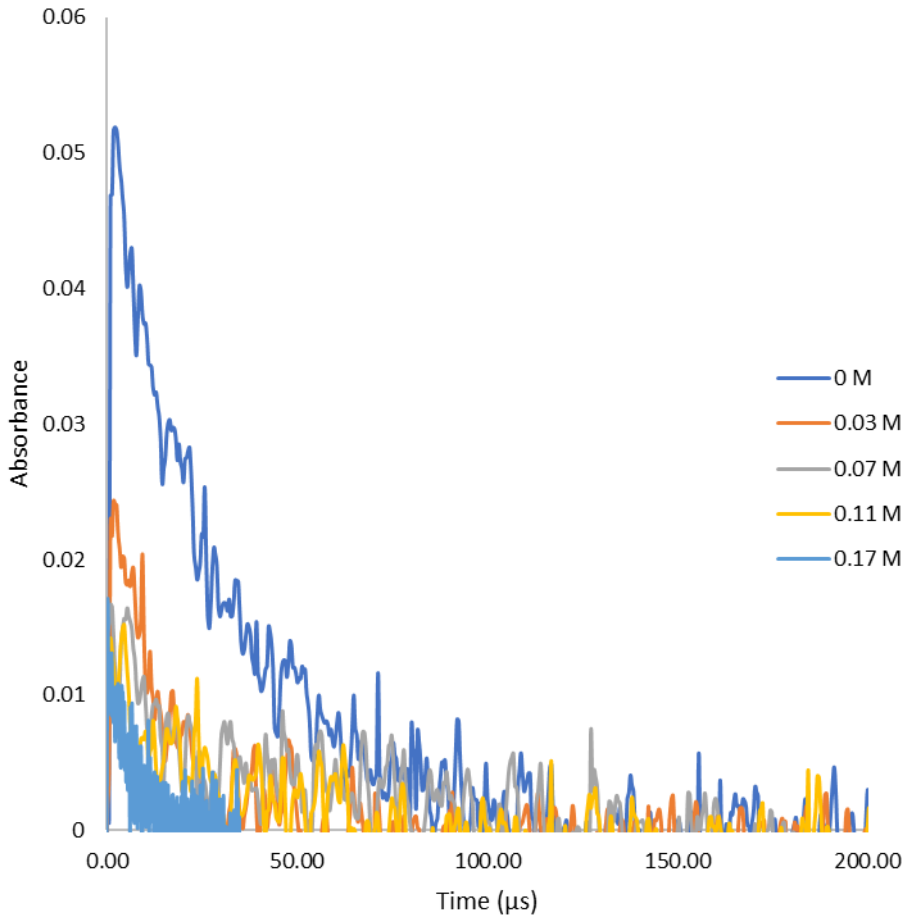

Figure B.39. Transient signal for the decay of $NO_3\cdot$ at 635 nm in the presence pivalic acid in neat CH_3CN generated by laser flash photolysis of 3×10^{-4} mol L^{-1} CAN.

Table B.26. Observed rate constants for hydrogen abstraction by $NO_3\cdot$ from various concentrations of pivalic acid in CH_3CN at 25 °C

[pivalic acid], M (CH_3CN)	$k_{obs} \times 10^{-4}$ s
0	2.87 ± 0.06
0.03	5.55 ± 0.24
0.07	8.18 ± 0.39
0.11	11.33 ± 0.48
0.17	17.40 ± 1.18

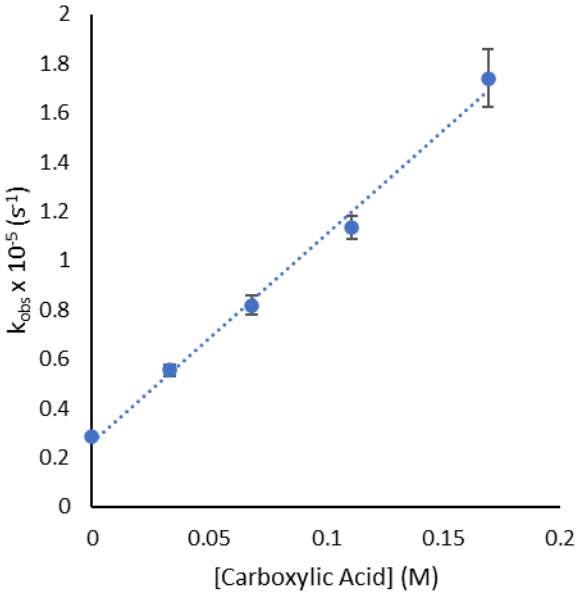

Figure B.40. Plot of the observed rate constant for $NO_3\cdot$ vs. pivalic acid concentration in CH_3CN at 25 °C; the slope is equal to the hydrogen abstraction rate constant ($k_{AN} = 8.4 \times 10^{-5}$ M s).

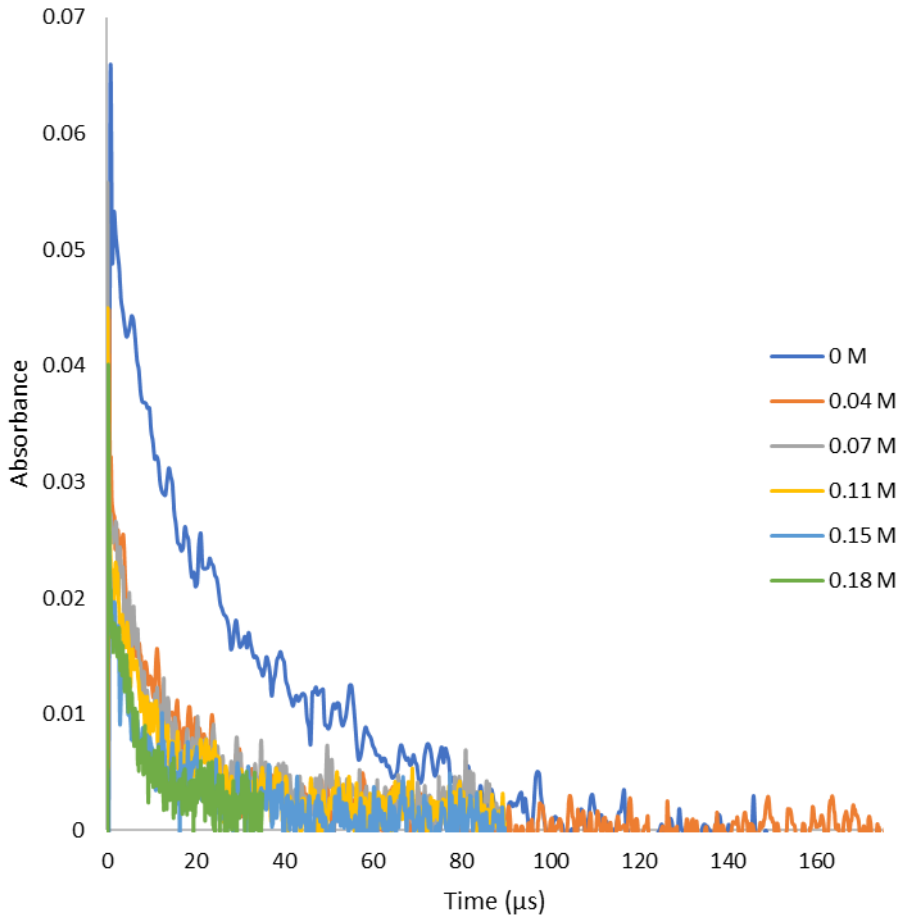

Figure B.41. Transient signal for the decay of $NO_3\cdot$ at 635 nm in the presence pentanoic acid in neat CH_3CN generated by laser flash photolysis of 3×10^{-4} mol L^{-1} CAN.

Table B.27. Observed rate constants for hydrogen abstraction by $NO_3\cdot$ from various concentrations of pentanoic acid in CH_3CN at 25 °C

[pentanoic acid], M (CH_3CN)	$k_{obs} \times 10^{-4}$ s
0	2.75 ± 0.68
0.04	6.16 ± 0.80
0.07	9.78 ± 0.54
0.11	9.39 ± 0.37
0.15	11.61 ± 1.79
0.18	19.33 ± 1.99

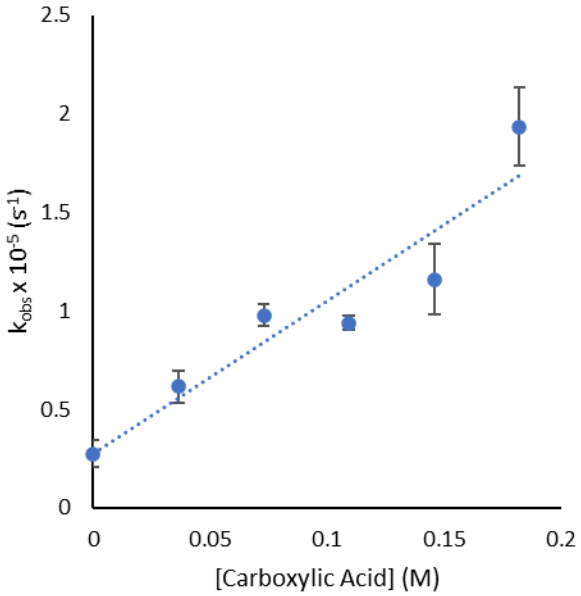

Figure B.42. Plot of the observed rate constant for $NO_3\cdot$ vs. pentanoic acid concentration in CH_3CN at 25 °C; the slope is equal to the hydrogen abstraction rate constant ($k_{AN} = 7.8 \times 10^{-5}$ M s).

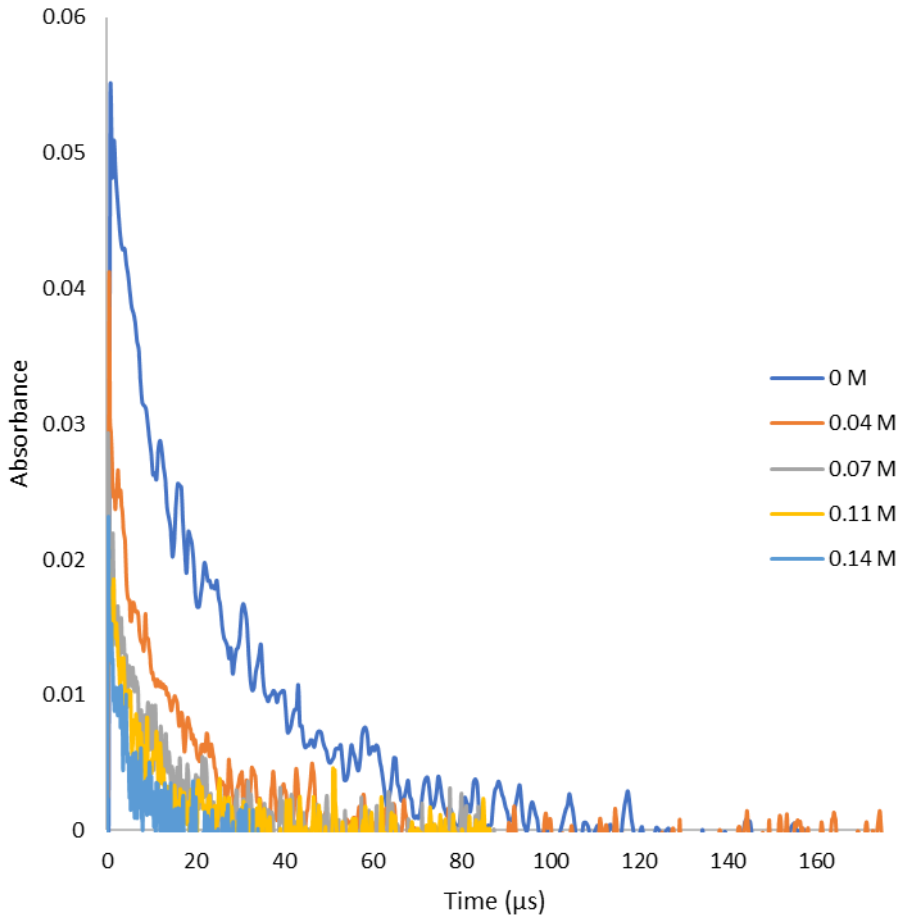

Figure B.43. Transient signal for the decay of $NO_3\cdot$ at 635 nm in the presence 3-methylpentanoic acid in neat CH_3CN generated by laser flash photolysis of 3×10^{-4} mol L^{-1} CAN.

Table B.28. Observed rate constants for hydrogen abstraction by $NO_3\cdot$ from various concentrations of 3-methylbutyric acid in CH_3CN at 25 °C

[3-methylbutyric acid], M (CH_3CN)	$k_{obs} \times 10^{-4}$ s
0	3.53 ± 0.73
0.04	5.94 ± 0.49
0.07	9.49 ± 0.82
0.11	11.29 ± 1.36
0.14	17.58 ± 2.64

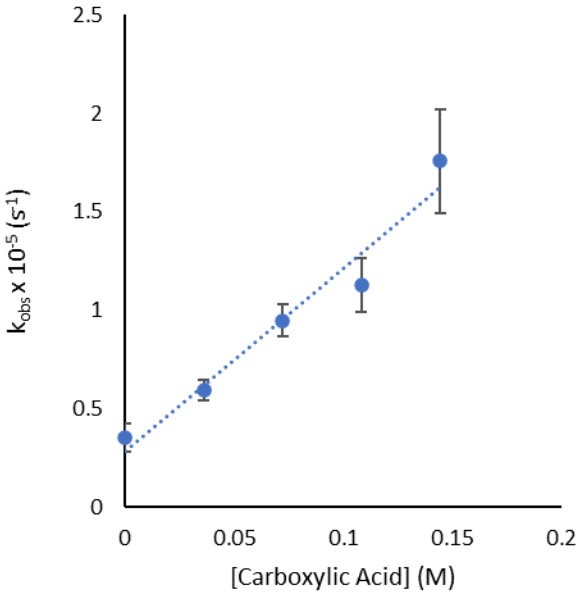

Figure B.44. Plot of the observed rate constant for $NO_3\cdot$ vs. 3-methylbutyric acid concentration in CH_3CN at 25 °C; the slope is equal to the hydrogen abstraction rate constant ($k_{AN} = 9.3 \times 10^{-5}$ M s).

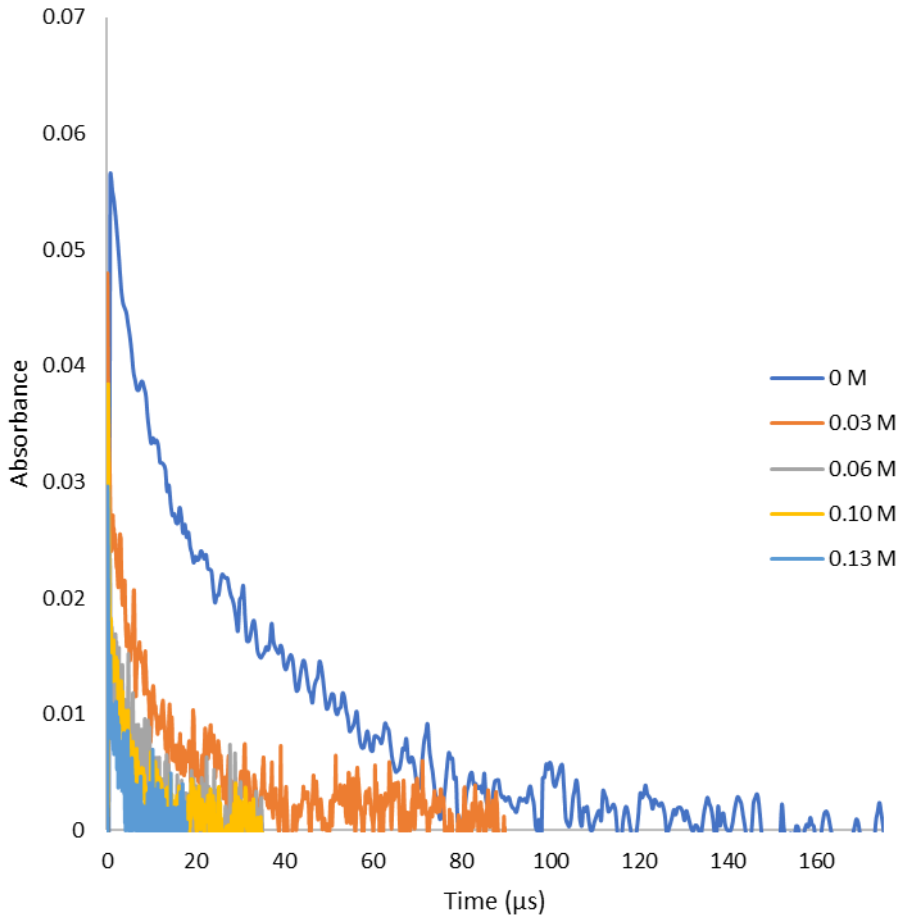

Figure B.45. Transient signal for the decay of $NO_3\cdot$ at 635 nm in the presence hexanoic acid in neat CH_3CN generated by laser flash photolysis of 3×10^{-4} mol L^{-1} CAN.

Table B.29. Observed rate constants for hydrogen abstraction by $NO_3\cdot$ from various concentrations of hexanoic acid in CH_3CN at 25 °C

[hexanoic acid], M (CH_3CN)	$k_{obs} \times 10^{-4}$ s
0	2.81 ± 0.56
0.03	9.54 ± 0.96
0.06	13.69 ± 1.88
0.10	21.23 ± 1.49
0.13	39.58 ± 3.37

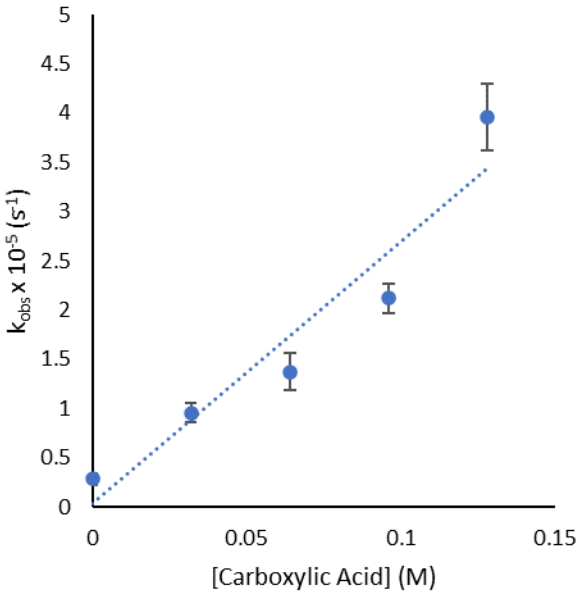

Figure B.46. Plot of the observed rate constant for $NO_3\cdot$ vs. hexanoic acid concentration in CH_3CN at 25 °C; the slope is equal to the hydrogen abstraction rate constant ($k_{AN} = 26.6 \times 10^{-5}$ M s).

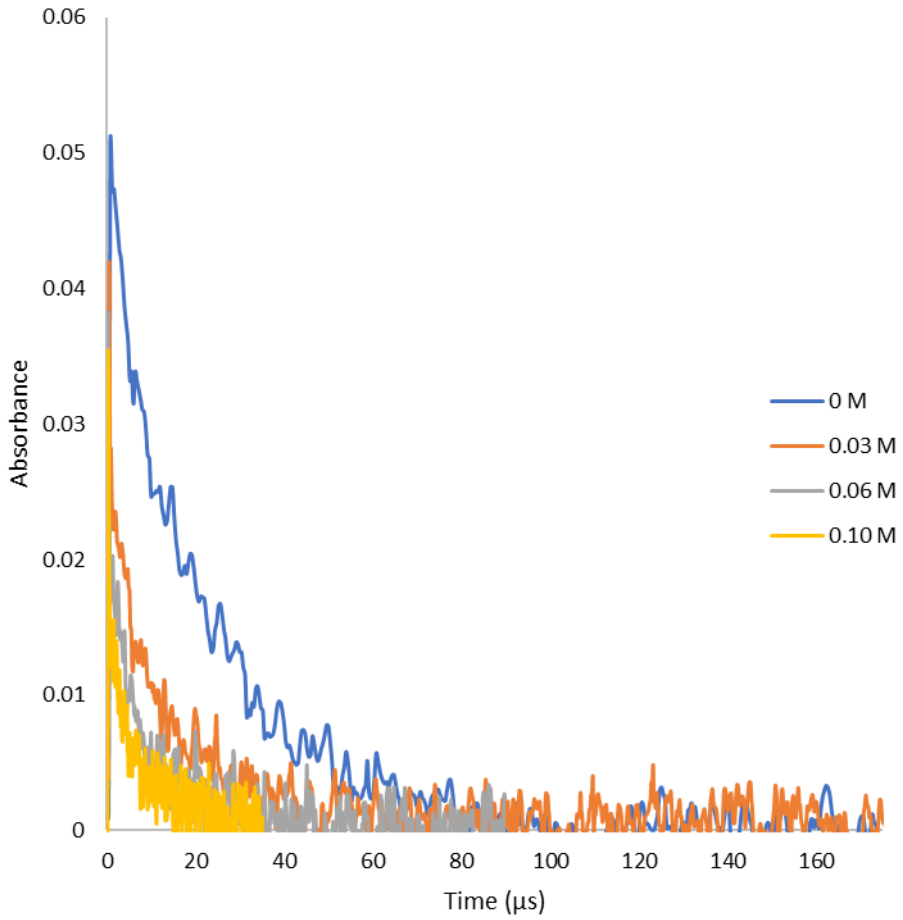

Figure B.47. Transient signal for the decay of $NO_3\cdot$ at 635 nm in the presence 4-methylpentanoic acid in neat CH_3CN generated by laser flash photolysis of 3×10^{-4} mol L^{-1} CAN.

Table B.30. Observed rate constants for hydrogen abstraction by $NO_3\cdot$ from various concentrations of 4-methylpentanoic acid in CH_3CN at 25 °C

[4-methylpentanoic acid], M (CH_3CN)	$k_{obs} \times 10^{-4}$ s
0	4.06 ± 0.54
0.03	7.87 ± 0.48
0.06	14.10 ± 2.72
0.10	28.01 ± 4.79

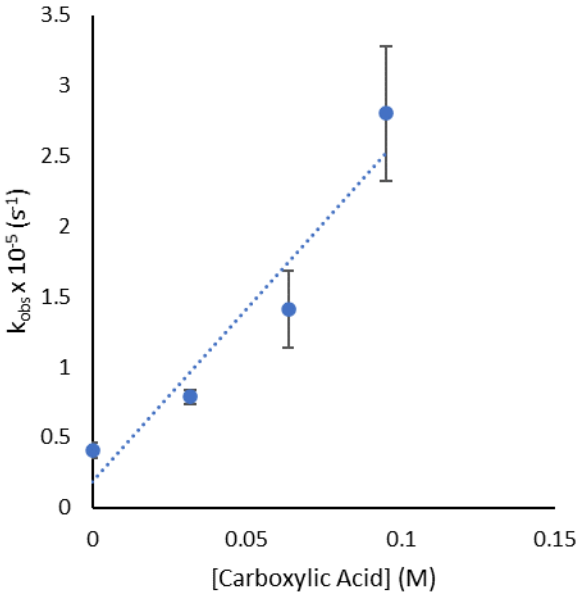

Figure B.48. Plot of the observed rate constant for $NO_3\cdot$ vs. 4-methylpentanoic acid concentration in CH_3CN at 25 °C; the slope is equal to the hydrogen abstraction rate constant ($k_{AN} = 24.6 \times 10^{-5}$ M s).

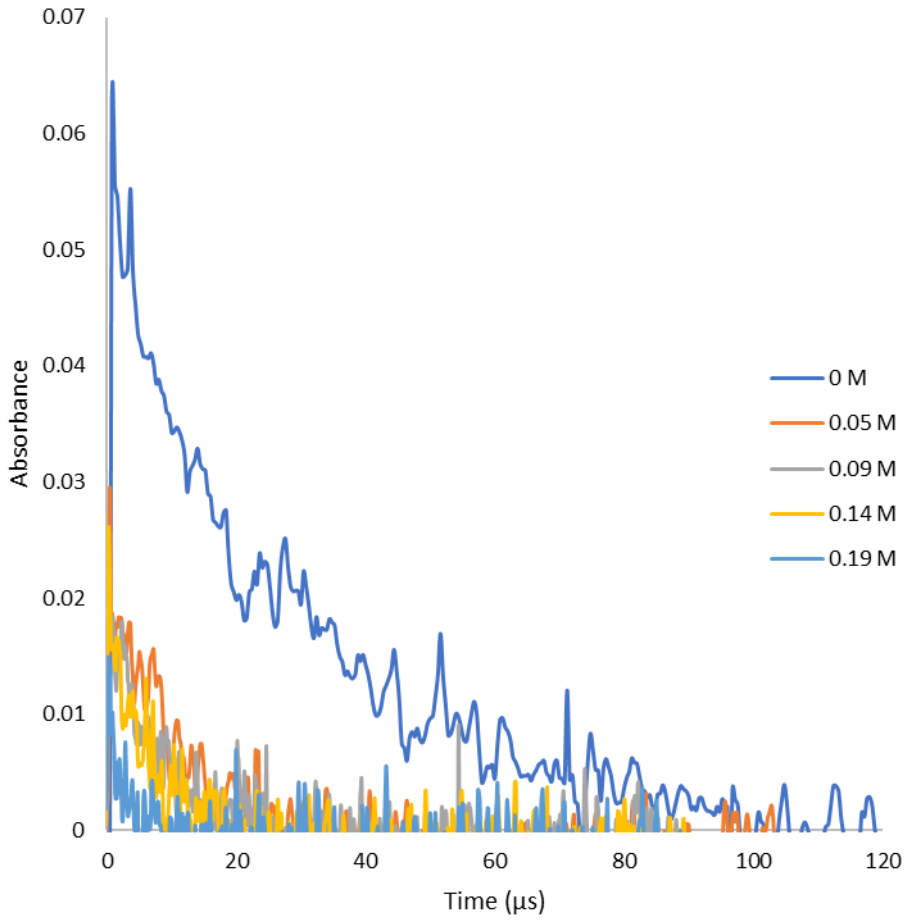

Figure B.49. Transient signal for the decay of $NO_3\cdot$ at 635 nm in the presence 3,3-dimethylbutyric acid in neat CH_3CN generated by laser flash photolysis of 3×10^{-4} mol L^{-1} CAN.

Table B.31. Observed rate constants for hydrogen abstraction by $NO_3\cdot$ from various concentrations of 3,3-dimethylbutyric acid in CH_3CN at 25 °C

[3,3-dimethylbutyric acid], M (CH_3CN)	$k_{obs} \times 10^{-4}$ s
0	3.08
0.05	7.04
0.09	10.25
0.14	14.60
0.19	22.81

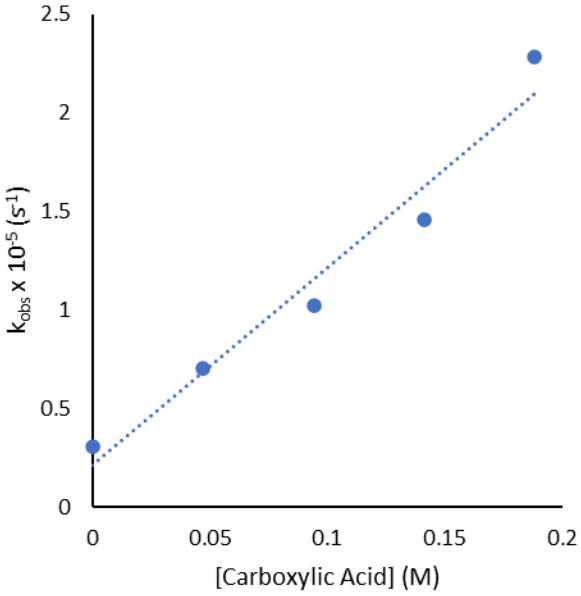

Figure B.50. Plot of the observed rate constant for $NO_3\cdot$ vs. 3,3-dimethylbutyric acid concentration in CH_3CN at 25 °C; the slope is equal to the hydrogen abstraction rate constant ($k_{AN} = 10.0 \times 10^{-5}$ M s).

Appendix C

Does Metal Ion Complexation Make Radical Clocks Run Fast? An Experimental Perspective

*Marwa K. Abdel Latif, Jared N. Spencer, Mark Paradzinsky, James M. Tanko**

DEPARTMENT OF CHEMISTRY, VIRGINIA POLYTECHNIC INSTITUTE AND STATE UNIVERSITY, BLACKSBURG, VIRGINIA, U.S.A.

Table C.1. Measured rate constants of β-scission of cumyloxyl radical as a result of added water to an acetonitrile solution (No electrolyte is added).

Concentration	H_2O $k/10^5\ s^{-1}$	D_2O $k/10^5\ s^{-1}$
0	7.8 (0.2)	8.6 (0.2)
0.6	7.8 (0.2)	8.7 (0.2)
1.1	8.2 (0.2)	9.0 (0.2)
1.7	8.7 (0.2)	9.4 (0.4)
2.2	9.3 (0.5)	9.7 (0.1)

Table C.2. Measured rate constants of β-scission of cumyloxyl radical as a result of added deionized water to an acetonitrile solution with a range of electrolyte concentrations of tetra-nbutylammonium perchlorate (TBAP).

DI water molarity (M)	No TBAP $k/10^5\ s^{-1}$	0.08 M TBAP $k/10^5\ s^{-1}$	0.15 M TBAP $k/10^5\ s^{-1}$	0.23 M TBAP $k/10^5\ s^{-1}$	0.39 M TBAP $k/10^5\ s^{-1}$
0	7.8 (0.2)	8.7 (0.1)	9.0 (0.2)	9.2 (0.1)	10.0 (0.3)
0.6	7.8 (0.2)	9.1 (0.2)	9.3 (0.3)	10.0 (0.2)	10.6 (0.1)
1.1	8.2 (0.2)	9.6 (0.4)	10.5 (0.4)	9.9 (0.4)	10.9 (0.5)
1.7	8.7 (0.2)	9.8 (0.4)	--	10.5 (0.2)	11.7 (0.6)
2.2	9.3 (0.5)	10.2 (0.1)	11.2 (0.3)	11.3 (0.1)	12.1 (0.6)

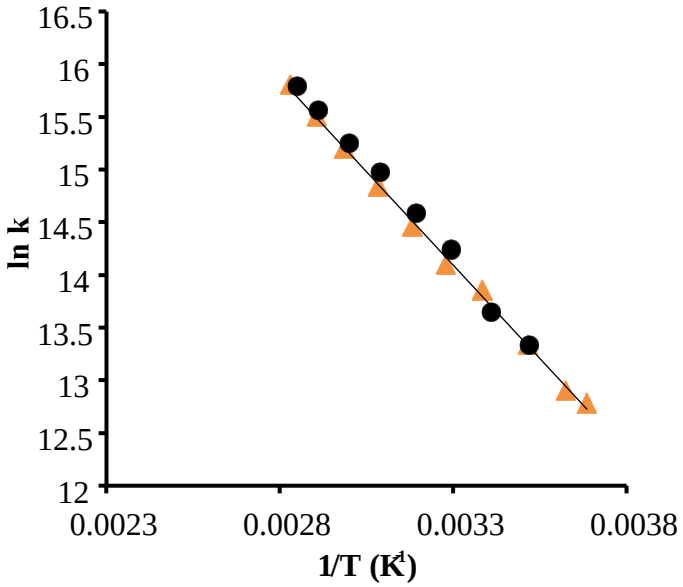

Figure C.1. Arrhenius plot showing no apparent isotopic effect for the β-scission of cumyl radical as a result 2.1 M of added H_2O (Black circles) or D_2O (Orange triangles) into the acetonitrile solution with no electrolyte present.

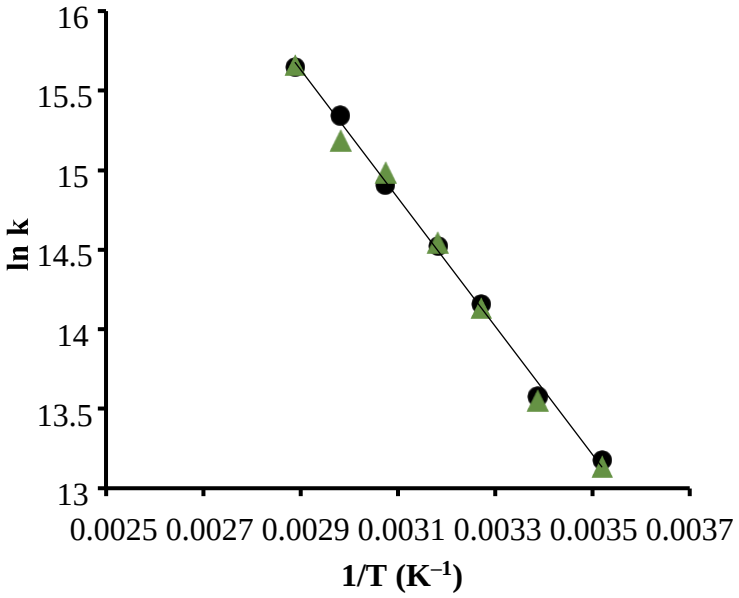

Figure C.2. Arrhenius plot showing no apparent isotopic effect for the β-scission of cumyloxyl radical as a result of 2.7 M added H_2O (Black circles) or D_2O (Orange triangles) into the acetonitrile solution with no electrolyte present.

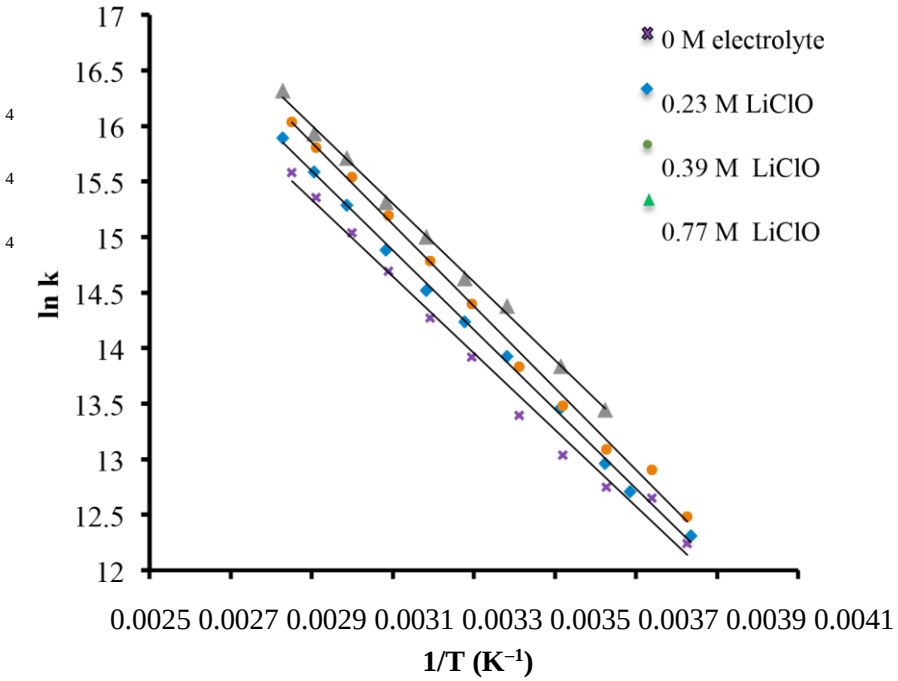

Figure C.3. Arrhenius plot for the β-scission of cumyloxyl radical with added lithium perchlorate electrolyte in anhydrous acetonitrile.

Table C.3. Activation barriers calculated from Arrhenius plots with estimated enthalpy and entropy of activation for the β-scission of cumyloxyl in acetonitrile as a solvent with a range of molarities of added electrolytes. Subtle changes cannot be detected by the activation energy profile.

Molarity of electrolyte (M)	E_a *(kcal/mol)*	*log A*	$\Delta H^{\ddagger}$ $(kcal/mol)$	$\Delta S^{\ddagger}$ $(cal/K.mol)$	^{a}k *(/10⁵ s⁻¹)*
0.23 $LiClO_4$	7.46 (0.27)	11.5 (0.2)	6.77 (0.26)	-8.18 (0.77)	14.4 (0.5)
0.39 $LiClO_4$	7.52 (0.48)	11.6 (0.4)	6.89 (0.46)	-7.43 (1.35)	17.6 (0.7)
0.77 $LiClO_4$	7.40 (0.66)	11.6 (0.9)	6.69 (0.61)	-7.60 (2.17)	21.8 (0.7)
0.39 $Mg(ClO_4)_2$	7.49 (0.74)	11.5 (-)	6.77 (0.69)	-8.54 (2.04)	12.7 (0.9)
0.39 $NaClO_4$	7.00 (0.57)	11.1 (0.2)	6.34 (0.56)	-9.82 (1.65)	13.7 (0.8)
0.39 TBAP	7.15 (0.58)	11.2 (0.6)	6.44 (0.58)	-9.60 (1.71)	12.8 (0.9)

[a]Calculated rate constants at 30 °C from Arrhenius plots

Table C.4. Rate Constants for the β-Cleavage of Cumyloxyl Radical in the Presence of Various Electrolytes in DMSO at 25 °C

	$k_\beta/10^5\ s^{-1}$	
[Electrolyte] /mol·L⁻¹	$LiClO_4$	$NaClO_4$
0.00	1.3 (0.1)	1.5 (0.1)
0.25	1.3 (0.1)	1.5 (0.1)
0.50	1.2 (0.1)	1.3 (0.1)
0.75	1.5 (0.1)	1.5 (0.1)
1.00	1.4 (0.1)	1.4 (0.1)

Cartesian coordinates and Gaussian log archival data for all optimized structures

tBu-O•

O	0.002590656301	-0.005843978732	-0.005852031797
C	-0.022967923032	0.051476625787	1.365818055186
C	1.399670111059	-0.008950532232	1.946816568046
C	-0.927555083411	-1.048149891306	1.946893511332
C	-0.649641745037	1.454904774584	1.640736074383
H	-0.709277183948	1.588513608548	2.720858706348
H	-1.648471434604	1.515834082658	1.214801222269
H	-0.028300076627	2.239297984961	1.214760621432
H	2.014178842672	0.784539899499	1.524269396836
H	1.860703577607	-0.966107749792	1.703238069818
H	1.383471660042	0.095531813502	3.032284074046
H	-0.994484110734	-0.966323151388	3.032362875216
H	-1.928603458486	-0.976070097475	1.524399307682
H	-0.522604914316	-2.030350089532	1.703314885903

Gaussian log archival data for CCSD single point job:

1\1\GINC-NR081\SP\UCCSD(T)-FC\Aug-CC-pVTZ\C4H9O1(2)\JNSPENCE\07-Jun-20 16\0\\#p gfinput iop(6/7=3) ccsd(t)/aug-cc-pvtz geom=checkpoint guess= read\\CCSD(T) singlie point of optimized C4H10O radical\\0,2\O,0,0.002 5906563,-0.0058439787,-0.0058520318\C,0,-0.022967923,0.0514766258,1.36 58180552\C,0,1.3996701111,-0.0089505322,1.946816568\C,0,-0.9275550834, -1.0481498913,1.9468935113\C,0,-0.649641745,1.4549047746,1.6407360744\ H,0,-0.7092771839,1.5885136085,2.7208587063\H,0,-1.6484714346,1.515834 0827,1.2148012223\H,0,-0.0283000766,2.239297985,1.2147606214\H,0,2.014 1788427,0.7845398995,1.5242693968\H,0,1.8607035776,-0.9661077498,1.703 2380698\H,0,1.38347166,0.0955318135,3.032284074\H,0,-0.9944841107,-0.9 663231514,3.0323628752\H,0,-1.9286034585,-0.9760700975,1.5243993077\H, 0,-0.5226049143,-2.0303500895,1.7033148859\\Version=ES64L-G09RevD.01\S tate=2-A\HF=-231.6234592\MP2=-232.5333899\MP3=-232.5841449\MP4D=-232.6 028268\MP4DQ=-232.5817185\PUHF=-231.6274597\PMP2-0=-232.5358287\PMP3-0 =-232.5856351\MP4SDQ=-232.5891402\CCSD=-232.5898178\CCSD(T)=-232.62799 48\S2=0.760138\S2-1=0.752185\S2A=0.750081\RMSD=9.246e-09\PG=C01 [X(C4H 9O1)]\\@

CH_3CN

C	0.001407249662	0.000000000002	0.053180193370

C	0.009667555253	0.000000000001	1.507764235212
N	0.016271717974	0.000000000001	2.656993055761
H	-0.511823977593	-0.885243583605	-0.319599959637
H	-0.511823980724	0.885243581802	-0.319599959619
H	1.021461643204	0.000000001810	-0.328285827401

Gaussian log archival data for CCSD single point job:

1\1\GINC-NR096\SP\RCCSD(T)-FC\Aug-CC-pVTZ\C2H3N1\JNSPENCE\06-Jun-2016\ 0\\#p gfinput iop(6/7=3) ccsd(t)/aug-cc-pvtz geom=checkpoint guess=read\\CCSD(T) single point of acetonitrile optimization\\0,1\C,0,0.0014072497,0.,0.0531801934\C,0,0.0096675553,0.,1.5077642352\N,0,0.016271718,0.,2.6569930558\H,0,-0.5118239776,-0.8852435836,-0.3195999596\H,0,-0.511823981,0.8852435816,-0.3195999596\H,0,1.0214616432,0.000000002,-0.3282858274\\Version=ES64L-G09RevD.01\State=1-A'\HF=-131.9754018\MP2=-132.497339\MP3=-132.5064127\MP4D=-132.5206517\MP4DQ=-132.5065679\MP4SDQ=-132.5123148\CCSD=-132.5108054\CCSD(T)=-132.5364851\RMSD=3.237e-09\PG=CS [SG(C2H1N1),X(H2)]\\@

tBu-O•/Li$^+$

C	-0.015774560709	0.004618581078	-0.010472369875
C	0.191877709030	-0.091648012578	1.504828382543
O	1.478038675766	0.025546825586	1.864907995763
Li	3.160384153077	0.159047309616	2.322308904486
C	-0.435823531179	1.276262382222	2.172735260554
H	-0.303328371878	1.246377375472	3.248352018334
H	-1.488252494213	1.222262056583	1.902946693146
H	0.039584202737	2.144673169755	1.730863646207
C	-0.507746922282	-1.283910624305	2.166333845222
H	-1.574307406551	-1.267859746428	1.953179269764
H	-0.362479247129	-1.277651823850	3.244740912167
H	-0.092447525684	-2.207658659030	1.762968140650
H	-1.076402405576	0.036174425862	-0.249888273087
H	0.415525805557	-0.877238874759	-0.484599067817
H	0.465484205115	0.891005614774	-0.418901994456

Gaussian log archival data for CCSD single point job:

1\1\GINC-NR110\SP\UCCSD(T)-FC\Aug-CC-pVTZ\C4H9Li1O1(1+,2)\JNSPENCE\10-Jun-2016\0\\#p gfinput iop(6/7=3) CCSD(T)/aug-cc-pVTZ geom=checkpoint guess=read\\CCSD(T) single point of optimized C4H9O--Li+\\1,2\C,0,-0.0157745607,0.0046185811,-0.0104723699\C,0,0.191877709,-0.0916480126,1.5

048283825\O,0,1.4780386758,0.0255468256,1.8649079958\Li,0,3.1603841531
,0.1590473096,2.3223089045\C,0,-0.4358235312,1.2762623822,2.1727352606
\H,0,-0.3033283719,1.2463773755,3.2483520183\H,0,-1.4882524942,1.22226
20566,1.9029466931\H,0,0.0395842027,2.1446731698,1.7308636462\C,0,-0.5
077469223,-1.2839106243,2.1663338452\H,0,-1.5743074066,-1.2678597464,1
.9531792698\H,0,-0.3624792471,-1.2776518238,3.2447409122\H,0,-0.092447
5257,-2.207658659,1.7629681407\H,0,-1.0764024056,0.0361744259,-0.24988
82731\H,0,0.4155258056,-0.8772388748,-0.4845990678\H,0,0.4654842051,0.
8910056148,-0.4189019945\\Version=ES64L-G09RevD.01\State=2-A\HF=-238.9
085128\MP2=-239.8260998\MP3=-239.874432\MP4D=-239.8934255\MP4DQ=-239.8
719201\PUHF=-238.9139142\PMP2-0=-239.8295996\PMP3-0=-239.8766119\MP4SD
Q=-239.8805459\CCSD=-239.8837999\CCSD(T)=-239.9235704\S2=0.768576\S2-1
=0.755408\S2A=0.750211\RMSD=5.882e-09\PG=C01 [X(C4H9Li1O1)]\\@

[tBu-O•/Li$^+$]‡

C	0.001283208121	-0.002421905931	-0.009936939390
C	-0.000793535649	0.001525547315	2.041857807736
C	1.494249957000	0.000935348270	2.282609128447
O	-0.631970813189	1.089971208452	2.246345848872
Li	-1.459033296881	2.516608733832	2.704727445455
C	-0.742806221655	-1.296337390306	2.282857083797
H	-0.763803808092	-1.455815663168	3.365210451483
H	-0.244618736245	-2.151809609922	1.835094013208
H	-1.770554786059	-1.238244829868	1.932989430939
H	1.989215775234	-0.856421497695	1.834876868540
H	1.643277587496	-0.059903704403	3.364945210783
H	1.954244738338	0.921750799339	1.932532868482
H	0.535680523713	-0.923844312762	-0.191432221711
H	0.532073792580	0.914574423489	-0.219114999743
H	-1.058275299745	-0.007812173720	-0.218939384652

Gaussian log archival data for CCSD single point job:

1\1\GINC-NR119\SP\UCCSD(T)-FC\Aug-CC-pVTZ\C4H9Li1O1(1+,2)\JNSPENCE\12-
Jun-2016\0\\#p gfinput iop(6/7=3) ccsd(t)/aug-cc-pvtz geom=checkpoint
guess=read\\CCSD(T) SP energy of transistion state of C4H9O--Li+ --> C 3H6O--Li+ +
CH3\\1,2\C,0,0.0012832081,-0.0024219059,-0.0099369394\C,0,
-0.0007935356,0.0015255473,2.0418578077\C,0,1.494249957,0.0009353483,2
.2826091284\O,0,-0.6319708132,1.0899712085,2.2463458489\Li,0,-1.459033
2969,2.5166087338,2.7047274455\C,0,-0.7428062217,-1.2963373903,2.28285
70838\H,0,-0.7638038081,-1.4558156632,3.3652104515\H,0,-0.2446187362,-
2.1518096099,1.8350940132\H,0,-1.7705547861,-1.2382448299,1.9329894309
\H,0,1.9892157752,-0.8564214977,1.8348768685\H,0,1.6432775875,-0.05990

37044,3.3649452108\H,0,1.9542447383,0.9217507993,1.9325328685\H,0,0.53
56805237,-0.9238443128,-0.1914322217\H,0,0.5320737926,0.9145744235,-0.
2191149997\H,0,-1.0582752997,-0.0078121737,-0.2189393847\\Version=ES64
L-G09RevD.01\State=2-A\HF=-238.8989454\MP2=-239.8286675\MP3=-239.86911
55\MP4D=-239.8897532\MP4DQ=-239.8681263\PUHF=-238.9045827\PMP2-0=-239.
8327951\PMP3-0=-239.8717634\MP4SDQ=-239.8774111\CCSD=-239.8762605\CCSD
(T)=-239.9167898\S2=0.785244\S2-1=0.766203\S2A=0.75051\RMSD=4.160e-09\
PG=C01 [X(C4H9Li1O1)]\\@

CH_3CN/Li^+

C	0.002686881551	-0.004653413039	-0.013073886035
C	-0.000523670883	0.000907513030	1.432054023447
H	1.025274921870	0.002316216432	1.800323072685
H	-0.514649944367	-0.886751729253	1.800323070578
H	-0.514635684271	0.891383699414	1.793478268282
N	0.005236182208	-0.009069090461	-1.160993249638
Li	0.009403638697	-0.016287847763	-3.040155624319

Gaussian log archival data for CCSD single point job:

1\1\GINC-NR126\SP\RCCSD(T)-FC\Aug-CC-pVTZ\C2H3Li1N1(1+)\JNSPENCE\10-
Ju n-2016\0\\#p gfinput iop(6/7=3) ccsd(t)/aug-cc-pvtz geom=checkpoint gu
ess=read\\CCSD(T) single point of optimized CH3CN--Li+ metal complex\\
1,1\C,0,0.0026868816,-0.004653413,-0.013073886\C,0,-0.0005236718,0.000
9075125,1.4320540234\H,0,1.0252749219,0.0023162164,1.8003230727\H,0,-0
.5146499444,-0.8867517293,1.8003230706\H,0,-0.5146356843,0.8913836994,
1.7934782683\N,0,0.0052361843,-0.0090690892,-1.1609932496\Li,0,0.00940 3643,-
0.0162878452,-3.0401556243\\Version=ES64L-G09RevD.01\State=1-A\H
F=-139.2847953\MP2=-139.8020025\MP3=-139.8123552\MP4D=-139.8256906\MP4
DQ=-139.8120135\MP4SDQ=-139.817702\CCSD=-139.8161915\CCSD(T)=-139.8412
942\RMSD=4.745e-09\PG=C01 [X(C2H3Li1N1)]\\@

$tBu\text{-}O\bullet/Na^+$

C	-0.042485059993	0.000019047727	-0.013761577532
C	0.150269168628	-0.072899338578	1.506455127016
O	1.454482003507	0.029788877508	1.861879836047
Na	3.520971075831	0.163215926448	2.406843184921
C	-0.455766633403	1.265302781484	2.161687334021
H	-0.327814385749	1.247818677228	3.239424506875

H	-1.514224484614	1.240120924925	1.907682279539
H	0.013638111962	2.142587108045	1.727834563940
C	-0.532466155140	-1.283884382883	2.155246857854
H	-1.598980013861	-1.281221635349	1.938141776462
H	-0.394892325835	-1.277822397266	3.235017574346
H	-0.106544016432	-2.202704774967	1.752636186070
H	-1.101826461191	0.021462277447	-0.262618654956
H	0.397968214199	-0.880738413535	-0.480670691554
H	0.432003248171	0.888955321765	-0.425494939450

Gaussian log archival data for CCSD single point job:

1\1\GINC-NR119\SP\UCCSD(T)-FC\Aug-CC-pVTZ\C4H9Na1O1(1+,2)\JNSPENCE\08-Jun-2016\0\\#p gfinput iop(6/7=3) ccsd(t)/aug-cc-pvtz geom=checkpoint guess=read\\CCSD(T) single point energy\\1,2\C,0,-0.04248506,0.0000190 477,-0.0137615775\C,0,0.1502691686,-0.0728993386,1.506455127\O,0,1.454 4820035,0.0297888775,1.861879836\Na,0,3.5209710758,0.1632159264,2.4068 431849\C,0,-0.4557666334,1.2653027815,2.161687334\H,0,-0.3278143857,1. 2478186772,3.2394245069\H,0,-1.5142244846,1.2401209249,1.9076822795\H, 0,0.013638112,2.142587108,1.7278345639\C,0,-0.5324661551,-1.2838843829 ,2.1552468579\H,0,-1.5989800139,-1.2812216353,1.9381417765\H,0,-0.3948 923258,-1.2778223973,3.2350175743\H,0,-0.1065440164,-2.202704775,1.752 6361861\H,0,-1.1018264612,0.0214622774,-0.262618655\H,0,0.3979682142,-0.8807384135,-0.4806706916\H,0,0.4320032482,0.8889553218,-0.4254949395 \\Version=ES64L-G09RevD.01\State=2-A\HF=-393.3335587\MP2=-394.2464773\ MP3=-394.2960435\MP4D=-394.3147815\MP4DQ=-394.2935537\PUHF=-393.338205 2\PMP2-0=-394.2494009\PMP3-0=-394.2978815\MP4SDQ=-394.301669\CCSD=-394 .3040258\CCSD(T)=-394.3430679\S2=0.763863\S2-1=0.753521\S2A=0.750139\R MSD=6.092e-09\PG=C01 [X(C4H9Na1O1)]\\@

[tBu-O•/Na$^+$]‡

C	0.003444422310	-0.005837328425	0.019000971993
C	-0.002202787119	0.003737152609	2.088404658880
C	1.496143276298	0.002184615450	2.325907871201
O	-0.635824568831	1.085363921884	2.279875856770
C	-0.733585249074	-1.303986735962	2.325872162785
Na	-1.653280362444	2.822271814351	2.857576212007
H	-0.752118535678	-1.471946215871	3.406646346370
H	-0.232030078469	-2.154311073399	1.871378168598
H	-1.761849451099	-1.250016494758	1.976685638305
H	1.992608979255	-0.851068287637	1.871313818652
H	1.651689190918	-0.063927907397	3.406677060749
H	1.951903573031	0.925555393620	1.976852450841

H 0.541849878461 -0.925388780266 -0.159663935738
H 0.530722887724 0.912286830531 -0.193277081717 H -
1.055254839232 -0.016315754448 -0.193324132067

Gaussian log archival data for CCSD single point job:

1\1\GINC-NR109\SP\UCCSD(T)-FC\Aug-CC-pVTZ\C4H9Na1O1(1+,2)\JNSPENCE\10-
Jun-2016\0\\#p gfinput iop(6/7=3) CCSD(T)/aug-cc-pVTZ geom=checkpoint
guess=read\\CCSD(T) single point of optimized TS for C4H9O--Na+ --> C3 H6O--Ni+ +
CH3\\1,2\C,0,0.0034444223,-0.0058373284,0.019000972\C,0,-0.
0022027871,0.0037371526,2.0884046589\C,0,1.4961432763,0.0021846154,2.3
259078712\O,0,-0.6358245688,1.0853639219,2.2798758568\C,0,-0.733585249 1,-
1.303986736,2.3258721628\Na,0,-1.6532803624,2.8222718144,2.85757621
2\H,0,-0.7521185357,-1.4719462159,3.4066463464\H,0,-0.2320300785,-2.15
43110734,1.8713781686\H,0,-1.7618494511,-1.2500164948,1.9766856383\H,0
,1.9926089793,-0.8510682876,1.8713138187\H,0,1.6516891909,-0.063927907
4,3.4066770607\H,0,1.951903573,0.9255553936,1.9768524508\H,0,0.5418498
785,-0.9253887803,-0.1596639357\H,0,0.5307228877,0.9122868305,-0.19327
70817\H,0,-1.0552548392,-0.0163157544,-0.1933241321\\Version=ES64L-G09
RevD.01\State=2-A\HF=-393.3126517\MP2=-394.2419835\MP3=-394.2825623\MP
4D=-394.3033432\MP4DQ=-394.281578\PUHF=-393.320207\PMP2-0=-394.2477499
\PMP3-0=-394.2863506\MP4SDQ=-394.2909724\CCSD=-394.2901695\CCSD(T)=-39
4.3309124\S2=0.804594\S2-1=0.778483\S2A=0.750916\RMSD=4.395e-09\PG=C01
[X(C4H9Na1O1)]\\@

CH_3CN/Na^+

C 0.002587569671 -0.004482136838 0.037415322601
C -0.000636200891 0.001102255479 1.485278075597
H 1.023963662136 0.002547185767 1.855655155597
H -0.514194236859 -0.885500654535 1.855655636966
H -0.514161813583 0.890563079338 1.848801403917
N 0.005130541027 -0.008886871525 -1.110773952404 Na
0.010102803305 -0.017497509326 -3.360075967275

Gaussian log archival data for CCSD single point job:

1\1\GINC-NR101\SP\RCCSD(T)-FC\Aug-CC-pVTZ\C2H3N1Na1(1+)\JNSPENCE\09-
Ju n-2016\0\\#p gfinput iop(6/7=3) ccsd(t)/aug-cc-pvtz geom=checkpoint gu
ess=read\\CCSD(T) single point of optimized CH3CN--Na+ metal ion compl
ex\\1,1\C,0,0.0025875697,-0.0044821368,0.0374153226\C,0,-0.0006362009,
0.0011022555,1.4852780756\H,0,1.0239636621,0.0025471858,1.8556551556\H ,0,-
0.5141942369,-0.8855006545,1.855655637\H,0,-0.5141618136,0.8905630
793,1.8488014039\N,0,0.005130541,-0.0088868715,-1.1107739524\Na,0,0.01

01028033,-0.0174975093,-3.3600759673\\Version=ES64L-G09RevD.01\State=1
-A\HF=-293.7033655\MP2=-294.221873\MP3=-294.2317349\MP4D=-294.2453049\
MP4DQ=-294.2315531\MP4SDQ=-294.2372639\CCSD=-294.2357374\CCSD(T)=-294.
2609795\RMSD=2.959e-09\PG=C01 [X(C2H3N1Na1)]\\@

tBu-O•/K⁺

C	-0.818540398847	1.282118262822	-0.607096184067
C	-0.192507505582	0.000186437775	-0.040672883260
O	1.163797650142	-0.000410595998	-0.168457085126
K	3.673391372521	-0.001431190819	-0.473559806759
C	-0.362268237453	-0.000958145081	1.544116266610
H	0.080831180900	-0.894574887902	1.973726323576
H	-1.437129847587	-0.000535889549	1.719441233944
H	0.081758270441	0.891528344873	1.975116590228
C	-0.819849237133	-1.280227620262	-0.609081978622
H	-1.890398711254	-1.300282054360	-0.412227587798
H	-0.366618792582	-2.165175058458	-0.165634745899 H -
0.673934864501	-1.315383413806	-1.688505513209	
H	-1.889070660095	1.302959047628	-0.410218475659
H	-0.672581273287	1.318804032515	-1.686462759539
H	-0.364412705420	2.165913548376	-0.162270845933

Gaussian log archival data for CCSD single point job:

1\1\GINC-NR122\SP\UCCSD(T)-FC\6-311+G(2df,pd)\C4H9K1O1(1+,2)\JNSPENCE\
11-Jun-2016\0\\#p gfinput iop(6/7=3) CCSD(T)/6-311+g(2df,pd) geom=chec kpoint
guess=read\\CCSD(T) single point of optimized C4H9O--K+\\1,2\C, 0,-
0.8185403988,1.2821182628,-0.6070961841\C,0,-0.1925075056,0.0001864
378,-0.0406728833\O,0,1.1637976501,-0.000410596,-0.1684570851\K,0,3.67
33913725,-0.0014311908,-0.4735598068\C,0,-0.3622682375,-0.0009581451,1
.5441162666\H,0,0.0808311809,-0.8945748879,1.9737263236\H,0,-1.4371298
476,-0.0005358895,1.7194412339\H,0,0.0817582704,0.8915283449,1.9751165
902\C,0,-0.8198492371,-1.2802276203,-0.6090819786\H,0,-1.8903987113,-1
.3002820544,-0.4122275878\H,0,-0.3666187926,-2.1651750585,-0.165634745
9\H,0,-0.6739348645,-1.3153834138,-1.6885055132\H,0,-1.8890706601,1.30
29590476,-0.4102184757\H,0,-0.6725812733,1.3188040325,-1.6864627595\H, 0,-
0.3644127054,2.1659135484,-0.1622708459\\Version=ES64L-G09RevD.01\S tate=2-
A\HF=-830.6393833\MP2=-831.7399991\MP3=-831.8125532\MP4D=-831.8
352493\MP4DQ=-831.8108708\PUHF=-830.6437567\PMP2-0=-831.7427189\PMP3-0
=-831.8142603\MP4SDQ=-831.8190177\CCSD=-831.8204908\CCSD(T)=-831.86361
63\S2=0.762322\S2-1=0.752952\S2A=0.750114\RMSD=4.689e-09\PG=C01 [X(C4H
9K1O1)]\\@

[tBu-O•/K⁺]‡

C	0.003802624915	-0.006312286438	-0.021264867679
C	-0.003118652732	0.004896090764	2.058748088308
C	1.497036639943	0.002583549154	2.295131320288
O	-0.638258275884	1.083250001612	2.243375558063
C	-0.728610205880	-1.308230658390	2.294768175657
K	-1.834430806575	3.114139125078	2.950208196399
H	-0.743247914944	-1.481570736009	3.374633968518
H	-0.226193235351	-2.155384737205	1.834896569762
H	-1.757912641397	-1.255768619818	1.948341473980
H	1.994359139643	-0.847696472449	1.835492163560
H	1.655462690222	-0.068534532838	3.375044906929
H	1.950419855077	0.928139716867	1.948695469124
H	0.544989654512	-0.924203312723	-0.199872795117
H	0.528034117411	0.913466949588	-0.233264761581
H	-1.054753418226	-0.019670826635	-0.233474996750

Gaussian log archival data for CCSD single point job:

1\1\GINC-NR122\SP\UCCSD(T)-FC\6-311+G(2df,pd)\C4H9K1O1(1+,2)\JNSPENCE\ 10-Jun-2016\0\\#p gfinput iop(6/7=3) ccsd(t)/6-311+g(2df,pd) geom=chec kpoint guess=read\\CCSD(T) SP energy of transistion state of C4H9O--K+ --> C3H6O--K+ + CH3\\1,2\C,0,0.0038026249,-0.0063122864,-0.0212648677
\C,0,-0.0031186527,0.0048960908,2.0587480883\C,0,1.4970366399,0.002583
5492,2.2951313203\O,0,-0.6382582759,1.0832500016,2.2433755581\C,0,-0.7
286102059,-1.3082306584,2.2947681757\K,0,-1.8344308066,3.1141391251,2.
9502081964\H,0,-0.7432479149,-1.481570736,3.3746339685\H,0,-0.22619323
54,-2.1553847372,1.8348965698\H,0,-1.7579126414,-1.2557686198,1.948341
474\H,0,1.9943591396,-0.8476964724,1.8354921636\H,0,1.6554626902,-0.06
85345328,3.3750449069\H,0,1.9504198551,0.9281397169,1.9486954691\H,0,0
.5449896545,-0.9242033127,-0.1998727951\H,0,0.5280341174,0.9134669496, -0.2332647616\H,0,-1.0547534182,-0.0196708266,-0.2334749967\\Version=E
S64L-G09RevD.01\State=2-A\HF=-830.6131476\MP2=-831.7311206\MP3=-831.79
43721\MP4D=-831.8192297\MP4DQ=-831.7942901\PUHF=-830.6219723\PMP2-0=-
8
31.7379929\PMP3-0=-831.7989472\MP4SDQ=-831.8040813\CCSD=-831.8032501\C
CSD(T)=-831.848313\S2=0.818699\S2-
1=0.787975\S2A=0.751229\RMSD=6.791e09\PG=C01 [X(C4H9K1O1)]\\@

CH_3CN/K^+

C	0.002390321699	-0.004128664233	0.094394503718
C	-0.000793161590	0.001372792132	1.544051067255

H 1.023053424046 0.002766463039 1.915884468048
H -0.513933341766 -0.884605006691 1.915876759370
H -0.513926643315 0.890151074882 1.909131184584
N 0.004950988113 -0.008553254845 -1.054444472442 K
0.011050741657 -0.019158053589 -3.712937835532

Gaussian log archival data for CCSD single point job:

1\1\GINC-NR112\SP\RCCSD(T)-FC\6-311+G(2df,pd)\C2H3K1N1(1+)\JNSPENCE\10
-Jun-2016\0\\#p gfinput iop(6/7=3) ccsd(t)/6-311+g(2df,pd) geom=checkp oint
guess=read\\CCSD(T) single point of optimized CH3CN--K+ cation co
mplex\\1,1\C,0,0.0023903217,-0.0041286642,0.0943945037\C,0,-0.00079316
16,0.0013727921,1.5440510673\H,0,1.023053424,0.002766463,1.915884468\H
,0,-0.5139333418,-0.8846050067,1.9158767594\H,0,-0.5139266433,0.890151
0749,1.9091311846\N,0,0.0049509881,-0.0085532548,-1.0544444724\K,0,0.0
110507417,-0.0191580536,-3.7129378355\\Version=ES64L-G09RevD.01\State=
1-A\HF=-731.0102085\MP2=-731.7316003\MP3=-731.7627174\MP4D=-731.780534
8\MP4DQ=-731.7630725\MP4SDQ=-731.7691479\CCSD=-731.76714\CCSD(T)=-731.
7980297\RMSD=4.183e-09\PG=C01 [X(C2H3K1N1)]\\@

tBu-O•/*n*Bu$_4$N$^+$

C -1.939929359468 0.428086130433 -4.143339653496
C -1.335868139914 0.998521638903 -2.856656624980
C -0.412779750443 -0.010547250620 -2.146984241410
C 0.118143937591 0.602057062639 -0.850016426088
N 1.169029727112 -0.210008152434 -0.073192369773
C 2.476952978846 -0.178764259017 -0.867352613584
C 3.650006514058 -0.994749166436 -0.321767498318
C 4.916032625698 -0.723979207736 -1.156709621214
C 6.113376581077 -1.555530852413 -0.686634629620
C 0.722395271392 -1.665352254308 0.094053777791
C -0.595047643936 -1.905640282192 0.834838369936
C -1.001671600373 -3.386179514452 0.708641821982
C -2.274571927602 -3.710170385596 1.496269316318
C 1.331393050749 0.409393499281 1.321592570355
C 1.863844557709 1.851287196186 1.420492149503
C 3.380769238919 2.025403016279 1.610054506645
C 3.754156094472 3.482308659074 1.904510884797
O -3.033874795239 0.640241334384 0.270406039409
C -4.294426167918 0.942545476689 0.750822445463
C -4.460800356745 0.457346055165 2.203197072776
C -5.231233631650 0.114706111396 -0.197239991258 C -
4.594150280085 2.445519123707 0.597828692752

H	0.591984072851	1.562204475927	-1.062566932715
H	-0.712213719966	0.777774541992	-0.164745205757
H	-0.984568759220	-0.920953326080	-1.935749228936
H	0.399933555227	-0.288198774284	-2.829220342564
H	-0.767238678363	1.909149971309	-3.089648052668
H	-2.134114318115	1.291806626925	-2.164400843991
H	-1.161217337868	0.146075449990	-4.861682106854
H	-2.586765714958	1.165562609169	-4.628846508206
H	-2.545423316574	-0.462726804282	-3.938893793257
H	1.535821894081	-2.168142651676	0.619199480489
H	0.677997742026	-2.076492944082	-0.917116018514
H	-0.481236569178	-1.664717438885	1.898345541028
H	-1.402884515106	-1.272309351303	0.453105233898
H	-0.180720059666	-4.025825853415	1.060539290063
H	-1.151847035213	-3.632183198653	-0.351449721672
H	-3.120653609508	-3.105686290157	1.148680759063
H	-2.140720515107	-3.516837304365	2.566883981903
H	-2.547023134318	-4.763704539119	1.380093396255
H	1.969649141091	-0.274561266778	1.886600877718
H	0.331788450392	0.358392579207	1.752767084558
H	1.370406684697	2.278524735096	2.302891725604
H	1.513603277070	2.465097741092	0.582487019535
H	3.711998819134	1.387825745575	2.441129657233
H	3.931709514995	1.687761463756	0.724011844315
H	3.261625862254	3.842072230985	2.815137922334
H	3.460254004768	4.144409373935	1.081515470264
H	4.834105439640	3.587552456620	2.046218168311
H	2.223632266174	-0.527087011338	-1.870189759834
H	2.747117825617	0.876325409862	-0.944714331929
H	3.428807922616	-2.066875597643	-0.362801008050
H	3.854130350392	-0.745935930355	0.725737629576
H	4.708717514118	-0.941590845714	-2.213207123970
H	5.165727664180	0.344547372199	-1.105164038151
H	6.997318915056	-1.340028157021	-1.294545553191
H	5.908605159978	-2.629365956440	-0.765686068263
H	6.365634055248	-1.337180826187	0.357505257284
H	-6.263146042731	0.297093250719	0.119659332826
H	-5.015701503129	-0.953768473166	-0.118053168271
H	-5.112661207993	0.435527574961	-1.234947732243
H	-3.908817169373	3.033057524222	1.218155719100
H	-5.617036319623	2.672411406620	0.915591097795
H	-4.473009812285	2.757895476945	-0.443820215386
H	-5.481523067286	0.632478748619	2.558271509666
H	-3.775919404953	0.999725214375	2.864084966955
H	-4.242318489297	-0.612395261681	2.278956356490

Gaussian log archival data for CCSD single point job:

1\1\GINC-NR004\SP\UCCSD-FC\6-31G(d)\C20H45N1O1(1+,2)\JNSPENCE\09-Nov-
2 016\0\\#p gfinput iop(6/7=3) ccsd(conver=6)/6-31g(d) geom=checkpoint g
uess=read\\CCSD(T) SP TBA/tbutoxyl radical\\1,2\C,0,-1.9399293595,0.42 80861304,-
4.1433396535\C,0,-1.3358681399,0.9985216389,-2.856656625\C,0
,-0.4127797504,-0.0105472506,-2.1469842414\C,0,0.1181439376,0.60205706
26,-0.8500164261\N,0,1.1690297271,-0.2100081524,-0.0731923698\C,0,2.47
69529788,-0.178764259,-0.8673526136\C,0,3.6500065141,-0.9947491664,-0.
3217674983\C,0,4.9160326257,-0.7239792077,-1.1567096212\C,0,6.11337658
11,-1.5555308524,-0.6866346296\C,0,0.7223952714,-1.6653522543,0.094053
7778\C,0,-0.5950476439,-1.9056402822,0.8348383699\C,0,-1.0016716004,-3
.3861795145,0.708641822\C,0,-2.2745719276,-3.7101703856,1.4962693163\C
,0,1.3313930507,0.4093934993,1.3215925704\C,0,1.8638445577,1.851287196
2,1.4204921495\C,0,3.3807692389,2.0254030163,1.6100545066\C,0,3.754156
0945,3.4823086591,1.9045108848\O,0,-3.0338747952,0.6402413344,0.270406 0394\C,0,-
4.2944261679,0.9425454767,0.7508224455\C,0,-4.4608003567,0.4
573460552,2.2031970728\C,0,-5.2312336317,0.1147061114,-0.1972399913\C,
0,-4.5941502801,2.4455191237,0.5978286928\H,0,0.5919840729,1.562204475
9,-1.0625669327\H,0,-0.71221372,0.777774542,-0.1647452058\H,0,-0.98456
87592,-0.9209533261,-1.9357492289\H,0,0.3999335552,-0.2881987743,-2.82
92203426\H,0,-0.7672386784,1.9091499713,-3.0896480527\H,0,-2.134114318
1,1.2918066269,-2.164400844\H,0,-1.1612173379,0.14607545,-4.8616821069
\H,0,-2.586765715,1.1655626092,-4.6288465082\H,0,-2.5454233166,-0.4627
268043,-3.9388937933\H,0,1.5358218941,-2.1681426517,0.6191994805\H,0,0
.677997742,-2.0764929441,-0.9171160185\H,0,-0.4812365692,-1.6647174389
,1.898345541\H,0,-1.4028845151,-1.2723093513,0.4531052339\H,0,-0.18072
00597,-4.0258258534,1.0605392901\H,0,-1.1518470352,-3.6321831987,-0.35
14497217\H,0,-3.1206536095,-3.1056862902,1.1486807591\H,0,-2.140720515
1,-3.5168373044,2.5668839819\H,0,-2.5470231343,-4.7637045391,1.3800933
963\H,0,1.9696491411,-0.2745612668,1.8866008777\H,0,0.3317884504,0.358
3925792,1.7527670846\H,0,1.3704066847,2.2785247351,2.3028917256\H,0,1.
5136032771,2.4650977411,0.5824870195\H,0,3.7119988191,1.3878257456,2.4
411296572\H,0,3.931709515,1.6877614638,0.7240118443\H,0,3.2616258623,3
.842072231,2.8151379223\H,0,3.4602540048,4.1444093739,1.0815154703\H,0
,4.8341054396,3.5875524566,2.0462181683\H,0,2.2236322662,-0.5270870113
,-1.8701897598\H,0,2.7471178256,0.8763254099,-0.9447143319\H,0,3.42880
79226,-2.0668755976,-0.362801008\H,0,3.8541303504,-0.7459359304,0.7257
376296\H,0,4.7087175141,-0.9415908457,-2.213207124\H,0,5.1657276642,0.
3445473722,-1.1051640382\H,0,6.9973189151,-1.340028157,-1.2945455532\H
,0,5.90860516,-2.6293659564,-0.7656860683\H,0,6.3656340552,-1.33718082
62,0.3575052573\H,0,-6.2631460427,0.2970932507,0.1196593328\H,0,-5.015
7015031,-0.9537684732,-0.1180531683\H,0,-5.112661208,0.435527575,-1.23
49477322\H,0,-3.9088171694,3.0330575242,1.2181557191\H,0,-5.6170363196
,2.6724114066,0.9155910978\H,0,-4.4730098123,2.7578954769,-0.443820215

4\H,0,-5.4815230673,0.6324787486,2.5582715097\H,0,-3.775919405,0.99972
52144,2.864084967\H,0,-4.2423184893,-0.6123952617,2.2789563565\\Versio
n=ES64L-G09RevD.01\State=2-A\HF=-912.639842\MP2=-915.592169\MP3=-915.8
013284\MP4D=-915.8749996\MP4DQ=-915.8228659\PUHF=-912.643249\PMP2-0=-9
15.5942296\PMP3-0=-915.8025905\MP4SDQ=-915.8486689\CCSD=-915.8553076\S
2=0.758952\S2-1=0.751847\S2A=0.750062\RMSD=1.925e-09\PG=C01 [X(C20H45N
1O1)]\\@

[tBu-O•/*n*Bu$_4$N$^+$]‡

C	-1.009047964151	0.990945455798	3.669671395557
C	-0.044988383147	-0.575474922819	2.574387717390
O	1.084448125975	-0.496926601605	3.126306766551
C	-0.977907916647	-1.720960801230	2.959906599667
C	-0.222129941456	-0.003073675643	1.169948531091
C	4.232355932852	0.452619937333	3.438917427150
C	5.147951088082	0.761492781845	2.252586889627
C	4.646243269787	2.020241691009	1.519657134508
C	5.512936097420	2.375712334547	0.307793700122
N	4.614809460924	-0.749931730124	4.317994509911
C	5.896288971936	-0.408618743794	5.077805128818
C	6.513547334090	-1.513590580604	5.937097389718
C	7.700966687136	-0.957224280281	6.744837498511
C	8.391284193623	-2.035241950083	7.585937437569
C	4.864551786407	-1.995802002095	3.465546000206
C	3.747870582095	-2.426218779507	2.513962921447
C	4.186212578630	-3.672654880995	1.723352219574
C	3.101882945276	-4.161456305139	0.758179121270
C	3.443063645907	-1.041860189350	5.272555458653
C	3.093098348616	0.027661032533	6.324395735354
C	3.704746522768	-0.142076532114	7.725475403482
C	3.119714828754	0.855494834720	8.730923320426
H	4.212404634564	1.310214086673	4.114543164589
H	3.208733019353	0.268998912817	3.104440369274
H	5.167269426970	-0.073496673411	1.543295106957
H	6.182336373573	0.933465203770	2.573196495623
H	4.628031794794	2.866112616304	2.220072415199
H	3.607980497870	1.861832114246	1.198605198365
H	6.550021239846	2.572721219593	0.603169370279
H	5.133937621860	3.272758800900	-0.191630645947
H	5.522346404756	1.563469818059	-0.428324822122
H	5.073882517504	-2.800380600473	4.172478845512
H	5.784923089564	-1.797666447032	2.910043457576
H	2.830437809536	-2.652914560187	3.065717336435

H	3.496052180466	-1.623846549935	1.812916574067
H	4.444013591815	-4.479129100601	2.423267234276
H	5.102977220658	-3.447462934142	1.161364015728
H	2.847085063251	-3.390084443862	0.021899568583
H	2.184643596325	-4.431483109622	1.294631357845
H	3.438459109415	-5.046373301923	0.209318657484
H	3.680037155370	-1.992197491693	5.757360058800
H	2.585468770721	-1.188117632182	4.616809697539
H	2.001568757078	-0.020410445595	6.427477963414
H	3.289084299856	1.038714595967	5.948301351898
H	3.516918283739	-1.166450081767	8.075431450425
H	4.794754797007	-0.022425367565	7.696946313762
H	2.034554272925	0.732906153138	8.825712987639
H	3.313223758168	1.890717941860	8.425544934426
H	3.558459504213	0.714546689848	9.723578649049
H	6.617229346925	-0.088799388380	4.323320671582
H	5.652353324524	0.462404894441	5.689567016058
H	6.873677015220	-2.335509790284	5.308552783298
H	5.776711540073	-1.935352887482	6.629872358919
H	8.428671223463	-0.504532559212	6.057668947196
H	7.350023863019	-0.147464957970	7.399021222325
H	9.227179155001	-1.610872087428	8.150453883655
H	8.789082191071	-2.838752468284	6.955443847358
H	7.697311949141	-2.484968232535	8.305480250318
H	-1.999876551394	0.971610950905	3.226066774025
H	-0.375704341313	1.833398744126	3.413461684241
H	-0.920868752848	0.610975226089	4.681816604643
H	-0.669992760303	-2.609608510948	2.391441699746
H	-2.023686237739	-1.520407370555	2.714041251974
H	-0.884632985256	-1.952154081199	4.023772141100
H	-1.266717914641	0.198803524156	0.920140383229
H	0.149899766788	-0.749639030423	0.454570613988

H 0.370677589605 0.906769560764 1.047693237912

Gaussian log archival data for CCSD single point job:

1\1\GINC-NR022\SP\UCCSD-FC\6-31G(d)\C20H45N1O1(1+,2)\JNSPENCE\27-Oct-2016\0\\#p gfinput iop(6/7=3) ccsd/6-31g(d) geom=checkpoint guess=read\ \CCSD(T) SP TS TBA/tbutoxyl radical\\1,2\C,0,-1.0090479642,0.9909454558,3.6696713956\C,0,-0.0449883831,-0.5754749228,2.5743877174\O,0,1.0844 48126,-0.4969266016,3.1263067666\C,0,-0.9779079166,-1.7209608012,2.9599065997\C,0,-0.2221299415,-0.0030736756,1.1699485311\C,0,4.2323559329,0.4526199373,3.4389174271\C,0,5.1479510881,0.7614927818,2.2525868896\C,0,4.6462432698,2.020241691,1.5196571345\C,0,5.5129360974,2.3757123345,0.3077937001\N,0,4.6148094609,-0.7499317301,4.3179945099\C,0,5.896288

9719,-0.4086187438,5.0778051288\C,0,6.5135473341,-1.5135905806,5.93709
73897\C,0,7.7009666871,-0.9572242803,6.7448374985\C,0,8.3912841936,-2.
0352419501,7.5859374376\C,0,4.8645517864,-1.9958020021,3.4655460002\C,
0,3.7478705821,-2.4262187795,2.5139629214\C,0,4.1862125786,-3.67265488
1,1.7233522196\C,0,3.1018829453,-4.1614563051,0.7581791213\C,0,3.44306
36459,-1.0418601894,5.2725554587\C,0,3.0930983486,0.0276610325,6.32439
57354\C,0,3.7047465228,-0.1420765321,7.7254754035\C,0,3.1197148288,0.8
554948347,8.7309233204\H,0,4.2124046346,1.3102140867,4.1145431646\H,0,
3.2087330194,0.2689989128,3.1044403693\H,0,5.167269427,-0.0734966734,1
.543295107\H,0,6.1823363736,0.9334652038,2.5731964956\H,0,4.6280317948
,2.8661126163,2.2200724152\H,0,3.6079804979,1.8618321142,1.1986051984\
H,0,6.5500212398,2.5727212196,0.6031693703\H,0,5.1339376219,3.27275880
09,-0.1916306459\H,0,5.5223464048,1.5634698181,-0.4283248221\H,0,5.073
8825175,-2.8003806005,4.1724788455\H,0,5.7849230896,-1.797666447,2.910
0434576\H,0,2.8304378095,-2.6529145602,3.0657173364\H,0,3.4960521805,-
1.6238465499,1.8129165741\H,0,4.4440135918,-4.4791291006,2.4232672343\
H,0,5.1029772207,-3.4474629341,1.1613640157\H,0,2.8470850633,-3.390084
4439,0.0218995686\H,0,2.1846435963,-4.4314831096,1.2946313578\H,0,3.43
84591094,-5.0463733019,0.2093186575\H,0,3.6800371554,-1.9921974917,5.7
573600588\H,0,2.5854687707,-1.1881176322,4.6168096975\H,0,2.0015687571
,-0.0204104456,6.4274779634\H,0,3.2890842999,1.038714596,5.9483013519\
H,0,3.5169182837,-1.1664500818,8.0754314504\H,0,4.794754797,-0.0224253
676,7.6969463138\H,0,2.0345542729,0.7329061531,8.8257129876\H,0,3.3132
237582,1.8907179419,8.4255449344\H,0,3.5584595042,0.7145466898,9.72357
8649\H,0,6.6172293469,-0.0887993884,4.3233206716\H,0,5.6523533245,0.46
24048944,5.6895670161\H,0,6.8736770152,-2.3355097903,5.3085527833\H,0,
5.7767115401,-1.9353528875,6.6298723589\H,0,8.4286712235,-0.5045325592
,6.0576689472\H,0,7.350023863,-0.147464958,7.3990212223\H,0,9.22717915
5,-1.6108720874,8.1504538837\H,0,8.7890821911,-2.8387524683,6.95544384
74\H,0,7.6973119491,-2.4849682325,8.3054802503\H,0,-1.9998765514,0.971
6109509,3.226066774\H,0,-0.3757043413,1.8333987441,3.4134616842\H,0,-0
.9208687528,0.6109752261,4.6818166046\H,0,-0.6699927603,-2.6096085109,
2.3914416997\H,0,-2.0236862377,-1.5204073706,2.714041252\H,0,-0.884632 9853,-
1.9521540812,4.0237721411\H,0,-1.2667179146,0.1988035242,0.92014
03832\H,0,0.1498997668,-0.7496390304,0.454570614\H,0,0.3706775896,0.90
67695608,1.0476932379\\Version=ES64L-G09RevD.01\State=2-A\HF=-912.6017
824\MP2=-915.5683627\MP3=-915.7703758\MP4D=-915.8457004\MP4DQ=-915.793
3685\PUHF=-912.6148116\PMP2-0=-915.5790655\PMP3-0=-915.7779005\MP4SDQ=
-915.8214527\CCSD=-915.8291878\S2=0.877509\S2-1=0.831377\S2A=0.752816\
RMSD=5.262e-09\PG=C01 [X(C20H45N1O1)]\\@

Appendix D

Higher Barrier Biosourced Polyester from Dimethyl [2,2'-bifuran]-5,5'-dicarboxylate

H. Eliot Edling [a], Hua Sun [b], Edward Paschke [c], David A. Schiraldi [b], James M. Tanko [d], Mark Paradzinsky [d], S. Richard Turner [a,]*

Supplemental Figures

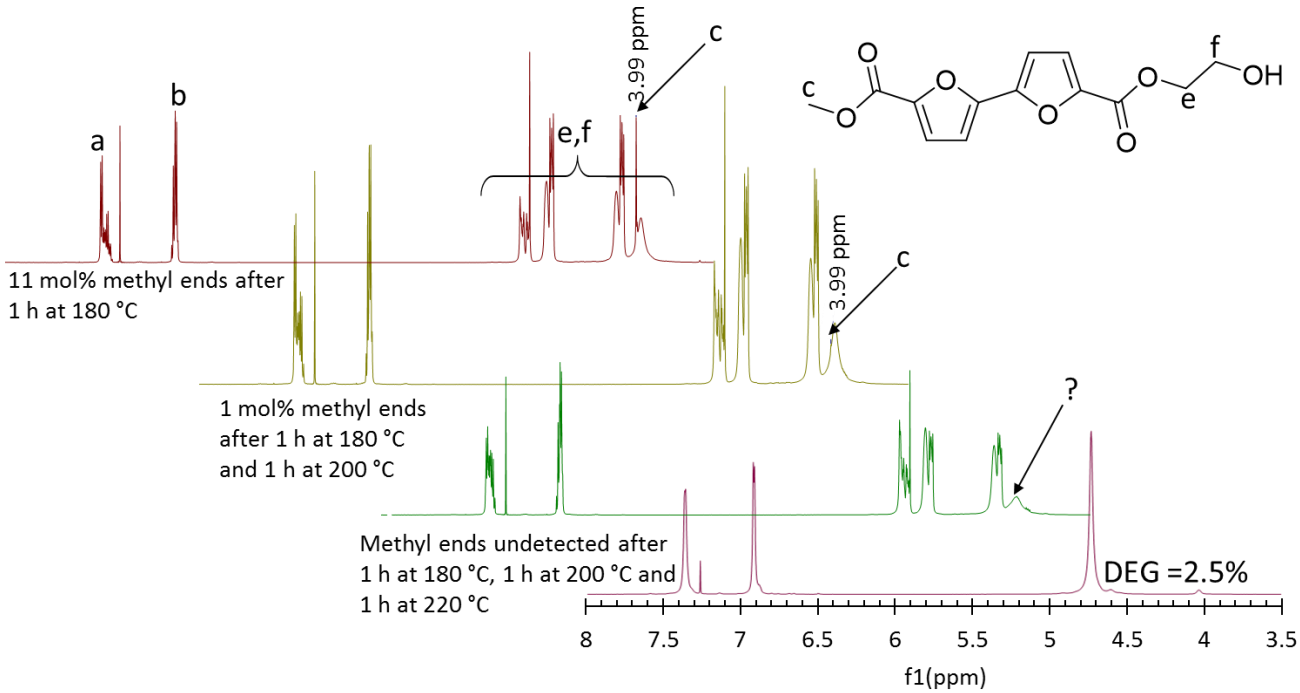

Figure D.1. Progress of transesterification was determined using ^{1}H NMR by following the concentration of methyl ends present in the melt. Transesterification is complete when methyl ends are no longer present.

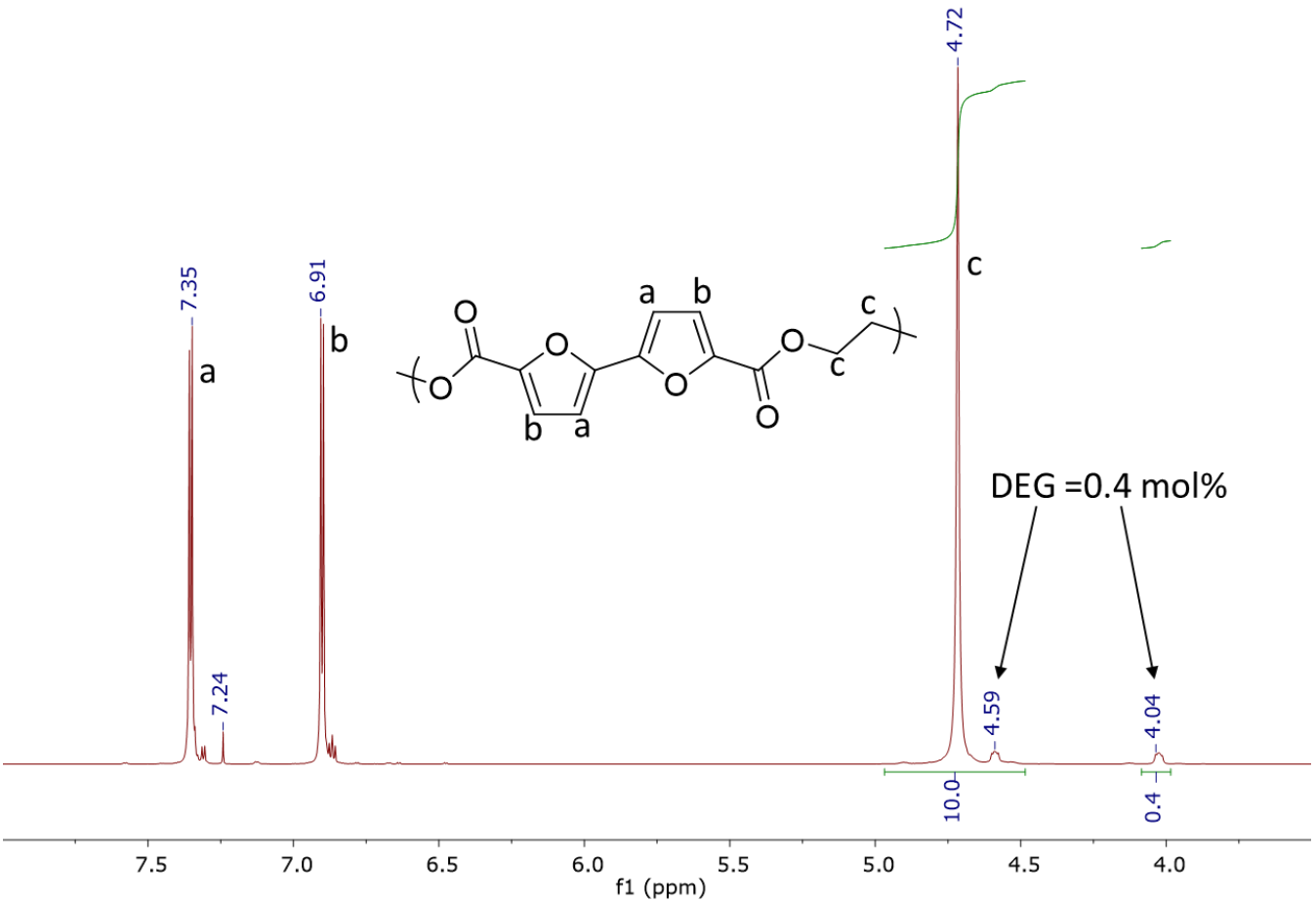

Figure D.2. ^{1}H NMR of PEBF produced from HBEBF

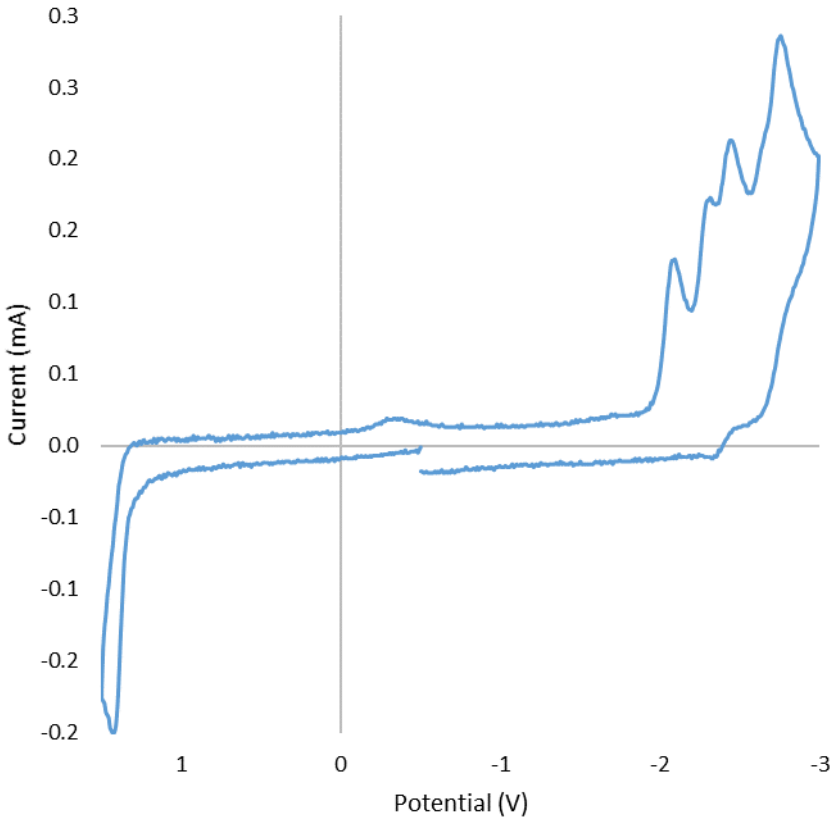

Figure D.3. Cyclic voltammogram of BFE at a scan rate of 100 mV s^{-1}.

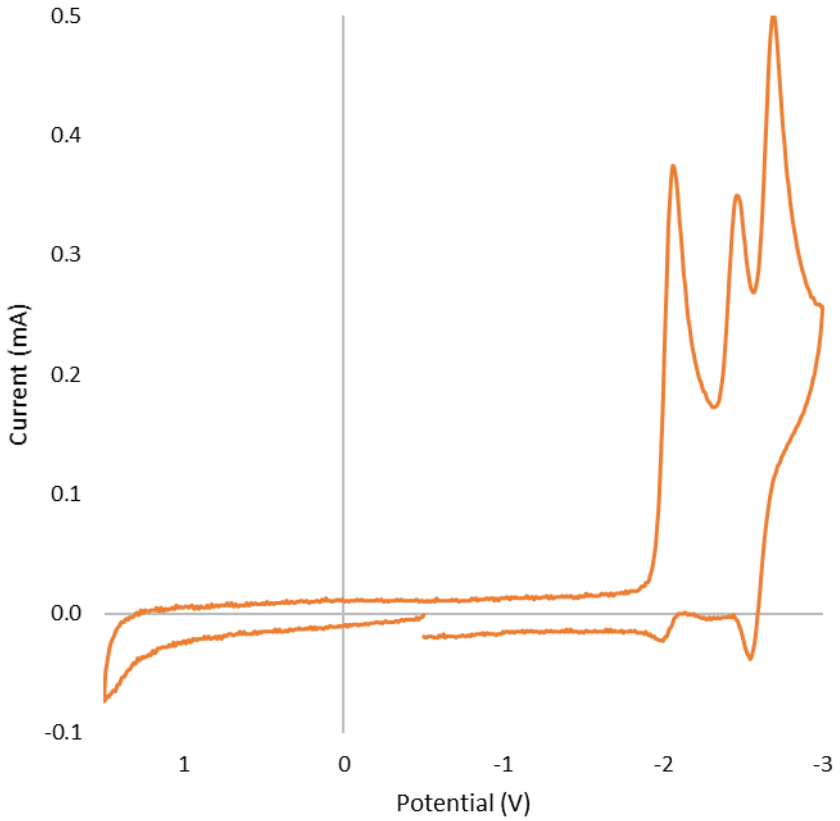

Figure D.4. Cyclic voltammogram of BE at a scan rate of 100 mV s^{-1}.

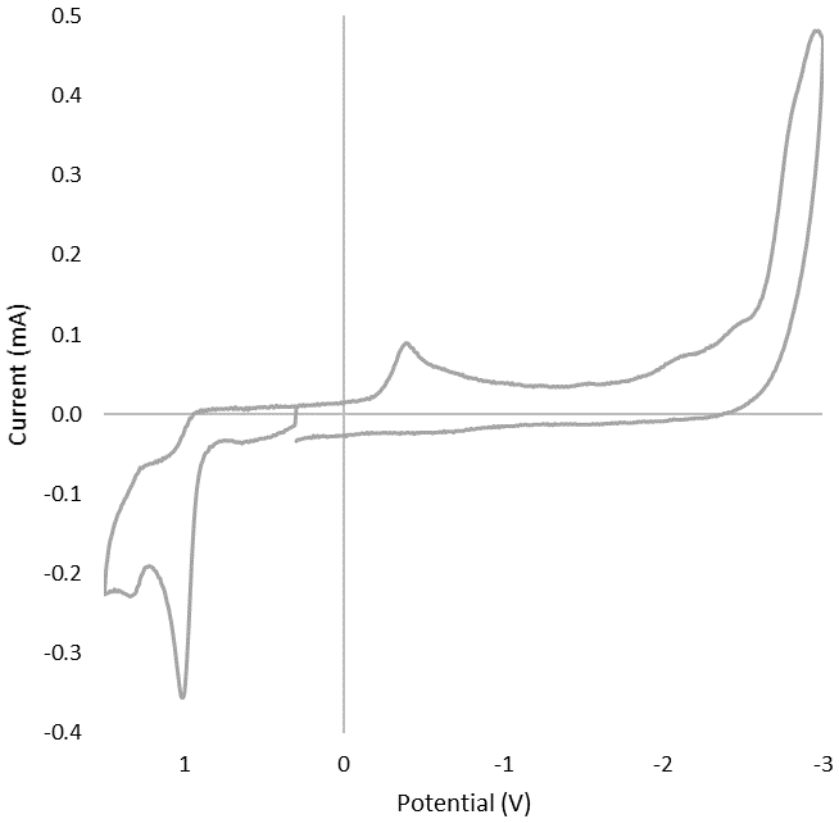

Figure D.5. Cyclic voltammogram of BFDMA at a scan rate of 100 mV s^{-1}.

Figure D.6. Uniaxially stretched dogbone

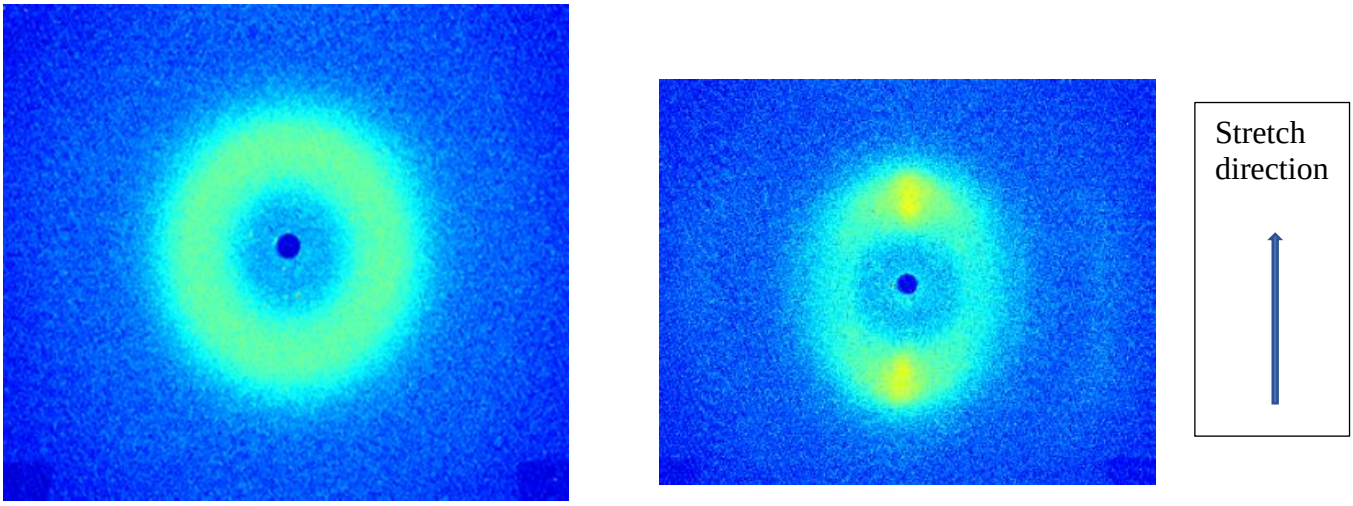

Figure D.7. WAXS before uniaxial stretch and after uniaxial stretch